Universidade do Minho
Escola de Engenharia

Rafael Ramírez Álvarez de Lara

Hygro–thermo–mechanical analysis of masonry: Experimental characterization and numerical simulations

January 2023

Hygro–thermo–mechanical analysis of masonry:
Experimental characterization and numerical simulations

Rafael Ramírez Álvarez de Lara

UMinho | 2023

FCT Fundação para a Ciência e a Tecnologia
REPÚBLICA PORTUGUESA | CIÊNCIA, TECNOLOGIA E ENSINO SUPERIOR
NORTE2020 PROGRAMA OPERACIONAL REGIONAL DO NORTE
PORTUGAL 2020
UNIÃO EUROPEIA Fundo Social Europeu

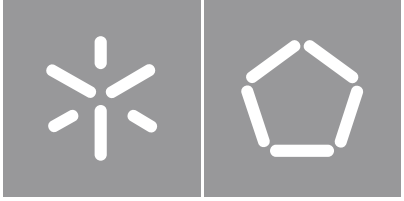

Universidade do Minho
Escola de Engenharia

Rafael Ramírez Álvarez de Lara

Hygro–thermo–mechanical analysis of masonry: Experimental characterization and numerical simulations

Doctoral Thesis
Civil Engineering

Work concluded under the supervision of:
Professor Paulo B. Lourenço
Professor Bahman Ghiassi
Professor Paloma Pineda

January 2023

DIREITOS DE AUTOR E CONDIÇÕES DE UTILIZAÇÃO DO TRABALHO POR TERCEIROS

Este é um trabalho académico que pode ser utilizado por terceiros desde que respeitadas as regras e boas práticas internacionalmente aceites, no que concerne aos direitos de autor e direitos conexos.

Assim, o presente trabalho pode ser utilizado nos termos previstos na licença abaixo indicada.

Caso o utilizador necessite de permissão para poder fazer um uso do trabalho em condições não previstas no licenciamento indicado, deverá contactar o autor, através do RepositóriUM da Universidade do Minho.

Licença concedida aos utilizadores deste trabalho

Atribuição-NãoComercial-CompartilhaIgual
CC BY-NC-SA

https://creativecommons.org/licenses/by-nc-sa/4.0/

Acknowledgements

This work would not have been possible without the effort and support of many people who have been directly or indirectly involved in the process. I would like to express my gratitude to all of them.

First and foremost, I would like to thank my supervisors for their fundamental assistance, their dedication, and their encouragement. To Professor Paulo B. Lourenço, thank you for giving me the chance to be part of the research group, for being a source of inspiration, and for giving me a push when I needed it. To Professor Bahman Ghiassi, thank you for your guidance, for all the knowledge that you shared, all your suggestions and discussions, and for your infinite patience with me. To Professor Paloma Pineda, thank you for introducing me to the world of scientific research, for taking me under your wing, and for your constant help throughout all these years.

I would like to extend my gratitude to all the professionals who have contributed to the development of this investigation; to Doctor Meera Ramesh and Doctor–to–be Georgios Karanikoloudis, for providing material support for the experimental works; to our colleagues at the University of Beira Interior, namely Professor João Castro–Gomes and Erick Grünhäuser Soares, who arranged and performed the mercury intrusion porosimetry tests; to the technicians of the Structures Laboratory at the University of Minho, for their assistance with the experimental campaign; to the COMSOL Support personnel, for their guidance with the software. My gratitude to the Portuguese Foundation for Science and Technology (FCT) for their financial support through the grant agreement SFRH/BD/117114/2016.

I would like to thank all the colleagues who became friends along the way: Maria Pia, Giorgos, Gianpaolo, Ioana, Maxime, Telma, Chandan, Nicoletta, Fabio, Sandra, Carolina, Abide... and so many others that they would not fit in just this one page. This experience would not have been the same without you. A special mention to my flatmates in Guimarães: Meera, Xinyu, Leslie, Antonio, Alberto, Elesban, and Pilar. You made Cappu's house feel like home.

Thanks to all my teachers and professors who showed me the value of knowledge and learning, and helped me get where I am.

Finally, I would like to dedicate this work to my family for their unconditional love and support. I will be eternally grateful to you.

STATEMENT OF INTEGRITY

I hereby declare having conducted this academic work with integrity. I confirm that I have not used plagiarism or any form of undue use of information or falsification of results along the process leading to its elaboration.

I further declare that I have fully acknowledged the Code of Ethical Conduct of the University of Minho.

Análise higro–termo–mecânica de alvenaria: Caracterização experimental e simulações numéricas

Resumo: As construções de alvenaria espalham–se por todo o mundo, não só em estruturas históricas como também em edifícios contemporâneos. As fachadas de alvenaria constituem uma parte principal da envolvente do edifício, enquanto as paredes portantes funcionam como parte integrante do sistema estrutural. Além disso, as paredes externas estão expostas a ações ambientais que afetam a resposta estrutural e produzem degradação a longo prazo. Neste contexto, os processos higrotérmicos são de especial interesse, uma vez que podem levar a danos significativos. Portanto, a prevenção e reparação de danos relacionados com a temperatura e a humidade na alvenaria precisam de uma compreensão acurada de seu comportamento higrotérmico. Esta tese investiga o comportamento higro–termo–mecânico da alvenaria submetida a condições ambientais. A metodologia engloba a caracterização experimental, bem como simulações numéricas do transporte de calor e humidade e sua influência no desempenho mecânico da alvenaria. A investigação centra–se na alvenaria de tijolo com dois tipos de argamassa, nomeadamente de cal hidráulica natural e de cimento. Como resultado do programa experimental, um conjunto consistente de propriedades do material foi obtido e posteriormente usado para validação de modelos numéricos. Em relação às simulações numéricas, um modelo de transporte de humidade por difusividade foi usado para reproduzir os resultados experimentais de absorção e secagem. Foi demonstrado que a difusividade precisa de ser ajustada de acordo com o processo (absorção/secagem). Além disso, a interface tijolo–argamassa introduz uma resistência hidráulica para a absorção. Um modelo higrotérmico totalmente acoplado foi utilizado para simular a transferência de calor e massa em uma parede de alvenaria. O modelo higrotérmico foi alargado para incorporar efeitos mecânicos e um modelo higro–termo–mecânico acoplado unidirecionalmente foi utilizado para analisar a distribuição de tensões em elementos de alvenaria afetados por variações de temperatura e humidade. Demostrou-se que as condições higrotérmicas alteram significativamente a distribuição de tensões internas da estrutura. A investigação apresentada avança o conhecimento do comportamento higro–termo–mecânico da alvenaria e contribui para a caracterização de materiais e estruturas. A aplicação de técnicas de modelação comumente utilizadas para a análise estrutural de alvenaria oferece grandes possibilidades para o estudo de problemas de transporte de calor e humidade.

Palavras-chave: alvenaria; análise higro–termo–mecânica; caracterização experimental; material multicamadas; modelação numérica.

Hygro–thermo–mechanical analysis of masonry: Experimental characterization and numerical simulations

Abstract: Masonry constructions are spread all around the world, not only in historical structures but in new buildings as well. Masonry facades make up a fundamental part of the building envelope, whereas load–bearing walls work as an integral part of the structural system. Additionally, the external walls are usually exposed to environmental actions that affect the structural response and produce degradation in the long–term. In this context, hygrothermal processes are of special interest since they may lead to significant damage. Thus, prevention and repair of heat– and moisture–related damage in masonry requires a thorough understanding of its hygrothermal behaviour. This thesis investigates the hygro–thermo–mechanical behaviour of masonry subjected to environmental conditions. The methodology encompasses experimental characterization as well as numerical simulations of heat and moisture transport and their influence on the mechanical performance of masonry. The research focuses on brick masonry with two types of mortar, namely natural hydraulic lime and cement mortar. The experimental program included tests on constituent materials and multi–layered masonry specimens. As a result, a consistent dataset of material properties was obtained and later used for input and validation of numerical models. Regarding the numerical simulations, a diffusivity moisture transport model was used to reproduce water absorption and drying in single materials and multi–layered cases. The model was calibrated and validated against the experimental results. It was demonstrated that the diffusivity function needs to be adjusted depending on the process (wetting/drying). Moreover, the brick–mortar interface works as a hydraulic resistance for water absorption. A fully–coupled hygrothermal model was employed to simulate heat and mass transfer in a brick masonry wall. The hygrothermal model was extended to incorporate mechanical effects and a unidirectionally coupled hygro–thermo–mechanical model was used to analyse the stress distribution of masonry elements as affected by temperature and moisture loads. It was shown that the imposed hygrothermal conditions significantly change the internal stress distribution of the structure. The presented research advances our understanding of hygro–thermo–mechanical behaviour of masonry and thus contributes to the characterization of masonry materials and structures. The application of modelling strategies commonly used for the structural analysis of masonry offers great possibilities for the study of heat and moisture transport problems.

Keywords: experimental characterization; hygro–thermo–mechanical analysis; masonry; multi–layered material; numerical modelling.

Table of contents

List of figures

This page has been intentionally left blank

List of tables

List of symbols

Abbreviations

B	Fired–clay brick
CHE	Coefficient of hygric expansion
CTE	Coefficient of thermal expansion
CM	Portland cement mortar
CoV	Coefficient of variation
HL	Hydrated lime
HT	Hygrothermal
HTM	Hygro–thermo–mechanical
Int.	Interface
IRA	Initial rate of absorption
IUPAC	International Union of Pure and Applied Chemistry
LB	Lower bound
LM	Natural hydraulic lime mortar
LMJ	Natural hydraulic lime mortar from masonry bed joints
MIP	Mercury intrusion porosimetry
ND	Not defined
NHL	Natural hydraulic lime
NRMSE	Normalised root mean square error
OPC	Ordinary Portland cement
REF	Reference
REV	Representative Elementary Volume
RH	Relative humidity
SS	Steady–state
SW	Southwest
TD	Time–dependent
UB	Upper bound

Latin symbols

Symbol	Units	Description
A	m^2	Area
A_w	$\mathrm{kg}/(\mathrm{m}^2 \cdot \mathrm{s}^{0.5})$	Coefficient of water absorption
a	$1/\mathrm{Pa}$	Fitting parameter (Mualem–van Genuchten sorption isotherm model)
a_V	–	Volume fraction of air–filled pores
b	–	Thermal conductivity supplement
$\mathcal{C}$	$\mathrm{m}^2/\mathrm{s}^2$	Derivative of the inverse moisture retention curve
C_p	$\mathrm{J}/(\mathrm{kg} \cdot \mathrm{K})$	Specific heat capacity of dry material
C_w	$\mathrm{J}/(\mathrm{kg} \cdot \mathrm{K})$	Specific heat capacity of liquid water
c_v	kg/m^3	Water vapour concentration
D_a	m^2/s	Water vapour diffusivity of still air
D_v	m^2/s	Water vapour diffusivity
D_w	m^2/s	Liquid water diffusivity
D_φ	m^2/s	Liquid conduction coefficient
d	m	Pore diameter
E	W/m^2	Emitted radiation
E	Pa	Elastic modulus
f_b	Pa	Flexural strength
f_c	Pa	Compressive strength
f_t	Pa	Tensile strength
G_c	N/m	Fracture energy in compression
G_f^I	N/m	Fracture energy in tension
G_v	kg/s	Mass change rate
g	$\mathrm{kg}/(\mathrm{m}^2 \cdot \mathrm{s})$	Moisture flux
g_v	$\mathrm{kg}/(\mathrm{m}^2 \cdot \mathrm{s})$	Water vapour flux
g_w	$\mathrm{kg}/(\mathrm{m}^2 \cdot \mathrm{s})$	Liquid water flux
g_{IF}	$\mathrm{kg}/(\mathrm{m}^2 \cdot \mathrm{s})$	Moisture flux across the interface
H	J/m^3	Enthalpy density
h	m	Height
h_m	s/m	Convective mass transfer coefficient
h_T	$\mathrm{W}/(\mathrm{m}^2 \cdot \mathrm{K})$	Convective heat transfer coefficient

$h_{T,c}$	$\mathrm{W/(m^2 \cdot K)}$	Convective heat transfer coefficient (not lumped)
$h_{T,r}$	$\mathrm{W/(m^2 \cdot K)}$	Radiative heat transfer coefficient (not lumped)
K_{IF}	$\mathrm{s/m}$	Interface hydraulic permeability
K_l	$\mathrm{kg/(m \cdot s \cdot Pa)}$	Liquid water permeability
k	$\mathrm{kg/m^{2.5}}$	Proportionality factor for temperature dependency of the absorption coefficient
L	$\mathrm{kN/m}$	Uniformly distributed load
L_v	$\mathrm{J/kg}$	Latent heat of vaporization
l	m	Length or thickness
M	–	Number of fitting parameters
m	–	Fitting parameter (Mualem–van Genuchten sorption isotherm model)
m_{dry}	kg	Dry mass
m_{im}	kg	Hydrostatic mass
m_{sat}	kg	Saturated mass
m_v	kg	Mass of water vapour
N	–	Number of measured data or number of data points in a population
n	–	Fitting parameter (Mualem–van Genuchten sorption isotherm model)
p	Pa	Ambient barometric pressure
p_0	Pa	Standard atmospheric pressure
p_c	Pa	Capillary pressure
p_s	Pa	Suction pressure
p_v	Pa	Partial vapour pressure
$p_{v,sat}$	Pa	Saturation vapour pressure
q	$\mathrm{W/m^2}$	Heat flux
R^2_{adj}	–	Adjusted R^2
R_v	$\mathrm{J/(kg \cdot K)}$	Universal gas constant for water vapour
R_{IF}	$\mathrm{m/s}$	Interface hydraulic resistance
R_T	$\mathrm{(m^2 \cdot K)/W}$	Thermal resistance
R_v	$\mathrm{J/(kg \cdot K)}$	Universal gas constant for water vapour
R^2	–	Coefficient of determination, R–squared
r	m	Pore radius
S_l	–	Saturation degree
T	K	Temperature
t	m	Thickness

t	s	Time
u	m	Displacement
V	m^3	Volume
V_{bulk}	m^3	Bulk volume
V_{neg}	–	Control parameter for hysteresis model
V_{pos}	–	Control parameter for hysteresis model
W_s	%	Water absorption
w	$\mathrm{kg/m}^3$	Moisture content
w_{cap}	$\mathrm{kg/m}^3$	Capillary moisture content
w_g	kg/kg	Gravimetric moisture content
w_{sat}	$\mathrm{kg/m}^3$	Saturation moisture content
w_V	$\mathrm{m}^3/\mathrm{m}^3$	Volumetric moisture content
x_{exp}	–	Measured values
x_{pre}	–	Predicted values

Greek symbols

Symbol	Units	Description
α	–	Absorptivity
α_h	m^3/kg	Coefficient of hygric expansion
α_T	$1/℃$	Coefficient of thermal expansion
β	m^3/kg	Coefficient of hygroscopic swelling
β_{IF}	$\mathrm{kg}/(\mathrm{m}^2 \cdot \mathrm{s})$	Interface moisture transfer coefficient
γ	–	Diffusivity factor
γ	$\mathrm{kN/m}^3$	Specific weight
δ_a	$\mathrm{kg}/(\mathrm{m} \cdot \mathrm{s} \cdot \mathrm{Pa})$	Water vapour permeability of still air
δ_v	$\mathrm{kg}/(\mathrm{m} \cdot \mathrm{s} \cdot \mathrm{Pa})$	Water vapour permeability
ε	–	Emissivity
ε	–	Strain
ε_h	–	Hygric strain
ε_T	–	Thermal strain
η	$\mathrm{Pa} \cdot \mathrm{s}$	Dynamic viscosity
θ	deg	Contact angle

ϑ	°C	Temperature
λ	$\mathrm{W/(m \cdot K)}$	Thermal conductivity
λ_0	$\mathrm{W/(m \cdot K)}$	Thermal conductivity of the solid matrix
μ	–	Water vapour resistance factor
μ_{dry}	–	Water vapour resistance factor (dry cup)
μ_{wet}	–	Water vapour resistance factor (wet cup)
ν	–	Poisson's ratio
ξ	$\mathrm{kg/m^3}$	Moisture storage capacity
ρ_{bulk}	$\mathrm{kg/m^3}$	Bulk density
ρ_w	$\mathrm{kg/m^3}$	Density of water
ρC	$\mathrm{J/(m^3 \cdot K)}$	Volumetric heat capacity
σ	$\mathrm{W/(m^2 \cdot K^4)}$	Stefan–Boltzmann constant
σ	$\mathrm{N/m}$	Surface tension
σ	Pa	Stress
σ_1	Pa	Maximum principal stress
σ_3	Pa	Minimum principal stress
τ	–	Tortuosity
φ	–	Relative humidity
ϕ_o	–	Open porosity
ψ	–	Fitting parameter (Künzel's sorption isotherm model)

Subscripts

Symbol	Description
αds	Adsorption
des	Desorption
ext	Exterior
EQ	Equivalent
int	Interior
ISO	Isotropic
v	Water vapour
w	Liquid water

This page has been intentionally left blank

CHAPTER 1

Introduction

This opening chapter presents the general framework and motivation for this research as well as its principal objectives. First, a brief exposition of the background is set out in order to understand the context of the work. Subsequently, the main objectives of the research are listed. Finally, a succinct description of the contents of the thesis and its structure is provided.

1.1 GENERAL FRAMEWORK AND MOTIVATION

Masonry has been traditionally used as the main construction material in historical structures all around the world. Nowadays, brickwork is still commonly used in veneer walls and infill walls within contemporary concrete and steel frame structures. Due to their enveloping nature, masonry facades play a major role in the overall energy efficiency of buildings and control of indoor conditions. In turn, load–bearing walls work as an integral part of the structural system. Additionally, the external walls are usually exposed to environmental actions, such as solar radiation, wind–driven rain, temperature and moisture variations, condensation and rising damp. Such environmental exposure affects the structural response and in the long–term produces degradation in each constituent material as well as in masonry as a whole (Ghiassi & Lourenço, 2019; Bompa & Elghazouli, 2020b; D'Altri & de Miranda, 2020). Hence, hygrothermal processes are of special interest from a durability standpoint since they may lead to significant damage, e.g. cracking due to induced volumetric changes, spalling caused by freeze–thaw cycles and (crypto)efflorescence due to salt crystallization (Brooks, 2015; Sciolti et al., 2015). Consequently, prevention and repair of heat– and moisture–related damage in masonry require a thorough understanding of its hygrothermal behaviour.

Considering the importance of hygrothermal phenomena on building performance, various models and numerical tools have been developed to simulate heat and moisture transport in porous building materials, e.g. Künzel et al. (2001), Straube & Burnett (2001), Hens, (2007). Most models for heat and mass transfer have put their focus on homogenous porous materials, whereas studies on multi–layered cases are still scarce. These multi–layered problems, however, are the most common scenario for building physics applications and demand specific requirements, such as the need to define a driving potential continuous across the interfaces, or the need for consideration of the interfacial impact on the

heat and mass transfer mechanisms. Regardless of the chosen approach, a series of material parameters is always necessary to describe the hygrothermal behaviour of a given porous medium.

Although the thermal properties of building materials and the corresponding testing methods have been well established in the literature, a reliable characterization of the moisture–related properties still needs more attention (Feng & Janssen, 2016). Numerous works have documented the hygric properties of clay brick, e.g. Kumaran (1996), Roels, Carmeliet, et al. (2003), Scheffler (2008), Aït Oumériane et al. (2021). However, the existent studies also reveal high intrinsic variability so the extrapolation of literature data to specific real case scenarios is not always straightforward. Moreover, most databases assume isotropic properties and very few references study the possible anisotropic behaviour, which has been nonetheless demonstrated for both moulded and extruded bricks (Gummerson et al., 1980; Krakowiak et al., 2011). Considering the composite nature of masonry, the analysis of mortar and brick–mortar combinations must be included for a consistent definition of the material. The most common mortars used in masonry structures are lime– and cement–based mixes. Lime mortars are more frequently found in historical constructions. However, most characterization studies have focused on cement–based mixes. Similarly, the available studies on brick masonry are mostly concerned with cement–based mortars, and few cases tackle the combination of brick and lime–based mixes, e.g. Groot & Gunneweg (2010a), Nunes et al. (2017), Delgado et al. (2019a), Calle et al. (2019). Moreover, experimental studies generally make use of mortar specimens cast in moulds under controlled laboratory conditions. However, it is known that the different curing conditions obtained between bricks in masonry joints can influence the final quality of the mortar.

The study of hygrothermal problems in multi–layered materials has attracted much attention during the last decades. The existing literature on the topic comprises experimental, analytic, and numerical works, which account for the interfacial effects from different points of view. More specifically, the experimental studies on moisture transport in layered composites have been covered to some extent in the literature, e.g. Wilson et al. (1995a, 1995b), Hall & Hoff (2009), Vereecken et al. (2020). However, the experimental works focused on moisture transport in masonry are still limited. In addition, most of the available research has been devoted to liquid water absorption, whereas drying has been scarcely studied. Likewise, only a few investigations have dealt with interface modelling for moisture transport problems in masonry and the conclusions from these works vary from one author to another depending on the adopted methodology and the eventual purpose of the study (Brocken, 1998; Derluyn et al., 2011; Janssen et al., 2012; Vereecken & Roels, 2013; Calle et al., 2019; X. Zhou et al., 2020). Therefore, a unified approach to characterize the brick–mortar interfaces has not been reached yet.

Most of the scientific advances in heat and mass transfer in porous building materials have come from the disciplines of Material Sciences and Building Physics. In this context, the improvement of hygrothermal models and the development of new numerical tools have allowed for more complex and detailed hygrothermal simulations. Nonetheless, the link between the heat and moisture fields and solid mechanics has not been exploited yet. On one hand, experimental studies on structural elements are normally conducted under controlled, standard laboratory conditions. On the other hand, numerical simulations usually neglect the influence of hygrothermal loads and assume ideal conditions. The study of hygro–thermo–mechanical effects has received more attention in concrete structures, e.g. curing of concrete for application in dams (Conceição et al., 2017; Ponce–Farfán et al., 2020). For masonry, some research has been devoted to the mechanical behaviour of walls under extreme scenarios such as high temperatures during fire, see e.g. R. G. Oliveira et al. (2021). However, the influence of temperature and moisture actions caused by normal environmental conditions are usually disregarded and so are the hygrothermal–induced stresses. To date, few studies have approached the mechanical response of masonry as affected by this type of environmental conditions, e.g. Khoshbakht & Lin (2010), Ramézani & Jeong, (2011), Castellazzi, de Miranda, Formica, et al. (2015), and therefore further research is required.

1.2 OBJECTIVES

Given the context explained above, the main objective of this thesis is to investigate the hygro–thermo–mechanical behaviour of masonry elements and structures subjected to real environmental conditions. Considering the broad extent of this topic, the investigation is limited to brick masonry walls built with two types of mortar, namely natural hydraulic lime and cement mortar. The focus is set on numerical simulations of heat and moisture transport and their influence on the mechanical performance of masonry. Additionally, the numerical investigation is complemented by the experimental characterization of material properties.

The detailed objectives of the work are given below:

- Build systematic knowledge for the hygro–thermo–mechanical behaviour of masonry by means of an integrated approach including numerical simulations and experimental tests. The final goal is to understand the hygrothermal response of masonry and how temperature and moisture variations affect the internal stress distribution of masonry structures.
- Develop a comprehensive database of hygro–thermo–mechanical material properties. For this investigation, the focus is placed on physical and moisture transport parameters. A commonly

used set of masonry materials is chosen for experimental characterization, namely solid extruded fired–clay brick, natural hydraulic lime mortar and cement mortar. Among the main goals of the experimental works there is the identification of possible anisotropic response of the materials, different behaviour between the selected mortars, and variation of the mortar properties depending on the curing conditions, namely cast in moulds or cured in masonry joints.

- Evaluate the impact of brick–mortar interfaces on the overall hygrothermal behaviour of masonry. The aim is to determine whether the hygrothermal response of masonry is equivalent to the simple addition of its constituent parts or if there are interfacial effects that need to be accounted for as well. If interfacial phenomena are detected, their impact should be calculated through numerical simulations.
- Evaluate the existence of hysteretic effects in the moisture storage properties of the material. For this purpose, it is necessary to study both wetting and drying processes and assess whether the materials present different sorption isotherms or moisture retention curves for adsorption and desorption. Similarly, the presence of hysteresis in moisture transport will be assessed by examining the diffusion mechanisms for wetting and drying.
- Define the list of input parameters necessary for the chosen hygro–thermo–mechanical model and its main calibration variables. Additionally, a series of sensitivity analyses will be performed to understand how each factor affects the overall response.
- Application of different modelling strategies to the study of coupled problems in masonry. To this aim, several techniques commonly used for the structural analysis of masonry will be employed, namely micro– and macro–modelling approaches.
- Assessment of the hygrothermal behaviour of masonry by means of numerical simulations. Heat and mass transfer will be analysed separately as well as combined in a coupled hygrothermal scheme. The main purpose is to establish differences and similarities between the heat and moisture fields in the context of masonry materials. In addition, the numerical models will be used to analyse the impact of different modelling choices on the overall response, e.g. the existence of interfacial effects or the selected type of mortar.

Assessment of the hygro–thermo–mechanical behaviour of masonry by means of numerical simulations. The hygrothermal model will be extended to incorporate mechanical effects with a one–way or unidirectional coupling scheme. The numerical models will be further employed to evaluate the impact of initial and boundary conditions on the overall response. Among the goals of the numerical studies is the

hygrothermal compatibility analysis of constituent materials according to the induced stress levels resulting from heat and moisture loads.

1.3 OUTLINE OF THE THESIS

The contents of the thesis are organized into eight chapters, including the present introduction.

Chapter 2 provides a brief review of the existing literature and the current state of knowledge about the topics included in this thesis. The literature review is primarily focused on the most relevant aspects of hygro–thermo–mechanical analysis of porous and multi–layered building materials. First, an overview of heat and mass transfer problems is presented, together with commonly used heat and moisture transport models adopted by various authors. A special emphasis is placed on the different formulations available for the so–called moisture transport diffusivity approaches. Moreover, the basic set of material properties necessary for the simulation models is discussed, and a compilation of hygrothermal properties available in the literature is collected. This is followed by a discussion on hygro–thermo–mechanical models and the coupling possibilities between the different fields. Consequently, the compilation of material parameters is extended to include mechanical, thermo–mechanical and hygro–mechanical properties. Finally, the review is concluded with relevant hygrothermal and hygro–thermo–mechanical studies on masonry materials.

Chapter 3 presents the experimental methodology adopted for material characterization. The experimental investigation is mainly focused on the definition of the physical and hygric properties of the selected materials as well as relevant thermo–mechanical and hygro–mechanical parameters. First, a description of the chosen materials (extruded fired–clay brick, natural hydraulic lime mortar, and ordinary Portland cement mortar) is provided. Then, the configuration of the single–material and multi–layered masonry specimens used throughout the study is introduced. The chapter concludes with a detailed description of the experimental procedures.

The results obtained from the experimental studies are reported in Chapter 4. At first, the results of the material characterization tests on constituent materials are presented. Special attention is drawn towards the orthotropic nature of extruded fired–clay brick as well as to the differences between the two studied types of mortar. Secondly, the tests performed on multi–layered masonry specimens are discussed. Thus, the characterization of the brick–mortar interface is done on the basis of capillary absorption and drying tests. It is noted that the experimental results presented in this chapter are employed as input and validation data for subsequent simulations.

Chapter 5 addresses the numerical analysis of moisture transport phenomena in brick masonry. First, a moisture transport diffusivity model is introduced and described in detail. Afterwards, a series of numerical simulations is presented. In particular, capillary absorption and drying processes are studied at the scale of the constituent materials, and then, the analyses are extended to multi–layered cases to evaluate the impact of brick–mortar interfaces. In this context, different model parameters are selected as variables for calibration and the results are validated against experimental data following an iterative fitting procedure. Additionally, a modelling strategy is implemented to capture the hysteresis observed between adsorption and desorption (wetting/drying). Lastly, the proposed model is extended to different modelling approaches commonly used for the structural analysis of masonry.

Chapter 6 presents the simulation of different hygrothermal phenomena and their relationship with the mechanical behaviour of masonry components. Initially, the moisture transport model validated in the previous chapter is linked to the thermal field and a fully–coupled hygrothermal model is proposed. Then, hygrothermal simulations using different environmental conditions are performed to study the response of a brick masonry wall. Subsequently, the analyses are extended to incorporate mechanical effects. Thus, a one–way coupled hygro–thermo–mechanical model is presented, and its application is demonstrated on the previously studied brick masonry wall.

Chapter 7 builds upon the hygro–thermo–mechanical model presented in the previous chapter and demonstrates its application to simulate the structural behaviour of a full–scale building. For this purpose, a historic masonry tower is selected as a case study. Moreover, different environmental scenarios are evaluated in order to assess the influence of temperature and moisture variations on the mechanical behaviour of the structure.

The main conclusions of the developed research are summarized in Chapter 8, together with suggestions and proposals for future works.

Finally, a series of Appendices is provided to supply additional information and extend the main concepts introduced throughout the thesis.

CHAPTER 2

Literature review

This chapter is devoted to the available literature concerning the theoretical and practical aspects of hygro–thermo–mechanical analyses of porous and multi–layered building materials. An initial overview is provided with focus on the specific features of hygrothermal analyses for civil engineering applications and the hygrothermal properties of porous building materials used in masonry constructions. Then, a summary of relevant mathematical models and case studies is presented, with a succinct revision of the assumptions, main contributions, limitations and drawbacks of each approach. Finally, the review is extended to the hygro–thermo–mechanical models and studies available in the literature.

2.1 HYGROTHERMAL ANALYSIS OF STRUCTURES: AN INTERDISCIPLINARY APPROACH

A number of structural components, such as load–bearing masonry walls, make up an essential part of the building envelope system and actively respond to the changes in the environment between indoor and outdoor conditions, namely temperature, air pressure and humidity. This results in a constant exchange of energy and mass (dry air, water vapour, liquid water) through the building component.

It is known that temperature and moisture variations in porous materials are related to a series of mechanical effects and degradation mechanisms, such as internal stresses, deformations, volumetric changes, cracks, etc. Moreover, hygrothermal actions in multi–layered components may cause further damage due to the presence of interfaces between dissimilar materials. For instance, deformation mismatches between the constituent components, debonding and cracking at the interface are typical results of multi–layered structures exposed to temperature and humidity fluctuations.

Therefore, it is of great importance to identify the main heat and moisture sources that affect the building structures as well as the different transport mechanisms associated with those hygrothermal actions. Moreover, it is necessary to understand how these actions affect the mechanical behaviour of the materials and under which conditions they may cause damage.

The main thermal effects on building structures are linked to temperature gradients between indoor and outdoor conditions as well as heat gain by solar radiation. On the other hand, the moisture transport mechanisms through the building envelope depend on the physical state of the water and the moisture source (Figure 2.1). Water can affect a building component in liquid form as rising damp, rain or roof–water leakage. At the same time, moisture may move through the structure as water vapour and condense

on the external/internal surfaces or at the interfaces between materials in the case of multi–layered components. In addition, the source of moisture may be internal, e.g. related to the formation process of materials such as mortar or concrete.

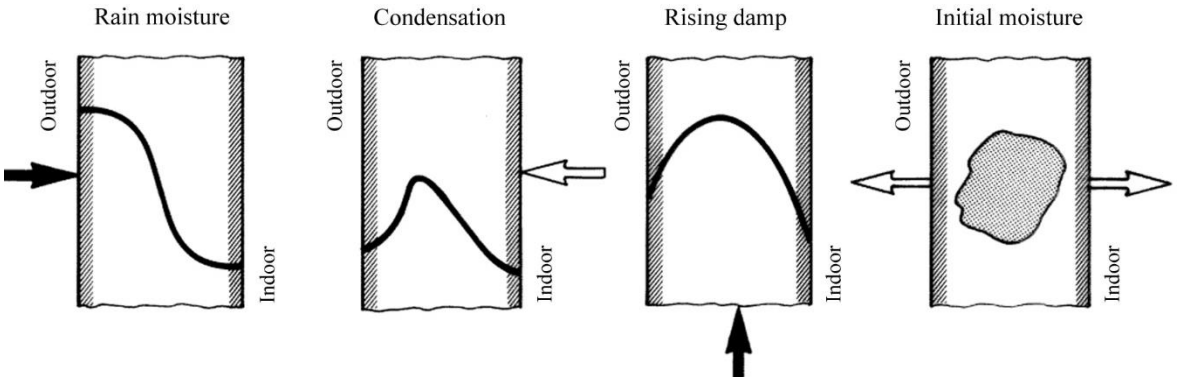

Figure 2.1. Schematic diagrams showing the effect and distribution of moisture in the cross–section of an exposed masonry wall. Adapted from Künzel (1995).

Table 2.1 provides a summary of the heat and moisture transport mechanisms that may take place in building components. It must be noted that not all the listed parameters are of interest to the present study. Several transport phenomena and their associated mechanisms will be neglected, namely airflow through the structure, and convection effects based on total pressure differences. The same applies to gravity effects, electrical fields and ion concentration gradients on moisture transport. In addition, freezing is outside the scope of the intended range of temperatures for the current research, and for analogous reasons, high–temperatures (fire conditions) are out of the discussion as well.

In the existing literature, it is possible to find numerous hygrothermal (HT) models to calculate the simultaneous heat and moisture transport in building materials and multi–layered components. However, the number of studies devoted to the coupled hygro–thermo–mechanical (HTM) analysis is still scarce. Hygro–thermo–mechanics is the generalisation of a triply coupled field of the single fields of temperature, moisture, and displacement (Szekeres, 2014). Hence, the focus of HTM studies is set on the mechanics of those materials that are thermoscopic, hygroscopic, and deformable.

According to Straube & Burnett (2001), any HTM analysis must comply with the following categories of information:

1) Geometrical configuration of the element.
2) Material properties.
3) Boundary conditions, and time–domain in the case of time–dependent analysis.
4) Physics of the coupled HTM problem.
5) Performance thresholds (failure criteria).

Each one of the categories mentioned above is also dependent on the consideration of:

a) Dimension, namely one–, two–, or three–dimensional (1–D, 2–D, 3–D).

b) Time, namely steady–state, quasi–static, or transient analysis.

c) Availability and quality of required information.

d) Stochastic nature of each data set.

Table 2.1. List of heat and moisture transport mechanisms, causes and driving potentials. Adapted from Künzel (1995).

	Transport mechanism	Cause and driving potential
Heat transport	Heat conduction	Temperature
	Heat radiation	Temperature in 4 th power
	Airflow	Total pressure, density differentials
	Enthalpy flows through moisture movement	Vapour diffusion with phase change and liquid transport flows in the temperature field
Vapour transport	Gas diffusion	Vapour pressure (temperature, total pressure)
	Molecular transport (Knudsen diffusion or effusion)	Vapour pressure
	Solution diffusion	Vapour pressure
Liquid transport	Capillary conduction	Capillary pressure
	Surface diffusion	Relative humidity
	Seepage flow	Gravitation
	Hydraulic flow	Total pressure differentials
	Electrokinesis	Electrical fields
	Osmosis	Ion concentration

2.2 HYGROTHERMAL BEHAVIOUR OF BUILDING MATERIALS

The thermal and hygric properties of porous materials are generally defined by non–linear functions dependent on the environmental conditions, namely temperature, relative humidity and air pressure. Moreover, there are mutual dependencies between the temperature and moisture fields, which entails an additional coupled problem. It must be noted that most of the available models do not include time–dependent hygrothermal material properties. This means that ageing, physical deterioration and exposure–related damage are generally not accounted for.

2.2.1 Thermal behaviour

Two main properties are used to describe the thermal behaviour of a building material, namely heat capacity and thermal conductivity. The specific heat capacity of a dry material, C_p $[\mathrm{J/(kg \cdot K)}]$, is defined as the energy required to increase the temperature of a unit mass of dry material by 1 K. If the material

is wet, the specific heat capacity, C $[\mathrm{J/(kg \cdot K)}]$, can be expressed as:

$$C = C_p + C_w \cdot (w/\rho_{bulk}) \tag{2.1}$$

where w $[\mathrm{kg/m^3}]$ is the moisture content, ρ_{bulk} $[\mathrm{kg/m^3}]$ is the bulk density of the material, and C_w $[\mathrm{J/(kg \cdot K)}]$ is the specific heat capacity of liquid water. The specific heat capacity of water has a weak thermal dependence for the range of temperatures of interest in this study. Therefore, it can be taken as a constant, $C_w = 4182\ \mathrm{J/(kg \cdot K)}$, which corresponds to the specific heat capacity of water at 20 °C. For a detailed list of saturated water properties, the reader is referred to Appendix 1 at the end of this document.

Additionally, it is useful to define the volumetric heat capacity, ρC $[\mathrm{J/(m^3 \cdot K)}]$, which is the energy required to increase the temperature of a unit volume of material by $1\ \mathrm{K}$. In wet conditions, the volumetric heat capacity can be calculated as:

$$\rho C = \rho_{bulk} C_p + w \cdot C_w \tag{2.2}$$

Along with the heat capacity, the thermal conductivity of a material characterizes its thermal behaviour. In particular, thermal conductivity refers to the ability of the material to conduct heat. Its definition stems from Fourier's Law for heat conduction, as the ratio between the heat flow at a point and the thermal gradient at that point in the direction of the flow (see Section 2.4.1 *Heat conduction*).

2.2.2 Hygric behaviour

A building material is dry if it contains no water or only chemically bonded water. In practice, this state is only possible in non–hygroscopic materials or in hygroscopic materials subjected to drying. Otherwise, hygroscopic materials in contact with moist will air adsorb water molecules from the environment within their pore structure until reaching a state of equilibrium with the ambient humidity. Similarly, capillary–active materials in contact with liquid water will absorb moisture by capillary suction until reaching a certain level of saturation. Hydrophobic materials, on the other hand, do not exhibit capillary suction.

Depending on the environmental conditions, moisture inside a building material can appear as vapour, liquid, ice, or a combination of all these phases. The different physical states can seldom be determined separately by direct measurements and phase changes are constantly taking place under natural conditions. Thus, it is only useful to analyse the total sum as a whole or so–called moisture content. Moisture content is the amount of water contained in a material. The moisture content of a building material is always expressed as a ratio, either as mass of moisture per unit volume of the dry material, w $[\mathrm{kg/m^3}]$, as mass of moisture per unit mass of the dry material, w_g $[\mathrm{kg/kg}]$, or as volume

of absorbed moisture per unit volume of the dry material, w_V [$\mathrm{m^3/m^3}$]. The moisture content can also be reported as saturation degree or percent of saturation, $S_l = w/w_{sat}$ [–], where w_{sat} is the saturation moisture content of the material expressed in any of the formats above.

The moisture content of a porous material varies from the dry state to a fully saturated condition, i.e. from null moisture content up to all the open pores filled with water (Figure 2.2). The moisture content corresponding to a fully saturated state is referred to as the saturation or maximum moisture content, w_{sat}, and is only achievable if water is forced into the pore structure, e.g. under vacuum. Otherwise, the saturation takes place at a lower moisture content level, defined as the capillary moisture content, w_{cap}. Between the dry condition and the saturation state, the moisture content changes to find an equilibrium with the water vapour pressure or relative humidity of the environment. The relation between the ambient humidity and the moisture content within the material is described by the moisture storage function. In general, moisture storage can be reported in the form of sorption isotherms or moisture retention curves. Sorption isotherms describe the moisture content with respect to relative humidity, whereas retention curves define the moisture content with respect to capillary pressure [(1)]. Numerous analytical expressions are available in the literature for the definition of these moisture storage functions. The different models vary in their flexibility and capacity to represent more complex moisture storage behaviour (e.g. hygroscopic materials and multi–modal curves), and in the number of fitting parameters. A discussion on the different moisture storage models is out of the scope of this review, so the interested reader is referred to specialized works, e.g. Sillers et al. (2001), Carmeliet & Roels (2002).

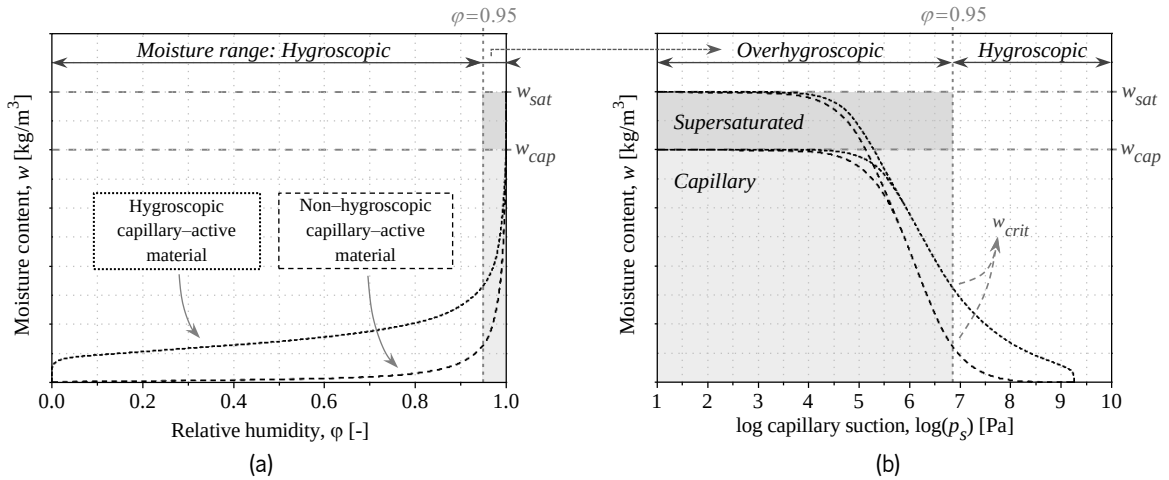

Figure 2.2. Moisture storage functions of hygroscopic and non–hygroscopic porous building materials: (a) sorption isotherm; (b) moisture retention curve.

(1) For wetting liquids in porous materials, $p_c \leq 0$, although this sign convention is not always consistent in the literature. In the present work, capillary suction, p_s, is used as the positive–valued capillary pressure, i.e. $p_s = -p_c$.

For practical purposes, the moisture storage function is divided into three different regions. The lower humidity range is called hygroscopic region and is usually described by sorption isotherms. It goes from the dry state (Figure 2.3a) until relative humidity values of 93–98 %, depending on the material (Künzel et al., 2001; Kumaran, 2006; Scheffler, 2008). In the lower range (Figure 2.3b), the moisture is in an adsorbed state and the transport is mainly characterised by vapour diffusion. At the higher end of the hygroscopic regime, moisture begins to condense within the pores, starting from the smaller ones and initially without continuity of the liquid phase at a macroscopic level (Kumaran, 2006). With higher relative humidity, increasingly larger pores are filled with water and the process continues until a critical moisture content, w_{crit}, defined as the lowest moisture content necessary to initiate moisture transport in the liquid phase. The region ranging from the critical moisture content to the capillary moisture content is defined as the overhygroscopic or capillary region (Figure 2.3c). Finally, the supersaturated region extends over the capillary moisture content until complete saturation (Figure 2.3d). This last state cannot be reached in normal conditions: it only occurs in laboratory through suction under pressure or through diffusion induced by temperature gradients.

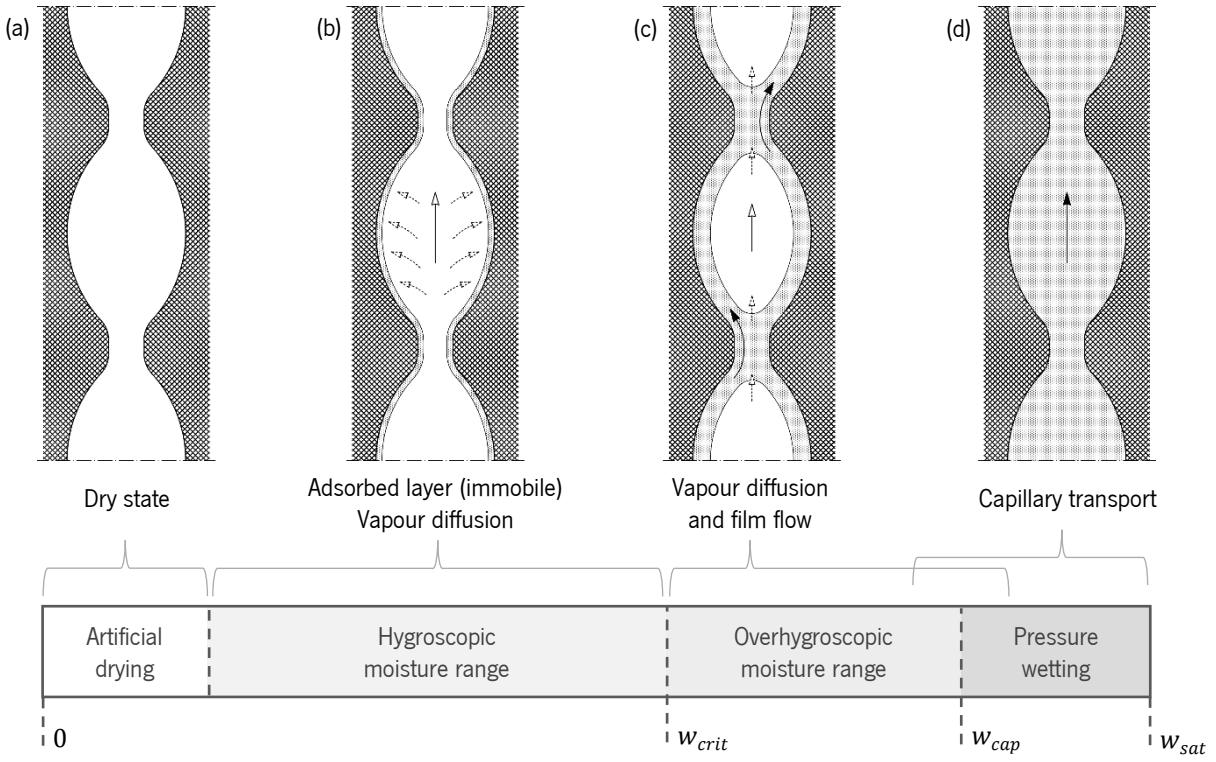

Figure 2.3. Moisture in idealised pores: (a) dry state; (b) hygroscopic region; (c) lower overhygroscopic region; (d) capillary and supersaturated region.

Most building materials are hygroscopic and capillary–active, and thus their behaviour may be described by a continuous transition between the three moisture regimes. Insulation materials normally exhibit a

hydrophobic, non–hygroscopic behaviour, and therefore can only be in dry or supersaturated states. Polymeric materials, on the other hand, are normally described only within their hygroscopic range, since they do not possess a capillary structure able to absorb liquid water. A direct jump from the sorption to the supersaturated regime may be possible as well in hygroscopic, capillary–active materials after a hydrophobic treatment.

The moisture storage function generally exhibits a hysteretic behaviour, which means that it is a process–dependent relation (Figure 2.4). In such cases, the wetting curve takes lower values than the drying curve. The hysteresis in moisture storage can be attributed to several factors, namely the ink–bottle effect, and the contact angle hysteresis or rain–drop effect. The ink–bottle effect is caused by the non–uniform width of interconnected pores. For example, in a capillary with successive wide and narrow passages, the processes of wetting from an initial dry state or drying from saturation result in two different stable configurations with dissimilar moisture content (Figure 2.4b). Hysteresis due to the ink–bottle effect will be more pronounced in porous media with a wide range of pores with different shapes and dimensions. On the other hand, the rain–drop effect or contact angle hysteresis derives from the different contact angles for advancing and receding liquids (Figure 2.4c). The matter of hysteresis in the moisture storage of porous media has been largely debated (Scheffler, 2008). Most material models neglect this effect and use only the wetting curve. Some researchers postulate that the difference between wetting and drying branches is usually not significant (Künzel et al., 2001). Other models consider the hysteresis but adopt a unique branch calculated as the mean of the absorption and desorption isotherms (Straube & Burnett, 2001). More advanced models assume the hysteretic behaviour and employ the main wetting and main drainage curves as lower and upper bounds, respectively, with a series of scanning curves in between, see e.g. Kaluarachchi & Parker (1987), Viaene et al. (1994), Maekawa et al. (2009).

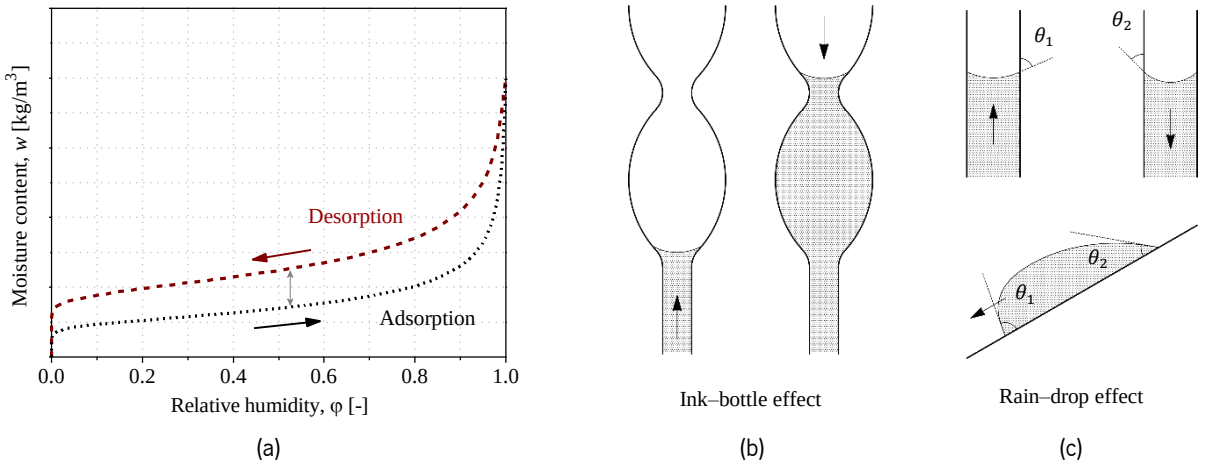

Figure 2.4. Moisture storage hysteresis: (a) typical shape of a hysteretic sorption isotherm; (b) ink–bottle effect resulting from the non–uniform width of interconnected pores; (c) rain–drop effect or contact angle hysteresis.

The number of material properties required for the simulation of hygrothermal processes depends on the accuracy and complexity of the chosen model. In general, a minimal set of material properties for HT models includes (Künzel et al., 2001; Kumaran, 2006):

- Bulk density.
- Open porosity.
- Thermal conductivity of the dry material as a function of temperature.
- Thermal conductivity as a function of moisture content.
- Heat capacity of the dry material.
- Heat capacity as a function of moisture content.
- Water vapour permeability or water vapour resistance as a function of relative humidity.
- Equilibrium moisture content as a function of relative humidity (sorption isotherm) and/or capillary pressure (moisture retention curve).
- Water absorption coefficient.
- Liquid transport coefficient, i.e. liquid water diffusivity or liquid permeability as a function of moisture content.

2.2.3 Experimental research on the characterization of hygrothermal material properties

As it was mentioned at the beginning of this section, the hygrothermal properties of porous building materials are not constant and vary greatly with the environmental conditions. Moreover, there are mutual dependencies between thermal and hygric parameters, which generally exhibit highly non–linear behaviour. Due to the complexity of the task, complete detailed data sets of hygrothermal material properties are extremely rare. On the other hand, when material data are available, the values tend to present a wide scatter. For reference, a summary of hygrothermal properties of masonry materials found in the literature has been collected in a dedicated appendix at the end of this thesis. The reader is referred to Appendix 2 for further details.

Although the thermal properties of building materials and the corresponding testing methods have been well established in the literature, a reliable characterization of the moisture–related properties still needs more attention (Feng & Janssen, 2016). Several round–robin initiatives have been launched to define and collect hygric properties of commonly used porous building materials, e.g. IEA Annex 24 (Kumaran, 1996) and EC HAMSTAD (Roels, Carmeliet, et al., 2003). Nevertheless, considerably large variations were reported for some materials, including certain types of masonry units and mortar mixes. The reason behind such deviations is manyfold. On one hand, ceramic products and mortars are hardly

free of intrinsic variability and inhomogeneities. Even industrially produced bricks can have highly variable properties depending on the raw materials and the forming and firing methods (Cultrone et al., 2004; Fernandes et al., 2010). Similarly, mortar mixes are in–situ prepared materials, and their final properties depend on the type and proportion of components as well as on the curing conditions. Moreover, the registered variation present in the literature may also come from the testing process itself, e.g. lack of a unified experimental setup, operator expertise and familiarity with the procedure, neglected factors such as temperature influence, etc. While intrinsic material variability can hardly be overcome univocally, the standardization and consistent implementation of experimental procedures is still a work–in–progress to minimize testing errors. Indeed, some works have focused on the repeatability and reproducibility of the testing methods to determine hygric properties (Roels et al., 2004; Feng et al., 2015, 2020). Shared conclusions from these studies are the importance of applying a unified approach, the value of providing a detailed report of testing conditions and procedures, and the need for a revision of the current vapour permeability testing method. In this context, a thorough material characterization contributes to improving the quality of available material databases as well as increasing our confidence in the reported values and test protocols.

For the development and application of HT models, considering the previous scenario, it is generally advisable to include an initial experimental campaign in order to collect the necessary information required for each specific case study, as well as for validation of the available material data, in case they exist. As a reference, Table 2.2 collects the set of basic experiments and derived material properties proposed by Scheffler (2008) for the characterization of a porous material over the entire moisture range.

2.2.4 Experimental research on the hygrothermal behaviour of multi–layered materials

Besides the characterization of constituent materials, the hygrothermal analysis of masonry requires the study of possible interfacial effects derived from its multi–layered nature. Regarding the thermal field, a perfect contact between adjacent layers is generally assumed. In other words, heat conduction between consecutive layers is not hindered and any interfacial effect is disregarded. It must be noted that the presence of air gaps resulting from damage (cracks) at the interface could induce a thermal resistance and reduce the heat flux through the discontinuity. However, cracks are usually localized and have a negligible impact on the overall thermal response.

In contrast, the interfacial effect on mass transfer is a more complex phenomenon. The experimental study of moisture transport in layered composites has been covered to some extent in the literature, e.g. Wilson et al. (1995a, 1995b), Hall & Hoff (2009), Nunes et al. (2017), Vereecken et al. (2020). Common

findings from these works are the existence of interfacial phenomena, the mismatching properties between material layers, and the directionality or influence of stacking order. Wilson et al. (1995a, 1995b) studied sorption phenomena in multi–layered building materials, namely plaster and plaster/sand mixtures. The authors used analytical expressions based on the sharp front model and assumed perfect hydraulic contact at the interface. Their experimental studies showed an overall good match with the analytical solutions, although some deviations were identified. The differences were explained as a consequence of the wet sharp front simplification. Hall & Hoff (2009) later extended this approach to account for imperfect hydraulic contact and introduced the interfacial resistance as an additional cause to explain the observed discrepancies.

Table 2.2. List of basic characterization experiments and derived material properties. Adapted from Scheffler (2008).

Material property / Experiment	Symbol	Unit
Bulk density / Vacuum saturation	ρ_{bulk}	$[\mathrm{kg/m^3}]$
Open porosity / Vacuum saturation	ϕ_o	$[\mathrm{m^3/m^3}]$
Saturation moisture content / Vacuum saturation	w_{sat}	$[\mathrm{kg/m^3}]$
Thermal conductivity / Heat flux measurement	λ	$[\mathrm{W/(m \cdot K)}]$
Heat capacity / Calorimeter experiment	C	$[\mathrm{J/(kg \cdot K)}]$
Sorption moisture content / Static gravimetric test	$w(\varphi)$	$[\mathrm{kg/m^3}]$
Suction moisture content / Pressure plate experiment	$w(p_c)$	$[\mathrm{kg/m^3}]$
Water vapour resistance / Dry–cup test	μ_{dry}	[–]
Water vapour resistance / Wet–cup test	μ_{wet}	[–]
Water absorption coefficient / Capillary absorption test	A_w	$[\mathrm{kg/(m^2 \cdot s^{0.5})}]$
Capillary moisture content / Capillary absorption test	w_{cap}	$[\mathrm{kg/m^3}]$
Drying data / Drying test	$w(t)$	$[\mathrm{kg/m^3}]$
Conductivity at effective saturation / Darcy flow measurement	$K_l(w_{sat})$	$[\mathrm{kg/(m \cdot s \cdot Pa)}]$
Unsaturated conductivity data / Infiltrometer experiment	$K_l(w)$	$[\mathrm{kg/(m \cdot s \cdot Pa)}]$

On the other hand, the experimental works focused on moisture transport in masonry are still limited. A possible explanation for the lack of experimental studies on this topic can be related to the intrinsic complexity of hygric characterization. The most accessible methods are based on direct weight measurement of the moisture content, being time–consuming and destructive. The measurement of internal relative humidity has been recognized as a more convenient and effective method for analogous studies in concrete (Granja et al., 2014), but its application to masonry is not straightforward due to its multi–layered character. Finally, the acquisition of detailed moisture profiles, e.g. via Nuclear Magnetic

Resonance, X-ray analysis, or Gamma-ray attenuation method, requires advanced techniques, specific equipment, and specialized personnel, and is therefore considerably costly. Consequently, the available literature on experimental characterization of mass transfer in masonry presents a significant scatter in terms of studied materials, specimen configurations and testing methods (see Table 2.3). In addition, most of the existing research has been devoted to liquid water absorption, whereas drying has been scarcely studied (Brocken, 1998; Delgado et al., 2019a). Nonetheless, the conclusions of the existing studies support the existence of interfacial phenomena between adjacent material layers.

Table 2.3. Literature database relating hygrothermal tests in masonry.

Author(s)	Specimen type	Type of analysis	Transfer direction	Results
Brocken (1998)	Fired–clay brick; cement mortar; cement–lime mortar; masonry triplets	Isothermal moisture transport	1–D	Moisture content profile
Belarbi et al. (2008)	Cement–-lime mortar	Non–isothermal moisture transport	1–D	Temperature profile, moisture ratio profile (1)
	Sandstone	Isothermal moisture transport	2–D	Moisture ratio profile (1)
Qin et al. (2008)	Sandstone	Isothermal and non–isothermal moisture transport (modified cup method)	1–D	Temperature profile, moisture ratio profile (1)
Qin et al. (2009)	Sandstone; cement–lime mortar; sandstone + cement–lime mortar	Non–isothermal moisture transport	1–D	Temperature profile, moisture ratio profile (1)
Qin et al. (2010)	Cement–lime mortar	Non–isothermal moisture transport	1–D	Temperature profile, moisture ratio profile (1)
	Sandstone	Isothermal moisture transport	2–D	Moisture ratio profile (1)
Groot & Gunneweg (2010a)	Masonry wallette (fired–clay brick + hydrated lime mortar/ natural hydraulic lime mortar)	Isothermal moisture transport	1–D	Transient moisture mass
Derluyn et al. (2011)	Masonry triplet (red fired–clay brick + cement mortar)	Isothermal moisture transport	1–D	Moisture content profile
Janssen et al. (2012)	Masonry triplet (red fired–clay brick + cement mortar)	Isothermal moisture transport	1–D	Moisture content profile

(1) Slicing method (destructive)

Table 2.3 (Continued). Literature database relating hygrothermal tests in masonry

Author(s)	Specimen type	Type of analysis	Transfer direction	Results
Johansson et al. (2014)	Masonry wall (brick + cement–lime mortar)	Non–isothermal moisture transport	1–D	Transient temperature and relative humidity at measured points
Guizzardi et al. (2015)	Masonry wall (external render + clay brick + cement mortar)	Non–isothermal moisture transport	1–D/2–D	Transient temperature and relative humidity at measured points, moisture content profile
Ferroukhi et al. (2016)	Red brick + polystyrene; red brick + plaster; chipboard + polystyrene; chipboard + plaster	Non–isothermal moisture transport	1–D	Temperature profile, relative humidity profile
Medjelekh et al. (2016)	Masonry wall (unfired clay brick + earth mortar)	Non–isothermal moisture transport	1–D	Transient temperature and relative humidity at measured points
Sassine et al. (2017)	Masonry wallette (clay brick, cement mortar)	Thermal analysis	1–D	Temperature profile
Allam et al. (2018)	Masonry wallette (clay brick, cement mortar)	Non–isothermal moisture transport	1–D/2–D	Temperature profile, relative humidity profile
Delgado et al. (2019a)	Ceramic brick; cement mortar; cement–lime mortar;	Isothermal moisture transport	1–D	Transient moisture mass; moisture content profile
Calle et al. (2019)	Masonry triplet (ceramic brick + natural hydraulic lime mortar)	Isothermal moisture transport	1–D	Moisture content profile
X. Zhou et al., 2020)	Masonry wallettes (brick + cement mortar)	Isothermal moisture transport	1–D/2–D	Moisture content profile

Considering the possible causes for the existence of a hydraulic resistance at the brick–mortar interface, a commonly accepted explanation is related to the curing conditions of the bedding mortar between bricks (Groot, 1997; Brocken, 1998). In particular, bricks absorb water from the fresh mortar during application, which leads to a drop in the water–binder ratio of the mixture. Furthermore, water extraction from the mortar is also connected to the transport of fine binder particles towards the interface and a stratification of the mortar across the joint thickness. Consequently, one would expect a denser, more compact mortar at the interface. However, this is not always the case since a more porous mortar near the interface may be equally found in real scenarios. To account for this fact, Groot & Larbi (1999) hypothesized a reversed water flow from brick to mortar after compaction and initial hydration of the mortar, with subsequent

impact on the interface development. Overall, the quality of brick–mortar interface seems to be highly dependent on the curing history of the mortar. Derluyn et al. (2011) and Janssen et al. (2012) studied the absorption behaviour of brick–cement masonry composites with different interfacial configurations, namely perfect hydraulic contact (kaolin layer), and wet– and dry–cured specimens. Their studies confirmed that the interfacial effects were proportional to the water extraction from the mortar during curing. Further causes for the existence of a hydraulic resistance at the brick–mortar interface can be the presence of air gaps resulting from damage (cracks) or due to poor workmanship during the application of the fresh mortar (Groot & Gunneweg, 2010a). Even if the application and curing conditions were optimal, a certain hydraulic resistance is expected due to the pore structure discontinuity between the materials (Brocken, 1998).

2.3 HYGROTHERMAL BOUNDARY CONDITIONS

Besides the characterisation of material properties, a comprehensive description of the boundary conditions is also necessary for a valid definition of the HT models. In Building Physics, these boundary conditions are usually classified into two groups according to the boundary location, namely indoor and outdoor. For indoor conditions, temperature and relative humidity are needed. For the outdoor conditions, temperature and relative humidity are equally necessary and depending on the complexity of the model, other data might be required as well, such as solar radiation, wind speed, precipitation, etc. Wind–driven rain is the largest source of moisture for any building structure (Karagiozis, 2001). However, it is a complex phenomenon, and the availability of data is still limited, so it is disregarded in many studies. The same applies to other phenomena commonly found in buildings, such as rising damp and roof leak.

Besides the temperature and relative humidity, external and internal convective transfer coefficients (CTCs) are also necessary to define heat flux and moisture flux boundary conditions. The empirical determination of CTCs is a difficult task since they show dependency on the geometry of the studied surface as well as on local air flow, temperature and moisture conditions (Künzel, 1995). For engineering applications, a simplified approach is usually adopted. Thus, CTCs are assumed constant and estimated from analytical formulas or taken from tabulated values (Hagentoft et al., 2004; Defraeye et al., 2013).

2.4 HYGROTHERMAL MODELS

Simultaneous heat and moisture transfer through porous media constitutes a highly coupled problem, that is, temperature balance and thermal material parameters vary with moisture content while the moisture–related properties and moisture equilibrium are dependent on the thermal distribution.

Comprehensive knowledge of each problem and their basic mechanisms is therefore necessary before tackling the combined phenomenon.

The heat and moisture transport approaches presented hereafter were developed on the basis of the continuum model theory, which assumes that "matter is a hypothetical substance that is continuous throughout the spatial domain it occupies and can be described in that domain by a set of variables which are continuous and differentiable functions of the spatial coordinates and of time" (Bear & Bachmat, 1990). Under this assumption, a detailed definition of the exact microstructure of the material is not necessary. Instead, the internal structure of the material is averaged through Representative Elementary Volumes (REVs). In the case of porous media, the REV contains a representative configuration of the different phases, namely solid, liquid and gas (Figure 2.5).

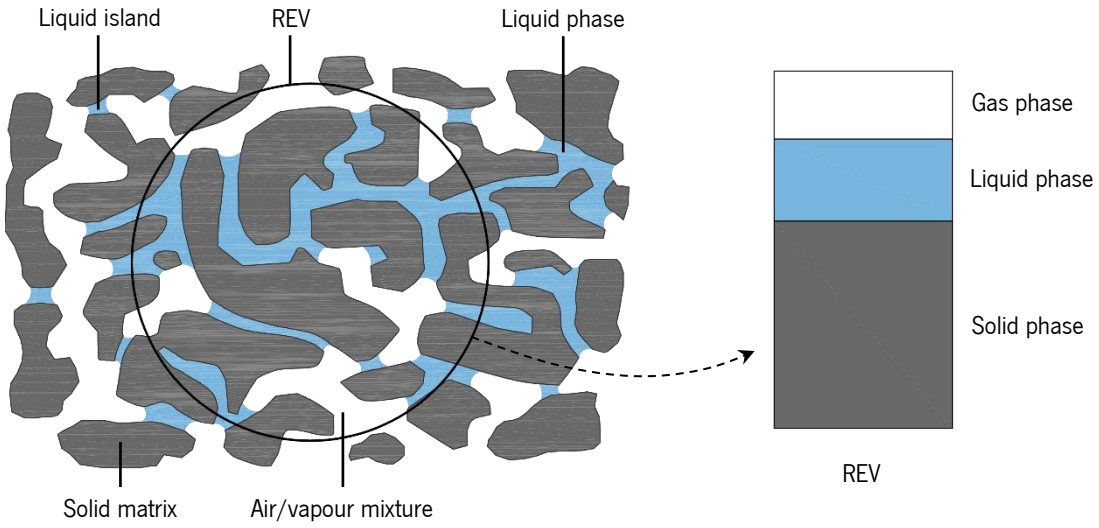

Figure 2.5. Schematic two–dimensional diagram of a non–saturated porous medium: representative elementary volume (REV) and its corresponding phases. Adapted from Pel (1995).

2.4.1 Heat problem

Heat transfer is the process of energy exchange due to a temperature difference. There are three main types of heat transfer mechanisms, namely conduction, convection and radiation. Heat always flows from warmer to colder substances and the flow rate depends on the temperature difference, the area exposed and the type of material in between. Conduction may occur within gases, liquids or solids, although it is generally associated with heat transfer in solid materials. In a conductive process, the heat is transferred by the internal vibration of molecules or the movement of free electrons inside the material. Convection is caused by the movement of a fluid (gas or liquid), in which the fluid carries heat from one place to another; as the movement progresses, the hot fluid is replaced by cooler fluid. Convective heat transfer is defined as free or natural if buoyancy forces alone move the fluid, but it can also be induced by

mechanical means (forced convection). Thermal radiation occurs through electromagnetic waves and is related to the energy emitted or absorbed by a body as a result of being at a certain temperature.

Heat conduction

In a layer of solid material with each face at a different temperature, the heat flows from the side with higher temperature to the one with lower temperature. The heat flux is determined by Fourier's Law, expressed for the one–dimensional case as:

$$q_x = -\lambda \frac{\partial T}{\partial x} \tag{2.3}$$

where q_x [$\mathrm{W/m^2}$] is the heat flux in x–direction, λ [$\mathrm{W/(m \cdot K)}$] is the thermal conductivity, and T [K] is the temperature. The heat flux is proportional to the thermal conductivity of the material and the temperature difference and is inversely proportional to the thickness of the layer. Note that it is also common to find the heat conduction properties of building materials expressed in the form of thermal resistance, $R_T = l/\lambda$ [$\mathrm{m^2 \cdot K/W}$], where l [m] denotes the thickness of the material layer.

In porous materials, heat fluxes may also be induced by moisture transport (Dufour effect). However, this effect has been proven negligible for the ranges of temperatures that are of interest for this research (Bažant & Thonguthai, 1987), and therefore it is not considered here.

Heat convection

The convective heat transfer between a surface and the environment is expressed by Newton's Law of Cooling:

$$q = h_T \left(T_{surf} - T_{env}\right) \tag{2.4}$$

where h_T [$\mathrm{W/(m^2 \cdot K)}$] is the convective heat transfer coefficient. The determination of h_T is one of the main difficulties when dealing with this type of problem. Due to the lack of generalised predictive equations, h_T is generally estimated from empirical correlations as a function of wind speed (Azenha, 2009).

Thermal radiation

Radiation is a heat transfer phenomenon that affects all bodies by the fact of being at a certain temperature. Thermal agitations within the molecular structure of any material produce energy in the form of electromagnetic waves, which are emitted from the surface of the body, thus carrying the energy

away. Radiation is the only heat transfer mechanism that can take place in the vacuum, that is to say without a material medium (fluid or solid).

Emissivity, ε [–], is the capacity of a body to emit radiation and it varies from $0 < \varepsilon < 1$, with $\varepsilon = 1$ as an ideal radiator or black body. The Stefan–Boltzmann law is used to determine the radiation emitted by a body:

$$E = \varepsilon \, \sigma \, T^4 \tag{2.5}$$

where E [$\mathrm{W/m^2}$] is the emitted radiation and $\sigma = 5.67\mathrm{E}{-8}\ \mathrm{W/(m^2 \cdot K^4)}$ is the Stefan–Boltzmann constant.

On the other hand, an object may also absorb radiation. The capacity of a body to absorb radiation is called absorptivity, α [–], and analogously to ε, it varies from $0 < \alpha < 1$, being $\alpha = 1$ the ideal black body. The net rate of radiation on a body can be calculated by the difference between the energy that is emitted by the surface and the irradiated energy being absorbed from the surroundings:

$$q = \varepsilon \, \sigma \, {T_{surf}}^4 - \alpha \, \sigma \, {T_{surr}}^4 \tag{2.6}$$

In the particular case of grey bodies, where $\varepsilon = \alpha$, Eq. (2.6) becomes:

$$q = \varepsilon \, \sigma \left({T_{surf}}^4 - {T_{surr}}^4 \right) \tag{2.7}$$

For thermal problems circumscribed to civil engineering applications, only a certain range of wavelengths within the whole electromagnetic spectrum is of interest, namely ultraviolet, visible and infrared. Particular effects related to thermal radiation such as night–sky cooling, incident direct radiation from the sun (shortwave) and longwave radiation are of special interest for a detailed analysis of heat problems in civil engineering structures. For the sake or brevity, these phenomena will not be further discussed here.

2.4.2 Moisture problem

The main moisture transport mechanisms in building materials are water vapour diffusion and liquid transport by capillarity. There is also bulk water vapour transport associated with airflow movements. However, the contribution of this factor to the overall moisture content is minor and it is therefore negligible (Scheffler, 2008). Similarly, the moisture fluxes induced by thermal gradients (Soret effect) can be disregarded (Janssen, 2011).

Water vapour transport

The main mechanism for water vapour transport in porous materials is vapour diffusion, which according to Fick's First Law can be expressed as:

$$g_{v,x} = -D_v \frac{\partial c_v}{\partial x} \tag{2.8}$$

where $g_{v,x}$ [kg/(m² · s)] is the vapour flux in x–direction, D_v [m²/s] is the vapour diffusivity or diffusion coefficient of vapour, and c_v [kg/m³] is the vapour concentration. Diffusion may be described as a transport process proportional to a concentration gradient. If moist air is considered an ideal gas:

$$p_v V = m_v R_v T \tag{2.9}$$

where p_v [Pa] is the partial vapour pressure, V [m³] is the volume, m_v [kg] is the mass of vapour, and $R_v = 461.5$ [J/(kg · K)] is the universal gas constant for water vapour. The previous expression can be rearranged to describe the water vapour concentration:

$$c_v = \frac{m_v}{V} = \frac{p_v}{R_v T} \tag{2.10}$$

Therefore, the vapour diffusion may be expressed as:

$$g_{v,x} = -\frac{D_v}{R_v T} \cdot \frac{\partial p_v}{\partial x} \tag{2.11}$$

By definition, relative humidity is expressed as:

$$\varphi = \frac{p_v}{p_{v,sat}(T)} \tag{2.12}$$

where $p_{v,sat}(T)$ [Pa] is the saturation vapour pressure dependent on temperature. Consequently, the vapour pressure may be defined as a function of relative humidity and temperature:

$$p_v = \varphi \, p_{v,sat}(T) \tag{2.13}$$

Different empirical formulas have been proposed for the definition of the saturation vapour pressure (Ochs et al., 2008). In this thesis, an adaptation of the expression by Murray (1967) presented in Monteith & Shatleworth (2013) will be used:

$$p_{v,sat} = 610.7 \cdot 10^{7.5\left(\frac{T-273.15}{T-35.85}\right)} \tag{2.14}$$

Considering Eq. (2.11), the vapour diffusion coefficient, the universal gas constant and the temperature are usually lumped together and expressed as ‘permeability’. Hence, the water vapour permeability of still air, δ_a [kg/(m · s · Pa)], is defined as follows:

$$\delta_a = \frac{D_a}{R_v T} \tag{2.15}$$

It must be noted that the definition of the vapour permeability of air is purely empirical and may be found with different expressions in the literature (Börjesson, 2013). In this thesis, the expression proposed by Schirmer (1938) will be used:

$$\delta_a = \frac{2.31 \cdot 10^{-5}}{R_v \cdot T} \frac{p_0}{p} \left(\frac{T}{273.15} \right)^{1.81} \tag{2.16}$$

where $p_0 = 101325$ [Pa] is the standard atmospheric pressure, and p [Pa] is the ambient barometric pressure. It is noted that Schirmer's original formulation has been later adapted by other authors and it may appear in the literature with different forms.

The vapour diffusion in porous materials is influenced by the pore structure of the material itself. In order to account for this fact, the vapour permeability of air is reduced by the so–called vapour diffusion resistance factor, μ, which is characteristic of each material:

$$\delta_v = \frac{\delta_a}{\mu} \tag{2.17}$$

where δ_v [kg/(m · s · Pa)] is the water vapour permeability of the material. Due to the air pressure influence in Eq. (2.16), the vapour permeability of porous materials is sensitive to barometric changes. In particular, hygroscopic materials show increasing vapour permeability for lower air pressure values, whereas this effect is less noticeable for non–hygroscopic materials (M. Zhou et al., 2022).

The vapour diffusion resistance factor, which represents the ratio of the permeability coefficients of water vapour in air and in the building material, may be further detailed as $\mu = 1/(\tau \cdot a_V)$, where τ [–] is a tortuosity factor and a_V [–] is the volume fraction of air–filled pores. The vapour resistance factor is independent of temperature (Tveit, 1966; McLean et al., 1990). Its dependence on the water content has been extensively discussed in the literature but a unified approach has not been achieved. An overall influence of the pore filling level seems reasonable since the increasing presence of liquid water reduces the pore space available for vapour diffusion (Scheffler, 2008). In effect, dry cup and wet cup test measurements usually result in different values of vapour permeability/resistance. On the other hand, some authors consider this influence negligible and treat the vapour transport coefficient as a constant (Künzel, 1995).

Liquid water transport

The liquid transport through a porous material may be explained by different approaches. The most common descriptions are the ones based on Fick's Law of diffusion (diffusivity approaches) and the ones based on Darcy's Law of permeability (conductivity approaches).

The diffusivity approaches make use of Fick's First Law of diffusion and assume that liquid water movement follows a moisture concentration gradient such as:

$$g_{w,x} = -D_w(w) \cdot \frac{\partial w}{\partial x} \tag{2.18}$$

where D_w $[\mathrm{m}^2/\mathrm{s}]$ is the liquid water diffusivity. It is known that D_w varies with temperature and is strongly dependent on moisture content (Künzel, 1995). Moreover, liquid diffusivity is not a pure material property since it not only depends on the porous medium but on the boundary conditions as well (Krus, 1996). More specifically, D_w is expected to change depending on the process, namely adsorption or desorption, and therefore it also presents hysteresis (Scheffler, 2008).

On the other hand, conductivity approaches propose an adaptation of Darcy's Law for unsaturated porous media (Galbraith, 1992) and use the capillary pressure gradient as the driving potential:

$$g_{w,x} = -K_l(w) \cdot \frac{\partial p_c}{\partial x} \tag{2.19}$$

where K_l $[\mathrm{kg}/(\mathrm{m} \cdot \mathrm{s} \cdot \mathrm{Pa})]$ is the liquid water conductivity (also called liquid water permeability), which is a property of the porous medium and a function of the moisture content.

Conductivity approaches may also use relative humidity as driving potential instead of the capillary pressure. Kelvin equation relates both parameters as follows:

$$p_c = \rho_w \, R_v \, T \;\; ln\, \varphi \tag{2.20}$$

By introducing Kelvin's relation in Eq. (2.19) and after additional operations and simplificationsn, it is possible to arrive to:

$$g_{w,x} = -D_\varphi(\varphi) \cdot \frac{\partial \varphi}{\partial x} \tag{2.21}$$

where D_φ $[\mathrm{kg}/(\mathrm{m} \cdot \mathrm{s})]$ is the liquid conduction coefficient, dependent on the porous medium and the relative humidity.

Note that from Eqs. (2.18) and (2.21), the following connection between diffusivity and conductivity approaches can be established:

$$D_\varphi = \frac{\partial w}{\partial \varphi} \cdot D_w = \xi \cdot D_w \tag{2.22}$$

where $\xi = \partial w/\partial \varphi$ is the moisture storage capacity $[\mathrm{kg}/\mathrm{m}^3]$.

Moreover, the connection between diffusivity and conductivity approaches can be established through their respective liquid transfer coefficients such as:

$$D_w(w) = \frac{\partial p_c}{\partial w} \cdot K_l(w) = \mathcal{C} \cdot K_l \tag{2.23}$$

where $\mathcal{C} = \partial p_c / \partial w$ is the derivative of the inverse moisture retention curve $[\mathrm{m}^2/\mathrm{s}^2]$.

2.4.3 Numerical modelling of heat and moisture transport

For the analysis of coupled hygrothermal phenomena in masonry structures, it is necessary to define first a multi–physics model able to describe moisture diffusion and heat transfer in porous materials and multi–layered components. Several hygrothermal models for porous building materials are available in the literature. These models differ in their dimension (one–, two– or three–dimensional), the type of flow (steady–state, quasi–static or dynamic), the variable used to describe the moisture potential (moisture content, capillary pressure, relative humidity, or vapour pressure), the number of parameters needed as input information, as well as their assumptions and limitations. Temperature is universally accepted as driving potential for heat transport. However, moisture transport might be defined by different potentials, namely the moisture content, partial vapour pressure, relative humidity, hydraulic potential, or capillary pressure. In general, all these potentials can be related to one another and can be used equivalently with the proper transformations (Straube & Burnett, 2001).

In addition to the chosen potential, the different models may be distinguished by their particular means of modelling the moisture component (Celia et al., 1990). Diffusivity approaches select a driving potential and lump all the transport mechanisms into a single moisture diffusivity equation. On the other hand, conductivity approaches separate vapour diffusion from liquid transport and model the flow as a parallel or series process.

The first models dealing with the hygrothermal behaviour of porous materials were developed by (Philip & de Vries, 1957) and (Luikov, 1964). Their approaches rely on a set of coupled governing equations for heat and mass transfer with moisture content and temperature as dependent variables. However, these studies are focused on single–material cases and their direct application to multi–layered systems might present some problems: in composite structures made up of materials with dissimilar moisture sorption and diffusion properties, the moisture content is not continuous at one and the other side of the interface (Künzel, 1995). In order to overcome this obstacle, several authors have proposed hygrothermal models based on alternative moisture driving potentials, such as partial vapour pressure, e.g. Qin et al. (2009), Allam et al. (2018), or relative humidity, e.g. Khoshbakht et al. (2006), Lin et al. (2006), which verify the interfacial continuity between layers. In the field of Building Physics, these models

have been further extended to incorporate air into the mass transport and thus investigate the coupled heat, air and moisture (HAM) transfer, e.g. Tariku et al. (2010), Belleudy et al. (2016).

Among the different approaches available in the literature, the hygrothermal model proposed by Künzel (1995) and extended by Künzel et al. (2001) is of especial interest for this research: it is a well–known approach applicable to multi–layered materials and uses transport coefficients that can be determined and validated through reasonably simple experimental tests. Künzel's model considers heat transfer by conduction and enthalpy flow (phase change), such as:

$$\frac{\partial H}{\partial t} = \nabla \cdot (\lambda \, \nabla T) + L_v \, \nabla \cdot (\delta_v \, \nabla p_v) \tag{2.24}$$

where H $[\mathrm{J/m^3}]$ is the enthalpy density, λ $[\mathrm{W/(m \cdot K)}]$ is the thermal conductivity, L_v $[\mathrm{J/kg}]$ is the latent heat of vaporization, δ_v $[\mathrm{kg/(m \cdot s \cdot Pa)}]$ is the water vapour permeability, and p_v $[\mathrm{Pa}]$ is the partial vapour pressure. In turn, moisture transport consists of a two–phase diffusion model, such as:

$$\frac{\partial w}{\partial t} = \nabla \cdot (D_w \, \nabla w) + \nabla \cdot (\delta_v \, \nabla p_v) \tag{2.25}$$

where w $[\mathrm{kg/m^3}]$ is the moisture content, and D_w $[\mathrm{m^2}/s]$ is the liquid water diffusivity.

For the liquid water diffusivity, Künzel (1995) proposes the following exponential expression:

$$D_w = 3.8 \cdot \left(\frac{A_w}{w_{cap}}\right)^2 \cdot 1000^{\left(\frac{w}{w_{cap}} - 1\right)} \tag{2.26}$$

where A_w $[\mathrm{kg/(m^2 \cdot s^{0.5})}]$ is the capillary absorption coefficient, and w_{cap} $[\mathrm{kg/m^3}]$ is the capillary moisture content. It is noted that other diffusivity models have suggested different analytical expressions for the liquid water diffusivity, e.g. Pel et al. (1996), Krus & Holm, (1999), Carmeliet, Hens, et al. (2004), Carmeliet et al.(2007). The different expressions vary in their flexibility, complexity, and the number of required variables. For a more in–depth discussion of diffusivity approaches available in the literature, the reader is referred to Scheffler (2008).

As mentioned in the section for the experimental works on multi–layered materials, a perfect contact is usually assumed for heat conduction through the interface. Consequently, the hygrothermal models commonly disregard any interfacial effects on heat transfer. On the other hand, the simulation of moisture transport in multi–layered cases still presents some challenges. Only a few investigations have focused on interface modelling for mass transfer problems in masonry, e.g. Brocken (1998), Derluyn et al. (2011), Calle et al. (2019), X. Zhou et al. (2020), and a unified approach to characterize the brick–mortar interfaces has not been reached yet. Moreover, the conclusions may vary from one author to another depending on the modelling technique and the eventual purpose of the simulation. For instance, as

demonstrated by Vereecken & Roels (2013), modelling the whole masonry as a homogenous brick layer may be allowed to simulate certain scenarios. A similar approximation has been used by other authors for 1–D hygrothermal simulations, e.g. Jensen et al. (2020), Soulios et al. (2021). Conversely, the most common approach for 2–D analyses is the distinction of brick and mortar layers although any type of interfacial effect is usually neglected (Castellazzi, de Miranda, Formica, et al., 2015; Jensen et al., 2020; X. Zhou et al., 2021). Nonetheless, several studies highlight the fact that moisture transport in masonry walls may be strongly affected by the interface resistance (Brocken, 1998; X. Zhou et al., 2020). Thus, further research on the hydraulic interface modelling is required.

From a practical perspective, the simulation tools generally used for this type of analysis may be divided into three categories, namely lumped models, Computational Fluid Dynamics (CFD) models, and Heat, Air and Moisture (HAM) transport models. The latter group is of particular interest to study damage and degradation phenomena of porous materials since their codes can relate to relevant degrading factors and mechanisms (Hendrickx & de Clercq, 2019). HAM models may be further classified into two groups attending to their numerical nature: Finite Element Method (FEM) and Finite Volume Method (FVM).

2.5 HYGRO–THERMO–MECHANICAL MODELS

Since the building materials are in constant equilibrium with the environment, internal stresses appear within the structures as a result of the continuous variation of temperature and moisture conditions. A temperature increment generally causes the material to dilate, in a proportional relation to its coefficient of thermal expansion, while shrinkage will take place if the temperature decreases. A similar situation occurs for changes in relative humidity and water content. Consequently, temperature and moisture distributions are related to the mechanical field and may be associated with different effects on the materials: internal stresses, displacements, volumetric changes, cracks, ageing, etc.

It must be noted that the stresses related to volumetric variations are intrinsically linked to a deformation constraint. In other words, if deformations are not restrained, the material will undergo a free dimensional change and no internal stresses will appear. However, constraints always exist in real applications and therefore stresses are expected. Moreover, in multi–layered and composites structures such as masonry, the interfaces between two dissimilar materials are naturally associated with stress concentrations.

2.5.1 Mechanical problem

The mechanical problem can be linked to the hygric and thermal fields through the extended Duhamel–Neumann equation or total strain additive decomposition (Szekeres, 2014): the total strain can be divided

into different components, namely mechanical strains, thermal strains and moisture–induced strains. This is based on the assumption of infinitesimal strains and small deformations and rotations, which is generally applicable to masonry structures (Ramézani & Jeong, 2011):

$$\varepsilon = \varepsilon_{elastic} + \varepsilon_{plastic} + \varepsilon_{thermal} + \varepsilon_{swelling} \tag{2.27}$$

The mechanical strains, $\varepsilon_{elastic}$ and $\varepsilon_{plastic}$, account for the effects caused by forces and moments, either in the elastic or inelastic ranges. On the other hand, the thermal and hygric strains are related to deformations caused by temperature and moisture variations, respectively.

The thermal–induced strain for an isotropic material is defined as:

$$\varepsilon_{thermal} = \alpha_T \left(T - T_{ref}\right) \tag{2.28}$$

where α_T $[1/°C]$ is the coefficient of thermal expansion of the material and T_{ref} is the reference temperature at which the thermal–induced strain is zero.

An analogous relation may be written for the moisture–induced strain:

$$\varepsilon_{swelling} = \alpha_h \left(w_g - w_{g,ref}\right) \tag{2.29}$$

where α_h [–] is the coefficient of hygric expansion of the material, w_g $[\mathrm{kg/kg}]$ is the gravimetric moisture content, and $w_{g,ref}$ is the reference moisture content for which the moisture–induced strain is zero. It is recalled that the moisture content may also appear as mass of absorbed water per volume of dry material, w $[\mathrm{kg/m^3}]$. In that case, if α_h is initially given in terms of gravimetric moisture content (dimensionless), then it must be divided by the density of the material, ρ_{bulk} $[\mathrm{kg/m^3}]$, to maintain the consistency of the units. Similarly, if the moisture content is expressed in its volumetric format or specific moisture content, w_V $[\mathrm{m^3/m^3}]$, then α_h must be multiplied by the density of water, ρ_w $[\mathrm{kg/m^3}]$, to maintain the consistency of the units. Since the moisture content is dependent on the relative humidity by means of the moisture storage function, the moisture–induced strain is also a non–linear function of the relative humidity.

Additional sources of strains can be implemented in Eq. (2.27) to represent different scenarios. For instance, the so–called chemical–based strain, $\varepsilon_{chemical}$, accounts for chemical reactions and other effects, namely the exothermic chemical reactions and microstructure modifications based on calcium dissolution, calcium leaching and salt crystallization phenomena (Ramézani & Jeong, 2011). Therefore, the chemical–based strain can be further decomposed into exothermic strains, dissolution–based strains, calcium–leaching strains and crystallization strains caused by the crystallization pressure. The analysis of these effects, however, is out of the scope of the current research.

Influence of temperature and moisture on mechanical properties

Further hygrothermal effects on the mechanical response can be taken into account, such as the impact of temperature and moisture on the mechanical properties. In the case of temperature, a direct influence of thermal variations on the mechanical properties of masonry can be considered negligible for the temperature range of interest in this study. On the contrary, it is well known that the mechanical performance of porous materials is greatly affected by moisture, which generally leads to a reduction of the mechanical properties. As an example, the modulus of elasticity of sandstone diminishes with increasing moisture content until stabilizing into a plateau close to saturation (Castellazzi, de Miranda, Formica, et al., 2015):

$$E = \frac{19.06}{100 \cdot S_l} + 3.12 \text{ [GPa]} \tag{2.30}$$

where S_l [–] is the liquid water saturation degree expressed as:

$$S_l = \frac{w}{\phi_o \cdot \rho_w} \tag{2.31}$$

where ϕ_o [–] is the open porosity and ρ_w $[\mathrm{kg/m^3}]$ is the density of water. However, Glucklich & Korin (1975) showed that the modulus of elasticity of cement mortar is slightly affected by changes in moisture content. Therefore, the relationship between moisture and Young's modulus appears to be material–dependent. Conversely, the Poisson's ratio is almost independent of moisture content (Ramézani & Jeong, 2011).

Regarding the compressive strength, the European standard EN 772–1 (2011) suggests that the compressive strength of masonry units in saturated conditions should be considered 80 % of the value obtained for normal environmental conditions. This approach is supported by experimental studies, e.g. Witzany et al. (2010), Foraboschi & Vanin (2014), Matysek et al. (2016), Bompa & Elghazouli (2021), which concluded that there is a univocal loss of compressive strength with increasing water saturation. Analogous trends were obtained for masonry specimens tested in saturated conditions (Amde et al., 2004; Franzoni et al., 2015; Bompa & Elghazouli, 2020b). These studies showed that the average compressive strength loss for saturated specimens was around 20 % of the strength obtained in normal conditions.

With respect to the shear behaviour, similar trends were obtained by experimental studies conducted on masonry triplets, e.g. Franzoni et al. (2014), Bompa & Elghazouli (2020a). These studies revealed that higher levels of moisture content resulted in reduced interfacial strength with respect to the specimens tested in dry conditions. In particular, the shear strength reduction for saturated specimens

depended on the type of masonry units and the type of mortar, reaching up to a 20 % loss for fired–clay brick triplets with hydraulic lime mortar.

Finally, the tensile strength of the material is also expected to decrease with increasing moisture content. Castellazzi, de Miranda, Formica, et al. (2015) proposed the following relation based on the experimental data collected by Glucklich & Korin (1975) for cement mortar:

$$f_t = -7\left(\frac{S_l - 10}{100}\right)^{1/5} + 21\ [\mathrm{MPa}] \tag{2.32}$$

In conclusion, the moisture–dependent mechanical behaviour of porous building materials consists of an overall loss of compressive, tensile and shear strengths with increasing moisture content. The extent to which moisture affects the modulus of elasticity seems to be material–dependent, although a certain decrease in stiffness is expected. Despite the obtained trends, further research is still needed to cover the mechanical behaviour over the whole moisture range. Likewise, further hygro–mechanical coupling effects, such as the influence of moisture on ductility and the post–peak non–linear behaviour of quasi–brittle materials need to be investigated as well. For a deeper insight into these issues, the reader is referred to e.g. Carmeliet (2015) and references therein.

2.5.2 Hygro–thermo–mechanical studies

Although several hygrothermal models for porous materials and multi–layered structures are available in the literature, the research on hygro–thermo–mechanical (HTM) problems is rather scarce. Considering the general lack of benchmarking standards, the availability of verification tools for coupled HTM models is also limited.

A series of HTM studies is available for timber structures, and especially the moisture–induced stresses in wooden components have been investigated more consistently. Jakieła et al. (2008) used a numerical approach to model the evolution of moisture and stress fields in a restrained wooden cylinder due to variations in temperature and relative humidity. Following that initial approach, Rachwał et al. (2012) later developed a 2–D finite element model to simulate the moisture transport and strains in multi–layered wood supports of panel paintings as a response to environmental changing conditions. Their model was then calibrated and validated by experimental data. The same study was later adapted and replicated by Williams–Portal et al. (2014) to validate their HTM model.

The study of hygro–thermo–mechanical effects in concrete structures has received more attention, e.g. early–age behaviour (Azenha, 2009; Jendele et al., 2014), curing for application in massive structures such as dams (Conceição et al., 2017; Ponce–Farfán et al., 2020), ageing and long–term

effects such as creep and shrinkage (Jendele et al., 2014; Gasch et al., 2016), or damage (cracking) induced by corrosion (Seetharam et al., 2019), among others.

In contrast, the research devoted to the hygro–thermo–mechanical analysis of masonry structures is still limited. Ramézani & Jeong (2011) developed a one–way coupled hygro–thermo–mechanical model to analyse the behaviour of a limestone masonry wall subjected to environmental loads. The authors prepared a two–dimensional finite element model and performed a series of non–isothermal, non–isohygral, steady–state analyses while isolating and combining the different physics. By individuating the mechanical, thermo–mechanical, and hygro–thermo–mechanical results, they were able to identify the contribution of each field to the overall response. In particular, the self–weight condition led to maximum principal stresses of about 0.10 MPa; the incorporation of thermal actions slightly changed the stress distribution and the principal stresses reached 0.15 MPa; the later addition of hygric loads resulted in tensile stresses up to 0.28 MPa. Moreover, it was shown that the distribution of stresses in the wall was geometry–dependent and the highest tensile values were concentrated in the vertical head joints and the corners of the masonry units. Transient analyses were also performed to analyse the evolution of the moisture and temperature distributions from the initial condition to the steady–state equilibrium. Time–dependent HTM analyses for variable environmental conditions were not performed and this type of analysis is still missing in the literature.

On the other hand, some authors have dealt with independent thermo–mechanical or hygro–mechanical problems in masonry. For the former, most research is devoted to the mechanical response of structural elements under high–temperature (fire) conditions, which are out of the scope of this thesis. Among the hygro–mechanical studies, Castellazzi, de Miranda, Formica, et al. (2015) developed a muti–scale numerical framework for the analysis of masonry walls subjected to water absorption, e.g. rising damp. In particular, the authors employed a two–dimensional discrete coupled hygro–mechanical model in order to assess the influence of the moisture field on the structural response as well as to incorporate the effect of mechanical degradation on the moisture transport process.

Related to the hygro–mechanical studies, the research on salt transport and crystallization in porous materials has received more attention in recent years, e.g. Koniorczyk & Gawin (2012), Derluyn et al. (2014), Choo & Sun (2018), among others. The investigation has been extended to masonry as well. For instance, Castellazzi et al. (2013) developed a coupled multi–phase model to evaluate the hygrothermal behaviour of masonry. The model was calibrated with respect to experimental tests on a brick masonry wall exposed to cyclic weathering conditions. Although the authors included the heat component in the model, isothermal conditions were assumed throughout the simulations. In addition, the mechanical

component was introduced through a simplified up–scaling procedure to predict the stresses induced by salt crystallization. The same approach was further extended by Castellazzi et al. (2016) to include non–isothermal transport. In turn, Grementieri et al. (2017) successively expanded the model and proposed a multi–scale approach for the simulation of mechanical effects induced by salt crystallization. The authors employ a numerical homogenization scheme to pass from the microstructure to the mechanical response at the structure level. The same multi–phase approach has been used to replicate experimental tests on salt transport and crystallization in masonry strengthened with composites (de Miranda et al., 2019). The proposed models have been proved able to predict the transport of salts and subsequent crystallization under different environmental scenarios. An all–encompassing analysis considering the additive effects of thermal dilation, hygric swelling and crystallization pressure is still missing.

On the other hand, scientific works on fully coupled hygro–thermo–mechanical problems in masonry are notably scarce. Regarding this aspect, further investigation is needed to determine the influence of moisture on the mechanical performance of the material, including linear and non–linear behaviour as well as damage. Similarly, more research is necessary to quantify and be able to reproduce the reverse coupling, i.e. the mechanical effects (stress variation, creep, volumetric changes, damage, cracking) on moisture transport. It is worth mentioning the studies developed by Mertens (2009) and Carmeliet (2015), focused on the non–linear hysteretic behaviour of quasi–brittle porous materials, with a special highlight on the effects of damage and moisture on the hysteresis.

Taking into consideration the everyday nature and relevance of HTM problems, the need for further investigation on this topic is evident. Similarly, experimental studies aimed at acquiring data for validation of the corresponding models are suggested for future research.

This page has been intentionally left blank

CHAPTER 3

Materials, specimens, and experimental methods

This chapter provides a brief overview of the studied materials, tested specimens and experimental methods used for material characterization. The chapter is organized in three different subsections. First, a general description of the chosen materials is provided. Subsequently, the configuration of the specimens used throughout the study is introduced. Finally, a detailed explanation of the different experimental procedures is given. The results obtained from the experimental tests as explained in this section will be introduced and discussed in the following chapter.

Part of the information presented in this chapter has been published in Ramirez et al. (2021).

3.1 MATERIALS

This section presents a description of the studied materials, namely fired–clay brick (B), Portland cement mortar (CM), natural hydraulic lime (NHL) mortar –both moulded (LM) and from masonry bed joints (LMJ)– and masonry composites. A selection of the studied material samples is shown in Figure 3.1.

Figure 3.1. Selection of material samples: fired–clay brick, Portland cement mortar, natural hydraulic lime mortar (moulded and extracted from masonry bed joints), and masonry composites. The scale bar is 20 cm long.

3.1.1 Extruded fired–clay brick

The masonry units selected for this study were commercial fired–clay solid extruded bricks. The extrusion process, as well as the drying and subsequent baking (or 'firing') were fully automated. According to the specifications of the manufacturer, the bricks were baked in a flash oven at 850 °C for 3 hours. Firing

temperatures below 1000 °C are considered low, and the resultant units are classified as 'soft' baked bricks (Fernandes et al., 2010). It must be noted that in this type of process, the actual baking temperature depends on the position of the units inside the oven, which may result in a certain level of variability between bricks of the same batch. An uneven heating of the brick mass is usually perceived within single units as well, which becomes apparent in the colour transition between the outer layer and the core (Figure 3.2). Clay particles become more sintered at higher baking temperatures, resulting in a lower porosity and a more intense red colour of the brick (Brocken, 1998).

(a) (b)

Figure 3.2. Cross–sections of fired–clay brick units: (a) transversal section through middle plane; (b) longitudinal section through middle plane.

3.1.2 Portland cement mortar

Portland CEM I – 42.5R, as classified by the standard EN 197–1 (2011), was used as a reference for comparison with the lime–based mortar used in this study. The cement mortar was prepared with a binder–aggregate ratio 1:5 by volume and water–binder ratio 1:3 by weight. Standard moulds with dimensions 160 $\mathrm{mm} \times 40\ \mathrm{mm} \times 40\ \mathrm{mm}$ were used to cast the mixture. After casting, the mortar was kept in controlled curing conditions, 20 °C and 90 % RH, for 48 hours. Then, the specimens were demoulded and immersed in water at 20 °C for more than a year.

3.1.3 Natural hydraulic lime mortar

The lime mixes analysed in this study were prepared using a commercial pre–mixed NHL–based mortar, NHL 3.5 (REABILITA Cal Consolidação). The mortar was prepared as suggested by the producer by blending 1 kg of the dry powder provided by the manufacturer with 0.15 kg of water. Standard moulds with dimensions 160 $\mathrm{mm} \times 40\ \mathrm{mm} \times 40\ \mathrm{mm}$ were used to cast the mixture. For moulded specimens, the freshly cast mortar was kept for 48 hours in controlled curing conditions, 20 °C and 90 % RH. Then, the specimens were demoulded and maintained in laboratory conditions, 20 °C and 60 % RH, for more than a year.

3.1.4 Masonry

Masonry samples (brick + mortar) were extracted from a wall using a diamond coring wet drilling machine. The wall was constructed using the same bricks and NHL–based mortar discussed above. The bricks were docked in water before placement to prevent undesired suction of water from the fresh mortar. The average thickness of the mortar joints was 12 mm. Right after the wall was built, it was covered with a polyethylene sheet for 48 hours to prevent water evaporation. After that, the cover was removed and the wall was kept in laboratory conditions, 20 °C and 60 % RH, for more than a year before the cores were extracted. Examples of the studied masonry specimens are shown in Figure 3.3.

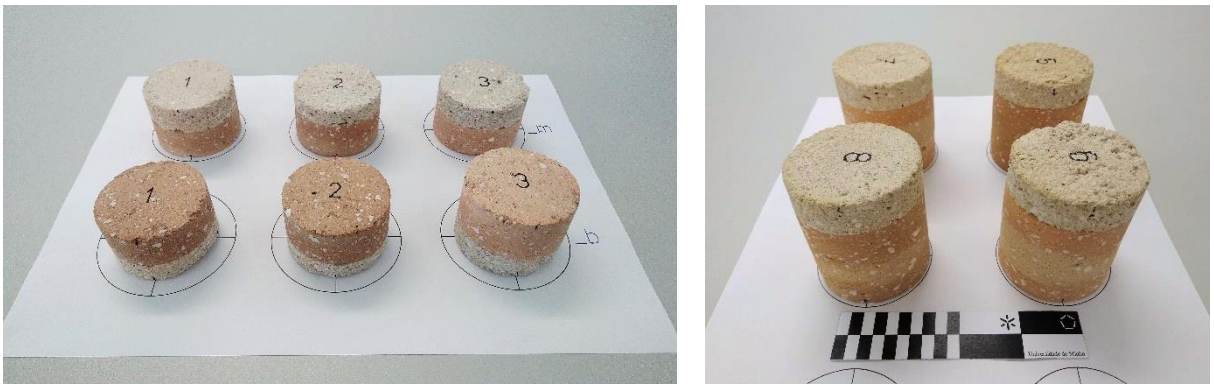

(a) (b)

Figure 3.3. Selection of masonry specimens: (a) cylinders for drying tests; (b) cylinders for capillary absorption tests.

3.2 SPECIMENS

Fired–clay extruded bricks were used in different formats depending on the corresponding test setup. Initially, whole brick units with nominal size 200 mm × 100 mm × 50 mm were tested. Subsequently, the external surfaces of the units (5 mm) were ground, and the resulting prisms were cut into smaller pieces for further testing (Figure 3.4).

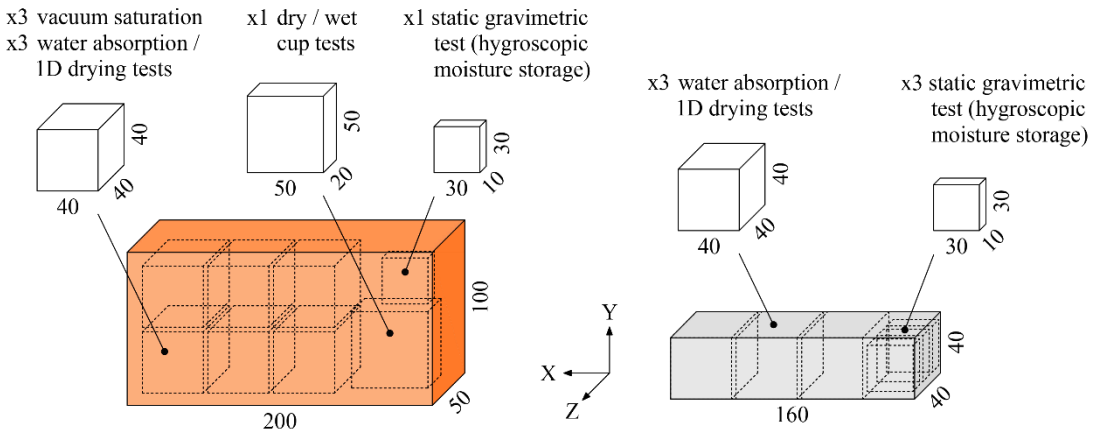

Figure 3.4. Cutting layout of brick units and mortar prisms (average dimensions in mm).

As for the mortars, standard moulds with dimensions 160 mm × 40 mm × 40 mm were used to cast the different mixes. Initially, whole mortar prisms were used. Then, the prisms were cut into smaller pieces for further testing (Figure 3.4). Additionally, lime mortar discs extracted from masonry bed joints (Figure 3.5) were analysed to determine differences with respect to the moulded counterpart.

The multi–layered specimens extracted from the masonry wall consisted of cylinders with different stacking arrangements, i.e. different B+LMJ configurations (Figure 3.5). The average diameter of the cylinders was Ø = 51.30 mm.

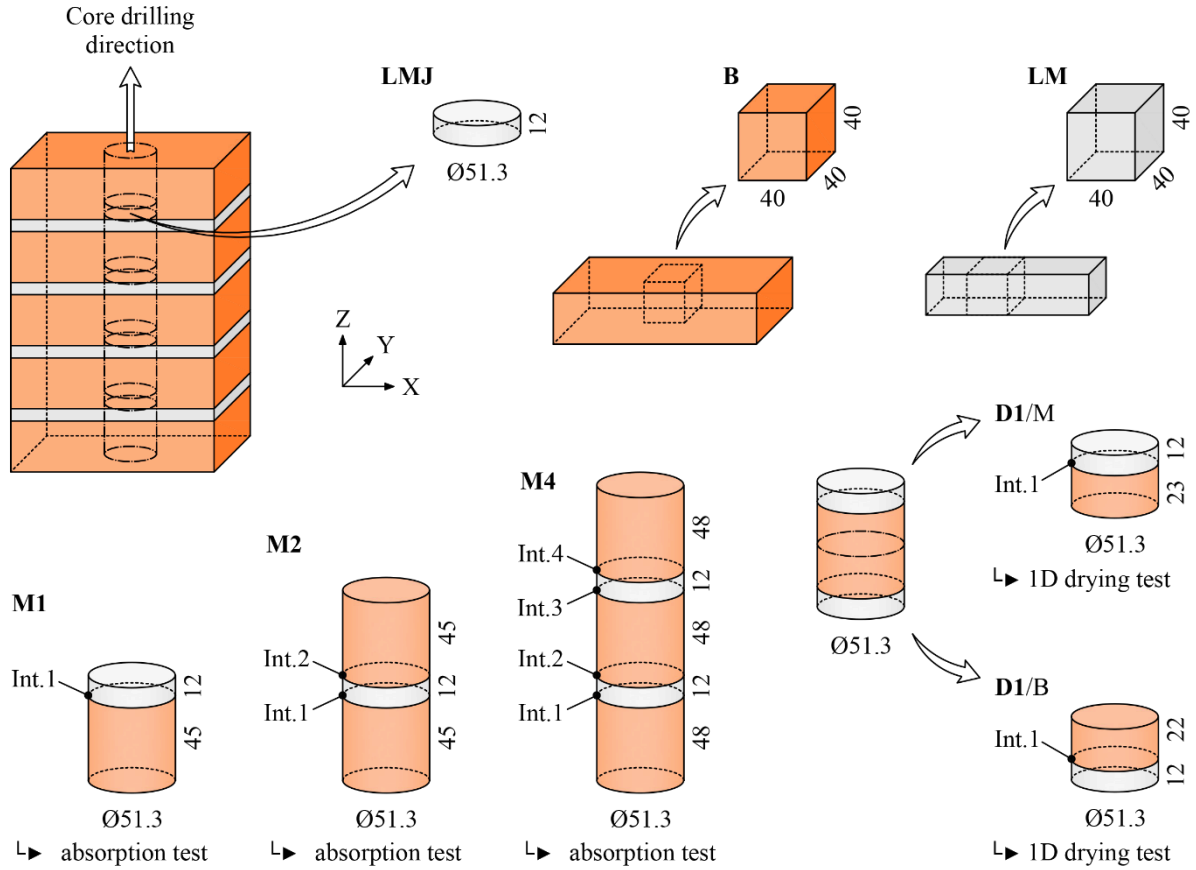

Figure 3.5. Lime mortar discs and multi–layered specimens extracted from masonry wall (schematic representation) (average dimensions in mm).

The number and type of specimens used for the characterization of single materials are summarized in . Additionally, the number and configuration of masonry specimens used for the characterization of multi–layered materials are summarized in Table 3.1.

Table 3.1. Number of single–material specimens tested.

Material	Specimen (dimensions in mm)	Test and test direction													
		Vacuum saturation	Immersion at atmospheric pressure	IRA	Sorption isotherm	Capillary absorption			1–D drying test			Vapour permeability	CTE	CHE	MIP
						X	Y	Z	X	Y	Z	Z	X	X	
B	200x100x50±2	10	10 (1)	10 (1)	–		5 (2)		–	–	–	–	–	–	–
	40x40x40±1	15 (3)	–	–	–	5 (3)	5 (3)	5 (3)	5 (4)	5 (4)	5 (4)	–	–	–	–
	50x50x20±1	–	–	–	–	–	–	–	–	–	–	5 (3)	–	–	–
	30x30x10±1	–	–	–	5 (3)	–	–	–	–	–	–	–	–	–	10 (5)
	160x40x40±0.5	–	–	–	–	–	–	–	–	–	–	–	6	6 (6)	–
CM	160x40x40±0.5	4	4 (1)	–	–		4 (1)		–	–	–	–	4 (1)	4 (6)	–
	40x40x40±0.5	3 (7)	–	–	–	3 (1)	–	–	3 (4)	–	–	–	–	–	–
	30x30x10±1	–	–	–	3 (7)	–	–	–	–	–	–	–	–	–	2 (5)
LM	160x40x40±0.5	4	4 (1)	–	–		4 (1)		–	–	–	–	4 (1)	4 (6)	–
	40x40x40±0.5	3 (7)	–	–	–	3 (1)	–	–	3 (4)	–	–	–	–	–	–
	30x30x10±1	–	–	–	3 (7)	–	–	–	–	–	–	–	–	–	2 (5)
LMJ	Ø51.3, h = 12±1	5	–	–	5	–	–	–	–	–	–	–	–	–	4 (5)

Note: IRA is the initial rate of absorption; CTE is the coefficient of thermal expansion; CHE is the coefficient of hygric expansion; MIP Is Mercury Intrusion Porosimetry

(1) Same specimens used for vacuum saturation

(2) 5–brick unit subset chosen from the initial 10 brick units tested for vacuum saturation, immersion at atmospheric pressure and IRA

(3) Cut from 5–brick unit subset

(4) Same specimens used for water absorption

(5) Small pieces cut from specimens used for sorption isotherm

(6) Same specimens used for CTE

(7) Cut from mortar prism

Table 3.2. Number of masonry specimens tested.

Masonry	Specimen (dimensions in mm)	Test and test configuration			
		Capillary absorption		1–D drying test	
		+Z	−Z	Drying from brick	Drying from mortar
M1	Cylinder Ø51.3 $h_B = 45\pm1$, $h_{LMJ} = 12\pm1$	8	8 (1)	–	–
M2	Cylinder Ø51.3 $h_B = 45\pm1$, $h_{LMJ} = 12\pm1$	8	8 (1)	–	–
M4	Cylinder Ø51.3 $h_B = 48\pm1$, $h_{LMJ} = 12\pm1$	6	–	–	–
D1	Cylinder Ø51.3 $h_B = 22\pm2$, $h_{LMJ} = 12\pm1$	–	–	6	6

Note: h_B is the height of the brick; h_{LMJ} is the height of the mortar joint; Z is the direction perpendicular to the bed joint and bed face of the brick

(1) Same specimens tested in the opposite direction

3.3 EXPERIMENTAL METHODS

Standard experimental procedures were followed in order to determine the material properties needed for a comprehensive hygro–thermo–mechanical characterization. The focus of the experimental studies was set on physical and moisture–related properties. Additionally, thermo– and hygro–mechanical properties were also studied to understand the material behaviour with respect to temperature and moisture changes. Finally, mercury intrusion porosimetry (MIP) tests were conducted to define the micro–structure of the materials. Examples of the experimental setups are shown in Figure 3.6.

3.3.1 Oven–drying for pre–conditioning of samples

Most experimental methods applied in the current study required an initial pre–drying of the materials. Such initial pre–conditioning was performed by means of oven–drying in accordance with ISO 12570 (EN ISO 12570:2000 + A1:2013, 2000). Oven–drying at 105°C was used for fired–clay bricks. Conversely, the drying temperature was reduced to 70 °C for mortar and masonry specimens to avoid microstructural damage or removal of chemically bound water from the cementitious matrix (Feng et al., 2013). The drying process was concluded when the change of mass between two consecutive weight measurements with a difference of at least 24 hours was less than 0.1 % of the total mass of the specimen.

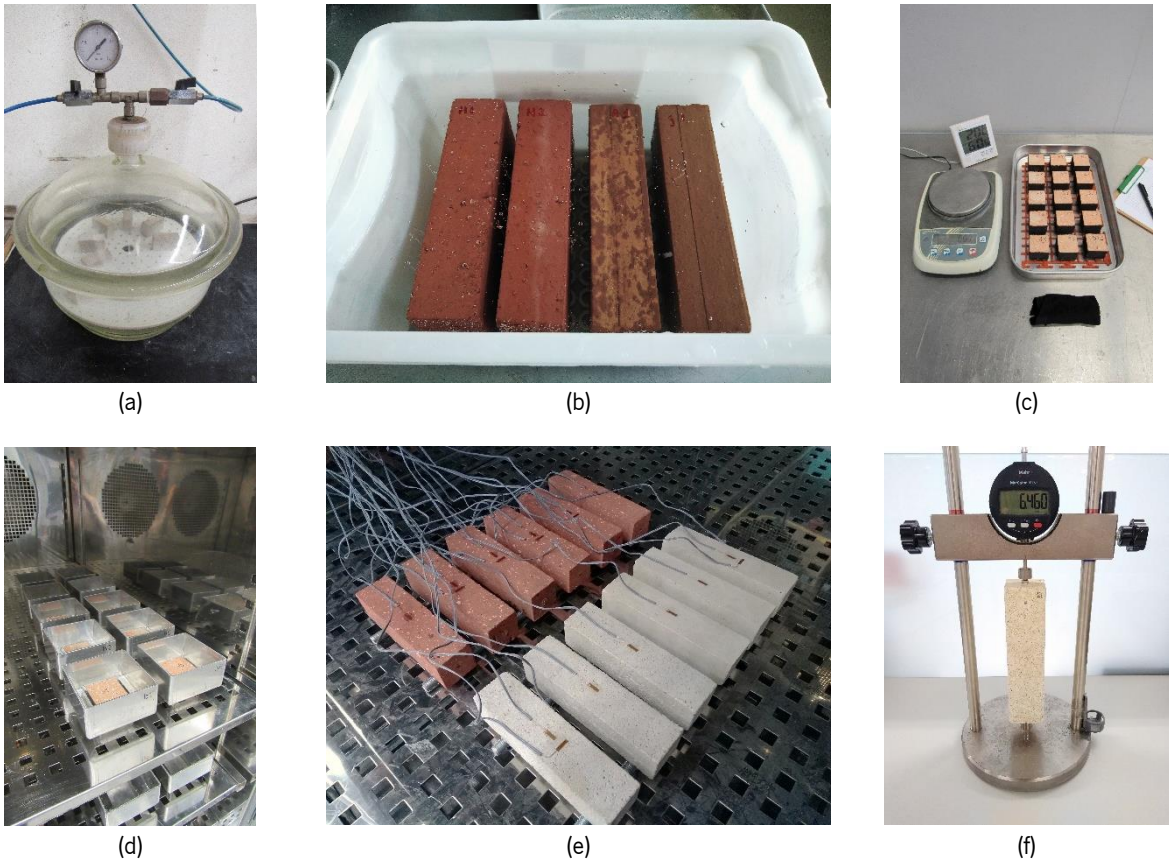

Figure 3.6. Examples of test setups used to determine material properties: (a) vacuum saturation; (b) immersion at atmospheric pressure; (c) capillary absorption; (d) cup test; (e) coefficient of thermal expansion; (f) coefficient of hygric expansion.

3.3.2 Vacuum saturation tests

Vacuum saturation tests were performed following the recommendations of RILEM TC 25–PEM (1980) to determine open porosity, ϕ_o [–], bulk density, ρ_{bulk} [$\mathrm{kg/m^3}$], and saturation moisture content, w_{sat} [$\mathrm{kg/m^3}$]. The studied samples comprised brick units, mortar prisms, brick and mortar cubes, and bed joint mortar discs (Table 3.1). Due to the high variability usually shown by fired–clay bricks, a sample of 10 randomly chosen units belonging to the same batch was analysed initially. Then, a subset of 5 statistically comparable specimens was selected for further studies. For mortar specimens, a sample of 4 prisms for each mortar type and 5 bed joint mortar discs were used.

Initially, the specimens were oven–dried following the procedure previously explained (see Section 3.3.1). The samples were left to cool down and then placed in an evacuation vessel where the pressure was lowered below 100 mbar to remove the air from the open pores of the material. The vacuum pressure was maintained for 4 hours. Subsequently, tap water at 15–20 °C was gradually introduced into the vessel until the water level was 1–2 cm above the specimens. Vacuum was maintained during the

introduction of water and for the following 4 hours. Subsequently, the system was set back to atmospheric pressure and the specimens were left under water for 24 hours. Finally, the immersed mass, m_{im} [kg], was determined by weighing under water (hydrostatic weighing). Then, the specimens were wiped with a dampened cloth and weighed in air to determine the saturated mass, m_{sat} [kg].

The bulk volume, V_{bulk} [m^3], was calculated from the masses measured in air and under water:

$$V_{bulk} = \frac{m_{sat} - m_{im}}{\rho_w} \tag{3.1}$$

where ρ_w [$\mathrm{kg/m}^3$] is the density of water, assumed 1000 $\mathrm{kg/m}^3$ in normal conditions. Consequently, the bulk density, ρ_{bulk} [$\mathrm{kg/m}^3$], was calculated as:

$$\rho_{bulk} = \frac{m_{dry}}{V_{bulk}} \tag{3.2}$$

Similarly, the open porosity, ϕ_o [–], was calculated as:

$$\phi_o = \frac{m_{sat} - m_{dry}}{m_{sat} - m_{im}} \tag{3.3}$$

Saturation moisture content, w_{sat} [$\mathrm{kg/m}^3$], was derived from open porosity as:

$$w_{sat} = \phi_o \cdot \rho_w \tag{3.4}$$

The total porosity, i.e. open + closed porosity, was not studied since the volume of closed pores does not take part in moisture transport.

3.3.3 Immersion at atmospheric pressure

Immersion tests were performed according to EN 772–21 (2011). This type of tests is meant to provide water absorption, W_s [%] or $W_{g,s}$ [kg/kg], and is exclusively focused on masonry units. In the present study, however, immersion tests were performed on mortar prisms as well. For all cases, the main guidelines defined by the standard procedure were followed. Initially dried specimens were placed in a tank with water at room temperature. After 24 hours immersion at atmospheric pressure, the specimens were taken from the tank, the excess of water removed with a damp cloth, and their mass was recorded. In the context of the present work, the main purpose of this procedure was to study the possibility of identifying a fixed capillary moisture content. Therefore, after the first measurement, the specimens were placed back in the tank and the procedure was repeated every 24 hours for several days.

3.3.4 Initial rate of absorption

The initial rate of water absorption, IRA, is a parameter used in masonry as a measure of brick suction. It represents the weight of water absorbed in 1 minute by the bed face of the brick when immersed in a shallow water basin, 5 ± 1 mm. The IRA may range from below 1 $\mathrm{kg/(m^2 \cdot min)}$ for low suction rate bricks up to 3–4 $\mathrm{kg/(m^2 \cdot min)}$ for high suction rate bricks (Groot & Larbi, 1999). The procedure for the initial rate of absorption test is established in EN 772–11 (2011). The tests were performed inside a climatic chamber with controlled temperature and humidity conditions of 20 °C and 60 % RH. The water used for the tests was conditioned to room temperature beforehand to avoid temperature–dependent phenomena associated with the change of viscosity of the water (Feng & Janssen, 2016). IRA was studied on the initial 10 brick units tested for vacuum saturation and immersion at atmospheric pressure.

3.3.5 Static gravimetric tests

The sorption isotherms (adsorption/desorption) of the materials were obtained through static gravimetric tests according to EN ISO 12571 (2013). The sorption isotherms represent the moisture storage capacity of a material in the hygroscopic range, namely from dry state, i.e. 0 % RH, to 93–95 % RH. In the over–hygroscopic or capillary range, i.e. above 93–95 % RH, the sorption isotherms become extremely steep and slight variations in relative humidity result in large changes in moisture content. Thus, the higher part of the moisture storage curve must be completed by other means, namely pressure plate experiments or results derived from mercury porosimetry (Krus, 1996).

The size of the specimens used for these tests (see Table 3.1) was chosen following the recommendations by Feng et al. (2013), who proved that smaller specimens help speed up the process without compromising the accuracy. Brick and mortar specimens were cut from the brick units and mortar prisms used for the previous tests (Figure 3.4): 1 brick piece from each unit (5 replicates in total) and 3 mortar pieces from a single prism (3 replicates for each type of mortar). Additionally, lime mortar discs extracted from masonry bed joints (5 replicates) were tested as well.

To define the sorption isotherms, the equilibrium moisture content of the materials was determined at different relative humidity levels. It must be noted that the moisture content is usually expressed either as mass of adsorbed water per volume of dry material, w [$\mathrm{kg/m^3}$], or as mass of adsorbed water per mass of dry material, w_g [kg/kg]. The latter format, known as gravimetric moisture content, is used for the static gravimetric tests. Nonetheless, both expressions are related through:

$$w = w_g \cdot \rho_{bulk} \tag{3.5}$$

Both adsorption and desorption were studied to assess the existence of hysteresis. The adsorption process started with initially dry samples and then, consecutive higher RH levels were imposed. A climatic chamber was used to provide constant RH levels and isothermal conditions ($\mathrm{T} = 23 \pm 1$ °C). For each level, the moisture content of the specimens was determined periodically. Equilibrium was considered when 3 successive weight measurements at intervals of at least 24 hours showed a relative mass variation below 0.1 %. Once the equilibrium was attained, the environmental RH was set to a new level. After the last step of the adsorption process (95 % RH), the specimens were saturated by immersion in water at atmospheric pressure for 3 hours until capillary moisture content, $w_{g,cap}$ [kg/kg], was reached. Subsequently, the desorption process began at $w_{g,cap}$, following a sequence of decreasing RH levels. The discrete measurement points determined with this method were then used to fit the moisture storage function of the materials by means of analytical expressions.

3.3.6 Cup tests

Dry and wet cup tests were performed on brick samples following the specifications of EN 15803 (2009), EN ISO 12572 (2016), and ASTM E96/E96M–22 (2022), to determine the water vapour permeability, δ_v [kg/(m · s · Pa)], or alternatively the water vapour resistance factor, μ [–]. Both properties are related by the following expression:

$$\delta_v = \frac{\delta_a}{\mu} \tag{3.6}$$

where δ_a [kg/(m · s · Pa)] is the water vapour permeability of still air, defined empirically (EN 15803, 2009):

$$\delta_a = \frac{2.31 \cdot 10^{-5}}{R_v \cdot T} \frac{p_0}{p} \left(\frac{T}{273.15} \right)^{1.81} \tag{3.7}$$

where $p_0 = 101325$ Pa is the standard atmospheric pressure, p [Pa] is the ambient barometric pressure, $R_v = 461.5$ J/(kg · K) is the universal gas constant for water vapour, and T [K] is the temperature.

These tests are based on stationary diffusion analysis in which the studied material acts as a filter between two environments with different vapour pressures. The test is defined as dry or wet cup depending on whether the relative humidity inside the cup is lower or higher than outside, respectively. The gradient of vapour pressure between the internal and external surfaces leads to a vapour flux across the specimen. By determining this vapour flux, the vapour permeability of the material can be derived:

$$\delta_v = \frac{g_v \cdot t}{\Delta p_v} = \frac{(G_v/A) \cdot t}{\Delta p_v} \tag{3.8}$$

where g_v [kg/(s · m²)] is the rate of water vapour flow, G_v [kg/s] is the average mass change rate, A [m²] and t [m] are the exposed area and the thickness of the test specimen, respectively, and Δp_v [Pa] is the vapour pressure difference between the two environments. The vapour pressure is calculated from the definition of relative humidity, φ [–]:

$$\varphi = \frac{p_v}{p_{v,sat}(T)} \tag{3.9}$$

where the saturation vapour pressure, $p_{v,sat}$ [Pa], is a non–linear function of temperature, T [K], and is described empirically by different authors, such as (Monteith & Shatleworth, 2013):

$$p_{v,sat} = 610.7[\text{Pa}] \cdot 10^{7.5\left(\frac{T-273.15}{T-35.85}\right)} \tag{3.10}$$

In the present work, the cups were customized to the shape and dimensions of the specimens (Figure 3.7), which were cut out from the previously studied units (Figure 3.2).

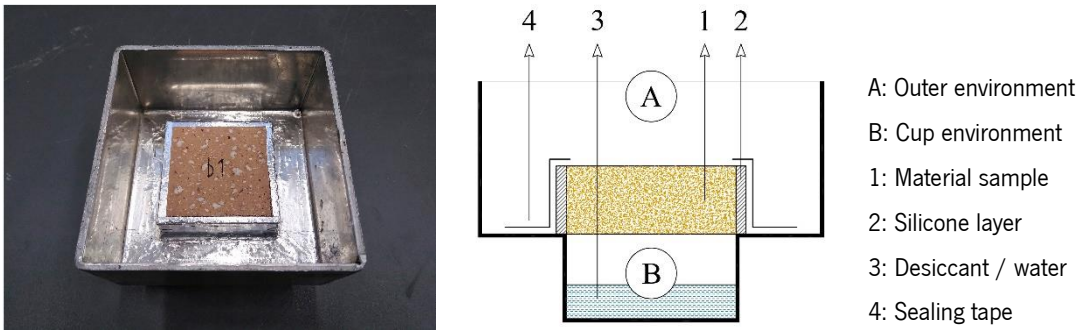

Figure 3.7. Cups used to determine water vapour permeability in brick samples.

One specimen per brick was studied, thus a total of 5 tested replicates. A thin layer of neutral silicone was applied to the lateral faces of the specimens to guarantee one–dimensional transport. The conditions used for the cup tests in this study are summarized in Table 3.3. The tests were performed inside a climatic chamber to ensure constant environmental conditions, namely 23 °C and 55 % RH. The specimens were pre–conditioned in the same environment until equilibrium was reached. Then, the cups were prepared by placing a piece of cotton saturated with distilled water (wet procedure) or silica gel desiccant (dry procedure) on the bottom of the container. The specimens were then placed and sealed on the opening of the cup with an adhesive aluminium tape to guarantee a vapour–tight system. The time was recorded from the moment when the system was sealed, and the evolution of mass was registered

periodically. The tests were concluded when a clear linear trend ($R^2 > 0.99$) could be established using at least 5 successive points measured at intervals of not less than 24 hours.

Table 3.3. Environmental conditions for cup tests.

Method	ϑ_{env} [°C]	RH_{env} [%]	RH_{cup} [%]	Δp_v [Pa]
Dry cup	23	55	3	1460.6
Wet cup	23	55	98	1207.8

For the processing of results, the masked edge effect was considered negligible. On the contrary, the air layer resistance inside the cup was taken into account as indicated by EN ISO 12572 (2016) and ASTM E96/E96M–22 (2022). Additionally, the air velocity above the specimens was assumed to be below $1\ \mathrm{m/s}$. Thus, an exterior surface transfer resistance was considered as well, and the corresponding correction was introduced according to ASTM E96/E96M–22 (2022).

3.3.7 Capillary absorption tests

Capillary absorption tests were performed according to the specifications of EN ISO 15148 (EN ISO 15148:2002+A1:2016, 2016) to determine the capillary absorption coefficient, A_w $[\mathrm{kg/(m^2 \cdot s^{0.5})}]$, and capillary moisture content, w_{cap} $[\mathrm{kg/m^3}]$. The tests were performed on whole brick units, brick cubes, mortar prisms, mortar cubes, and masonry cylinders (Table 3.1, Table 3.2). The bricks used for the vacuum saturation tests were used here again, i.e. 5 statistically comparable brick units. The same specimens were tested in all three directions: (a) header or extrusion direction, labelled X; (b) stretcher direction, labelled Y; (c) bed direction, labelled Z. Once the whole units were tested, brick cubes were cut out (Figure 3.4) for further water absorption tests. Thus, 3 cubes (1 for each testing direction) were extracted from each brick, resulting in 3 groups of 5 replicates for each direction. For the mortars, the specimens consisted of the same specimens used for vacuum saturation tests, i.e. 4 moulded prisms for each mortar type. The same specimens were studied in all three directions (X, Y, Z). Moreover, mortar cubes were cut out from a mortar prism of each type (Figure 3.4). Therefore, 3 mortar cubes were analysed as well (testing direction X). Finally, water absorption tests were performed on masonry cylinders with different B+LMJ configurations, in the direction perpendicular to the joints.

Before the tests, the specimens were oven–dried according to the procedure previously introduced. After cooling down, the lateral faces of the specimens were wrapped with an adhesive aluminium tape to prevent evaporation and guarantee a 1–D moisture flow. Nevertheless, the bottom part of the lateral faces

(8–10 mm) was left unwrapped to avoid interfacial water uptake between the brick surface and the film. Additionally, the uppermost face was left uncovered to facilitate air evacuation. The specimens prepared in this way were then placed into a shallow water basin so that they were submerged 5 mm approximately. The level of the water was kept constant throughout the test. Note that the water used during the test was conditioned to room temperature beforehand to avoid temperature–dependent phenomena associated with the change of viscosity of the water (Feng & Janssen, 2016). The tests were performed in a climatic chamber with controlled laboratory conditions, namely 20 °C and 60 % RH. The specimens were regularly taken out of the bath, the excess of water was removed with a dampened cloth, and the weight was measured. The water absorption coefficient was then determined by the one–tangent method: the water mass inflow per unit area was plotted against the square root of time and the slope of the initial linear trend (first stage) was defined as A_w. The tests terminated when the inflow reached a plateau (second stage). The average value of the last three points in the plateau was defined as the capillary moisture content, w_{cap}.

When the same specimens were planned to be studied in different directions, i.e. brick units and mortar prisms, after the conclusion of each test, the specimens were unwrapped and oven–dried before the subsequent analysis in a different direction. For the specimens that were tested just once, i.e. brick and mortar cubes, a neutral silicone was chosen to cover the lateral faces. For these cases, the full height of the lateral faces was covered assuming that no water uptake would occur between the interface of the two materials, i.e. silicone and substrate.

For the case of masonry cylinders, a transparent adhesive film was used to wrap the lateral surfaces. Different configurations of masonry composites were studied (Figure 3.5). The first set was made up by 8 cylinders with 2 layers (1 interface), i.e. B+LMJ. The specimens were tested twice, once sucking up water from the mortar side and the second time absorbing water from the brick. The second group of masonry specimens was composed of 8 cylinders with 3 layers (2 interfaces), namely B+LMJ+B. Similarly, these cylinders were tested twice, each time sucking up the water from a different brick. The purpose of these tests was to verify the existence of a hydraulic resistance at the interface between the two materials.

3.3.8 Drying tests

Drying tests were carried out following the recommendations of EN 16322 (2013), i.e. subjecting initially capillary saturated specimens to 1–D drying from a single surface. The mass of the specimens was measured periodically and the moisture mass loss with time was calculated accordingly. The tests were

performed in a climatic chamber with controlled laboratory conditions, namely 23 °C and 55 % RH. These tests were used to study the drying kinetics of the selected materials. Furthermore, drying results may be used for identification of transport properties, such as liquid permeability, by means of inverse modelling (Zhang & Scherer, 2018).

The tests were performed on a total of 15 brick cubes (5 specimens for each direction, i.e. X, Y, Z) and 3 mortar cubes for each mortar type (testing direction X) which were initially saturated by means of capillary absorption tests. Once the capillary moisture content was attained, w_{cap}, the specimens were kept partially immersed in water and the upper face was sealed using neutral silicone (note that the lateral faces were already sealed with the same material prior to capillary tests). Once the silicone was dry, the specimens were placed in a climatic chamber with controlled environmental conditions, namely 23 °C and 55 % RH, to dry from the unsealed surface. The specimens were weighed periodically to establish the mass loss until a plateau was reached.

Drying tests were also performed on masonry cylinders (Figure 3.5). The initial cylinders were made up by three layers, namely LMJ+B+LMJ. Subsequently, they were cut in half, so two pieces LMJ+B were obtained. The pieces were then prepared following the same procedure described for the single–material cubes. From each pair, one was prepared to dry from the mortar face and the other one to dry from the brick. A total of 12 specimens were tested, 6 per each case.

3.3.9 Coefficient of thermal expansion

In order to determine the coefficient of thermal expansion (CTE) of the studied materials, a set of specimens were prepared and placed in a climatic chamber. In particular, prismatic specimens with dimensions 160 mm × 40 mm × 40 mm were used. The specimens were placed on roller supports to allow free movement. For all the samples, the material deformations were monitored with strain gauges in the longitudinal direction. Moreover, half the brick specimens were instrumented with strain gauges in the transversal directions to consider possible orthotropic effects.

Different temperature cycles were defined for the climatic chamber while maintaining a constant relative humidity of 55 %. The temperature started at 20 °C and was kept for 120 minutes until the system stabilized. Then, the temperature was lowered and kept at 10 °C for 120 minutes. From then on, the temperature was increased by 10 °C in a stepwise manner, maintaining each new level constant for 60 minutes: 20, 30, 40, 50 and 60 °C. After the last step, the temperature was set back to 20 °C and the system was dismantled. The conditions recorded inside the chamber are presented in Figure 3.8.

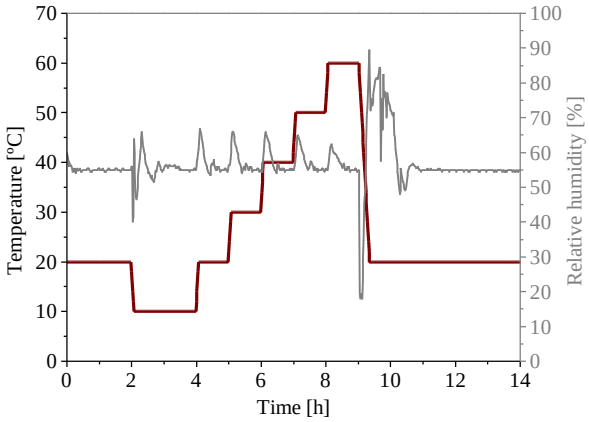

Figure 3.8. Conditions imposed for calculation of the coefficient of thermal expansion.

Strain gauges were used to monitor the deformation of the specimens during the test. In particular, TML BF series strain gauges were used. The operational temperature of this series reaches up to 200 °C and it provides temperature compensation between 10 °C and 80 °C for materials with coefficients of thermal expansion of 3.0E–6 $°C^{-1}$, 5.0E–6 $°C^{-1}$, or 8.0E–6 $°C^{-1}$. These strain gauges were glued on the previously polished and cleaned material surfaces using cyanoacrylate.

Finally, the coefficient of thermal expansion, α_T [$1/°C$ or $1/K$] was calculated as:

$$\alpha_T = \frac{\varepsilon_{T_{i+1}} - \varepsilon_{T_i}}{T_{i+1} - T_i} \tag{3.11}$$

where ε_T [–] is the strain caused by the thermal difference between two consecutive steps, ΔT [K], and T [K] is the temperature. In the present work, the strains for each temperature interval were calculated as the average strain in the range where the deformations stabilized into a plateau.

3.3.10 Coefficient of hygric expansion

The coefficient of hygric expansion (CHE) was determined following the specifications of the European standard EN 13009 (2000). Basically, the material samples were placed inside a climatic chamber and subjected to different moisture conditions in order to induce swelling. For each exposure step, the length of the specimens was measured periodically until a plateau was identified. For the current studies, the specimens were initially measured for dry state, which was attained in a desiccator with silica gel. Then, the specimens were moved to the climatic chamber and subjected to isothermal conditions, 23 °C, and the following relative humidity steps: 55, 80, 90 and 96 %. As a final moisture conditioning, the materials were immersed in water at atmospheric pressure.

The same prismatic specimens, 160 mm × 40 mm × 40 mm, used to calculate the coefficient of thermal expansion were used here. The specimens were placed on roller supports to allow free

deformation. The specimens were measured in their longitudinal direction using a digital dial gauge in a fixed frame (see Figure 3.6f). The coefficient of hygric expansion, α_h $[\mathrm{m}^3/\mathrm{kg}]$ or $\alpha_{h,g}$ $[\mathrm{kg}/\mathrm{kg}]$, was determined for each exposure step as:

$$\alpha_h = \frac{\varepsilon_{h_{i+1}} - \varepsilon_{h_i}}{w_{i+1} - w_i} \tag{3.12}$$

where ε_h [–] is the strain caused by the moisture content difference between two consecutive steps, Δw $[\mathrm{kg}/\mathrm{m}^3]$, and w $[\mathrm{kg}/\mathrm{m}^3]$ is the moisture content (which may be expressed as gravimetric moisture content, w_g $[\mathrm{kg}/\mathrm{kg}]$, as well). Finally, an analytical expression for the coefficient of hygric expansion, i.e. $\alpha_h(w)$, was derived from the slope of the curve relating hygric strains and moisture content:

$$\alpha_h(w) = \frac{d\varepsilon_h}{dw} \tag{3.13}$$

3.3.11 Mercury intrusion porosimetry

The pore size distribution of the materials was determined by mercury intrusion porosimetry (MIP) according to ASTM D4404–18 (2018). The procedure is derived from fluid behaviour in an unsaturated medium assuming that a fluid intrusion, in this case mercury, is dependent on pressure. Hence, mercury is forced into the pores of the material following incremental pressure steps, and the relation between intruded mercury content and applied pressure is recorded.

Assuming a cylindrical pore model (Krus, 1996), the Young–Laplace equation defines the pressure at which a pore fills (or empties) according to its pore opening size:

$$p_c = \frac{2\sigma}{r} \cdot cos\,(\theta) \tag{3.14}$$

where σ $[\mathrm{N}/\mathrm{m}]$ is the surface tension, r $[\mathrm{m}]$ is the pore radius, and θ is the contact angle. Therefore, knowing the pressure applied at each level and with the appropriate values of surface tension and contact angle for mercury, it is possible to obtain the effective capillary size and consequently the pore size distribution (Figure 3.9). It is noted that MIP can provide relevant information about the microstructural characteristic of the materials within the macro–pore and meso–pore ranges, namely 2–50 nm and >50 nm, respectively, according to the pore size ranges defined by IUPAC (International Union of Pure and Applied Chemistry) (IUPAC, 1972). However, for the lower meso–pore and micro–pore ranges, different methods must be used, e.g. physisorption.

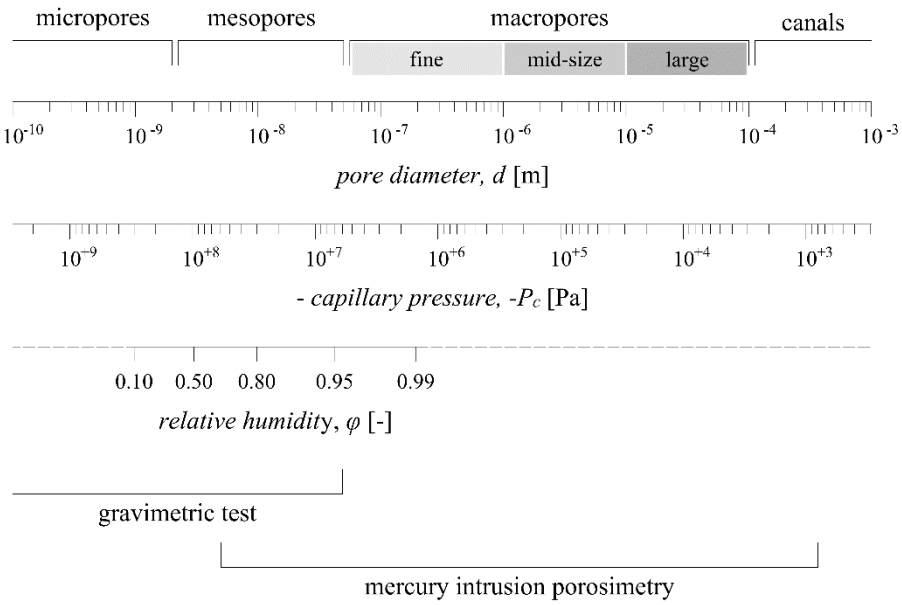

Figure 3.9. Relation between pore size, capillary pressure, and relative humidity according to Young–Laplace and Kelvin equations, together with the classification of pores according to IUPAC and the measuring range of the experimental methods. Adapted from Brocken (1998).

For the current study, the tests were performed using a mercury porosimeter equipment (Micromeritics AutoPore IV 9500 V1.07) with a range of applied pressure between 32990 psia (227.46 MPa) and 0.53 psia (3.65 kPa), corresponding to minimum and maximum pore sizes of 0.005 μm and 345 μm, respectively. The contact angle for the intruding mercury meniscus was defined as 130° (Ma, 2014). In addition, mercury surface tension and mercury density were assumed 0.485 N/m and 13.5335 g/ml, respectively.

The specimens for MIP were taken from the samples previously used for the determination of sorption isotherms. From each material specimen, 2 pieces were cut for MIP testing and the obtained results were averaged. The resulting pieces had a mass ranging from 0.90 g to 1.95 g. Before the test, the specimens were stored in a glass desiccator with silica gel until dry state was attained.

Finally, with the appropriate transformations for the values of surface tension and contact angle, MIP results can be transformed into the (desorption) moisture retention curve. In this regard, the surface tension and contact angle for liquid water were defined as 0.072 N/m and 0°, respectively.

This page has been intentionally left blank

CHAPTER 4

Experimental results

The current chapter presents the results of the material characterization and experimental testing procedures introduced in the previous chapter. The chapter is divided into two main subsections. The first section is dedicated to the experimental results obtained for single constituent materials. In turn, the second part is devoted to the hygric tests performed on multi–layered masonry specimens. Relevant discussions of the experimental procedures and the obtained results are given in the corresponding section. The results presented herein will be used as input and validation data for the moisture transport simulations as explained in the following chapter.

Part of the information presented in this chapter has been published in Ramirez et al. (2021).

4.1 RESULTS ON SINGLE CONSTITUENT MATERIALS

The results obtained from experimental tests in mono–material specimens are presented herein. The experimental campaign comprised vacuum saturation, immersion at atmospheric pressure, gravimetric tests to determine the moisture storage curves, cup tests, initial rate of absorption, capillary absorption, drying tests, tests to determine the coefficients of thermal expansion and hygric expansion, and mercury intrusion porosimetry.

4.1.1 Vacuum saturation tests results

The properties derived from vacuum saturation tests are collected in Table 4.1. In the table, CoV indicates the coefficient of variation.

Vacuum saturation tests performed on whole bricks and on brick cubes extracted from those initial units produced the same results in terms of bulk density and open porosity. Similarly, no difference was observed between mortar prisms and mortar cubes cut out of them. Therefore, the use of smaller specimens is justified and is recommended to speed up the process and guarantee the saturation of the innermost spaces.

As it was expected, the properties of the lime mortar obtained from masonry bed joints differed from those obtained from moulded specimens even though the mixes were prepared with the same composition and in the same controlled environment. Overall, LMJ showed higher bulk density and lower open porosity, and consequently lower saturation moisture content.

Table 4.1. Results from vacuum saturation tests (CoV between parentheses).

Material	ρ_{bulk} [$\mathrm{kg/m^3}$]	ϕ_o [–]	w_{sat} [$\mathrm{kg/m^3}$]
Brick (B)	1900 (2.69)	0.280 (6.76)	280 (6.76)
Cement mortar (CM)	2000 (0.15)	0.210 (1.05)	210 (1.05)
Lime mortar (LM)	1990 (0.81)	0.255 (2.53)	255 (2.53)
Lime mortar joints (LMJ)	2060 (1.32)	0.230 (6.93)	230 (6.93)

4.1.2 Immersion at atmospheric pressure

The results of the immersion tests at atmospheric pressure are presented in Figure 4.1. The graphs show the evolution of gravimetric moisture content, w_g [kg/kg], with immersion time for brick units (Figure 4.1a) and mortar prisms (Figure 4.1b). As defined in EN 772–21 (2011), $W_{g,s}$ [kg/kg] is determined for clay bricks after 24 hours of immersion at atmospheric pressure. Thus, the average value for the studied units $W_{g,s} = 0.128\ \mathrm{kg/kg}$. However, it must be noted that the bricks continued absorbing water with prolonged immersion time. This phenomenon is expected due to air entrapment in the pore structure during the imbibition process (Descamps, 1997). Thus, the saturation level of bricks at 24 hours was around 97.3 % the level of saturation attained after 72 hours of immersion. Conversely, the mortar specimens had reached ca. 99 % the final saturation already after the prescribed period of 24 hours. The bigger volume of masonry units is thought to be the reason for the slower saturation process observed in the brick material. In other words, air entrapment is more evident in bigger specimens.

4.1.3 Initial rate of absorption

The average initial rate of absorption (IRA) obtained for brick units was $0.30\ \mathrm{kg/(m^2 \cdot min)}$, with a coefficient of variation CoV = 15.42 %. According to the classification by Groot & Larbi (1999), this value indicates that the studied fired–clay bricks belong to the low suction rate category, i.e. IRA < $1\ \mathrm{kg/(m^2 \cdot min)}$. The high CoV reveals a certain scatter within the tested sample, which can be related to the presence of defects or irregularities in the outermost layer of the brick units. Moreover, the short duration of IRA tests might exacerbate any difference that could otherwise stabilize with prolonged contact with water.

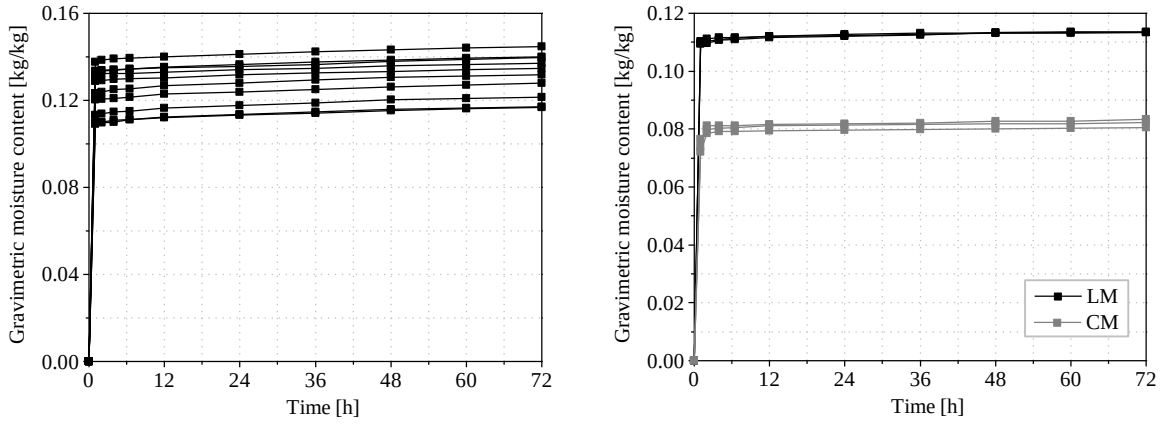

Figure 4.1. Results of the immersion test at atmospheric pressure: (a) brick units; (b) cement mortar (CM) and lime mortar (LM) specimens.

4.1.4 Moisture isotherm

The data collected from static gravimetric tests are shown in Figure 4.2. The results showed clear similarities between brick and lime mortar, whereas cement mortar and lime mortar from joints followed a different trend. On one hand, B and LM hardly showed moisture adsorption until high RH values, revealing a low hygroscopic response. Moreover, no significant differences were found between adsorption and desorption. Conversely, hysteresis was observed in CM and LMJ. CM showed considerable moisture adsorption for lower RH levels, confirming a markedly hygroscopic nature. Likewise, LMJ showed moisture adsorption for lower RH levels, and therefore a more hygroscopic response than its moulded counterpart.

The experimental measurements were fitted with analytical expressions found in the literature. In particular, the model proposed by Künzel (1995) was used to describe the sorption behaviour of B and LM. For CM and LMJ, the model established by Mualem (Mualem, 1976) was adopted. The expression proposed by Künzel can be written as:

$$w(\varphi) = w_{cap} \cdot \frac{(\psi - 1) \cdot \varphi}{\psi - \varphi} \tag{4.1}$$

where $w(\varphi)$ [$\mathrm{kg/m^3}$] is the moisture content as a function of relative humidity, φ [–], w_{cap} [$\mathrm{kg/m^3}$] is the capillary moisture content, and ψ [–] is a fitting parameter. Künzel's model stems from a simplified form of the BET equation (Brunauer et al., 1938) and is applicable to sorption curves with a marked exponential trend, i.e. non–hygroscopic, capillary–active materials.

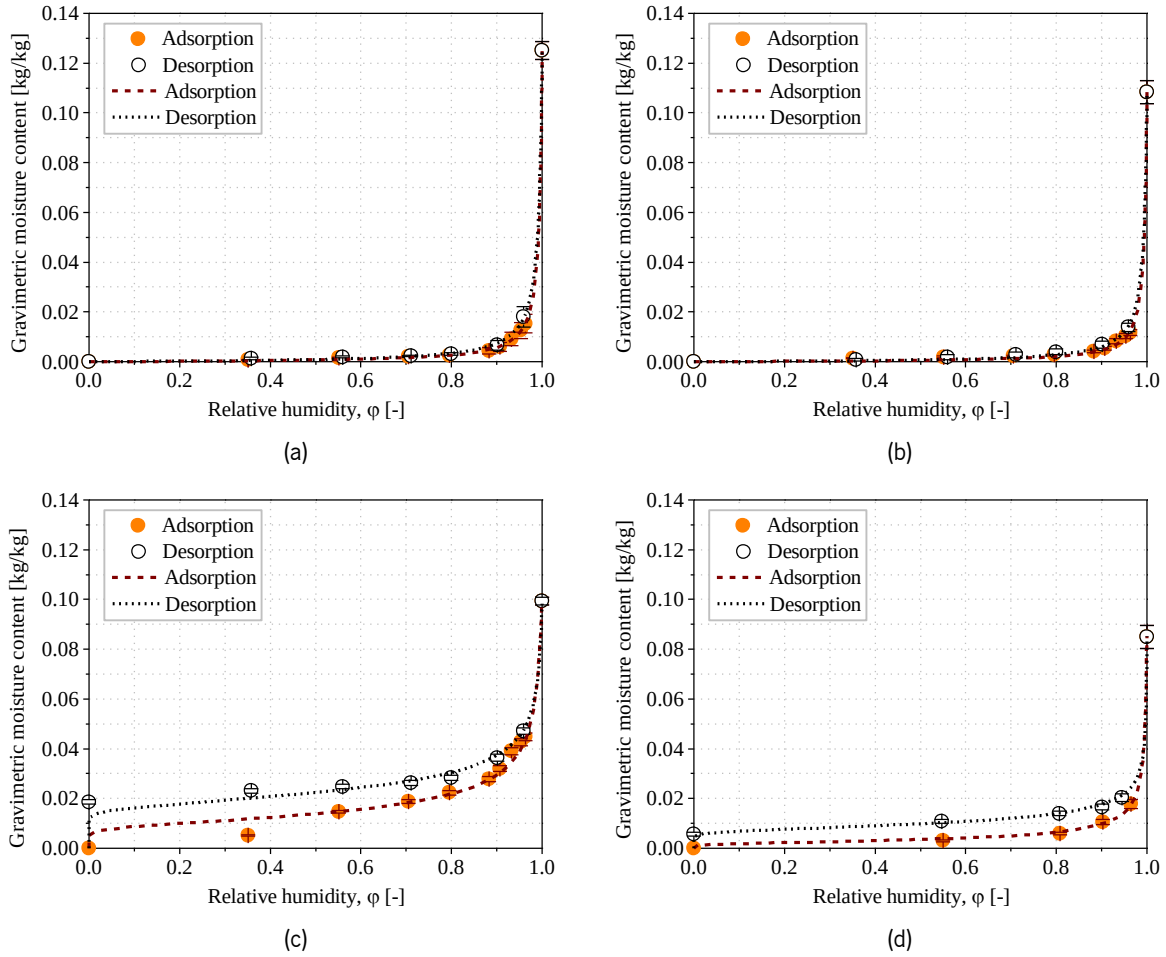

Figure 4.2. Static gravimetric tests results and fitting curves for the sorption isotherms of the studied materials at 23 °C: (a) brick (B), and (b) lime mortar (LM), fitted with Künzel's model (Künzel, 1995); (c) cement mortar (CM), and (d) lime mortar from masonry joints (LMJ), fitted with Mualem's model (Mualem, 1976).

On the other hand, the model proposed by Mualem is extensible to hygroscopic materials. This model is a constrained form of the more generalized equation proposed by van Genuchten (1980):

$$w(p_c) = w_{cap} \cdot [1 + (a \cdot p_c)^n]^{-m} \tag{4.2}$$

where $w(p_c)$ [kg/m^3] is the moisture content as a function of capillary pressure, p_c [Pa], and a [1/Pa], n [–] and m [–] are fitting parameters. It is noted that capillary pressure and relative humidity can be related through the Kelvin equation, such as:

$$p_c = \rho_w \cdot R_v \cdot T \cdot ln\, \varphi \tag{4.3}$$

where ρ_w [kg/m^3] is the density of water, R_v [J/(kg · K)] is the universal gas constant for water vapour, and T [K] is the absolute temperature.

Considering van Genuchten's expression, Mualem fixed $m = 1 - 1/n$ (Mualem, 1976):

$$w(p_c) = w_{cap} \cdot \left[1 + (a \cdot p_c)^{1/(1-m)}\right]^{-m} \tag{4.4}$$

The curves obtained from these analytical expressions are plotted in Figure 4.2 together with the experimental points. The corresponding fitting parameters for the different cases are presented in Table 4.2 together with relevant criteria to evaluate the accuracy of the model. In this case, the accuracy was determined by the adjusted coefficient of determination (R^2_{adj}) and the normalised root mean square error (%NRMSE) between predicted and measured points. The adjusted R^2 takes into account the effect of the number of fitting parameters and is given as:

$$R^2_{adj} = \frac{(N-1)R^2 - (M-1)}{N-M} \tag{4.5}$$

where N is the number of measured data and M is the number of fitting parameters.

The %NRMSE is expressed as a percentage and is defined as follows:

$$\%\mathrm{NRMSE} = \frac{1}{\sum_{i=1}^{N} x_{exp,i}/N} \sqrt{\frac{1}{N}\sum_{i=1}^{N}\left(x_{exp,i} - x_{pre,i}\right)^2} \tag{4.6}$$

where x_{exp} and x_{pre} are the measured values from the experiments and the predicted values from the fitted curves, respectively. A lower value of %NRMSE indicates a better match.

Table 4.2. Fitting parameters and accuracy of the modelled sorption isotherms.

Material	Künzel (Eq. (4.1))	Mualem (Eq. (4.4))	R^2_{adj}	%NRMSE
B	$\psi_{ads} = 1.0055$	–	0.999	2.30%
	$\psi_{des} = 1.0070$	–	0.999	2.49%
LM	$\psi_{ads} = 1.0052$	–	0.999	5.30%
	$\psi_{des} = 1.0066$	–	0.999	4.49%
CM	–	$a_{ads} = 1.43\text{E}{-6}$ [1/Pa] $m_{ads} = 0.285$	0.989	8.26%
	–	$a_{des} = 2.51\text{E}{-6}$ [1/Pa] $m_{des} = 0.213$	0.982	8.10%
LMJ	–	$a_{des} = 3.80\text{E}{-6}$ [1/Pa] $m_{des} = 0.352$	0.990	11.63%
	–	$a_{des} = 1.19\text{E}{-5}$ [1/Pa] $m_{des} = 0.235$	0.999	2.42%

4.1.5 Vapour permeability

The results from dry cup and wet cup tests performed on brick specimens gave $\mu_{dry} = 34.14$ (CoV = 12.64 %) and $\mu_{wet} = 13.50$ (CoV = 17.85 %), respectively. Vapour permeability was only tested in the bed direction (Z) since the cutting of the original units after removal of the outermost layer (5 mm) did not allow to obtain the specimens for the other directions (Figure 3.4). It must be noted that the results obtained from cup measurements showed the highest scatter among the tests performed in this study. A low reliability for this type of test has been indicated before, see e.g. Roels et al. (2004), Feng et al. (2015), Hens (2016), Feng et al. (2020).

The water vapour resistance factor, μ, indicates how many times lower the vapour diffusion in the material is in comparison with vapour diffusion in still air. By definition, $\mu = 1$ for stagnant air. Expressing the water vapour permeability through the vapour resistance factor by means of Eq. (3.6) has the advantage of assigning the temperature and pressure dependencies of water vapour diffusion to the empirical term $\delta_a\ (T, p)$, so that the vapour resistance factor is independent of these variables and becomes a constant characteristic for each material. Nonetheless, as the values for our brick specimens show, vapour diffusion tests performed at different relative humidity levels, e.g. dry and wet cups, usually result in different permeability values for the same material (Kumaran, 1996; Roels, Carmeliet, et al., 2003). Consequently, vapour diffusion (expressed through either vapour permeability or vapour resistance factor) must be a function of moisture content. There have been considerable efforts in the literature to explain this phenomenon, e.g. Künzel (1995), Krus (1996), Scheffler (2008), but a univocal standpoint has not been reached. Most authors agree on the overall influence of the pore–saturation level since the presence of water islets in the pore system modifies the effective space available for vapour diffusion (Scheffler, 2008). However, the debate appears when defining the effect of moisture condensation in the pores for high moisture contents and subsequent reduction of the space accessible to vapour transport. Künzel (1995) argued that vapour diffusion might be either obstructed or (this is the most common assumption) enhanced through the water islets depending on the local conditions of temperature and moisture content inside the material. On the other hand, Krus (1996) introduced the phenomenon of surface diffusion, i.e. advective water transport along the adsorbed liquid film on pore walls, to explain the differences observed experimentally between dry and wet cup tests. Surface diffusion becomes noticeable at high humidity levels, but in practice, it cannot be distinguished from vapour transport and therefore it is lumped together with diffusion, which could cause the observed differences in apparent vapour permeability. The additional liquid transport superimposed on diffusion would be likely to increase the observed vapour permeability, therefore providing a lower resistance value for wet cup

measurements. Indeed, this is in agreement with the observations made for the brick specimens in our study.

4.1.6 Capillary absorption

Water uptake tests for material characterization were performed on whole units, brick cubes and mortar prisms along different directions. The results are summarized in Table 4.3.

Table 4.3. Results from water absorption tests (CoV between parentheses).

Material	$A_{w,X}$ $[\mathrm{kg/(m^2 \cdot s^{0.5})}]$	$A_{w,Y}$ $[\mathrm{kg/(m^2 \cdot s^{0.5})}]$	$A_{w,Z}$ $[\mathrm{kg/(m^2 \cdot s^{0.5})}]$	A_w (1) (2) $[\mathrm{kg/(m^2 \cdot s^{0.5})}]$	w_{cap} (3) $[\mathrm{kg/m^2}]$
B units	0.118	0.090	0.068	–	250
	(8.43)	(5.51)	(7.36)		(2.35)
B cubes	0.104	0.089	0.061	–	240
	(6.31)	(7.78)	(5.86)		(1.07)
LM	0.237	0.234	0.233	0.235	225
	(1.62)	(1.59)	(1.46)	(1.57)	(2.05)
CM	0.059	0.059	0.060	0.059	180
	(3.96)	(5.32)	(7.77)	(6.49)	(2.45)

(1) Isotropic

(2) Sample of 4 moulded prisms

(3) Average of all tests

The capillary moisture content, w_{cap} $[\mathrm{kg/m^3}]$, was determined as the average moisture content at the end of the water absorption tests. It should be noted that the capillary moisture content is always lower than the saturation moisture content defined from open porosity, i.e. $w_{cap} < w_{sat}$, due to air entrapment in the pore structure during imbibition (Descamps, 1997). For prolonged imbibition or immersion times, w_{cap} will approach w_{sat} as the air trapped in the pores dissolves into the water (Scheffler, 2008). This phenomenon was already pointed out in the specimens subjected to immersion at atmospheric pressure (see Section 4.1.2), which exhibited a slow, progressive saturation process. Thus, it can be concluded that w_{cap} is more a fuzzy limit than a fixed value. For the studied materials, the comparison between saturation and capillary moisture contents gave $w_{cap} \approx 80\ \%$ – $90\ \%\ w_{sat}$, which is an indication of the quantity of pores that can be classified as capillaries with respect to the overall open porosity.

The results obtained for whole bricks are shown in Figure 4.3 for the three studied directions: (a) header or extrusion direction, labelled X; (b) stretcher direction, labelled Y; (c) bed direction, labelled Z. Note that each set of tests ended up in a different plateau since the exposed surface was not the same

for each case; nonetheless, the moisture content at the end of all tests was equivalent. The rate of absorption per unit area was fastest in the extrusion direction (X) and slowest in the bed direction (Z). Considering the bed direction as a reference (it is usually the most reported one), we obtain $A_{w,B-X} \cong 170\ \%\ A_{w,B-Z}$ and $A_{w,B-Y} \cong 130\ \%\ A_{w,B-Z}$. This entails that the absorption behaviour of a brick wall might be considerably underestimated if the properties of the bed face are generalized to other directions, e.g. lateral wetting from wind–driven rain. Note that the different cases analysed here made use of the same specimens and the geometrical parameters do not influence the absorption process (water inflow is normalised by area and heights are too small to produce any significant pressure head). Thus, the different behaviour in the three directions can only be explained by an anisotropic pore system or by the existence of imperfections, such as hollows, fissures or cracks within the brick mass.

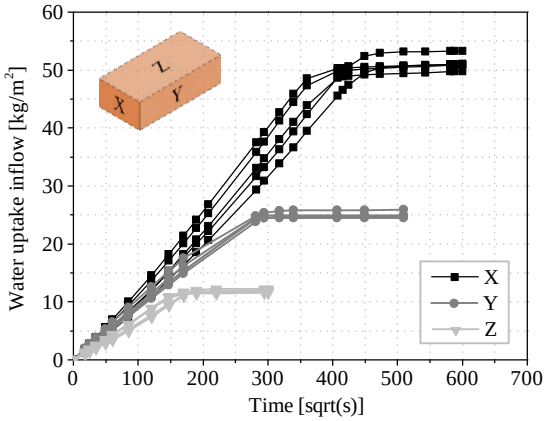

Figure 4.3. Capillary absorption results for brick units in the three studied directions.

The results of the water uptake tests in brick cubes are shown in Figure 4.4 for the three studied directions. The same overall trends observed in full–size bricks hold for the case of brick cubes: the capillary absorption rate was faster in the extrusion direction (X), followed by the stretcher direction (Y), and finally, bed direction (Z) was the slowest one. Using the bed direction as a reference, we obtain $A_{w,b-X} \cong 170\ \%\ A_{w,b-Z}$ and $A_{w,Y} \cong 150\ \%\ A_{w,b-Z}$. In this occasion, the exposed area and height were equal for all specimens, so any geometrical influence was discarded. Consequently, the results point at an anisotropic structure of the material, the presence of internal imperfections, or a combination of both.

By careful examination of the specimens, the main cause for the anisotropic behaviour was associated to the existence of rifts or canals within the bulk mass of the brick. The reader is referred to Figure 3.2 where these imperfections are clearly visible, with a more noticeable presence in the longitudinal direction. Therefore, the forming process of the bricks (in this case extrusion) is deemed to be the reason behind the anisotropic behaviour for water absorption. Furthermore, the impact of internal canals on the water uptake process may be observed in brick cubes B2X and B2Y (individuated in Figure

4.4). For these two cases, signs of absorbed water were spotted on the upper part of the specimens very early on in the process, starting from a particular location and spreading from there to the rest of the surface. This could be linked to the presence of a discontinuity across the specimen (bottom–to–top) from where the water was sucked up faster. In fact, the absorption curves for B2X and B2Y show a distinct non–linear trend with a faster absorption rate in comparison with the rest of the cases. Such behaviour can be explained by the so–called 'free–water' transport through canals (pores with diameter greater than 100 μm), which is faster than water suction through capillaries (Roels et al., 2003; Carmeliet et al., 2004; Groot & Gunneweg, 2010).

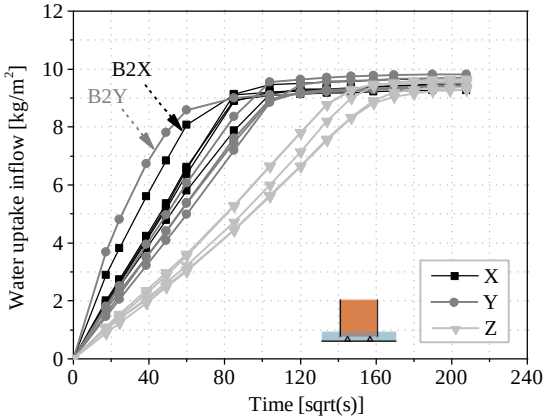

Figure 4.4. Capillary absorption results for brick cubes in the three studied directions.

Overall, the results obtained from full–size bricks and brick cubes are comparable, as expected. However, the capillary moisture content and the water absorption coefficients (all 3 directions) are slightly higher for the whole bricks. As no size effect is expected in the capillary test results (Feng & Janssen, 2018), these differences can be attributed to variations in the microstructure of the superficial layer of the bricks (which was removed in the cubes) compared to the core mass (Feng et al., 2020). The existence of an external layer may be associated with the different temperatures reached during firing and consequently, different degrees of sintering of the clay and density/porosity values. Moreover, local defects associated to the manufacturing process, as mentioned before, can be another reason for the observed difference in the capillary absorption coefficients obtained from brick units and brick cubes. Note that the brick cubes that showed evidence of canals were discarded for the calculation of average values although their curves are shown in the figures.

The results of the water absorption tests for CM and LM are shown in Figure 4.5. In contrast to the bricks, the results did not show significant deviations for different directions, confirming the isotropic behaviour of these materials. The two mortars showed a clearly distinct behaviour: the absorption process in LM was the fastest, even faster than the bricks, whereas CM showed a very slow water uptake rate.

Taking as a reference the water absorption coefficient for the bed direction of whole bricks, we obtain $A_{w,LM} \cong 335\ \% A_{w,B-Z}$ and $A_{w,CM} \cong 85\ \% A_{w,B-Z}$. Provided that these properties were directly applicable to multi–layered masonry walls, the expected absorption performance would vary considerably depending on the brick–mortar configuration. For combinations B+LM, the fastest path would be the mortar joint, whereas the joints in B+CM cases would act as a retardant barrier.

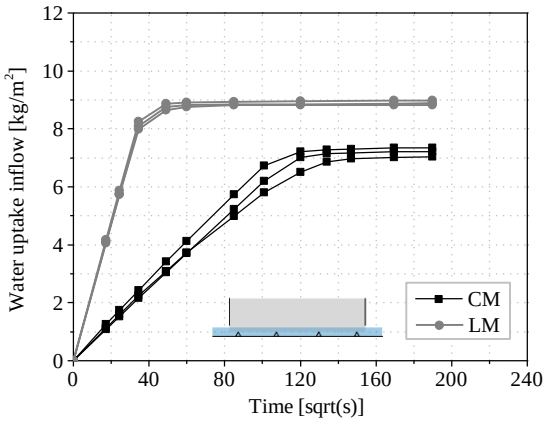

Figure 4.5. Capillary absorption results for cement mortar (CM) and lime mortar (LM) prisms.

Due to the small thickness of the specimens, the absorption tests on LMJ did not render reliable results in terms of water absorption coefficient. However, a clear plateau was reached at the end of the tests, from where capillary moisture content was calculated, $w_{cap,LM-joint} = 185\ \mathrm{kg/m^3}$ (CoV = 6.47 %). This value agrees with the relation $w_{cap} \approx 80\ \%$ – $90\ \% w_{sat}$, observed for the other materials.

Comparison of water absorption rates between different materials has to be done with caution. It must be borne in mind that the water absorption coefficient is a phenomenological parameter and does not describe any real physical property. After all, different pore systems may result in the same water absorption coefficient, e.g. a small number of coarse pores may produce the same water absorption rate as a greater number of small pores (Groot, 1997).

4.1.7 Drying

The mass loss curves obtained from drying tests in brick cubes are shown in Figure 4.6 for the three studied directions. The results are expressed in terms of gravimetric moisture content. Considering the rate of mass loss, three main stages may be distinguished in the global drying process of porous materials. During the initial phase or Stage I, there is a high concentration of moisture at the surface of the material and the drying rate is controlled by environmental conditions, such as wind speed, air temperature, air humidity, etc. (Hall & Hoff, 2009). At this stage, the drying rate is constant, which is evidenced by a linear mass loss. In this phase, moisture transport within the material is faster than the

mass transfer to the atmosphere at the surface. Stage II begins when the moisture supply to the surface can no longer balance the evaporation rate. In other words, the amount of water moved to the surface by capillary transport is less than the liquid being evaporated. Accordingly, the drying rate drops, and the drying process becomes dependent on the moisture transport properties of the material. The last phase or Stage III is characterized by a residual, slow drying rate, close to steady–state condition. The beginning of this phase is not clear–cut and is usually established as a virtual limit (Selih et al., 1996). At this stage, the liquid water movement is limited to the thinnest pores that remain saturated or partially saturated in equilibrium with the environment and the main mechanism of moisture transport is vapour diffusion (Azenha, 2009).

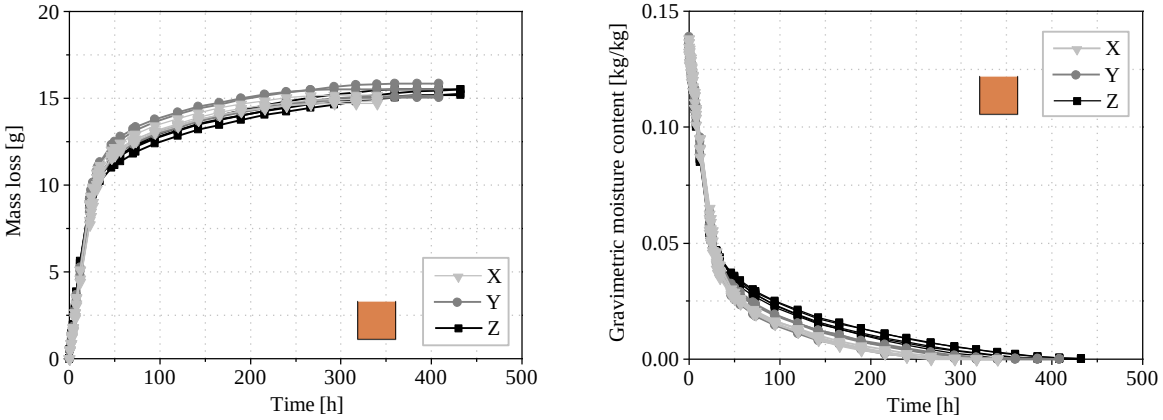

(a) (b)

Figure 4.6. Drying test results for brick cubes in the three studied directions: (a) moisture mass loss as a function of time; (b) moisture content as a function of time.

The drying curves of brick cubes (Figure 4.6) evidence the first and second stages while the third phase is not present. The first stage is identical for all the directions whereas slight differences appear in the second one. Since the second phase is dependent on the transport properties of the bricks, the differences between the samples can be attributed to the anisotropic behaviour previously shown. Indeed, drying trends are consistent with the capillary water absorption results: faster drying is observed in the extrusion direction (X), followed closely by the specimens oriented in the stretcher direction (Y), and finally bed direction (Z) specimens reached equilibrium more slowly.

The mass loss curves obtained from drying tests in mortar cubes are shown in Figure 4.7 for the two types of mortar studied. Mortar specimens were tested only in one direction (longitudinal with respect to the original moulded prism, X) since the isotropic hygric behaviour was confirmed by the previous analyses. It is noticeable that the drying of CM is much slower than B or LM. Moreover, the steady–state condition reached at the end of the test reveals the hygroscopic nature of CM, i.e. the material still

withholds a certain amount of water when equilibrium at 55 % RH is reached through desorption from capillary saturation. This is in agreement with the observed moisture storage behaviour (see Figure 4.2c).

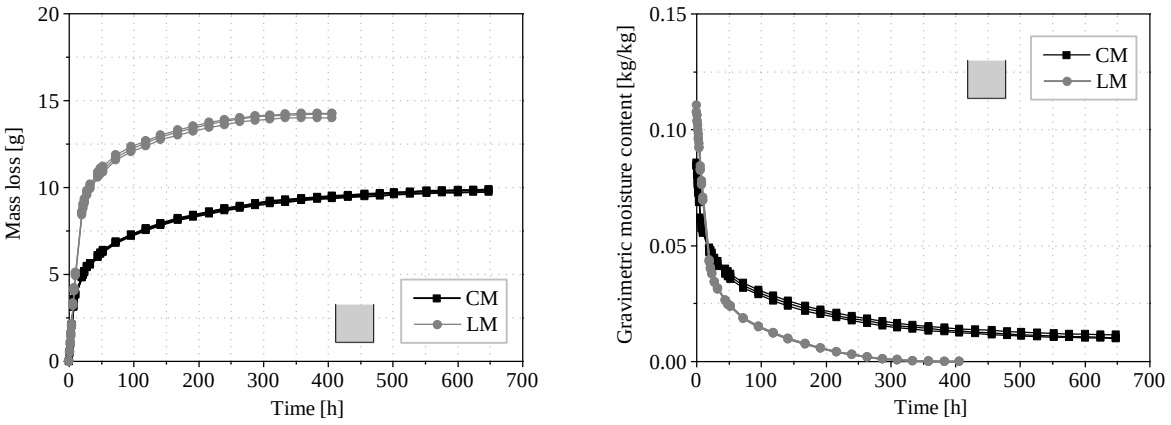

(a) (b)

Figure 4.7. Drying test results (X-direction) for cement mortar (CM) and lime mortar (LM) cubes: (a) moisture mass loss as a function of time; (b) moisture content as a function of time.

The drying process is highly dependent on the boundary conditions. Higher temperature or lower air humidity would result in enhanced mass transfer and therefore higher drying rates (steeper mass loss). The fact that the first drying phase is not dependent on the material is demonstrated in Figure 4.6 and Figure 4.7, where the initial slope of the mass loss curves is the same for all the studied cases. Considering equivalent environmental conditions, the duration of the first drying stage depends on the material capacity to transport liquid water towards the surface where evaporation occurs. Therefore, it provides information about how easily liquid water flows through the medium. In the case of bricks, the range of constant drying rate extends from the initial capillary moisture content, w_{cap}, until 30 % – 40 % w_{cap}, in line with the studies by Hall & Hoff (2007). LM follows a similar trend, with the first drying stage ending at a moisture content value about 40 % w_{cap}. Finally, CM shows a very short first phase that finishes at ca. 70 % w_{cap}. The development of the second drying stage is also indicative of the liquid water permeability of the material. Thus, a shorter second phase is registered for strongly capillary–active materials, e.g. B and LM. Conversely, a long, gradual second stage is generally observed in materials with a more pronounced hygroscopic behaviour, such as CM.

Given the relation between the drying rate during Stage I and the environmental conditions, the mass loss during the initial phase may be used to determine the convective moisture flux by inverse calculation. Thus, the convective mass transfer coefficient can be calculated from the first drying phase assuming constant vapour flux and constant boundary conditions (Scheffler, 2008):

$$h_m = \frac{g_v}{p_v(T_{surf}, \varphi_{surf}) - p_v(T_{env}, \varphi_{env})} \tag{4.7}$$

where g_v [kg/(m^2 · s)] is the vapour mass flow density, and p_v [Pa] is the vapour pressure calculated from Eqs. (3.9) and (3.10) considering the temperature and relative humidity conditions at the material surface and in the surrounding environment, i.e. T_{surf}, φ_{surf}, and T_{env}, φ_{env}, respectively. The relative humidity at the material surface can be assumed 100 % (capillary saturation) during the first drying phase. Moreover, the surface temperature may be assumed as the wet bulb temperature corresponding to the conditions of drying air in the environment.

4.1.8 Coefficient of thermal expansion

The results of the tests to determine the coefficient of thermal expansion (CTE) of the studied materials are presented in Table 4.4. With regard to the thermal effects, the behaviour of extruded bricks seems to have a less pronounced orthotropic nature since the obtained CTE values are similar for the longitudinal (extrusion) and transversal directions, namely $\alpha_{T,B-X}$ = 2.36E–6 °C^{-1}, $\alpha_{T,B-Y}$ = 2.57E–6 °C^{-1}, and $\alpha_{T,B-Z}$ = 2.80E–6 °C^{-1}. It is noted that the extrusion direction reveals the lowest thermally induced deformations. Nonetheless, considering the rather small deviation between the different directions, an isotropic average value is proposed, i.e. $\alpha_{T,B}$ = 2.56E–6 °C^{-1}. The CTE of LM, $\alpha_{T,LM}$ = 3.04E–6 °C^{-1}, is around 20 % higher than the average value established for B. The different thermal response of these two materials is associated to the development of thermally induced stresses in brick–lime mortar composites. Finally, the CTE value obtained for CM, $\alpha_{T,CM}$ = 7.38E–6 °C^{-1}, is the highest among the three studied materials, nearly three times higher than the average CTE of brick. The bigger gap between these two values indicates a lower thermal compatibility between bricks and cement mortar.

Table 4.4. Coefficient of thermal expansion of the studied materials.

Material	$\alpha_{T,X}$ [1/°C]	$\alpha_{T,Y}$ [1/°C]	$\alpha_{T,Z}$ [1/°C]	$\alpha_{T,ISO}$ (1) [1/°C]
B	2.32E–6	2.57E–6	2.80E–6	2.56E–6
LM	–	–	–	3.04E–6
CM	–	–	–	7.38E–6

(1) Isotropic value for brick specimens calculated as the average of all directions

4.1.9 Coefficient of hygric expansion

The results for the coefficient of hygric expansion (CHE) of the studied materials are presented in Figure 4.8, together with the fitted curves representing the CHE as a function of moisture content. It is noted that the CHE changes considerably for lower moisture contents, whereas the variation is small for higher moisture contents. The CHE obtained for B (Figure 4.8a) is much higher than the ones calculated for LM and CM (Figure 4.8b), which are in the same range and similar to one another. All the studied cases are well described by a power type (allometric) function with respect to the gravimetric moisture content.

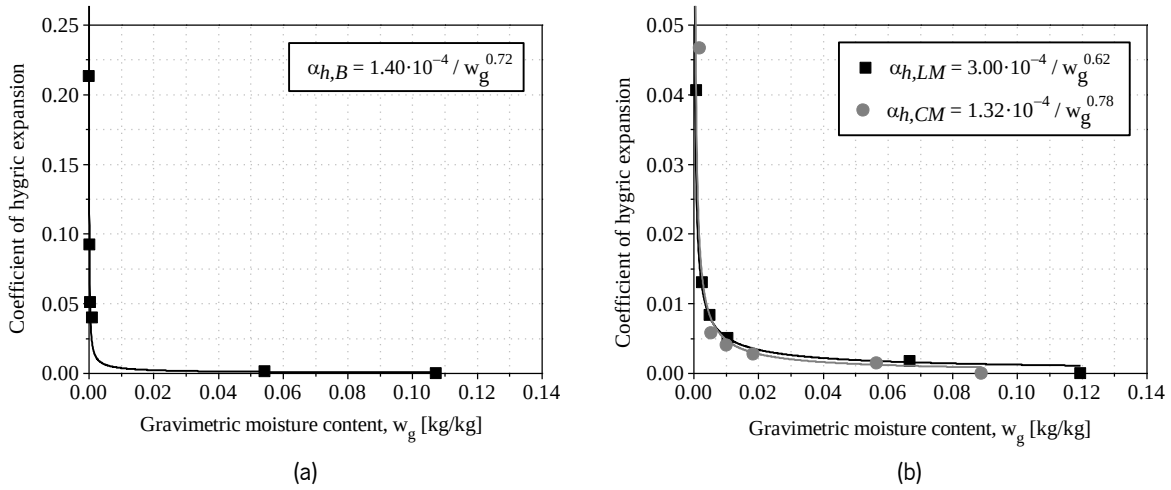

Figure 4.8. Coefficient of hygric expansion and fitting curves for the studied materials: (a) brick (B); (b) lime mortar (LM) and cement mortar (CM).

In the literature, the CHE can appear as a linear relation, such as $\varepsilon_h = \beta(w - w_0)$. In this context, the CHE is commonly known as coefficient of hygroscopic swelling (CHS). The linear assumption is generally valid to describe the material behaviour in a certain portion of the hygroscopic range. However, the same simplification may prove faulty for higher moisture contents and therefore its application is not recommended for cases dealing with the whole moisture range. For reference, the CHS values obtained for the different materials analysed in this study are presented hereunder, expressed in strain per 1 % moisture mass gain: $\beta_B = 0.0520$, $\beta_{LM} = 0.0098$, and $\beta_{CM} = 0.0048$. These values were calculated as the slope of the linear regression curve relating the hygric strains and moisture contents calculated for 55, 80 and 90 % RH.

4.1.10 Mercury intrusion porosimetry

The mercury intrusion porosimetry (MIP) results for the studied materials are shown in Figure 4.9, Figure 4.10 and Figure 4.11, in terms of cumulative porosity and percentage of porous volume occupied by each pore size, percentage of pores with respect to pore size, and differential intruded volume as a

function of pore size, respectively. The criteria defined by IUPAC is followed here to classify the pore size, namely macro–pores (> 0.050 μm), meso–pores (0.002–0.050 μm), and macro–pores (< 0.002 μm) (IUPAC, 1972). It is noted that MIP does not provide information about the lower meso–pore and micro–pore ranges.

As pointed out in the literature, e.g. Roels (2000), the results of the mercury intrusion porosimetry must be interpreted with caution. Since MIP is an invasion percolation method, it does not measure a true distribution of pore sizes but an 'apparent' pore volume distribution dependent on the connectivity of the microstructure. In other words, if large pores are only accessible by narrow throats (ink–bottle effect), they will not become filled with mercury at the expected pressure according to the Young–Laplace equation (see Eq. (3.14)). Instead, mercury will only reach these isolated large pores once the intrusion pressure has attained a value high enough to fill the finer pores (throats or passages). This may lead to an underestimation of the volume of large pores and an overestimation of the fine pore volume.

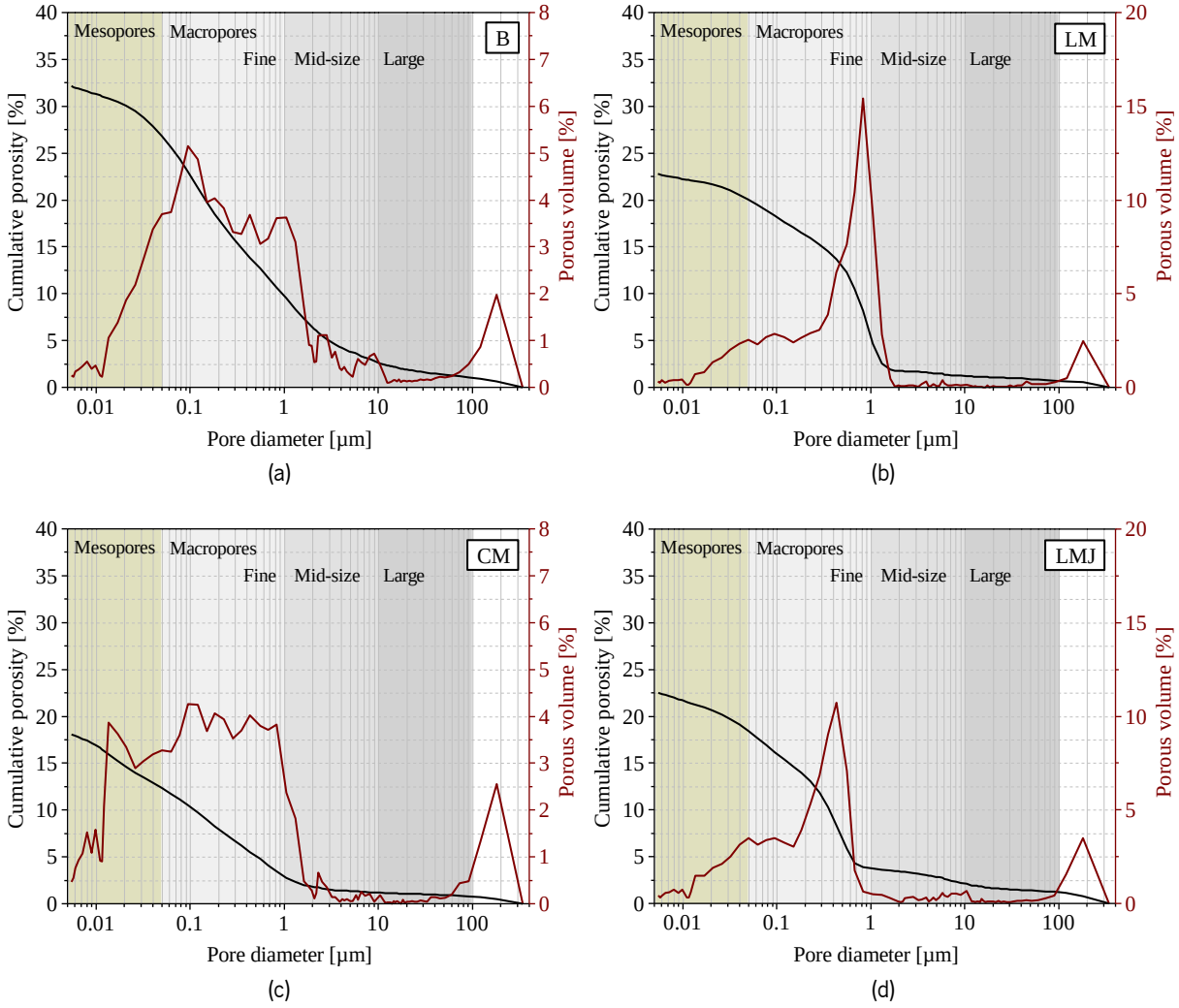

Figure 4.9. MIP analysis – Cumulative porosity and percentage of porous volume occupied by each pore size: (a) brick (B); (b) lime mortar (LM); (c) cement mortar (CM); (d) lime mortar from masonry joints (LMJ).

The percentage of porous volume is presented in Figure 4.9 for the different studied materials with the following distribution: (a) B: 80.54 % of the porous volume occupied by macro–pores, 16.63 % of the porous volume occupied by meso–pores; (b) LM: 85.03 % macro–pores, 12.03 % meso–pores; (c) CM: 64.25 % macro–pores, 31.87 % meso–pores; (d) LMJ: 76.67 % macro–pores, 18.27 % meso–pores. The remaining porous volume identified by MIP is occupied by canals or pores with diameter greater than 100 μm.

Although the greatest portion of the porous system is dominated by the macro–pore volume, there is a larger number of meso–pores, as shown in Figure 4.10. The percentage of number of pores according to pore size is distributed as follows: (a) B: 99.39 % of pores between 0.004 μm and 0.050 μm and 0.61 % of pores between 0.050 μm and 100 μm; (b) LM: 99.56 % meso–pores, 0.44 % macro–pores; (c) CM: 99.79 % meso–pores, 0.21 % macro–pores; (d) LMJ: 99.62 % meso–pores, 0.38 % macro–pores.

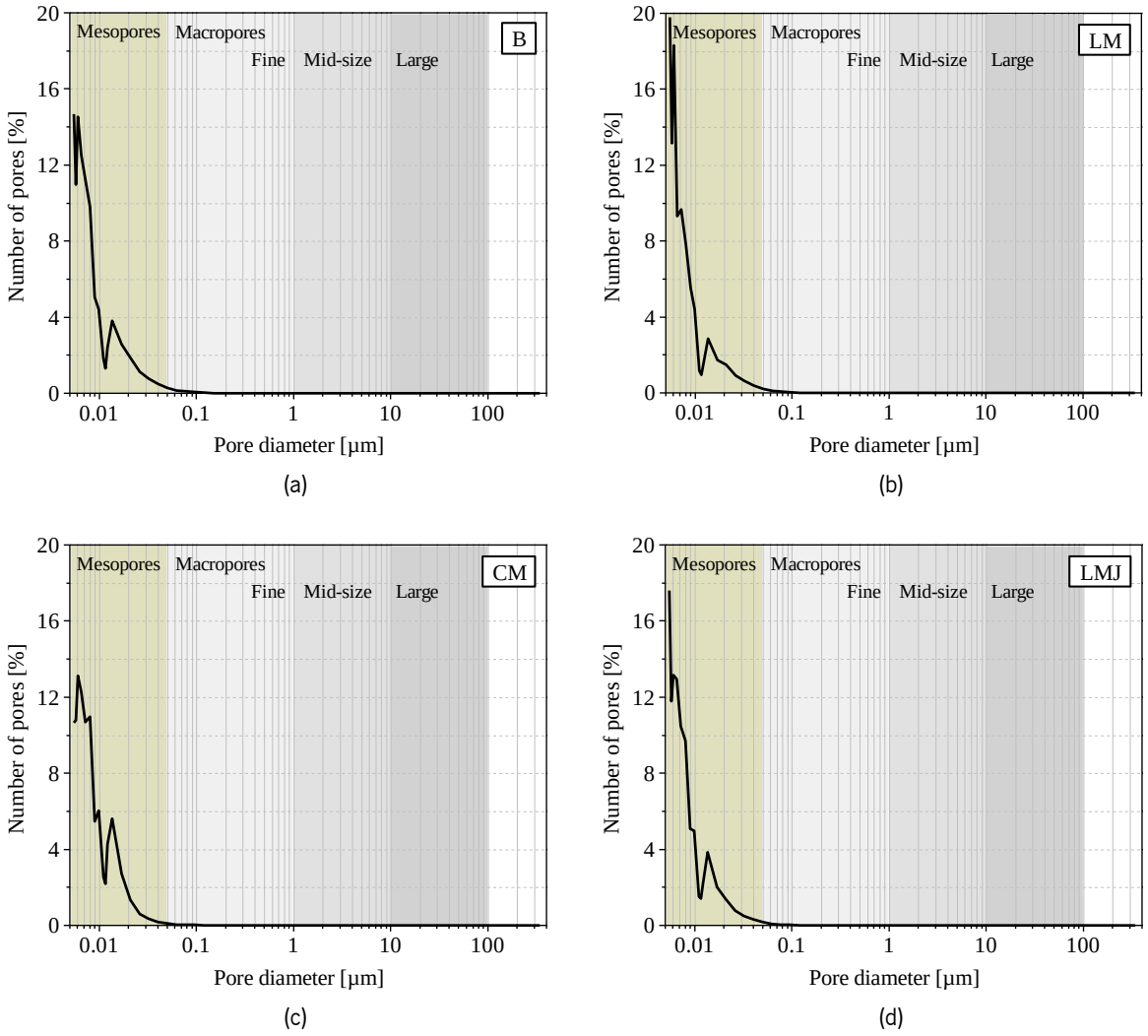

Figure 4.10. MIP analysis – Percentage of pores according to size: (a) brick (B); (b) lime mortar (LM); (c) cement mortar (CM); (d) lime mortar from masonry joints (LMJ).

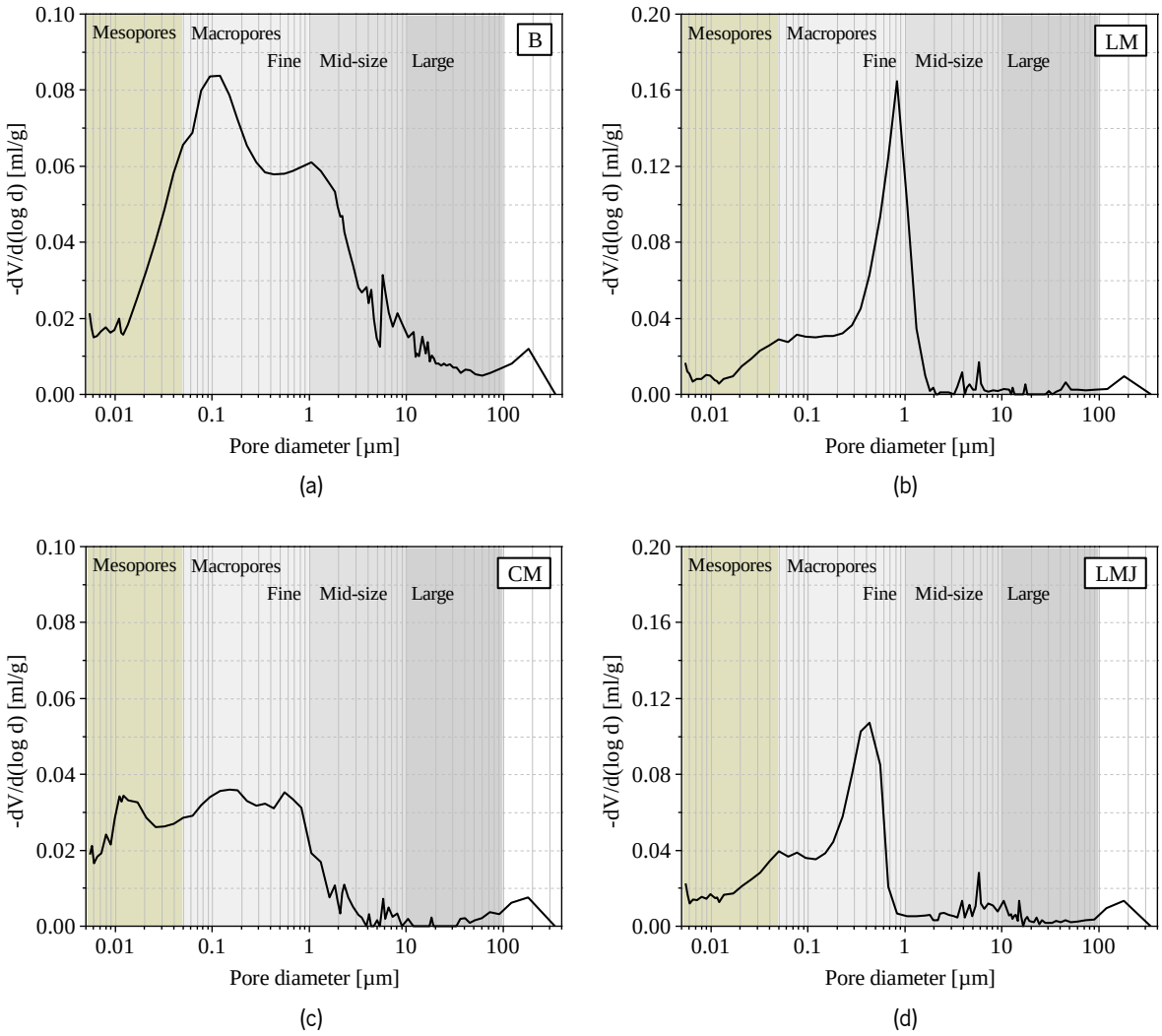

Figure 4.11. MIP analysis – Differential intrusion or $-\mathrm{d}V/\mathrm{d}(\log d)$, with V the intruded volume and d the pore diameter, as a function of pore size: (a) brick (B); (b) lime mortar (LM); (c) cement mortar (CM); (d) lime mortar from masonry joints (LMJ). Note that the vertical axis scale is not constant.

Considering the results from MIP data, the following remarks are presented as a summary of the main findings regarding the microstructure of the studied materials:

a) The results for B present a broad porous distribution with most pores (75 %) between 0.02 μm and 2.00 μm diameter. Two intruded volume peaks (bi–modal distribution) are noticeable at ca. 0.10 μm and 1.00 μm, respectively (Figure 4.11a). Moreover, there is a considerable presence of large pores. Similar results may be found in the literature for ceramic brick, but they often present a more mono–modal distribution with a peak for pores around 0.80 μm to 2.00 μm in diameter (Carmeliet & Roels, 2001, 2002; Nunes et al., 2017).

b) LM shows a much smaller range of pore sizes, with a maximum intruded volume at ca. 0.80 μm (Figure 4.11b). Pores larger than 1.30 μm constitute less than 10 % of the total pore volume.

The rest of the pore system is made up by finer pores between 0.01 μm and 0.20 μm. These results are consistent with other research works, e.g. Lanas et al. (2004), Maravelaki-Kalaitzaki et al. (2005).

c) The results for CM show a broad, quite uniform distribution of pores between 0.01 μm and 1.00 μm (Figure 4.11c). The presence of pores greater than 2 μm is of little significance and accounts for less than 10 % of the total pore volume. Other results in the literature support the greater presence of finer pores, with further peaks of intruded volume between 1–10 nm (Depraetere et al., 1999; Derluyn et al., 2011). These works also indicate a more marked bi–modal distribution and less presence of pores above 0.20 μm diameter.

d) Finally, LMJ presents a more complex pore distribution with two main peaks, with a maximum intruded volume around 0.40 μm accounting for ca. 50 % of the pore volume, and a secondary system between 0.05–0.08 μm (Figure 4.11d). Moreover, there is a significant presence of pores bigger than 1.0 μm and up to 300 μm, which constitute around 20 % of the total pore volume. Furthermore, the distribution of these larger macro–pores is rather scattered.

The different curing conditions of LM and LMJ entailed significant changes in the pore structures of the two mortars. Taking LM as the reference, LMJ presents a shift of the main peak towards smaller pore diameters together with a decrease of the intruded volume associated with this peak. Likewise, there is a shift of the secondary system towards slightly smaller diameters, but the range of finer pores shows an increase of pore intruded volume. Finally, the presence of larger pores (> 1.00 μm diameter) is more significant in LMJ.

The pore size distribution of the studied materials can be associated to certain hygric properties discussed in previous sections. For instance, the larger presence of finer pores in CM (31.87 % of the porous volume is occupied by meso–pores) is directly related to its markedly hygroscopic behaviour. Similarly, LMJ revealed a slight hygroscopic behaviour and it shows a significant volume of finer pores as well (18.27 % meso–pores). On the other hand, hysteresis in the moisture storage curves, which was observed in CM and to some extent LMJ, may be linked to a particularly heterogeneous distribution of pore sizes as well as the greater presence of finer pores. In this regard, the obtained results also provide a good approximation of the observe trends. Nonetheless, it is recalled that MIP alone does not cover the whole microstructure range, so these remarks should be further complemented with detailed information about the fine meso– and micro–pore range.

MIP results can be transformed into points on the (desorption) moisture retention curve with the appropriate transformations for the values of surface tension, σ, and contact angle, θ (see Eq. (3.14)).

In particular, for liquid water $\sigma = 0.072$ N/m and $\theta = 0°$. The corresponding results are shown in Figure 4.12 together with the points obtained with static gravimetric tests and the desorption isotherms fitted using analytical models found in the literature (see Section 4.1.4). The results are consistent with moisture retention curves starting from vacuum saturation, w_{sat}, which is in agreement with other studies in the literature, e.g. Roels (2000), Qiu (2003). Consequently, the moisture retention curves lay above the corresponding desorption isotherms defined gravimetrically from capillary moisture content, w_{cap}, especially for lower values of suction pressure (high relative humidity).

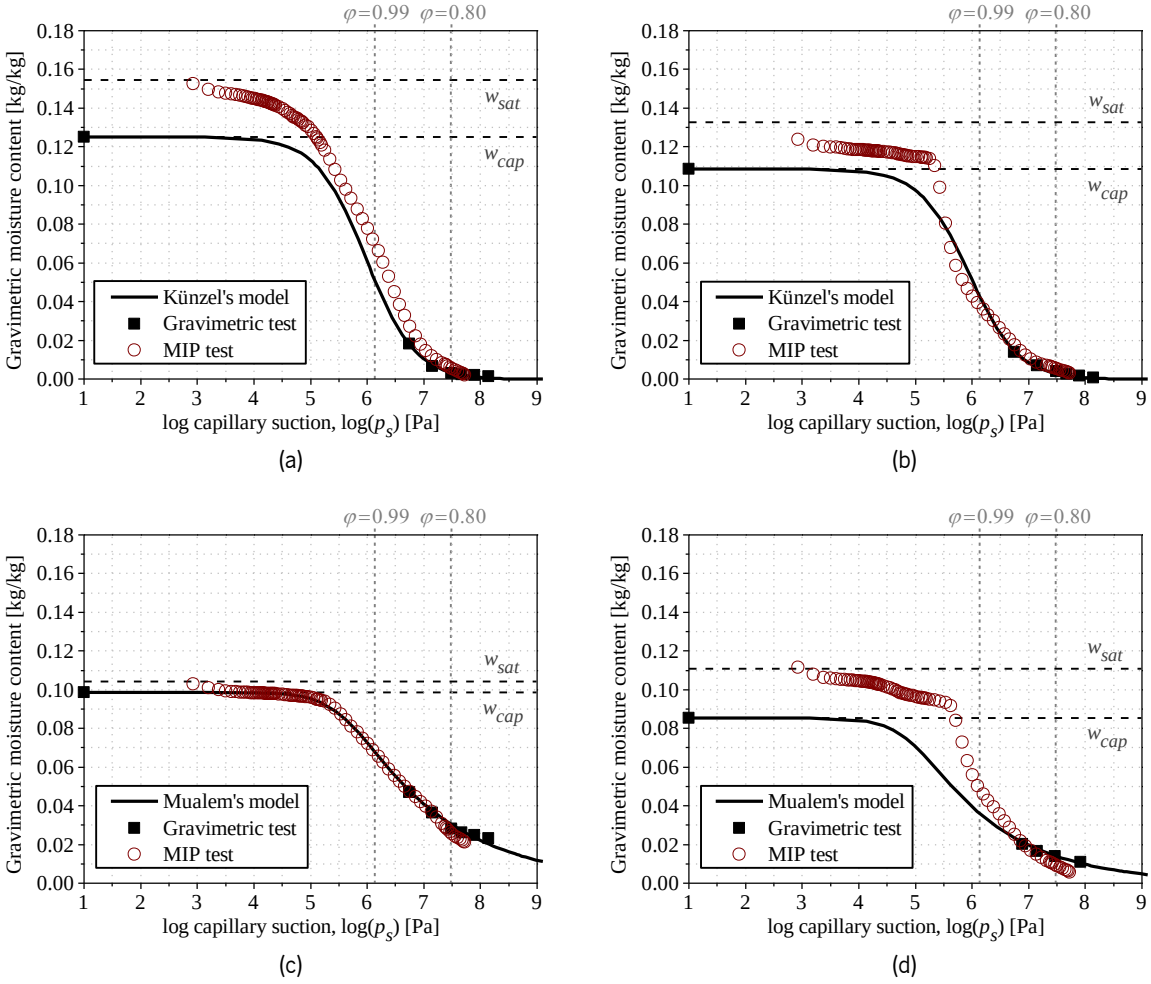

Figure 4.12. Experimental points from MIP and static gravimetric tests, and (de)sorption isotherms of the studied materials: (a) brick (B), and (b) lime mortar (LM), fitted with Künzel's model (Künzel, 1995); (c) cement mortar (CM), and (d) lime mortar from masonry joints (LMJ), fitted with Mualem's model (Mualem, 1976).

Finally, the open porosity values obtained from MIP are presented in Table 4.5 together with the results from the evacuation method or vacuum saturation tests (see Section 4.1.1). Despite some discrepancies, mercury porosimetry tests provide results within acceptable ranges.

Table 4.5. Open porosity, ϕ_o [–], obtained from MIP and vacuum saturation tests.

Method	Material			
	B	CM	LM	LMJ
Vacuum saturation test	0.280	0.210	0.255	0.230
Mercury Intrusion Porosimetry	0.321	0.181	0.228	0.225
Error [%]	14.64	–13.81	–10.59	–2.17

4.2 RESULTS ON MASONRY COMPOSITES

The results obtained from hygric tests in multi–layered specimens are presented and discussed in this section. Two main group of experiments were performed on masonry specimens, namely capillary absorption and drying tests.

4.2.1 Capillary absorption tests

The results of the capillary absorption tests for two–layer (1 interface) masonry composites, are shown in Figure 4.13 for the two studied directions, namely LMJ–to–B, labelled M1–M (Figure 4.13a), and B–to–LMJ, labelled M1–B (Figure 4.13b). The cross–sectional area of all the cylinders is the same so direct comparison of the water uptake mass is possible. Note that the tests for the configuration M1–M were concluded before the brick reached capillary saturation.

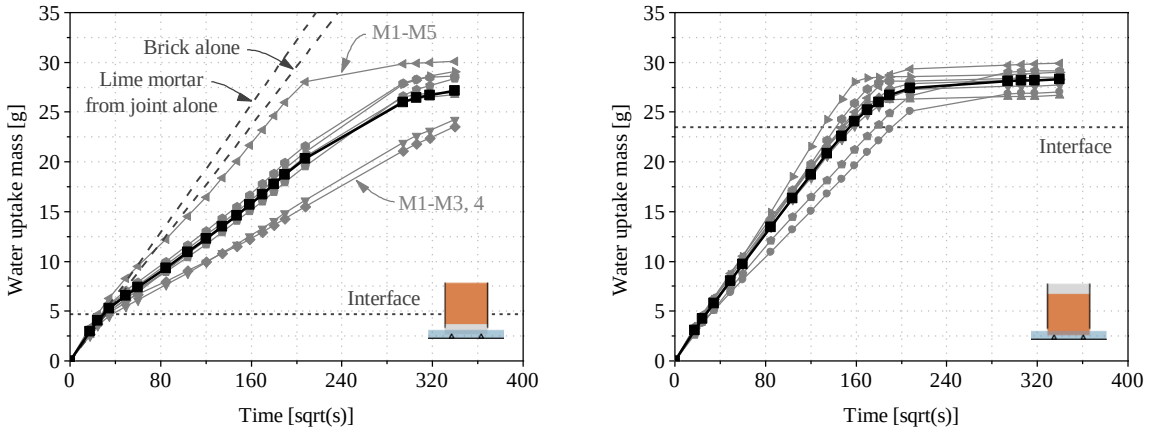

Figure 4.13. Water absorption results for masonry specimens M1 (B+LMJ): (a) LMJ–to–B configuration, M1–M; (b) B–to–LMJ configuration, M1–B. Grey curves represent test results, and the black curve is the average. The location of the interface is estimated from the average volume of each material layer.

By comparison of the two cases in Figure 4.13, it is evidenced that the uptake rate is influenced by the presence of the interface. In Figure 4.13a, the slope of the moisture inflow per square root of time falls

after a point. This point is identified as the interface and matches the expected capillary saturation for LMJ calculated as the average $w_{cap,LMJ} \cdot V_{bulk,LMJ} \cong 4.60$ g. Above the interface, the uptake mass curves are less steep than expected from the absorption rate of B alone. Similarly, the location of the interface in Figure 4.13b is estimated from the capillary saturation of the brick layer calculated as the average $w_{cap,B} \cdot V_{bulk,B} \cong 23.50$ g. However, the influence of the interface for the M1–B cases is less evident. This may be explained by several reasons, namely the smaller thickness of the mortar layer, which causes any difference to dissipate faster; and the higher suction capacity of the mortar, which counteracts the apparent retardant effect of the interface. Moreover, the further the distance of the interface with respect to the water source, the lower the interfacial effect (Vereecken et al., 2020).

Dissimilar properties have been already discussed between LM and LMJ (Table 4.1). These differences were also evidenced in the water uptake tests for composite cylinders. Considering the first portion of the uptake curves in Figure 4.13a, the average water absorption coefficient for LMJ is $A_{w,LMJ} = 0.076\ \mathrm{kg/(m^2 \cdot s^{0.5})}$ (CoV = 7.39 %), which is about three times smaller than the coefficient obtained for LM (Table 4.3). In turn, the average water absorption of the brick counterparts (initial slope of the curves in Figure 4.13b), $A_{w,B} = 0.073\ \mathrm{kg/(m^2 \cdot s^{0.5})}$ (CoV = 11.25 %), was slightly higher than the value obtained for brick units in the same direction (bed or Z), though still in the same range (Table 4.3). Thus, the water absorption coefficient of LMJ turned out to be similar to that of the adjacent B.

From the results for M1–M (Figure 4.13a), it is possible to distinguish a global trend with upper (M1–M5) and lower (M1–M3, M1–M4) boundaries. To a greater or lesser extent, all cases revealed an absorption rate reduction associated with the presence of the interface. In general, two main factors may explain the absorption rate drop: (a) the nature and quality of the interface, namely the presence of cracks, voids, or discontinuities; and (b) the hydraulic affinity of the materials in contact, which has to do with the pore structure of each material. For instance, assuming cylindrical pores, the Young–Laplace equation (recalled here for clarity) defines the pressure at which a pore fills (or empties) according to its pore opening size:

$$p_c = \frac{2\sigma}{r} \cdot cos(\theta) \tag{4.8}$$

where σ [N/m] is the surface tension, r [m] is the pore radius, and θ is the contact angle. According to Eq. (4.8), a material with finer pores will exert higher capillary pressure and thus withhold water when in contact with a material with bigger pores. Furthermore, even if the material can withdraw the water from the previous layer, its absorption rate will be limited by the behaviour of the source material. This phenomenon was defined by Wilson et al. (1995b) as ‘starvation’ of the second medium. In other words,

the effective absorption rate will be determined by the slowest layer 'up–the–stream'. In this sense, the water uptake process in multi–layered materials may be understood as a unidirectional series circuit with specific conductive (permeability) properties for each layer and a certain hydraulic resistance associated to the interfaces between them (Brocken, 1998).

The results of the capillary absorption tests for the three–layer masonry composites, labelled M2 (2 interfaces), are shown in Figure 4.14 for the two studied configurations, namely B(a)–LMJ–B(b), and the opposite, B(b)–LMJ–B(a). Direct comparison of the water uptake mass is possible since the cross–sectional area of all the cylinders is the same. The location of the interfaces in the figure is estimated from the capillary saturation levels calculated from the capillary moisture content and average volume of each material layer.

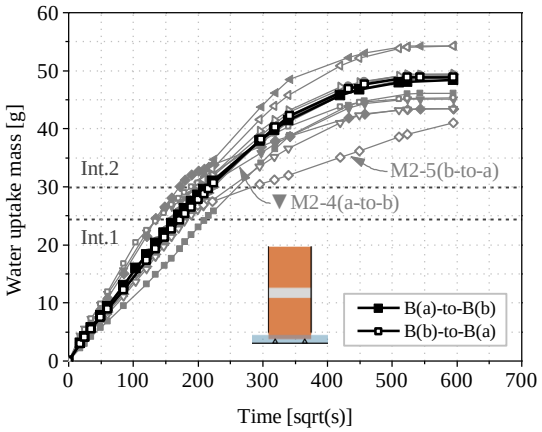

Figure 4.14. Water absorption results for masonry specimens M2 (B+LMJ+B). Grey curves represent test results and black curves are the corresponding average. The location of the interfaces is estimated from the average volume of each material layer.

The curves in Figure 4.14 reveal that the variability of the material response increases with the increasing number of elements involved. This is expected considering the more complex configuration of the specimens. Two main factors, namely variability of the brick layers and quality of the interfaces, give rise to the differences observed between the different specimens and the same specimens in the opposite direction. The purpose of studying the same specimens in both directions is twofold. On one hand, the absorption properties of each brick layer may be assessed individually from the first portion of the water uptake curves. This helps identifying unavoidable variability from the bricks that could otherwise obscure the results. Secondly, a two–way analysis provides information about the directional nature of the interface. Indeed, if the interface is linked to a change in pore structure, it may become apparent when the flow goes from one material to the other but not the opposite. By testing the same components in the two directions, we were able to confirm the existence of such phenomenon.

As it was observed for the masonry specimens M1–M (Figure 4.13b), cases with slight, medium and high interfacial impact were detected as well for the three–layer composites (Figure 4.14). Most specimens showed hardly any absorption rate reduction between the first brick and the mortar joint. Only two cases, namely M2–4(a–to–b) and M2–5(b–to–a) (individuated in Figure 4.14), presented a considerable absorption rate drop at the first interface, most probably associated to local defects. Conversely, a more noticeable deviation was generally observed between the mortar joint and the uppermost brick. This confirms the directional behaviour of the interface and points at a microstructure change between B and LMJ. The pore quality difference between both materials is therefore assumed to be the main factor affecting the suction capacity of the following layer. In this case, the porous medium with finer pores tends to withhold water due to the higher capillary suction and thus the liquid transfer to a material with bigger pores is impeded.

Considering the average behaviour of all the cases (black curves in Figure 4.14), the response of masonry specimens M2 showed no significant hydraulic resistance at the first interface (water moving from B to LMJ), whereas the second interface (water moving from LMJ to B) involved a certain flow reduction. Furthermore, the match between the averages of the two tested configurations proves that the behaviour of the composite was independent of the analysed direction.

The results of the capillary absorption tests for five–layer masonry composites, labelled M4 (4 interfaces), are shown in Figure 4.15. As in the previous cases, the cross–sectional area of all the cylinders is the same, which allows the direct comparison of the water uptake mass. Moreover, the location of the interfaces in the figure is estimated from the capillary saturation levels calculated from the capillary moisture content and average volume of each material layer.

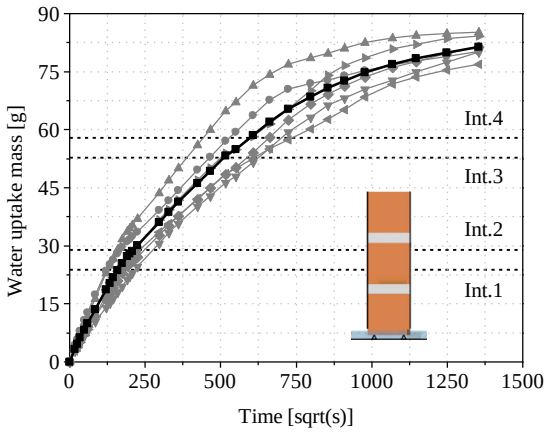

Figure 4.15. Water absorption results for masonry specimens M4 (B+LMJ+B+LMJ+B). Grey curves represent test results and black curves are the corresponding average. The location of the interfaces is estimated from the average volume of each material layer.

The trends observed in Figure 4.15 are consistent with the results obtained for M2 specimens previously analysed. In particular, the results for M4 confirm that the variability of the material response increases with increasing complexity of the configuration, as expected. Moreover, the differences between specimens of the same type can be directly related to the variability of the brick layers and the quality of the interfaces. In general, the five–layer composites showed slight absorption rate reduction when the moisture flow went through the brick–to–mortar interfaces, whereas a more noticeable deviation was observed in the mortar–to–brick interfaces. Thus, the directional behaviour of the interface associated to the microstructure change between B and LMJ is confirmed.

4.2.2 Drying tests

The drying tests performed on two–layer (1 interface) masonry composites are analysed in the following section. Figure 4.16 collects the results obtained for the two tested configurations, namely cylinders drying from the LMJ surface, labelled D1–M, and cylinders drying from the brick layer, labelled D1–B. The results are plotted as gravimetric moisture content with respect to the dry mass of the whole specimen (B+LMJ). For each case, the location of the interface is estimated from the capillary saturation level calculated from the capillary moisture content and average volume of the exposed layer.

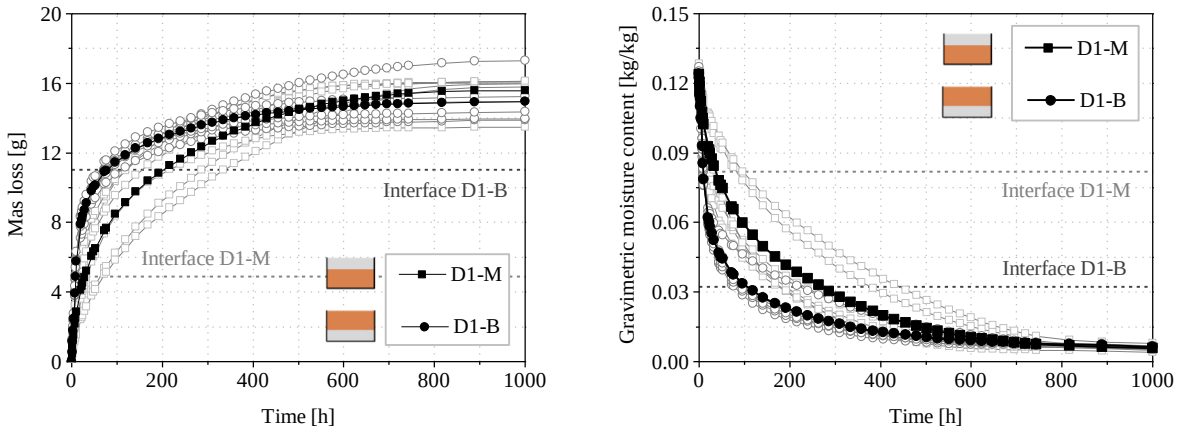

Figure 4.16. Drying test results for masonry specimens D1 (B+LMJ): (a) moisture mass loss as a function of time; (b) moisture content as a function of time. Grey curves represent test results and black curves are the corresponding average. The location of the interfaces is estimated from the average volume of the exposed material layer.

The curves in Figure 4.16 show two distinct drying trends depending on the configuration of the composite. The specimens drying from the brick layer experienced a long initial phase (Stage I with linear mass loss) and a quite fast second stage. The same trend was observed for the drying tests of B and LM cubes (Figure 4.6, Figure 4.7). This response means that the stacked materials have the capacity to effectively transport the liquid water towards the surface where evaporation takes place. Conversely, the

cylinders drying from LMJ showed a shorter initial drying phase and a prolonged, gradual second stage. This trend contrasts with the drying behaviour of B and LM and is more related to the behaviour of CM (Figure 4.6, Figure 4.7). Therefore, the LMJ on top rapidly exhausts its liquid transport capacity and then the drying behaviour slows down considerably, shifting to vapour diffusion as the main transport mechanism for drying. This behaviour may be explained by the presence of smaller pores in LMJ, since finer pores withhold water due to their higher capillary pressure. Additionally, the presence of smaller pores is supported by the residual moisture content at the end of the experiments, which indicates the existence of a hygroscopic component, which was already anticipated by the sorption isotherms for LMJ (Figure 4.2d).

When comparing both cases, it is evident that the LMJ layer on top limits the drying rate of B below, which would be naturally faster as witnessed in the D1–B configuration. Considering the sharp front approximation to be extensible to drying processes, a receding drying front may be assumed (Pel et al., 1996). Taking into account this receding moisture front, the existence of an interfacial resistance was expected to appear as a discontinuity in the mass loss curve, as it was observed for the water absorption cases in multi–layered compounds. Nonetheless, the mass loss figures reveal no clear influence of the interface. In general, the curves are smooth, and no significant change is perceived beyond the transition from Stage I to Stage II. The effect of the mortar–brick interface in the drying process was also studied by Brocken (1998) for brick–cement masonry specimens. Similarly, the author could not qualify the nature of the interface as having perfect or imperfect hydraulic contact.

Without further certainties about the role of the interface, we may assume a perfect hydraulic contact. In this scenario, two causes for the observed trends may be mentioned. On one hand, it seems conclusive that B has higher liquid transport capacity as well as higher vapour permeability. This would explain the longer Stage I and a considerably rapid Stage II for the configuration D1–B. Conversely, considering the D1–M cases, the liquid transport capacity of LMJ wears out quicker and a likely lower vapour permeability further limits the drying process of the brick layer behind. The low liquid permeability of LMJ observed in these drying tests contrasts with the absorption capacity of the same material observed in the previous water uptake experiments. The disparity between absorption and drying confirms the hysteretic behaviour observed in moisture storage for LMJ (Figure 4.2d).

4.3 CHAPTER CONCLUSIONS

An extensive experimental campaign was conducted to determine the physical and hygric properties of brick masonry, as well as some relevant thermo–mechanical and hygro–mechanical parameters. First,

the constituent materials were assessed individually. Subsequently, masonry was studied as a multi–layered composite material. The experimental program included vacuum saturation, immersion at atmospheric pressure, gravimetric tests to determine the moisture storage curves, cup tests, initial rate of absorption, capillary absorption, drying tests, tests to determine the coefficients of thermal expansion and hygric expansion, and mercury intrusion porosimetry. The obtained properties make up a consistent dataset which might be used as input for numerical models as well as for validation of simulation results.

Regarding the testing methods to determine the hygric behaviour of porous building materials, it is shown that the results from the different experimental procedures are consistent and present acceptable variation. Nevertheless, vapour permeability measurements present poorer reliability, which has been documented by other authors as well, e.g. Roels et al. (2004), Feng et al. (2015), Hens (2016), Feng et al. (2020).

With respect to the hygric performance of single materials, extruded fired–clay bricks show a distinct anisotropic behaviour, more noticeable for faster processes such as water absorption. This behaviour is explained by the existence of imperfections within the mass of the bricks derived from the extrusion process. On the other hand, there are notable differences between the hygric response of the two studied moulded mortars. This is most evident when comparing the moisture storage curves. LM shows low hygroscopicity and strong capillary–active behaviour with negligible hysteresis. Conversely, CM shows hygric activity in both the hygroscopic and capillary ranges with a marked hysteresis. Thus, the behaviour of LM is much closer to that of the studied fired–clay brick.

The properties of the NHL–mortar prepared in moulds differ from the same mixture cured in masonry bed joints. The discrepancies are associated with the different water–binder ratio resulting from water extraction by the bricks upon placement. The vacuum saturation tests on LMJ reveal lower open porosity and therefore lower saturation moisture content. The moisture storage curves obtained for LMJ show a more hygroscopic behaviour than its moulded counterpart, with non–negligible hysteresis. Water absorption tests performed on masonry cylinders M1–M show slower water uptake than expected from LM, thus a lower water absorption coefficient is assumed for LMJ. Furthermore, drying tests on masonry specimens drying from LMJ reveal mass loss curves with a short initial drying stage, which is indicative of an enhanced water retention capacity and the presence of fine pores. Finally, the dissimilar trends observed for water uptake and drying processes confirm the hysteresis in moisture storage for LMJ.

Considering the observed behaviour of multi–layered masonry specimens, the existence of an imperfect hydraulic contact at the brick–mortar interface is demonstrated for water absorption. The imperfect contact may be assumed as a hydraulic resistance and its effect varies from a slight reduction

to considerable retardation of the water flow. The interfacial effect is mostly detected when the water movement goes from LMJ to B. Thus, discontinuity in the pore structure of the materials (finer pores in LMJ) is assumed as the main reason for the interfacial effect, which may become more pronounced due to the presence of local imperfections. On the other hand, the interfacial effect on drying kinetics is not evident. Further studies on the drying behaviour of multi–layered masonry materials are necessary. In particular, more severe environmental conditions are suggested since the laboratory hygrothermal conditions induce reduced moisture flow, which may not be sufficient to trigger interfacial phenomena (Azevedo, 2019).

Due to the existence of an imperfect interfacial contact, the hygric properties obtained individually from testing the constituent materials separately cannot be directly extrapolated to multi–layered masonry cases. Two main phenomena must be taken into consideration in order to avoid erroneous estimations, namely: (a) for water absorption cases, there is a hydraulic interfacial resistance derived from the dissimilar pore structure between the materials in contact; (b) for water absorption and drying cases, the impact of curing conditions on the properties of mortars cast in masonry joints must be considered.

The results from mercury intrusion porosimetry (MIP) allow for a comparison of the microstructure properties of the studied materials. The percentage of porous volume occupied by macro–pores is the highest in LM, followed by B, LMJ and finally CM, which has a significant volume of finer pores. The larger presence of finer pores can be related to the hygroscopic character of the materials, especially CM and to some extent LMJ as well. Moreover, the different curing conditions of LM and LMJ seem to have entailed significant changes in the pore structures of the two mortars. LMJ presents a shift towards smaller pore diameters and a less accentuated distribution with a lower intruded volume peak. Likewise, there is a shift of the secondary system towards slightly smaller diameters and the range of finer pores shows an increase of pore intruded volume. In addition, the presence of larger pores is more significant in LMJ. Finally, MIP data can be used to describe the (desorption) moisture retention curves of the materials starting from vacuum saturation. The obtained results complement the sorption isotherm data and provide information about the higher end of the moisture storage range.

This page has been intentionally left blank

CHAPTER 5

Numerical simulations I: Moisture transport

The present chapter focuses on numerical simulations and discussion of moisture transport phenomena in brick masonry. Initially, water absorption and drying processes are studied at the scale of the constituent materials. Then, the analyses are extended to multi–layered cases to evaluate the impact of brick–to–mortar interfaces. In this context, the material parameters and experimental results presented in the previous chapter are used as a basis for input and validation of the simulation results. The chapter is organized into different sections as follows. First, a moisture transport model is introduced and described in detail. Then, a series of numerical simulations are presented, and the model parameters are calibrated in order to fit the experimental results. Subsequently, a modelling strategy is implemented to capture the hysteresis observed between adsorption and desorption (wetting/drying) processes. Finally, the proposed model is extended to different modelling approaches commonly used for mechanical studies of masonry.

Part of the contents presented in this chapter has been published in Ramirez et al. (2023).

5.1 MOISTURE TRANSPORT MODEL

This first section presents the multiphase model adopted for moisture transport simulations. Masonry is described as a porous medium made up of a matrix of interconnected pores inside a solid skeleton. This solid phase is assumed to be continuous, homogenous, inert (no chemical reactions), isotropic and non–deformable. On the other hand, pores are assumed cylindrical, with a homogenous, isotropic distribution inside the material. The void space defined by the pores is filled in different proportions with a liquid and a gaseous phase. The liquid phase is pure and incompressible, whereas the air phase is an ideal mixture of dry air and water vapour at atmospheric pressure. For simplicity, advective air flow is not implemented in the model and pressure gradients are considered negligible. Additionally, a local, instantaneous thermodynamic equilibrium is assumed between the liquid and gaseous phases. Based on this, the contributions of liquid water and water vapour may be combined to define a global moisture content. Nonetheless, the contribution of water vapour to the total moisture content is negligible. Knudsen flow is not considered, and it is assumed that the capillary forces are dominant so that the effect of gravity is neglected.

5.1.1 Governing equations

The chosen moisture transport model belongs to the so–called diffusivity approaches, which are based on Fick's laws of diffusion:

$$\xi \frac{\partial \varphi}{\partial t} = \nabla \cdot (\xi D_w \nabla \varphi) + \nabla \cdot \left(\delta_v \nabla (\varphi \, p_{v,sat}) \right) \tag{5.1}$$

where $\xi = \partial w / \partial \varphi$ [kg/m^3] is the moisture storage capacity, w [kg/m^3] is the moisture content, φ [–] is the relative humidity, t [s] is the time, D_w [m^2/s] is the liquid water diffusivity, δ_v [kg/(m · s · Pa)] is the water vapour permeability, $p_{v,sat}$ [Pa] is the saturation vapour pressure. In turn, the water vapour permeability is defined as:

$$\delta_v = \frac{\delta_a}{\mu} \tag{5.2}$$

where δ_a [kg/m^3] is the water vapour permeability of still air, and μ [–] is the vapour diffusion resistance factor of the porous material.

In Eq. (2.1), the first term on the right–hand side represents liquid water transport, whereas the second term stands for water vapour diffusion. It must be noted that the moisture content is usually expressed either as mass of adsorbed water per volume of dry material, w [kg/m^3], as mass of adsorbed water per mass of dry material, w_g [kg/kg], known as gravimetric moisture content, or as volume of adsorbed water per volume of dry material, w_V [m^3/m^3], known as volumetric moisture content. The three expressions are related through:

$$w = w_g \cdot \rho_{bulk} = w_V \cdot \rho_w \tag{5.3}$$

where ρ_{bulk} [kg/m^3] is the bulk density of the porous material, and ρ_w [kg/m^3] is the density of liquid water.

For the sake of simplicity, isothermal conditions are assumed, thus cancelling additional thermal influences that could affect temperature–dependent parameters, such as relative humidity, water vapour permeability, etc.

Different analytical formulations may be found in the literature to account for the liquid water diffusivity. For the present study, a modified version of the exponential expression proposed by Künzel (1995) is used:

$$D_w = \gamma \cdot \left(\frac{A_w}{w_{cap}} \right)^2 \cdot 10^{3 \cdot \left(\frac{w}{w_{cap}} - 1 \right)} \tag{5.4}$$

where γ [–] is a diffusivity factor depending on the material and transport process (wetting/drying), A_w [$\mathrm{kg/(m^2 \cdot s^{0.5})}$] is the capillary absorption coefficient, and w_{cap} [$\mathrm{kg/m^3}$] is the capillary moisture content. The original formulation by Künzel uses a fixed value $\gamma = 3.80$. In this work, γ is left as an adjustable parameter in order to accommodate a variety of material transport processes. The main advantage of the chosen expression comes from the fact that it is defined by means of reasonably simple measurable properties, namely the capillary absorption coefficient, and it has only one adjustable parameter, which nonetheless guarantees a great deal of flexibility.

5.1.2 Interface modelling

The simulation of moisture transport in multi–layered materials such as masonry requires specific considerations due to the combination of media with different hygric properties and the presence of interfacial zones between consecutive layers (Brocken, 1998; Derluyn et al., 2011; Janssen et al., 2012; X. Zhou et al., 2020). In the context of the present studies, the interfacial zone between bricks and mortar is treated macroscopically, thus a phenomenological interface with zero thickness is assumed.

Considering the combination of dissimilar materials, due to the discontinuity between their moisture storage properties, a formulation based on a continuous potential, such as capillary pressure, vapour pressure, or (as the case here) relative humidity is necessary. Then, the type of interface contact must be considered. If the transition from one layer to the other has no impact on moisture transport, the interface is assumed to have perfect hydraulic contact. However, in most multi–layered materials, some retardation of the moisture flux across the interface is observed, which reveals the existence of an imperfect hydraulic contact. This phenomenon can be attributed to the discontinuity between the pore structures of the materials (natural contact), the existence of an air gap between the adjacent layers, or a combination of both cases (Brocken, 1998).

In order to account for these phenomena, Brocken (1998) proposed the introduction of a parameter to describe the interface permeability, K_{IF} [$\mathrm{s/m}$], or alternatively an interface resistance, R_{IF} [$\mathrm{m/s}$]. It is noted that the interface (either perfect or imperfect contact) has zero thickness and no hygroscopic capacity. If a constant interface resistance is assumed, the water flow across the interface, g_{IF} [$\mathrm{kg/(m^2 \cdot s)}$], can be described by:

$$g_{IF} = K_{IF} \frac{\partial p_c}{\partial x} = \frac{1}{1/K_{IF}} \frac{\partial p_c}{\partial x} = \frac{\Delta p_c}{\frac{1}{K_{IF}} \cdot \Delta x} = \frac{\Delta p_c}{R_{IF}} \tag{5.5}$$

where p_c [Pa] is the capillary pressure. Therefore, the imperfect hydraulic contact translates into a drop in capillary pressure across the interface. Since the presented model uses relative humidity as driving

potential, a change of variable becomes necessary. It is recalled that Kelvin equation can be used to link relative humidity with capillary pressure, such as:

$$p_c = \rho_w \cdot R_v \cdot T \cdot ln\,\varphi \tag{5.6}$$

where ρ_w [kg/m^3] is the density of water, R_v [J/(kg · K)] is the universal gas constant for water vapour, and T [K] is the absolute temperature. Assuming the applicability of Kelvin's equation, the water flow across the interface can be redefined with respect to the relative humidity:

$$g_{IF} = K_{IF}\frac{\partial p_c}{\partial \varphi}\frac{\partial \varphi}{\partial x} = K_{IF}\frac{\rho_w \cdot R_v \cdot T}{\varphi}\frac{\partial \varphi}{\partial x} = \frac{\rho_w \cdot R_v \cdot T}{\varphi}\frac{\Delta\varphi}{\frac{1}{K_{IF}} \cdot \Delta x} = \frac{\rho_w \cdot R_v \cdot T}{\varphi}\frac{\Delta\varphi}{R_{IF}} \tag{5.7}$$

5.1.3 Initial and boundary conditions

The model is completed by introducing the initial conditions and the boundary conditions (BC). In particular, the boundary conditions can be of Dirichlet (also called first) or Neumann (second) type. The Dirichlet BC indicates:

$$\varphi = \bar{\varphi} \tag{5.8}$$

where $\bar{\varphi}$ [–] is the prescribed relative humidity at the boundary. Conversely, the Neumann BC is defined as a flux derived from a vapour pressure difference:

$$g = h_m\left(p_v - p_{v,ext}\right) \tag{5.9}$$

where g [kg/(m^2 · s)] is the convective moisture flux, h_m [s/m] is the convective mass transfer coefficient, and $p_{v,ext}$ [Pa] and p_v [Pa] are the partial vapour pressures defined for the environment and at the model boundary, respectively. Partial vapour pressure and relative humidity are related by:

$$\varphi = \frac{p_v}{p_{v,sat}(T)} \tag{5.10}$$

where the saturation vapour pressure, $p_{v,sat}$ [Pa], may be described empirically as a non–linear function of temperature, T [K], as defined in Chapter 3:

$$p_{v,sat} = 610.7[\text{Pa}] \cdot 10^{7.5\cdot\left(\frac{T-273.15}{T-35.85}\right)} \tag{5.11}$$

5.2 NUMERICAL SIMULATIONS AND MODEL VALIDATION

The moisture transport model described in Section 5.1 is applied in the following to simulate the hygric behaviour of single materials (brick and mortar) and multi–layered (masonry) specimens. The material properties presented in Chapter 4 are used as numerical input parameters. For the sake of clarity, a summary of the material properties of interest is given in Table 2.2. Similarly, the moisture storage curves used for each material are presented in Figure 4.2.

Table 5.1. Summary of material properties used for moisture transport simulations.

Material	Property	Symbol	Value	Units	Source
B	Bulk density	ρ_{bulk}	1900	$\mathrm{kg/m^3}$	Experimental
	Open porosity	ϕ_o	0.280	–	Experimental
	Capillary moisture content	w_{cap}	240	$\mathrm{kg/m^3}$	Experimental
	Fitting parameter for sorption isotherm	ψ	1.0070	–	Experimental
	Water absorption coefficient (X–direction)	$A_{w,X}$	0.104	$\mathrm{kg/(m^2 \cdot s^{0.5})}$	Experimental
	Water absorption coefficient (Y–direction)	$A_{w,Y}$	0.089	$\mathrm{kg/(m^2 \cdot s^{0.5})}$	Experimental
	Water absorption coefficient (Z–direction)	$A_{w,Z}$	0.061 (1)	$\mathrm{kg/(m^2 \cdot s^{0.5})}$	Experimental
	Water vapour resistance factor	μ	34.14	–	Experimental
CM	Bulk density	ρ_{bulk}	2000	$\mathrm{kg/m^3}$	Experimental
	Open porosity	ϕ_o	0.210	–	Experimental
	Capillary moisture content	w_{cap}	180	$\mathrm{kg/m^3}$	Experimental
	Fitting parameter for adsorption isotherm	a_{ads}	1.43E–6	$\mathrm{1/Pa}$	Experimental
		m_{ads}	0.285	–	Experimental
	Fitting parameter for desorption isotherm	a_{des}	2.51E–5	$\mathrm{1/Pa}$	Experimental
		m_{des}	0.213	–	Experimental
	Water absorption coefficient (isotropic)	$A_{w,ISO}$	0.060	$\mathrm{kg/(m^2 \cdot s^{0.5})}$	Experimental
	Water vapour resistance factor	μ	25.00	–	Prangnell (1971)
LM	Bulk density	ρ_{bulk}	1990	$\mathrm{kg/m^3}$	Experimental
	Open porosity	ϕ_o	0.255	–	Experimental
	Capillary moisture content	w_{cap}	225	$\mathrm{kg/m^3}$	Experimental
	Fitting parameter for sorption isotherm	ψ	1.0066	–	Experimental
	Water absorption coefficient (isotropic)	$A_{w,ISO}$	0.235	$\mathrm{kg/(m^2 \cdot s^{0.5})}$	Experimental
	Water vapour resistance factor	μ	15.00	–	Prangnell (1971)

(1) For multi–layered cases, $A_{w,B-Z} = 0.075\ \mathrm{kg/(m^2 \cdot s^{0.5})}$

Table 5.1 (Continued). Summary of material properties used for moisture transport simulations.

Material	Property	Symbol	Value	Unit	Source
LMJ	Bulk density	ρ_{bulk}	2060	$\mathrm{kg/m^3}$	Experimental
	Open porosity	ϕ_o	0.230	–	Experimental
	Capillary moisture content	w_{cap}	190	$\mathrm{kg/m^3}$	Experimental
	Fitting parameter for adsorption isotherm	a_{ads}	3.80E–6	$\mathrm{1/Pa}$	Experimental
		m_{ads}	0.352	–	Experimental
	Fitting parameter for desorption isotherm	a_{des}	1.19E–5	$\mathrm{1/Pa}$	Experimental
		m_{des}	0.235	–	Experimental
	Water absorption coefficient (isotropic)	$A_{w,ISO}$	0.080	$\mathrm{kg/(m^2 \cdot s^{0.5})}$	Experimental
	Water vapour resistance factor	μ	15.00	–	Prangnell (1971)

The simulations presented herein are based on finite element analysis and were performed using COMSOL Multiphysics (COMSOL, 2021). Since the analysed cases can be reduced to a 1–D phenomenon, linear elements with quadratic shape functions were used for the discretization of the model. Preliminary sensitivity analyses were performed to determine the optimal mesh size and, as a result, the average element size for all the models was set to $1\ \mathrm{mm}$. The primary variable, i.e. the relative humidity φ, was interpolated based on standard Lagrangian shape functions. Moreover, the backward finite difference method was used for automatic time discretization during the analysis. Finally, an iterative procedure based on the Newton–Raphson method was applied to solve the non–linear differential equations.

The imposed boundary conditions are summarized as follows:

a) Water absorption simulations; $\varphi = 1$ was defined at the base to represent liquid water, whereas null flux condition $g = 0\ \mathrm{kg/(m^2 \cdot s)}$ was imposed at the top face. The boundary condition at the base was introduced progressively using a smoothed step function.

b) Drying simulations; the bottom node was insulated whereas a convective flux was imposed at the top face, such as $g = h_m(p_v - p_{v,ext})$, with $h_m = 6.05\text{E–}8\ \mathrm{s/m}$. The partial vapour pressure of the environment was defined assuming $\vartheta = 23$ °C and $\varphi = 0.55$. Note that the value for the convective mass transfer coefficient was calculated from the drying tests performed on single materials, as explained in Section 5.2.2.

Additionally, the initial conditions were taken as:

a) Water absorption simulations; $\varphi(t = 0) = 0$, i.e. dry conditions. For the multi–layered configurations, $\varphi = 0$ is incompatible with the definition of the moisture transfer coefficient

applied at the interfaces, see Eq. (5.7). Hence, for such cases a small value was assumed, i.e. $\varphi(t = 0) = 0.01$, which can still be considered equivalent to the dry state.

b) Drying simulations; $\varphi(t = 0) = 1$, i.e. capillary saturation.

Finally, a qualitative curve–fitting process was used to estimate the necessary hygric properties, namely the liquid water diffusivity for drying and the interface hydraulic resistance. Thus, the average trend of the measured data was used for comparison against the simulated curves to calibrate the corresponding parameters until an optimized solution was found. It must be noted that, in this context, the accuracy of the model is considered based on the predictions of water uptake mass and moisture mass loss in capillary absorption and drying tests, respectively. Therefore, the global response of the system is used as a reference for validation. It is recalled, however, that a full validation would require the additional study of moisture profiles inside the specimens, which is out of the scope of the present work.

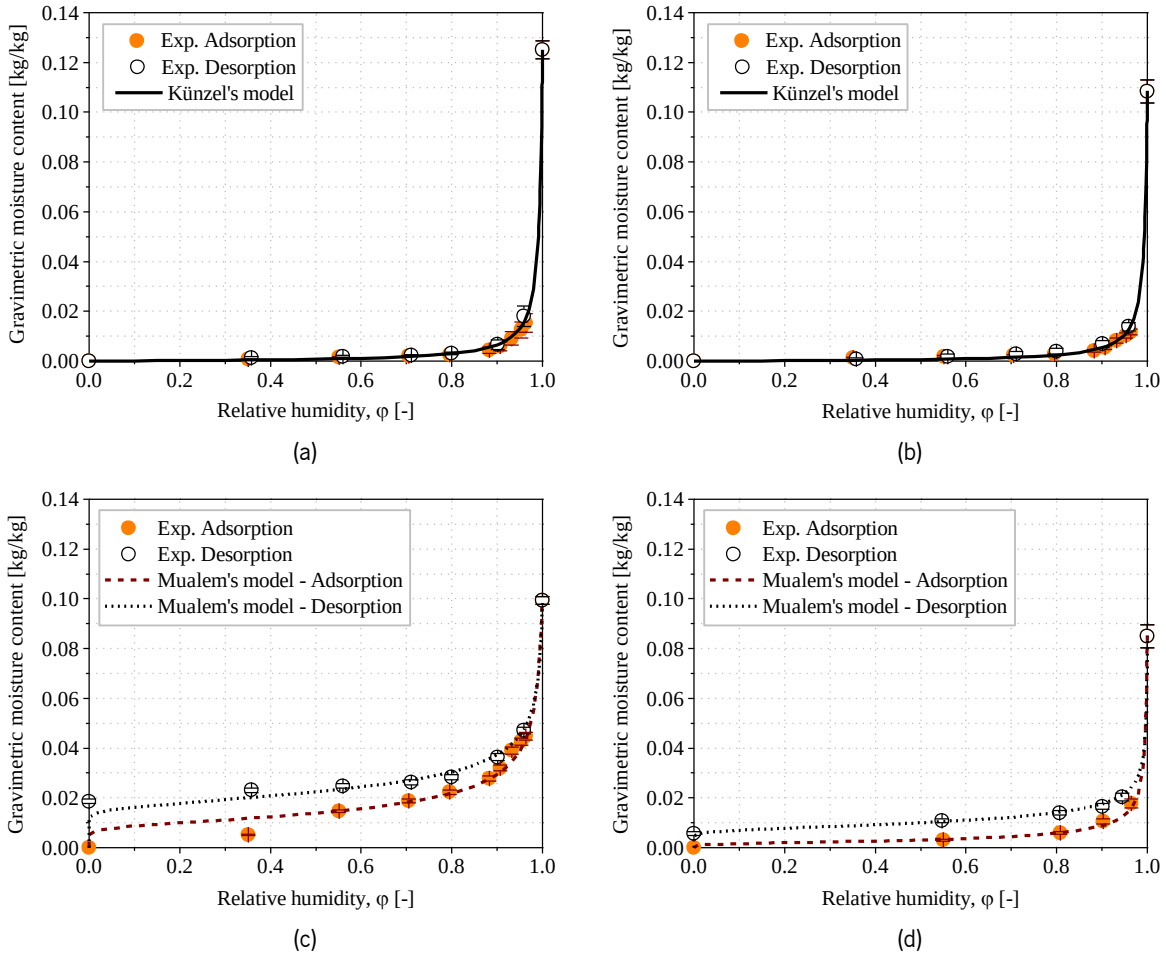

Figure 5.1. Moisture storage curves used for simulations: (a) brick (B), and (b) lime mortar (LM), fitted with Künzel's model (Künzel, 1995); (c) cement mortar (CM), and (d) lime mortar from masonry joints (LMJ), fitted with Mualem's model (Mualem, 1976).

In parallel to the development of the following sections, a series of parametric studies was carried out to understand the influence of each model parameter in the hygric response. These parametric studies are collected in a dedicated appendix, where the corresponding discussion and conclusions are also presented. The reader is referred to Appendix 3 for further details.

5.2.1 Water absorption in single materials

The results for the capillary absorption tests on single materials, namely B, CM and LM, are shown in Figure 5.2 together with the simulated curves. From the comparison between experimental and numerical results, it is clear that the proposed moisture transport model can capture the observed behaviour with great accuracy.

For all the absorption cases, the diffusivity factor introduced in Eq. (5.4) was defined using the original value of γ proposed by Künzel (1995), i.e. $\gamma_{ads} = 3.80$. Two other parameters were needed to determine the water uptake response of the model, namely (a) the capillary absorption coefficient, A_w, and (b) the capillary moisture content, w_{cap}. Note that both parameters were directly obtained from capillary absorption tests. As demonstrated by the numerical simulations, the capillary absorption coefficient is related to the water absorption rate: the higher A_w, the steeper the mass gain with respect to the square root of time. In other words, higher A_w values entail a faster absorption process, as expected. This relation is clearly evidenced by the studied materials since $A_{w,LM-ISO} > A_{w,B-X} > A_{w,B-Y} > A_{w,B-Z} \approx A_{w,CM-ISO}$. On the other hand, w_{cap} determines the equilibrium plateau attained at the end of the absorption process, which can be verified from the volume of the specimen, V, such as $V\ [\mathrm{m^3}] \times w_{cap}\ [\mathrm{kg/m^3}]$.

5.2.2 Drying in single materials

The results of the drying tests on single materials, namely B, CM and LM, are shown in Figure 5.3 together with the simulated curves. Considering the consistency between experimental and numerical results, it can be concluded that the model is able to reproduce the drying behaviour with excellent accuracy.

For these cases, an adjustment of the liquid water diffusivity function (Eq. (5.4)) was needed to match the experimental results. In particular, the diffusivity factor γ was indirectly estimated to calibrate the numerical response against the experimental data. The updated values of the diffusivity factor γ employed for drying cases, i.e. γ_{des}, are collected in Table 4.4.

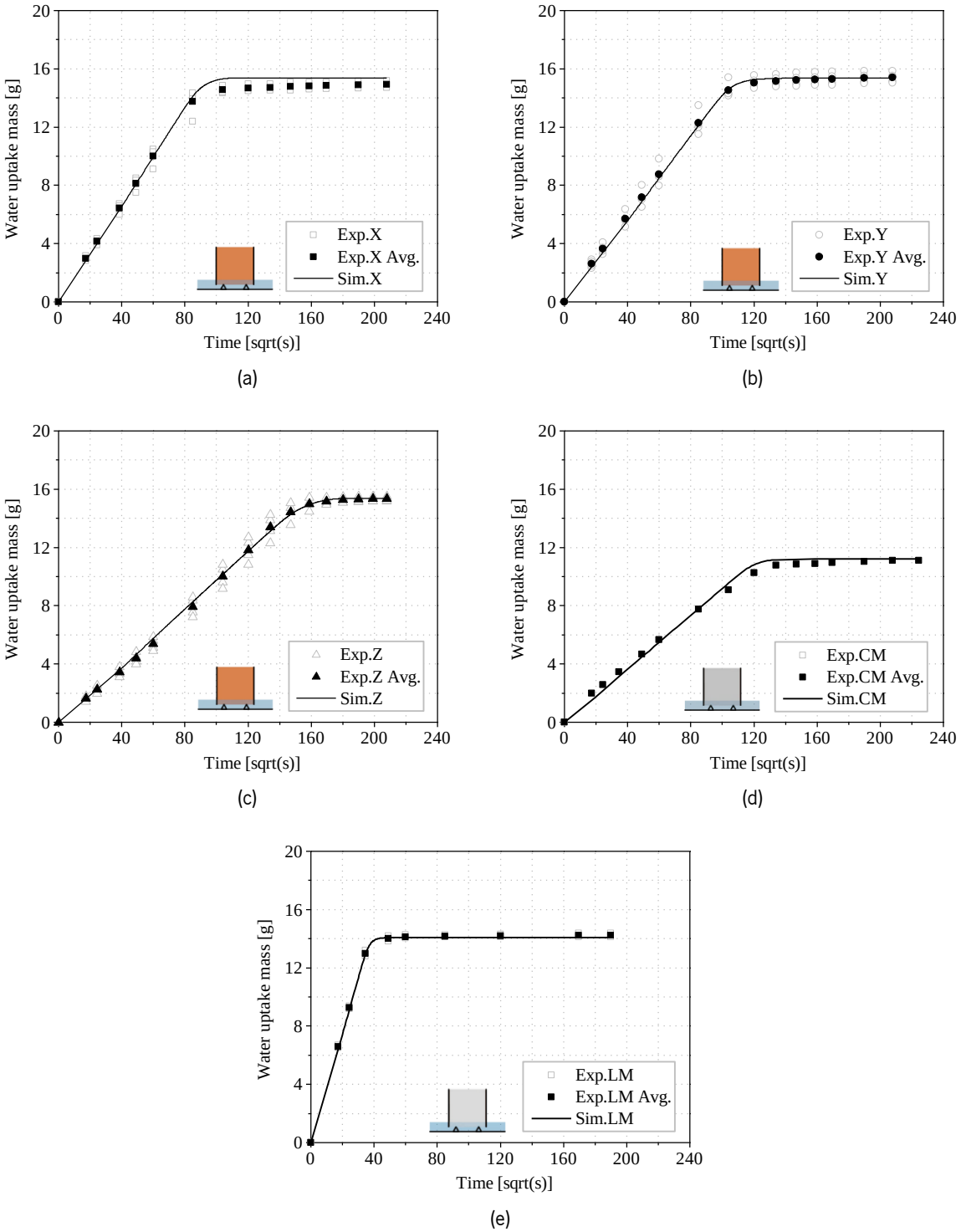

Figure 5.2. Capillary absorption results for single materials: (a) B, X or extrusion direction; (b) B, Y or stretcher direction; (c) B, Z or bed direction; (d) CM, isotropic; (e) LM, isotropic.

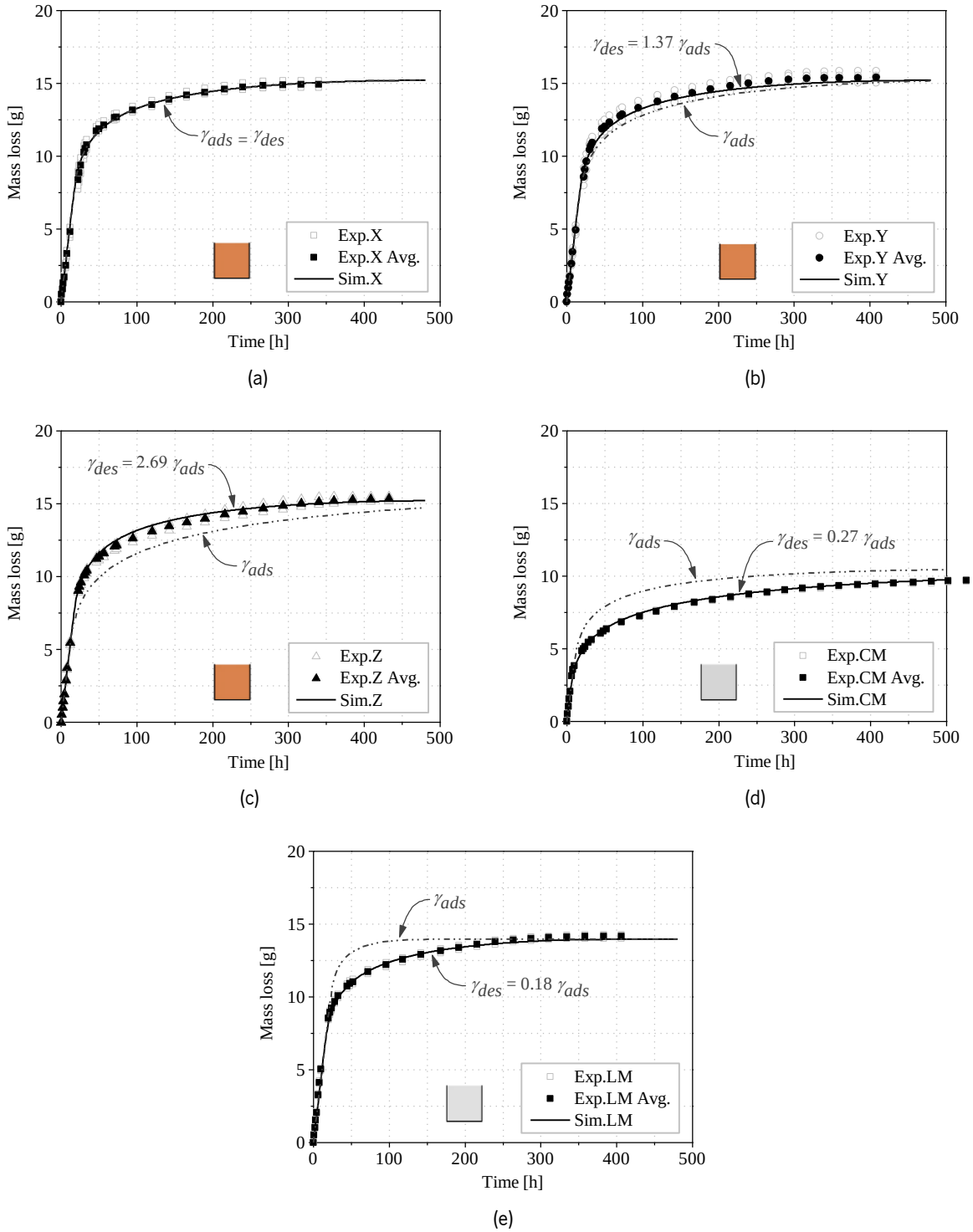

Figure 5.3. Drying results for single materials: (a) B, X or extrusion direction; (b) B, Y or stretcher direction; (c) B, Z or bed direction; (d) CM, isotropic; (e) LM, isotropic.

The adjustment of the original liquid diffusivity function is in agreement with the studies by Scheffler (2008), who discussed the existence of hysteretic transport functions for material models based on the diffusivity approach (Fick's law). Likewise, Krus (1996) explained this phenomenon by the different velocities for wetting and drying processes. In other words, since drying and wetting occur at different rates, their corresponding liquid transport coefficients can differ. Therefore, two diffusivity functions are necessary, namely one for adsorption, $D_{w,ads}$, and one for desorption, $D_{w,des}$. However, no analytical expression is available in the literature specifically for drying. As an indication, Künzel (1995) showed that for certain porous stones, the liquid diffusivity for desorption at capillary saturation could be approximately 3–5 times (finely porous stone) to one order of magnitude (coarse porous stone) lower than the diffusivity for adsorption at w_{cap}. Other studies demonstrated that the diffusivity for desorption can be adjusted by means of numerical simulations based on drying experiments (Scheffler, 2008). For instance, Krus & Holm (1999) proposed an analytical expression for the liquid water diffusivity as a function of moisture content. Their formulation can be directly applied to absorption cases, whereas for drying, a curve fitting process must be used to determine the diffusivity. For moisture conditions below 50 $\%\ \mathrm{RH}$, these authors proposed a fixed value $D_w = 2.0\text{E+}10\ \mathrm{m^2/s}$, applicable to both transport processes. For higher moisture contents, however, drying would require a lower liquid transport coefficient. In particular, for their studied set of building porous materials, the relation $D_{w,abs}/D_{w,des}$ at capillary saturation ranged between 1.5 for fired–clay brick, 2.0–3.0 for natural stones and up to 5.0 for lime silica brick.

In the present study, the relation $D_{w,abs}/D_{w,des}$ at capillary saturation reached 3.70 for CM and 5.67 for LM (Table 4.4), which is consistent with the literature and points out a significantly slower drying process compared to wetting. In fact, the drying simulation performed for both mortars using the adsorption diffusivity, i.e. $\gamma_{ads} = 3.80$, resulted into a much quicker mass loss with respect to the experimental evidence (see Figure 5.3d and Figure 5.3e). Interestingly, the behaviour of the extruded fired–clay brick followed a different trend. The drying simulation for the extrusion direction, $\mathrm{B_X}$, did not require any update to fit the experimental results, that is $\gamma_{des} = \gamma_{ads}$ (Figure 5.3a). For the other two directions, however, the numerical results obtained using γ_{ads} resulted into lower mass loss rates when compared with the experimental data (Figure 5.3b and Figure 5.3c). Thus, $D_{w,abs}/D_{w,des} < 1$ for the stretcher and the bed directions of the brick, $\mathrm{B_Y}$ and $\mathrm{B_Z}$, respectively. In other words, higher diffusivity values were needed to match the tests results. This behaviour seems contrary to most trends described in the literature for porous building materials. However, a possible explanation can be found in the orthotropic nature of extruded bricks due to their manufacturing process. In fact, when analysing the diffusivity values with respect to the extrusion direction, significant relations come to light (see Table 4.4).

As concluded from the water absorption simulations, the orthotropic behaviour of the studied brick is noticeable for adsorption, which is manifest in the relations $D_{w,ads,B-Y}/D_{w,ads,B-X} = 0.73$ and $D_{w,ads,B-Z}/D_{w,ads,B-X} = 0.34$ (values calculated at capillary saturation, w_{cap}). On the contrary, the diffusivity values for desorption show a more isotropic behaviour, namely $D_{w,des,B-Y}/D_{w,des,B-X} = 1.00$ and $D_{w,des,B-Z}/D_{w,des,B-X} = 0.93$ (values obtained at w_{cap}).

Table 5.2. Updated values of the diffusivity factor γ for drying.

Material/Direction	γ_{ads}	γ_{des}	$D_{w,ads}/D_{w,des}$ (1)	$D_{w,ads}/D_{w,ads,B-X}$ (1)	$D_{w,ads}/D_{w,des,B-X}$ (1)
BX	3.80	3.80	1.00	1.00	1.00
BY	3.80	5.19	0.73	0.73	1.00
BZ	3.80 (2)	10.22 (2)	0.37	0.34	0.93
CM	3.80	1.03	3.70	–	–
LM	3.80	0.67	5.67	–	–
LMJ	3.80	0.28	13.72	–	–

(1) Calculated at capillary saturation, w_{cap}

(2) For multi–layered cases, $\gamma_{ads} = 3.80$; $\gamma_{des} = 1.37$

In the proposed moisture transport model, the parameter that controls the mass loss rate during the first drying stage (linear trend) is the convective mass transfer coefficient, h_m [s/m], which defines the convective flux imposed as boundary condition. As it was mentioned in Section 4.1.7, the value of the mass transfer coefficient was calculated from the linear mass loss phase assuming constant vapour flux and constant boundary conditions (Scheffler, 2008). The formulation is reintroduced here for clarity:

$$h_m = \frac{g_v}{p_v(T_{surf}, \varphi_{surf}) - p_v(T_{env}, \varphi_{env})} \tag{5.12}$$

where g_v [kg/(m^2 · s)] is the vapour mass flow density, $p_v(T_{surf}, \varphi_{surf})$ [Pa] and $p_v(T_{env}, \varphi_{env})$ [Pa] are the vapour pressures defined at the exposed surface and for the environment, respectively. For this calculation, $\varphi_{surf} = 1$ (capillary saturation) was assumed at the material surface during the first drying phase. Moreover, the surface temperature, T_{surf}, was assumed as the wet bulb temperature corresponding to the conditions of drying air in the environment. Thus, after the necessary calibration, the convective mass transfer coefficient was defined $h_m = 6.05\text{E}{-8}$ s/m. In practice, h_m represents a phenomenological transfer parameter that summarizes thermo–dynamical and fluid–mechanical effects and is dependent on the environmental conditions, namely temperature, relative humidity and wind speed (Hall & Hoff, 2009). It must be noted that during the first drying stage, a temperature drop is expected at

the exposed surface due to the evaporation of water (Zhao et al., 2022). For the sake of simplicity, isothermal conditions were assumed in the simulations. Notwithstanding this approximation, excellent trends were obtained for the first drying stage in all the studied cases. An example of drying simulation with explicit account for thermal effects (hygrothermal model) is included in a dedicated appendix at the end of this thesis, where a set of parametric studies and the corresponding discussion and conclusions are also presented. The reader is referred to Appendix 4 for further details.

On the other hand, the end of the first drying stage and the development of the second stage are dependent on the moisture transport properties, namely the liquid water diffusivity and to a lesser extent the water vapour permeability. The final state of equilibrium with the environment is defined for each material from the moisture storage function or sorption isotherm.

5.2.3 Water absorption in multi–layered materials

The results for water absorption on masonry specimens are presented in Figure 5.4 together with the simulated curves. The location of the interfaces in the graphs is estimated from the volume of each material layer and the corresponding capillary moisture content, i.e. $\sum_i^n V_{bulk,i}$ $[\mathrm{m}^3] \times w_{cap,i}$ $[\mathrm{kg/m}^3]$.

It is noted that the existence of an interface resistance as presented in Eq. (5.7) was introduced in COMSOL Multiphysics as an internal boundary condition or barrier to the moisture flux:

$$\beta_{IF} = \frac{\rho_w \cdot R_v \cdot T}{\varphi \cdot R_{IF}} \tag{5.13}$$

where β_{IF} $[\mathrm{kg/(m^2 \cdot s)}]$ is the interface moisture transfer coefficient.

As discussed in Section 4.2.1, the first set of experimental tests involved masonry samples with two layers, namely B+LMJ, and therefore with a single interface. The same cylinders were analysed twice, once absorbing water from the mortar side (Figure 5.4a, configuration M1/M), and a second time absorbing water from the brick side (Figure 5.4b, configuration M1/B). The presence of the interface was barely perceptible for the configuration M1/B. Conversely, a clear drop in the measured inflow rate was noticeable for the cylinders M1/M. Therefore, the existence of an imperfect hydraulic contact was confirmed by the change of inflow rate in M1/M samples. Moreover, the difference between M1/B and M1/M supports the assumption of a natural contact between brick and mortar, most surely derived from a discontinuity in their pore structure (smaller pores in LMJ). In other words, the impact of the interface depends on the direction of the moisture flux and is more pronounced when the transfer occurs from a finely porous material to a medium with coarser pores.

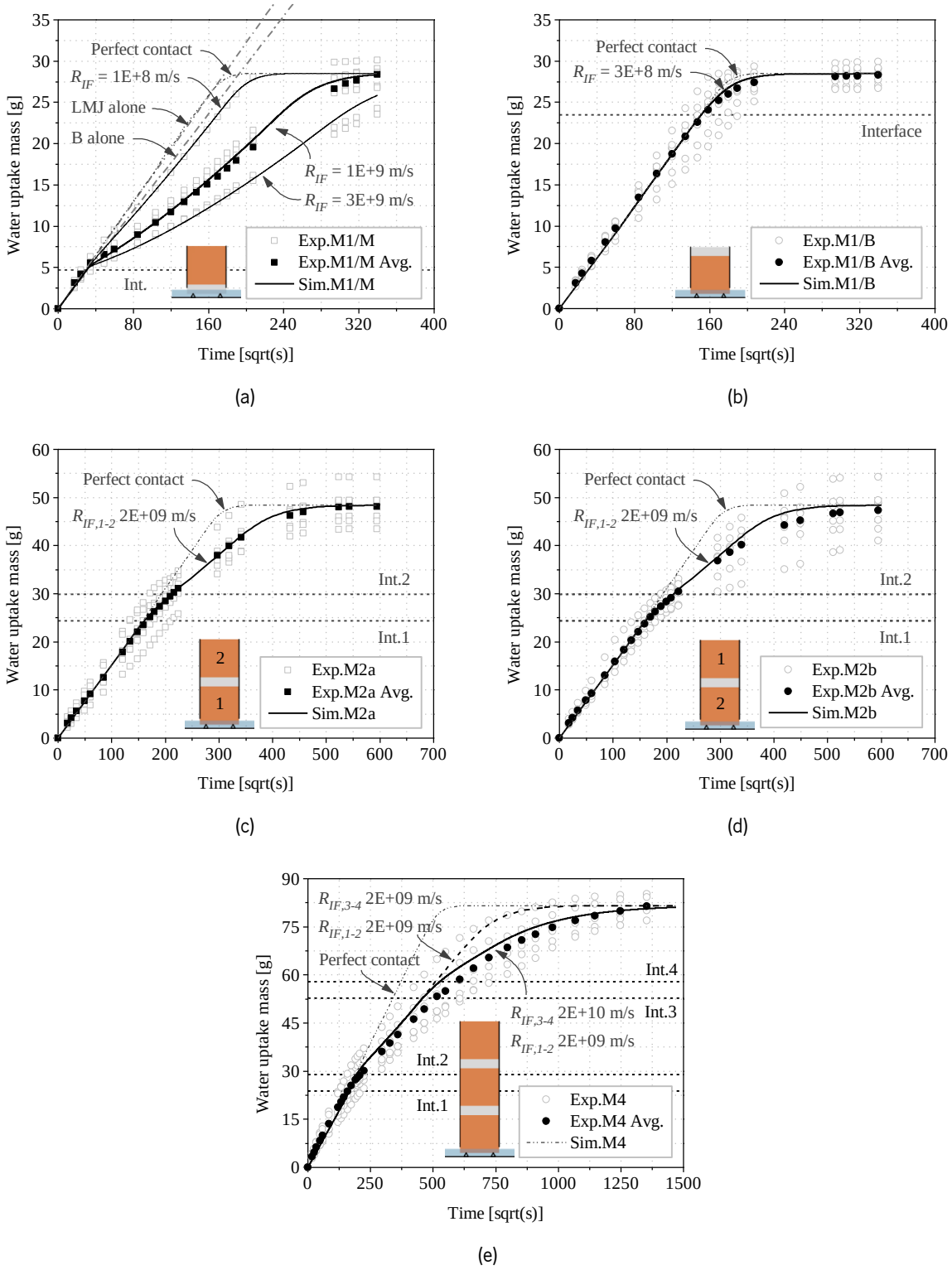

Figure 5.4. Capillary absorption results for masonry specimens: (a) M1/M or LMJ–B configuration; (b) M1/B or B–LMJ configuration; (c) M2a or B1–LMJ–B2 configuration; (d) M2b or B2–LMJ–B1 configuration; (e) M4 or B–LMJ–B–LMJ–B configuration.

For the numerical simulations, the M1/M scenario was studied first (see Figure 5.4a). A model assuming perfect contact (no hydraulic interface) showed mass gain rates within the range expected for the monolithic cases, that is considering the whole cylinder was brick or mortar. Then, the implementation of an interface resistance, R_{IF} as in Eq. (5.13), provided accurate results. To achieve the best fit, R_{IF} values were obtained iteratively. Three different cases were considered, as shown in Figure 5.4a: (a) low impact interface, $R_{IF} = 0.1\text{E+9}\ \mathrm{m/s}$, with only a slight retardation of the water mass inflow; (b) middle impact interface, $R_{IF} = 1.0\text{E+9}\ \mathrm{m/s}$, corresponding to the average behaviour of the experimental values; (c) higher impact interface, $R_{IF} = 3.0\text{E+9}\ \mathrm{m/s}$, which causes a more significant drop of the water absorption rate. Conversely, these three scenarios caused little variations of the results for the configuration M1/B, as shown in the Figure 5.4b where the most severe case, $R_{IF} = 3.0\text{E+9}\ \mathrm{m/s}$, is depicted against the model assuming perfect contact. This phenomenon may be explained by the proximity of the interface to the top face of the specimen, which implies that the water front reaches the interface when the material is already close to its equilibrium state, i.e. capillary saturation. In such circumstances, any deviation in the moisture absorption rate caused by the interface is obscured by the transition of the mass uptake curve towards the final plateau.

The second group of analyses performed on masonry specimens consisted of cylinders with three layers, namely B+LMJ+B, thus two interfaces (Figure 5.4c and Figure 5.4d). Experimentally, the cylinders were tested twice, each time absorbing water from one of the opposite bricks, i.e. B1–LMJ–B2, labelled M2a configuration, and B2–LMJ–B1, labelled M2b configuration. For both situations, only a slight absorption retardation was perceived at the first interface, whereas a more noticeable drop was noticed when the water was moving from mortar to brick (second interface). Overall, the apparent equivalency between M2a and M2b cases reassured the assumption of a natural contact between the materials. In other words, the fact that the M2 specimens showed the same trend for both tested directions indicates that there are no localized defects at the interface and most surely the cause of the imperfect hydraulic contact is the discontinuity between the pore structure of the adjacent materials. Numerically, accurate results were obtained when an interface resistance $R_{IF} = 2.0\text{E+9}\ \mathrm{m/s}$ was applied at the two interfaces.

Finally, water absorption analyses were performed on masonry specimens with five layers, B+LMJ+B+LMJ+B, thus four interfaces (M4). The experimental results and the simulated mass gain curves are presented in Figure 5.4e. The trends observed for the previous cases are applicable to M4 cases as well, in particular the lesser impact of the brick–to–mortar interface. It is noted that when the hydraulic resistance applied for M2 cases was used, i.e. $R_{IF,1} = R_{IF,2} = R_{IF,3} = R_{IF,4} = 2.0\text{E+9}\ \mathrm{m/s}$, the simulation provided an acceptable response for the first two interfaces but it failed to capture the

mass gain drop caused by the second mortar layer. Considering the experimental evidence and the simulation results, it is hypothesized that the successive appearance of interfaces gives rise to an additive retardation effect over the moisture flux. Consequently, a much higher resistance value was required for the second pair of interfaces to match the experimental data. In particular, a good fit was obtained when two sets of interface resistances were used, namely $R_{IF,1} = R_{IF,2} = 2.0\text{E+}9\ \mathrm{m/s}$ for the first two interfaces (this value is consistent with the previously studied configuration, M2), and $R_{IF,3} = R_{IF,4} = 2.0\text{E+}10\ \mathrm{m/s}$ for the third and fourth interfaces.

5.2.4 Drying in multi–layered materials

The results of drying tests and simulations on masonry specimens are presented in Figure 5.5. Two configurations were studied, namely cylinders drying from the brick face, labelled D1/B, and cylinders drying from the mortar face, D1/M. The convective mass transfer coefficient used for drying simulations in single materials, i.e. $h_m = 6.05\text{E–}8\ \mathrm{s/m}$, was employed for multi–layered cases as well. Overall, the match with the average behaviour of the experimental data is evident.

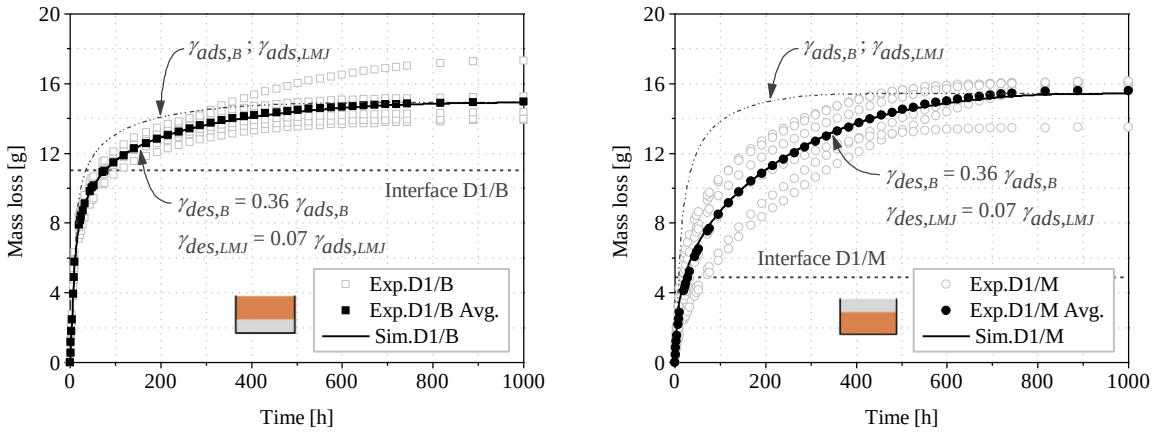

Figure 5.5. Drying results for masonry specimens: (a) D1/B or drying–from–brick configuration; (b) D1/M or drying–from–mortar configuration.

As it was mentioned for the drying studies on single materials, updating the diffusivity factor γ was necessary to calibrate the numerical response of multi–layered drying cases as well. In particular, the calibration process consisted of a parallel iterative tuning of $\gamma_{des,B}$ and $\gamma_{des,LMJ}$, so that the model could fit both experimental scenarios. Overall, it was found that the diffusivity of the material exposed to the environment was the most decisive parameter for each case. In other words, D1/B was more sensitive to variations in $\gamma_{des,B}$, whereas D1/M was mostly defined by $\gamma_{des,LMJ}$. As a result of the updating process, the corresponding values for the diffusivity factors were found, namely $\gamma_{des,B} = 1.37$ and

$\gamma_{des,LMJ} = 0.28$ (Table 4.4). The diffusivity factor for LMJ showed the same trend defined in Section 5.2.2 for the moulded mortar, LM, in this case with an even greater difference between adsorption and desorption ($D_{w,abs}/D_{w,des} = 13.72$ at w_{cap}).

For the brick material in multi–layered specimens, however, the updated liquid diffusivity followed a different trend compared to the drying cases of single–brick cubes. On this occasion, the factor γ_{des} needed to be reduced with respect to the wetting diffusivity in order to accommodate a slower mass loss rate ($D_{w,abs}/D_{w,des} = 2.77$ at w_{cap}). It must be noted that, despite deviating from the observations made for mono–layered brick cases, this behaviour is in line with the studied mortars and other materials reported in the literature (Künzel, 1995; Krus & Holm, 1999). Nonetheless, considering that the bricks used in masonry specimens showed a different capillary absorption coefficient (Table 2.2), variability of the material could be at the base of these dissimilarities as well.

The possible impact of the interfaces was also studied as part of the drying response of multi–layered specimens. Simulations assuming both perfect and imperfect contact were performed. However, by considering R_{IF} values as the ones proposed for the absorption cases, the results obtained with and without the interface resistance were virtually the same. The imposed R_{IF} needed to be in the order of 2.0E+10 $\mathrm{m/s}$ (the highest value used in the absorption simulation M4) in order to produce a slight deviation with respect to the perfect contact case. Therefore, it was acknowledged that the presence of natural contact interfaces plays a minor role in the drying process of multi–layered masonry specimens. This fact supports the conclusions of the experimental studies in Section 4.2.2, where no interfacial effects were identified on drying kinetics. In view of this, the perfect contact assumption can be applied to drying cases studied individually. For analyses involving both absorption and drying, the interface resistance must be tuned with respect to the wetting phase; it can be equally applied to the desorption process as it will not alter the response. For instance, the simulated curves reported in Figure 5.5 were obtained with an interface resistance $R_{IF} = 1.0\text{E+}9\ \mathrm{m/s}$, as the middle impact interface defined for the absorption case M1/M.

5.3 HYSTERESIS MODEL

In the previous section, hysteresis was observed in the moisture transport functions of the studied building materials. In particular, different liquid water diffusivity functions needed to be defined in order to represent adsorption and desorption processes. Consequently, the implementation of a hysteresis model becomes necessary for simultaneous wetting/drying simulations.

5.3.1 Numerical implementation

Inspired by the work of Zhang et al. (2015), a hysteresis index $WorD$ ('wetting or drying') is introduced and assigned to each element during the numerical simulations. This auxiliary index ranges between 0 and 1, and indicates the current state of each node, namely drying ($WorD = 0$) or wetting ($WorD = 1$). The initial value of $WorD$ must be defined manually at the beginning of the analysis according to the initial step of the process. Then, the index is automatically updated by examining the sign of the relative humidity difference between the current time step and the previous one, $\Delta\varphi(i)$. Assuming initial wetting, if $\Delta\varphi(i)$ is positive, then the material is indeed wetting, so $WorD$ is kept equal to 1. Conversely, if $\Delta\varphi(i)$ becomes negative, then the material has changed to drying and $WorD$ transitions towards 0. Thus, the switching expression is defined as:

$$\frac{\partial WorD}{\partial t} = if\left(\frac{\partial \varphi}{\partial t} > 0, V_{pos}, V_{neg}\right) + StepNeg(WorD) + StepPos(WorD) \tag{5.14}$$

where $V_{pos} = -V_{neg}$ are control parameters defining the transition between the target values, and $StepNeg$ and $StepPos$ are two correction functions. In this work, $V_{pos} = 1.0\text{E}{-5}$ and $V_{neg} = -1.0\text{E}{-5}$. It is worth noting that V_{pos} and V_{neg} can be tuned and set to higher values, which will make the transition between the two target functions more abrupt. However, a sharper transition may cause convergence problems. Moreover, $StepNeg$ and $StepPos$ are defined as smooth step functions which become active when $WorD$ goes below 0 or above 1, and so redirect the index towards values within the pre–established range. As an additional safeguard, the hysteresis index may be replaced by an expression such as "max(min($WorD$,1)0)". The max() and min() operators return the maximum and minimum value of the two arguments so they ensure that the hysteresis index cannot become smaller than 0 or larger than 1.

Once the hysteresis parameters have been defined, the resulting index is introduced in the expression for the liquid water diffusivity function:

$$D_w(\varphi) = WorD \cdot D_{w,ads}(\varphi) + (1 - WorD) \cdot D_{w,des}(\varphi) \tag{5.15}$$

The implementation of this hysteresis index ensures that the proposed moisture transport model can adjust automatically to any arbitrary wetting/drying cycles.

Hysteresis was observed as well in the sorption isotherms of CM and LMJ, both materials with marked hygroscopic behaviour. In order to capture the moisture storage hysteresis, a procedure analogous to the one applied for the liquid diffusivity function can be used. More specifically, an additional control parameter $AorD$ ('adsorption or desorption') must be defined as in Eq. (5.14) and applied to the moisture storage function of the material as in Eq. (5.15).

5.3.2 Benchmark models

A simple benchmark is proposed herein in order to validate the hysteresis model proposed for the liquid transport coefficient D_w. The model is based on data collected from capillary absorption and drying tests for cement mortar cubes (see Sections 5.2.1 and 5.2.2). This material is chosen since it presented significant differences between wetting and drying responses. Hence, 1–D numerical models are prepared to simulate the following scenarios: (a) water absorption with subsequent drying; (b) drying followed by water absorption.

Case study I: Absorption followed by drying

An initially dry mortar cube is subjected to free water uptake; the lower end is in contact with water (Dirichlet BC, $\varphi = 1$) whereas null flux condition (Neumann BC, $g = 0\ \mathrm{kg/(m^2 \cdot s)}$) is imposed on the opposite side. Once capillary saturation has been attained, the boundary conditions change so that the mortar undergoes drying; null flux condition is defined at the bottom, whereas a convective flux condition given by $g = h_m(p_v - p_{v,ext})$ is imposed at the top. The absorption conditions are maintained for the first 24 hours, whereas drying follows in the period 24–500 hours. Both processes take place under controlled environmental conditions, namely 23 °C and 55 % RH.

The results obtained for the first case study, i.e. wetting followed by drying, are presented in Figure 5.6. Three different scenarios are distinguished. First, the two processes are modelled separately, each one with the corresponding liquid diffusivity function, namely $D_{w,ads}$ for water absorption and $D_{w,des}$ for drying. Subsequently, both processes are modelled continuously using a single diffusivity function, in this case $D_{w,ads}$, which corresponds to the initial wetting phase. The new drying curve shows a clear deviation from the results obtained with the independent drying simulation. In particular, the moisture mass loss is faster for the model using $D_{w,ads}$ to describe the whole process. This is expected since $D_{w,ads} > D_{w,des}$ for the case of cement mortar (see Section 5.2.2). Finally, the hysteresis model is implemented so that the diffusivity function is automatically updated according to the type of process. As in the previous case, water absorption and drying are modelled continuously. Moreover, several calculations are performed using different values for $V_{pos} = -V_{neg}$. In general, the obtained results reproduce the target behaviour accurately. In particular, the moisture mass curve obtained with the hysteresis model $V_{pos} = -V_{neg} = 5.0\text{E}{-5}$ perfectly matches the curves calculated with the independent analyses.

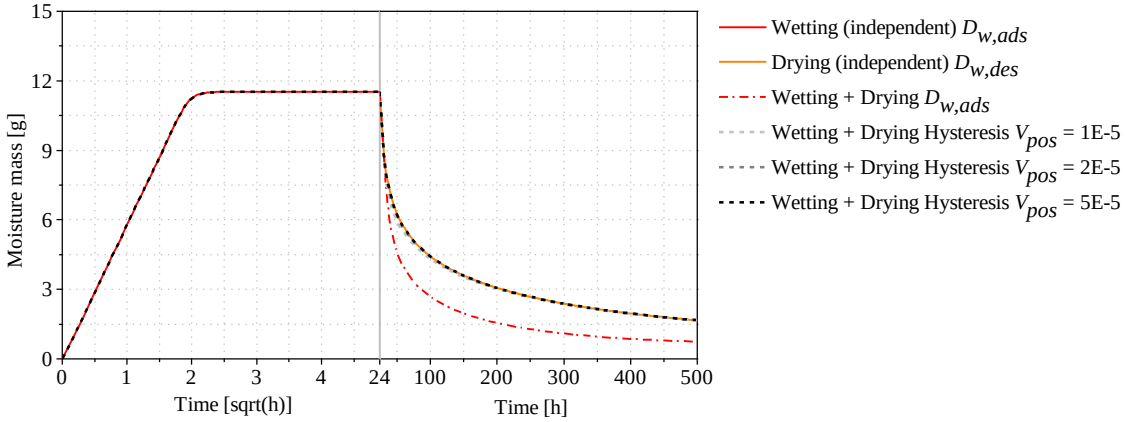

Figure 5.6. Moisture transport simulations to validate the hysteresis model. Case study I: wetting followed by drying. Note that two different scales are used for the horizontal axis.

Case study II: Drying followed by absorption

An initially capillary–saturated mortar cube is subjected to drying from a single face; a convective flux condition $g = h_m(p_v - p_{v,ext})$ is defined for the exposed surface, whereas null flux condition is imposed on the opposite side. After 500 hours, the boundary conditions change to represent capillary absorption; the bottom is placed in direct contact with water ($\varphi = 1$), and null flux is imposed at the top. The water absorption conditions are maintained for 24 hours. Both processes occur under controlled environmental conditions, namely 23 °C and 55 % RH.

The results obtained for the second case study, i.e. drying followed by wetting, are presented in Figure 5.7. Once more, three different scenarios are identified. First, the two processes are modelled separately, each one with the corresponding liquid diffusivity function, namely $D_{w,des}$ for drying and $D_{w,ads}$ for wetting. Subsequently, both processes are modelled continuously using a single diffusivity function, in this case $D_{w,des}$ since it corresponds to the initial drying. The moisture mass curve obtained with the new simulation shows a clear deviation with respect to the water absorption results calculated independently. In particular, the moisture mass gain is slower for the model using $D_{w,des}$ to describe the whole process. This is due to the lower diffusivity for desorption, i.e. $D_{w,des} < D_{w,ads}$, observed for cement mortar (see Section 5.2.2). Finally, the hysteresis model is implemented so that the diffusivity function is automatically updated according to the type of process. As in the previous case, drying and water absorption are modelled continuously. Moreover, different values of $V_{pos} = -V_{neg}$ are used for the calculations.

It is noted that for the same $V_{pos} = -V_{neg}$ values, the hysteresis model gives less accurate results than for the previous case study, i.e. wetting followed by drying. This fact is not surprising since water

absorption is a much faster process, and a quicker transition would be necessary. Thus, higher values of the controlling parameters $V_{pos} = -V_{neg}$ should be used: higher values entail a quicker transition between both diffusivity functions and consequently produce more accurate solutions. However, as it was mentioned, sharper transitions between the diffusivity functions may induce numerical instabilities. Indeed, a model with $V_{pos} = -V_{neg} = 1.0E{-}4$ was tried, but it suffered from convergence problems. Nevertheless, it is clear that the implementation of hysteresis implies a considerable improvement with respect to the scenario where only one diffusivity function is used.

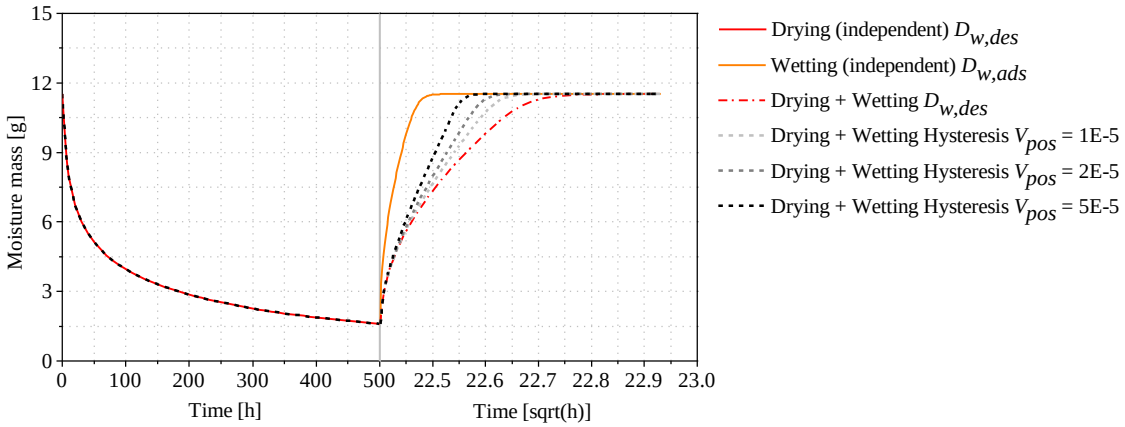

Figure 5.7. Moisture transport simulations to validate the hysteresis model. Case study II: drying followed by wetting. Note that two different scales are used for the horizontal axis.

5.4 MODELLING STRATEGIES

From a mechanical analysis point of view, different computational strategies have been reported in the literature to deal with the study of masonry and masonry structures. Figure 3.4 summarizes the most common approaches. In terms of complexity, there are two major types of modelling strategies, namely micro– and macro–modelling (Lourenço, 1996). Several phenomenological models accounting for the microstructure of the material represent a further development within the micro–modelling approach (Petracca et al., 2017). The micro–modelling strategies account for the mechanical behaviour of masonry by means of non–linear interface elements, continuum elements with non–linear behaviour or a combination of both. In turn, macro–modelling strategies assume a homogenized continuum material usually described by non–linear constitutive laws. Depending on the masonry texture or the level of complexity of the study, macro–models may assume isotropic or orthotropic continua.

Although the focus of these structural mechanics studies is usually different, several lessons may be learned from a cross–disciplinary approach. In this sense, certain parallelisms may be drawn between the mechanical and the moisture transport (possibly extendable to hygrothermal) modelling strategies.

Moreover, couplings between the different fields may be created as well. For this type of multi–physics analyses, the link between the hygric and mechanical fields is usually established through a one–way simple coupling process. This implies that the moisture distribution is calculated first and the obtained hygric strains are used as initial input for the mechanical analysis by means of the total strain decomposition principle (Ramézani & Jeong, 2011). The influence of moisture content on mechanical properties may be considered as well (Carmeliet, 2015).

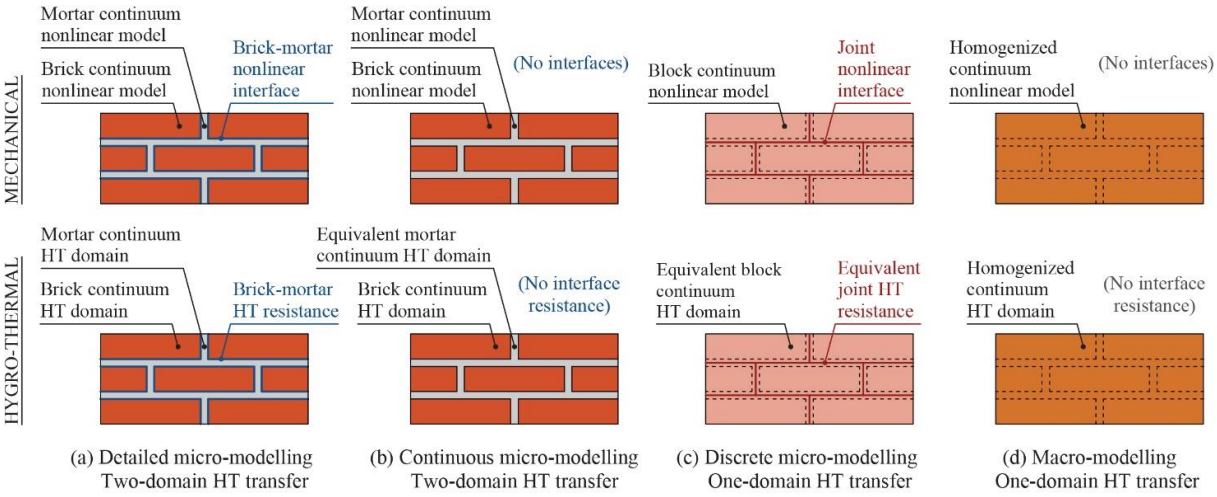

Figure 5.8. Modelling strategies for masonry. Adapted from D'Altri et al. (2018), following Lourenço (1996), and Petracca et al. (2017).

In Sections 5.2.3 and 5.2.4, an application of the detailed micro–modelling approach (Figure 3.4a) was presented and validated for water absorption and drying processes. The following subsections describe how the moisture transport simulations can be extended to other modelling strategies commonly used for mechanical studies of masonry. The same experimental data previously presented were used to calibrate the necessary model parameters and evaluate the accuracy of the simulations. In particular, the capillary absorption tests performed on masonry specimens M2 and M4 were employed as case studies. Thus, the corresponding moisture transport analyses were performed assuming the other strategies presented in Figure 3.4, namely continuous micro–modelling approach (Figure 3.4b), discrete micro–modelling approach (Figure 3.4c), and macro–modelling approach (Figure 3.4d). Additionally, a comparison between the different strategies is presented in terms of accuracy, level of complexity, flexibility, requirements, and limitations.

In general, an iterative curve–fitting procedure was used to calibrate the numerical parameters and obtain a good correlation between simulated and experimental results. In particular, the models that explicitly account for the interfaces (detailed micro– and discrete micro–) were calibrated by tuning the

interface resistance R_{IF} whereas the models without interfaces (continuous micro– and macro–) were calculated using the diffusivity factor γ as fitting parameter.

Moreover, an averaging procedure was used to calculate the equivalent properties needed for the discrete micro– and the macro–modelling approaches, which rely on homogenization. This concept is based on the volume fraction of each material with respect to the total volume, in the original configuration. Therefore, an equivalent property X_{EQ} is calculated as:

$$X_{EQ} = \sum_{i}^{n} X_i \frac{V_i}{V_{Total}} \tag{5.16}$$

where X represents the original value of the studied parameter, V is the volume, and i represents the material layer in a n–layered composite.

It must be recalled that the constituent materials, B and LMJ, have been defined in the present work by two different moisture storage models (Figure 4.2). In the current section, the distinction between the sorption isotherms was kept for the models with explicit consideration of the two materials (detailed micro– and continuous micro–). However, for the models with an equivalent continuum (discrete micro– and macro–), a simplification was employed, and the sorption isotherm of the brick alone (Künzel's model) was chosen to be representative of the equivalent behaviour. It is noted that this generalization is applicable to capillary–active materials and absorption processes, in which the porous medium is exposed to high relative humidity boundary conditions. In such circumstances, mass transport is governed mainly by liquid water movement (Zhang & Scherer, 2018). In other words, the absorption process involves the uppermost portion of the moisture storage curve. However, the same generalization may prove faulty in drying simulations with hygroscopic materials, such as LMJ. For such cases, the equivalent behaviour could be captured more accurately through a Mualem's type formulation (see Eq. (4.3)).

5.4.1 Continuous micro–modelling

The moisture transport equation and boundary conditions presented in Section 5.1 were applied to simulate the capillary absorption tests in M2 and M4 specimens by means of a continuous micro–modelling strategy (Figure 3.4b). For the continuous micro–modelling approach, brick and mortar were modelled with their original properties, that is, as obtained experimentally or with the corresponding values taken from the literature (Table 2.2). In order to account for the interfacial impact on moisture flux, the diffusivity factor γ associated to the mortar joints was tuned until a good agreement with the experimental data was found. Hence, the necessary parameters and updated material properties are presented in Table 5.3 and the corresponding results are shown in Figure 5.9a and Figure 5.9b.

Note that when the original $\gamma_{ads,LMJ} = 3.80$ is used, the problem is equivalent to the detailed micro–model with perfect contact (no interface resistance). The best match is found when the diffusivity factor is reduced to a 10 % of its original value, that is $0.10 \times \gamma_{ads,LMJ}$. Additionally, for the M4 configuration, different γ values were needed to account for the incremental effect of successive interfaces. The best fit was obtained with $0.10 \times \gamma_{ads,LMJ}$ for the first interface (to be consistent with the previous case) and $0.02 \times \gamma_{ads,LMJ}$.

Table 5.3. Input parameters used for the different masonry modelling strategies (shaded cells show calibration parameters).

Modelling strategy	Case study	Material/ Element	Parameters							
			γ_{ads}	w_{cap}	ψ	a	m	A_w (1)	μ	R_{IF}
			[–]	[kg/m^3]	[–]	[1/Pa]	[–]	[kg/(m^{2}s$^{0.5}$)]	[–]	[m/s]
Detailed micro–	M2	B	3.80	240	1.0070	–	–	0.075	34.14	–
		LMJ	3.80	190	–	3.8E–6	0.352	0.080	15.00	–
		Int.1/2	–	–	–	–	–	–	–	2.0E+9
	M4	B	3.80	240	1.0070	–	–	0.075	34.14	–
		LMJ	3.80	190	–	3.8E–6	0.352	0.080	15.00	–
		Int.1/2	–	–	–	–	–	–	–	2.0E+9
		Int.3/4	–	–	–	–	–	–	–	2.0E+10
Continuous micro–	M2	B	3.80	240	1.0070	–	–	0.075	34.14	–
		LMJ	0.40	190	–	3.8E–6	0.352	0.080	15.00	–
	M4	B	3.80	240	1.0070	–	–	0.075	34.14	–
		LMJ1	0.40	190	–	3.8E–6	0.352	0.080	15.00	–
		LMJ2	0.08	190	–	3.8E–6	0.352	0.080	15.00	–
Discrete micro–	M2	Eq.B	3.80	234	1.0070	–	–	0.076	31.84	–
		Int.1	–	–	–	–	–	–	–	4.0E+9
	M4	Eq.B	3.80	232	1.0070	–	–	0.076	31.21	–
		Int.1	–	–	–	–	–	–	–	4.0E+9
		Int.2	–	–	–	–	–	–	–	4.0E+10
Macro–	M2	Eq.B	3.04	234	1.0070	–	–	0.076	31.84	–
	M4	Eq.B	3.04	232	1.0070	–	–	0.076	31.21	–

(1) For 2–D models, B and Eq.B have orthotropic behaviour, $A_{w,X} = 0.104$ kg/(m^{2}s$^{0.5}$)

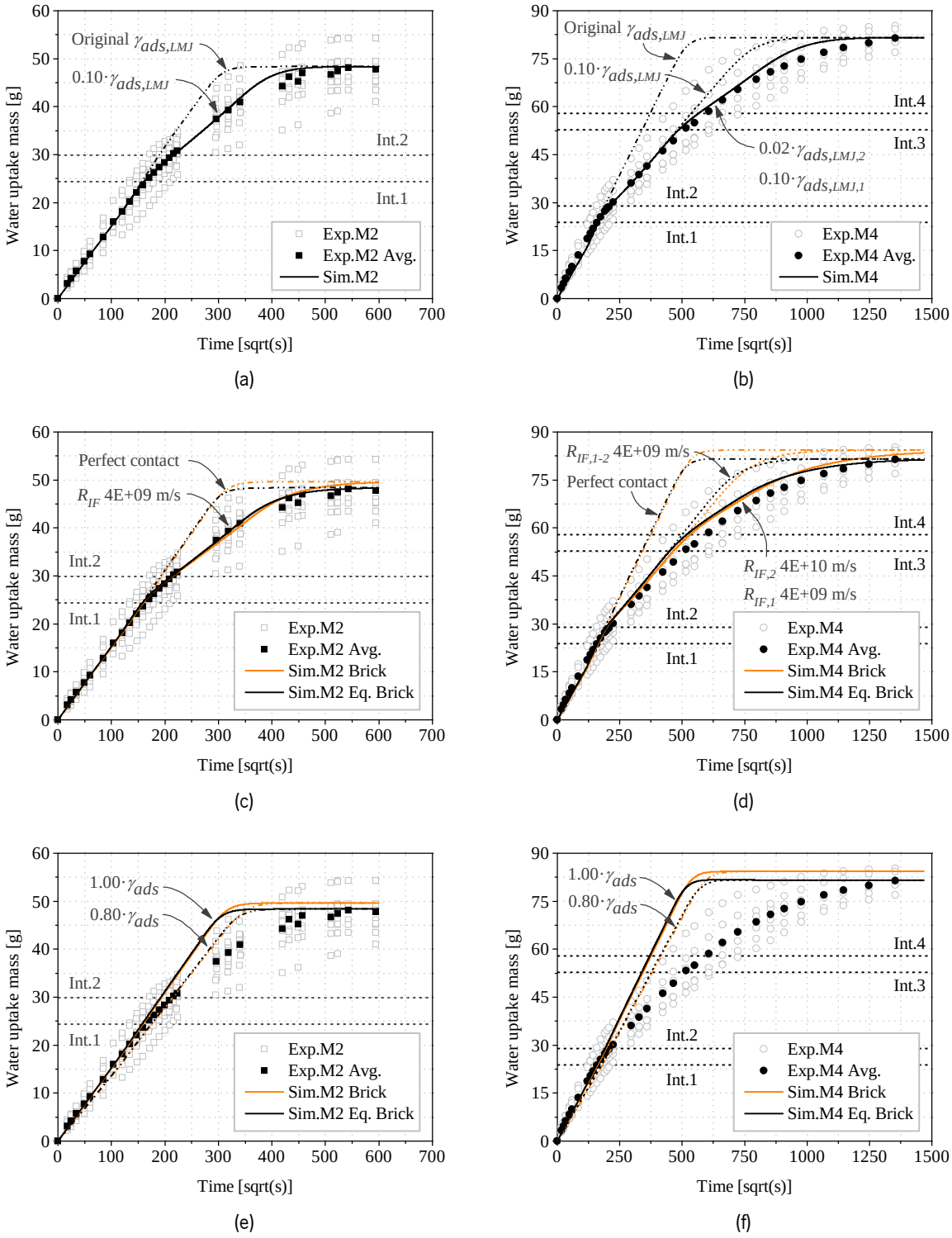

Figure 5.9. Capillary absorption simulated using different modelling strategies: (a) continuous micro–modelling, M2; (b) continuous micro–modelling M4; (c) discrete micro–modelling, M2; (d) discrete micro–modelling M4 (e) macro–modelling, M2; (f) macro–modelling, M4.

In terms of requirements, the same input material parameters demanded by the detailed micro–modelling approach are needed for the continuous micro–model. The latter does not consider hydraulic interfaces and therefore the calibration must be done through the diffusivity factor γ. Since there are no interfaces, the complexity of the model is relatively low. In general, the continuous micro–modelling approach can provide good accuracy of results and it may be recommended in cases where interfaces need to be explicitly avoided.

5.4.2 Discrete micro–modelling

The results for water absorption simulations using the discrete micro–modelling strategy (Figure 3.4c) are presented in Figure 5.9c and Figure 5.9d. The necessary parameters and updated material properties are presented in Table 5.3. Considering the discrete micro–modelling strategy, masonry was represented by the combination of two components: the bricks were modelled as a continuum with equivalent material properties and extended size, whereas interfaces were used to simulate the presence of mortar joints and brick–mortar interfaces. If the properties of both materials are known, the volume fraction of each material may be used to define equivalent properties. Otherwise, brick properties may be assumed without compromising the accuracy (see curves using brick versus equivalent brick properties in Figure 5.9c and Figure 5.9d).

The main parameter used for calibration within the discrete micro–model strategy are the hydraulic resistances, R_{IF}, imposed at the interfaces. It was found that a value $R_{IF} = 4.0\text{E+}9\ \mathrm{m/s}$ provided a good fit for the M2 configuration. Note that this value is double the resistance originally used for the detailed micro–model. This is expected since now a single interface must stand for the two interfaces of the detailed micro–model. On the other hand, two sets of values were used to match the experimental results of M4 configuration, namely $R_{IF} = 4.0\text{E+}9\ \mathrm{m/s}$ for the first interface (consistent with the M2 case) and $R_{IF} = 4.0\text{E+}10\ \mathrm{m/s}$ for the second interface. The higher value for the second interface is consistent with the hypothesis of an in–series interfacial phenomenon, that is the additive effect of successive interfaces. Once again, it is noted that the value imposed at the second interface is double the resistance used for the corresponding detailed micro–modelling case.

In terms of requirements, the discrete micro–modelling approach has the advantage of needing fewer input material parameters than the other micro–modelling approaches. If the properties of brick and mortar are known, an equivalent material may be calculated by volume averaging as presented in Eq. (5.16). Otherwise, the model may produce considerably accurate results assuming only the properties of the brick (compare the curves produced using brick versus equivalent brick properties in Figure 5.9c

and Figure 5.9d). This simplification is valid as long as the volume proportion of masonry units is higher than the corresponding volume of mortar joints, which is usually the case in brickwork masonry. Due to the extended geometry of the bricks, the geometric definition of the system may be somewhat more complex than the other strategies. On the other hand, the model is simplified by assuming only one material. Moreover, interfaces can capture localized phenomena such as the imperfect contact between adjacent layers.

Overall, the discrete micro–modelling technique provides high accuracy and is a good compromise between simplicity and quality of results. Its use is encouraged when mortar properties are not known.

5.4.3 Macro–modelling

Finally, water absorption simulations were performed considering a macro–modelling strategy (Figure 3.4d). The results are shown in Figure 5.9e and Figure 5.9f. Following the macro–modelling approach, masonry was idealized as a continuum with equivalent material properties. On this occasion, the homogenized medium must capture the overall behaviour of the system so that it provides an average trend. As in the discrete micro–modelling case, the volume fraction of each material may be used to define equivalent properties if both brick and mortar parameters are known. Otherwise, brick properties may be applied to the system and similar results can be obtained (see curves using brick versus equivalent brick properties in Figure 5.9e and Figure 5.9f).

The diffusivity factor γ was used as a calibration parameter for curve–fitting. The curves obtained with the original factor $\gamma_{ads} = 3.80$ were able to capture the initial water uptake but largely overestimated the absorption rate as time evolved. This was expected since it is the usual response of a monolithic specimen (see absorption of single materials in Figure 5.2). For the M2 configuration, a reduction of the diffusivity parameter, e.g. $0.80 \times \gamma_{ads}$, was needed to produce a water uptake curve that could fit the overall experimental envelope. This type of correction provides an average approximation: the initial absorption rate is underestimated, whereas the absorption rate for prolonged times is overestimated. Note that the same reduction applied to M4 cases is not quite satisfactory since it deviates considerably from the experimental results.

Macro–modelling approaches are commonly used for global structural analyses and their application to moisture transport is conveniently straightforward. The geometry is very simple and only one material is modelled. Moreover, the properties of brick and mortar may be used to define an equivalent medium or solely brick properties may be considered. Nonetheless, this strategy proves very little flexibility, and the simulation cannot capture the changes in moisture flux with evolving time or localized phenomena

such as the existence of hydraulic interfaces. Overall, the accuracy of the macro–model approach is far lower than the one achievable via micro–modelling.

5.4.4 Rising damp in a masonry wallette

To further demonstrate the capabilities of the proposed approach, a two-dimensional (2–D) masonry wallette was studied under capillary absorption conditions. This type of analysis is representative of rising damp, which is a rather common phenomenon in load–bearing masonry structures. The wallette was modelled using the different strategies discussed in the previous sections, namely detailed micro–, continuous micro–, discrete micro– and macro–modelling. The geometry of the wallette is that presented in Figure 3.4 for each modelling technique, assuming symmetry conditions through the middle vertical plane. In the original configuration, the bricks had dimensions 200 $\mathrm{mm} \times 100\ \mathrm{mm} \times 50\ \mathrm{mm}$ and the mortar joints were 12 mm thick. The same brick and mortar materials previously presented for the multi–layered masonry cases and the different modelling approaches were used here (Table 5.3). Additionally, the orthotropic response of the bricks was considered in the 2–D simulations and the capillary absorption coefficient for the extrusion direction was used for brick and equivalent brick materials, namely $A_{w,X} = 0.104\ \mathrm{kg/(m^2 \cdot s^{0.5})}$ (see Table 2.2).

The finite element mesh used for all the models consisted of quadrilateral Lagrangian quadratic elements with average size 2 mm. The total amount of elements for each model was around 11000. To represent rising damp exposure, the boundary conditions were taken as for free water absorption, namely direct contact with water at the base, $\varphi = 1$, and null flux, $g = 0\ \mathrm{kg/(m^2 \cdot s)}$, at the top face. The boundary condition at the base was introduced progressively using a smoothed step function. Sealed conditions were assumed for the lateral faces and symmetry was imposed at the mid–section vertical plane. Finally, 'dry' initial conditions were considered, $\varphi(t = 0) = 0.01$.

The results obtained with the different modelling strategies are presented in Figure 5.10 in terms of evolution of the internal relative humidity with time. For the models with an explicit account of the mortar joints (detailed micro–, Figure 5.10a, and continuous micro–modelling, Figure 5.10b), the presence of vertical joints became relevant. This was expected since the studied natural hydraulic lime mortar, either moulded (LM) or cast directly in masonry bed joints (LMJ), showed a higher capillary absorption coefficient than brick. Higher A_w entails a higher liquid water diffusivity and consequently the joints in masonry act as a moisture bridge, accelerating the absorption. In the present simulations, this fact was particularly evident in the vertical joints, in which the moisture front advanced faster than in the adjacent bricks. Note

that this phenomenon is in contrast with other cases with cement mortar, where the less permeable cement acts as a moisture barrier (X. Zhou et al., 2020).

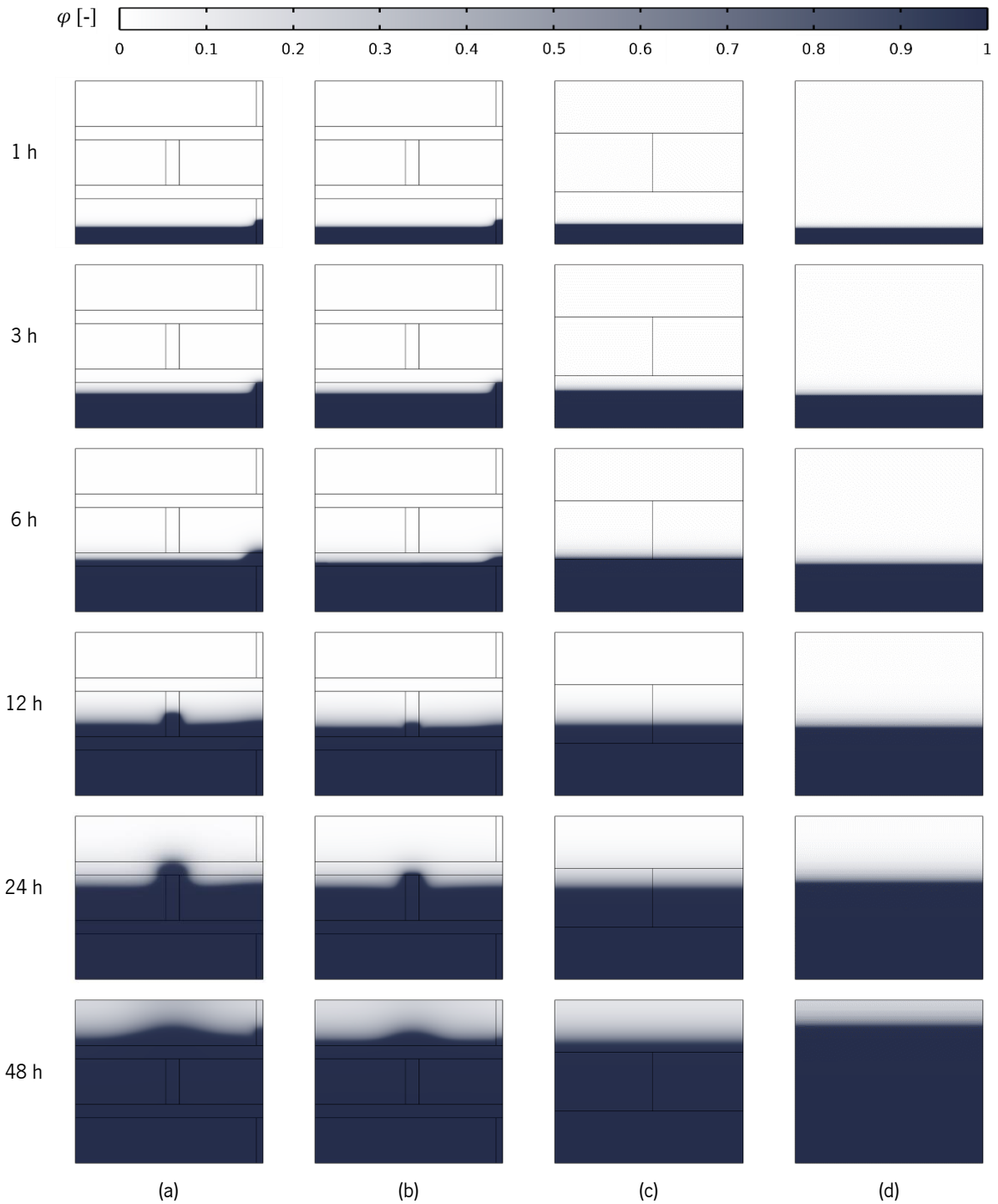

Figure 5.10. Evolution of internal relative humidity in masonry wallettes simulated using different modelling strategies: (a) detailed micro–modelling; (b) continuous micro–modelling; (c) discrete micro–modelling; (d) macro–modelling.

Only slight differences in moisture distribution were registered for the detailed micro– (Figure 5.10a) and the continuous micro–modelling approaches (Figure 5.10b). The discrete micro–model (Figure 5.10c) could not capture the disturbances induced by the vertical joints but overall, the obtained moisture front evolution was comparable to the detailed micro– and continuous micro–modelling cases. Finally, the macro–modelling strategy (the presented results were calculated with a correction $0.80 \times \gamma_{ads}$) revealed the same flaws anticipated in Section 5.4.3 for this type of approach, namely underestimation of the initial moisture absorption and overestimation of the absorption rate for prolonged times. A common feature presented by all the models was a continuous diffusion of the moisture front with evolving time. In other words, the wet front (normally assumed sharp) became dimmer and dimmer as it advanced through the material.

5.5 CHAPTER CONCLUSIONS

This chapter presents a moisture transport model to study a series of moisture–related phenomena in multi–layered porous materials, namely water absorption and drying. First, the moisture transport model is presented. Then, numerical simulations based on the finite element method are performed with the aid of COMSOL Multiphysics. Simulation results are compared against the experimental evidence, and material parameters are calibrated to improve curve fitting.

A set of physical and hygric–related material properties are needed as input for the model: bulk density, open porosity, capillary moisture content, capillary absorption coefficient, moisture storage curves (adsorption/desorption), and water vapour permeability/resistance. Moreover, two parameters are chosen as calibration variables to fit the experimental results. In particular, the interface hydraulic resistance is chosen as the calibration parameter for capillary absorption tests, whereas the diffusivity factor γ defined for the liquid water diffusivity function is used to calibrate drying.

A commonly used expression for liquid water diffusivity originally proposed by Künzel (1995) is validated with capillary absorption and drying tests results. However, it is demonstrated that the diffusivity function needs to be adjusted depending on the process (wetting/drying). A diffusivity factor γ is proposed as an adjustable parameter to accommodate both processes. The original analytical formulation with $\gamma_{ads} = 3.80$ can be used directly for the wetting processes together with the water absorption coefficient calculated from capillary absorption tests. Conversely, the expression for diffusivity in desorption processes lacks a consistent definition, thus inverse analysis from experimental data is needed for each case. Since the materials exhibit different behaviour according to the type of process, validation of

moisture transport models should always consider both absorption and desorption. In other words, validation from only wetting or only drying tests would be insufficient.

No analytical approach was found to evaluate the interface hydraulic resistance consistently. The interface behaviour depends on the materials in contact, the geometric arrangement of the layers and specific conditions of each case, such as the existence or not of previous discontinuities. In the current work, the interface impact is estimated for water absorption cases by an iterative process of curve–fitting. It is proven that for the studied conditions the interface resistance has a negligible impact on drying kinetics. Considering the case–specific issues derived from the interfacial contact, direct extrapolations of the presented resistance values must be treated with caution. Further works are needed to define a general approach for the study of moisture–related interface phenomena.

A hysteresis model is defined in order to capture the observed differences between water absorption and drying processes. In particular, a hysteresis index is implemented to control the transition between adsorption and desorption liquid diffusivity functions. The results for the case where wetting is followed by drying perfectly match the target behaviour. Conversely, the transition from drying to wetting requires a much more abrupt change and the simulated results show less accuracy. Nonetheless, the obtained trends are still considered adequately accurate.

Different modelling approaches commonly used in solid mechanics for masonry structures and materials are extrapolated to the study of moisture transport problems. Considering the higher accuracy and flexibility of the models with an explicit account of interfaces, the use of the detailed micro– or the discrete micro–modelling techniques is preferred. All the analysed moisture transport modelling strategies are suitable for coupling with mechanical studies to define hygro–mechanical models.

Overall, the proposed moisture transport model is able to capture water absorption and drying processes in multi–layered masonry materials with considerable accuracy. In the following chapter, the studies will be extended to non–isothermal problems, incorporating the necessary temperature–dependent properties. The application of transient boundary conditions (cyclic temperature and relative humidity) will also be implemented to reproduce applications closer to service–life conditions. Future works should further go in depth over the characterization of interface hydraulic resistances, with special emphasis on the additive effect of consecutive discontinuities. Finally, subsequent studies should also account for the presence of vertical joints and possible moisture bridges through open cracks.

This page has been intentionally left blank

CHAPTER 6

Numerical simulations II: Hygro–thermo–mechanical coupling

This chapter deals with the simulation of different hygrothermal phenomena and their relationship with the mechanical behaviour of masonry elements. The discussion addresses the coupling between fields and the role of different modelling approaches and input parameters on the simulation output. First, the moisture transport model presented in the previous chapter is linked to the thermal field and a coupled hygrothermal model is proposed. In order to understand the capabilities of the model, a brick masonry wall is simulated under different environmental conditions. Subsequently, the hygrothermal analysis is extended to incorporate mechanical effects. Thus, a one–way coupled hygro–thermo–mechanical model is presented, and its application is demonstrated on the wall studied previously.

6.1 HYGROTHERMAL MODEL

This first section presents the numerical model adopted for hygrothermal simulations. The theoretical bases and assumptions introduced in Chapter 5 for the moisture transport model are briefly recalled here for clarity. Masonry is described as a porous medium made up of a matrix of interconnected pores inside a solid skeleton. This solid phase is assumed to be continuous, homogenous, inert (no chemical reactions), isotropic and non–deformable. On the other hand, pores are assumed cylindrical, with a homogenous, isotropic distribution inside the material. The void space defined by the pores is filled in different proportions with a liquid and a gaseous phase. The liquid phase is pure and incompressible, whereas the air phase is an ideal mixture of dry air and water vapour at atmospheric pressure. For simplicity, advective air flow is not implemented in the model and pressure gradients are considered negligible. Additionally, a local, instantaneous thermodynamic equilibrium is assumed between the liquid and gaseous phases. Based on this, the contributions of liquid water and water vapour may be combined to define a global moisture content. Nonetheless, the contribution of water vapour to the total moisture content is negligible. Knudsen flow is not considered, and the effect of gravity is neglected since capillary forces are dominant.

The volume fraction of (moist) air inside the porous space does not contribute to the overall thermal conductivity and specific heat capacity of the material. Heat flux induced by moisture transport (Dufour

effect) as well as moisture flux induced by temperature gradients (Soret effect) are considered negligible. The coupling between heat and moisture fields will be further discussed in the following sections.

The effect of imperfect contact interfaces in multi–layered cases is considered for moisture transport by means of hydraulic resistances as presented in Chapter 5. For heat transfer, the impact of interfaces between adjacent materials is disregarded so that the temperature profiles are continuous between layers.

6.1.1 Governing equations

The heat transfer model considers conductive heat transfer according to Fourier's Law and accounts for the heat of vaporization:

$$\rho C \frac{\partial T}{\partial t} = \nabla \cdot (\lambda \nabla T) + L_v \nabla \cdot \left(\frac{\delta_a}{\mu} \nabla (\varphi \, p_{v,sat}) \right) \tag{6.1}$$

where ρC $[\mathrm{J/(m^3 \cdot K)}]$ is the volumetric heat capacity at constant pressure, T is the temperature [K], t [s] is time, λ $[\mathrm{W/(m \cdot K)}]$ is the thermal conductivity, L_v [J/kg] is the latent heat of evaporation, δ_a $[\mathrm{kg/(m \cdot s \cdot Pa)}]$ is the water vapour permeability of still air, μ [–] is the water vapour resistance of the material, φ [–] is the relative humidity, and $p_{v,sat}$ [Pa] is the vapour saturation pressure. The second term on the right–hand side of Eq. (2.1) represents the latent heat of vaporization associated with liquid/gas phase change.

On the other hand, the moisture transport equation presented in Chapter 5 is recalled here for clarity:

$$\frac{\partial w}{\partial \varphi} \frac{\partial \varphi}{\partial t} = \nabla \cdot \left(\frac{\partial w}{\partial \varphi} D_w \nabla \varphi \right) + \nabla \cdot \left(\frac{\delta_a}{\mu} \nabla (\varphi \, p_{v,sat}) \right) \tag{6.2}$$

where w $[\mathrm{kg/m^3}]$ is the moisture content, and D_w $[\mathrm{m^2/s}]$ is the liquid water diffusivity. The remaining parameters are the same as presented in Eq. (2.1). The modified version of the exponential expression proposed by Künzel (1995) is used to describe the liquid water diffusivity:

$$D_w = \gamma \cdot \left(\frac{A_w}{w_{cap}} \right)^2 \cdot 10^{3 \cdot \left(\frac{w}{w_{cap}} - 1 \right)} \tag{6.3}$$

where γ [–] is a diffusivity factor depending on the material and transport process (wetting/drying), A_w $[\mathrm{kg/(m^2 \cdot s^{0.5})}]$ is the capillary absorption coefficient, and w_{cap} $[\mathrm{kg/m^3}]$ is the capillary moisture content.

6.1.2 Hygrothermal coupling

The variety of relations and inter–dependencies between the heat and moisture fields are discussed in this section. First, the moisture dependency of heat transfer parameters is addressed. Then, the thermal effects on mass transport properties are discussed.

Moisture dependency of thermal parameters

To begin with, the heat capacity of a porous material is directly related to its moisture content. In particular, if the material is wet, the effect of moisture on heat capacity can be taken into account:

$$\rho C = \rho_{bulk} C_p + w \cdot C_w \tag{6.4}$$

where ρC $[\mathrm{J/(m^3 \cdot K)}]$ is the volumetric heat capacity of the material, ρ_{bulk} $[\mathrm{kg/m^3}]$ is the bulk density of the material, C_p $[\mathrm{J/(kg \cdot K)}]$ is the specific heat capacity of the dry material, w $[\mathrm{kg/m^3}]$ is the moisture content, and C_w $[\mathrm{J/(kg \cdot K)}]$ is the specific heat capacity of liquid water. The specific heat capacity of water has a weak thermal dependence for the range of temperatures of interest in this study. Therefore, it is taken as a constant, $C_w = 4182\ \mathrm{J/(kg \cdot K)}$, which corresponds to the specific heat capacity of water at 20 °C. For a detailed list of saturated water properties, the reader is referred to Appendix 1 at the end of this document.

Additionally, the moisture influence on the thermal conductivity of a wet porous material can be determined through the following expression:

$$\lambda = \lambda_0 \left(1 + b \cdot w/\rho_{bulk}\right) = \lambda_0 \left(1 + b \cdot w_g\right) \tag{6.5}$$

where λ_0 $[\mathrm{W/(m \cdot K)}]$ is the thermal conductivity of the solid matrix, and b [–] is a material–dependent thermal conductivity supplement. The supplement b is commonly expressed as a percentage as well, so that it represents the fractional increase [in %] of the thermal conductivity per mass–% moisture content, i.e. moisture mass per unit mass of dry material × 100. Thermal conductivity has a minor dependence on temperature for normal environmental conditions and therefore its thermal dependency is disregarded. For detailed information about the thermal behaviour of porous building materials, the reader is referred to specialized literature, e.g. Cammerer (1995).

For practical applications, the thermal conductivity of porous materials is often given as a linear relationship based on experimental values determined for different moisture content conditions. For instance, an expression of the form $\lambda = A + B \cdot w$ has been extensively used in the literature to describe the thermal conductivity of brick (Hagentoft et al., 2003; Janssen et al., 2007; Defraeye et al., 2013). In the previous expression, the intercept $\lambda(w = 0)$ stands for the thermal conductivity of the dry material,

λ_0. In turn, the slope of the curve represents the increase in thermal conductivity per moisture content and according to Eq. (6.5) it must equal $\lambda_0 \cdot b/\rho_{bulk}$.

Temperature dependency of hygric parameters

The coefficient of thermal expansion of most building materials lies in the order of 1.0E–5 to 1.0E–6 $°C^{-1}$ for normal temperatures. Consequently, any volumetric change induced by temperature variations within the normal temperature range falls outside ordinary measurement capabilities (Feng & Janssen, 2016). Thus, it is generally accepted that open porosity, ϕ_o [–], and bulk density, ρ_{bulk} [kg/m^3], can be considered as constant for the range of temperatures of interest in this study (Salager et al., 2007). Moreover, once the volumetric variation of the porous solid matrix is disregarded, the influence of temperature on the saturation moisture content, w_{sat} [kg/m^3], stems solely from the water density, which has a weak dependency on temperature (see Appendix 1), with less than a 1.20 % decline between 0 °C and 50 °C. As a result, w_{sat} [kg/m^3] can be considered as a constant independent of temperature. In the present study, an analogous logic is followed for the definition of the capillary moisture content, w_{cap} [kg/m^3], which is considered a constant. However, it must be mentioned that a widely accepted theory to describe the relationship between w_{cap} and temperature is still lacking in the literature.

Apart from the saturation state boundaries, w_{cap} and w_{sat}, the equilibrium moisture content of unsaturated porous materials is dependent on the temperature. The thermal dependency of moisture storage implies a shift in the moisture storage function (sorption isotherm or water retention curve). This behaviour is expected since higher temperatures are associated with higher energy levels, which cause faster transport and release of water molecules (K. K. Hansen, 1986). For this reason, both adsorption and desorption curves corresponding to higher temperatures lie below the 'colder' isotherms (Pavlík et al., 2012). The thermal dependency of moisture storage can be expressed analytically through temperature–dependent fitting parameters. As an example, the original function proposed by Künzel (see Eq.(4.1)) can be rewritten as (Castellazzi et al., 2014):

$$w(\varphi) = w_{cap} \cdot \frac{\psi(T) - 1}{\psi(T) - \varphi} \cdot \varphi \tag{6.6}$$

where $\psi(T)$ [–] is a fitting parameter dependent on temperature. It is noted that ψ is inversely proportional to the temperature, i.e. ψ decreases with increasing temperature. The correlation between ψ and T must be established from experimental data. However, the influence of temperature on moisture storage has not been sufficiently studied and experimental data are still scarce in the literature. Nonetheless, the available information suggests a negligible temperature dependency for barely

hygroscopic materials, such as fired–clay brick (Feng & Janssen, 2016). For the sake of simplicity, the thermal effects on moisture storage are not considered in the simulations presented in this thesis.

The influence of temperature on vapour diffusion is partly considered through the water vapour permeability of still air, δ_a [kg/(m · s · Pa)], which was introduced in Chapter 3 and is recalled here:

$$\delta_a = \frac{2.31 \cdot 10^{-5}}{R_v \cdot T} \frac{p_0}{p} \left(\frac{T}{273.15} \right)^{1.81} \tag{6.7}$$

where $p_0 = 101325$ Pa is the standard atmospheric pressure, p [Pa] is the ambient barometric pressure, $R_v = 461.5$ J/(kg · K) is the universal gas constant for water vapour, and T [K] is the temperature.

Additionally, the saturation vapour pressure, $p_{v,sat}$ [Pa], is a non–linear function of temperature, as it was defined in Chapter 3:

$$p_{v,sat} = 610.7[\text{Pa}] \cdot 10^{7.5\left(\frac{T-273.15}{T-35.85}\right)} \tag{6.8}$$

The impact of temperature on the liquid transport term has been studied by different authors, in particular its effect on the water absorption coefficient, A_w [kg/(m^2 · s$^{0.5}$)], or sorptivity, $S = A_w/\rho_w$ [m/s$^{0.5}$], e.g. Gummerson et al. (1980), Guizzardi et al. (2016), Feng & Janssen (2016, 2017), Hanumanthu & Sarkar (2021). The reported results support the validity of the Lucas–Washburn law, which describes the water penetration depth x [m] after a period of time t [s] (Washburn, 1921):

$$x = \sqrt{\frac{\sigma\, r\, cos\, \theta}{2\, \eta}} \cdot \sqrt{t} \tag{6.9}$$

where σ [N/m] is the surface tension of water, r [m] is the equivalent hydraulic capillary radius, θ is the contact angle, and η [Pa · s] is the viscosity of water. The previous expression states that liquid water flow is influenced by a series of factors. In order to understand how variations of temperature affect the overall liquid flow, it is convenient to study the impact of temperature on each of those factors separately. First, assuming that the porous structure undergoes negligible changes due to thermal (or hygric) expansion, it is reasonable to assume a constant r. Moreover, temperature has only a slight impact on the contact angle θ (see Appendix 1), so its influence can be disregarded. Therefore, the remaining temperature–dependent parameters are the surface tension σ and the viscosity η. Finally, by comparing the definition of the capillary absorption coefficient with the Lucas–Washburn equation, it is possible to establish a relation of proportionality as suggested by (Gummerson et al., 1980):

$$A_w \propto \sqrt{\sigma/\eta} \tag{6.10}$$

Considering the previous relation, Feng & Janssen (2016) fitted tabulated values for σ and η (valid for temperatures between 0 °C and 50 °C) and established a linear model to describe the relationship between A_w and T:

$$A_w = k\sqrt{\sigma/\eta} = k\,[0.095(T - 273.15) + 6.566] \tag{6.11}$$

where k [$\mathrm{kg/m^{2.5}}$] is a microstructure–dependent but temperature–independent factor. As an example, these authors studied the absorption behaviour of different building materials under several temperature conditions and determined $k = 0.0059$ for brick ($A_w = 0.052$ at 22.5 °C). For cement mortars, Hanumanthu & Sarkar (2021) found $k = 0.0019$–0.0023 ($A_w = 0.016$–0.020 at 20 °C), whereas for NHL mortar, the data presented by Karagiannis et al. (2016) were reinterpreted by Feng & Janssen (2017), who established $k = 0.0125$ ($A_w = 0.106$ at 20 °C).

6.1.3 Initial and boundary conditions

The hygrothermal model is completed by introducing the initial and boundary conditions. The Dirichlet boundary condition yields:

$$T = \bar{T} \tag{6.12}$$

$$\varphi = \bar{\varphi} \tag{6.13}$$

where $\bar{T}$ [K] and $\bar{\varphi}$ [–] are the prescribed temperature and relative humidity at the boundary, respectively.

Conversely, the Neumann boundary condition is defined as a flux derived from a temperature or vapour pressure difference, such as:

$$q = h_T(T - T_{ext}) \tag{6.14}$$

$$g = h_m\left(p_v - p_{v,ext}\right) \tag{6.15}$$

where q [$\mathrm{W/m^2}$] is the convective heat flux, h_T [$\mathrm{W/(m^2 \cdot K)}$] the heat transfer coefficient, T_{ext} [K] is the temperature of the environment and T [K] is the temperature at the boundary, g [$\mathrm{kg/(m^2 \cdot s)}$] is the convective moisture flux, h_m [s/m] is the convective mass transfer coefficient, $p_{v,ext}$ [Pa] and p_v [Pa] are the partial vapour pressures defined for the environment and at the boundary, respectively. In the present work, h_T accounts for the combined effects of convection and long–wave radiation exchanges with the environment. Thus, this lumped convective/radiative heat transfer coefficient is defined as:

$$h_T = h_{T,c} + h_{T,r} \tag{6.16}$$

where $h_{T,c}$ [$\mathrm{W/(m^2 \cdot K)}$] is the convective heat transfer coefficient, and $h_{T,r}$ [$\mathrm{W/(m^2 \cdot K)}$] is the radiative heat transfer coefficient. The heat transfer coefficient is dependent on the local air flow conditions, the temperature, the geometry and the orientation of the studied element, which makes an accurate estimation significantly complex. For building applications, a simplified approach is usually adopted, and the heat transfer coefficient is assumed to be constant (Künzel, 1995).

6.2 HYGROTHERMAL SIMULATIONS OF A BRICK MASONRY WALL

In this section, the model described in the previous paragraphs is used to simulate the hygrothermal behaviour of a brick masonry wall. First, the main features of the numerical model are described: geometry, material properties and boundary conditions. Then, two sets of analyses are performed, namely steady–state and time–dependent or transient analyses. Finally, the results of the simulations are presented in terms of temperature and relative humidity profiles, and the obtained trends are discussed.

Like the moisture transport simulations presented in Chapter 5, the analyses described in the following paragraphs are based on the finite element method and were performed using the software COMSOL Multiphysics (COMSOL, 2021).

6.2.1 Description of the numerical model

A common type of load–bearing masonry wall was selected as a case study to perform the hygrothermal simulations. In particular, the chosen wall is made up of bricks with dimensions 205 mm × 95 mm × 50 mm, and mortar joints 15 mm thick. The resulting structure is a 315 mm thick (three–wythe brick) masonry wall with a total height of 2650 mm. The geometrical configuration of the wall is depicted in Figure 5.2. Finally, the described geometry was used to prepare a two–dimensional (2–D) model.

The material properties used for the hygrothermal simulations are presented in Table 2.2. Two types of mortar were considered for the analyses, namely natural hydraulic lime mortar (LMJ) and cement mortar (CM). Moreover, the brick–mortar interfaces were assumed to have perfect contact for heat transfer, whereas an imperfect contact was considered for moisture transport. Thus, a hydraulic resistance $R_{IF} = 2\mathrm{E}{+}9\ \mathrm{m/s}$ was assigned to the brick–mortar interfaces.

The wall is assumed located in Guimarães (Portugal), which has an annual average temperature $\vartheta = 13.5$ °C; and an annual average relative humidity $\mathrm{RH} = 74$ % (*Climate and Average Weather Year–Round in Guimarães, Portugal*, 2022). Furthermore, the wall is considered to have initial conditions equal to these yearly average values, thus $\vartheta_0 = 13.5$ °C and $\varphi_0 = 0.74$. One face of the wall is exposed to the exterior, whereas the opposite face is in contact with a conditioned interior space with constant temperature and relative humidity, respectively 20 °C and 50 % RH. It must be noted that the presented

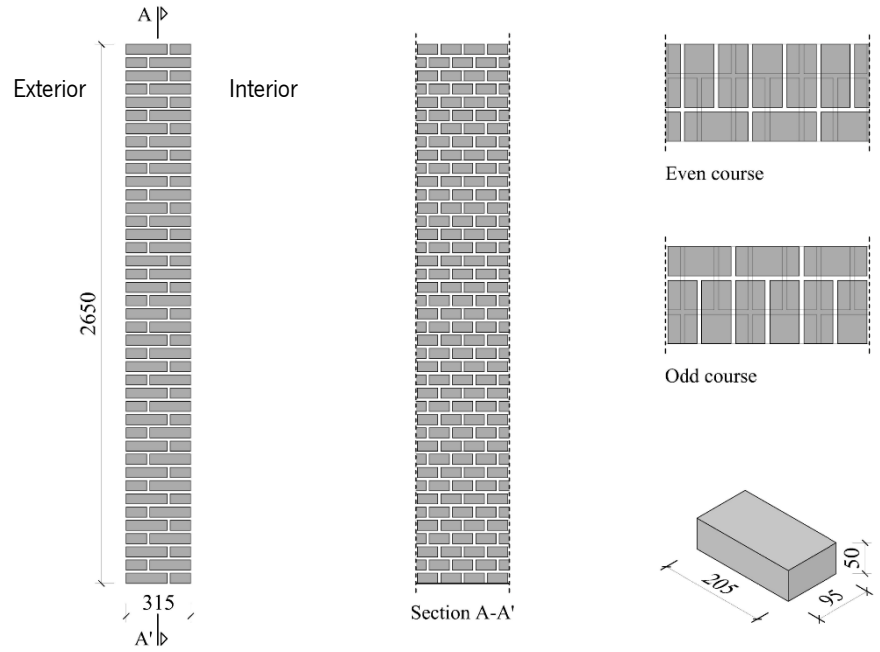

Figure 6.1. Schematic geometrical configuration of the brick masonry wall: (a) transversal cross–section; (b) vertical cross–section; (c) bond arrangement and brick blocks geometry. Dimensions in mm.

configuration is rather unusual for a building envelope in contact with a modern habitable interior space since it lacks any type of dedicated moisture barrier or thermal insulation. Nonetheless, this configuration is expedient for the analyses at hand, in which thermal and moisture gradients are of interest. In the case of a masonry wall with good insulation on the interior side, adiabatic boundary conditions could be assumed for the internal face.

Table 6.1. Summary of material properties used for the hygrothermal simulations.

Material	Property	Symbol	Value	Units	Source
B	Bulk density	ρ_{bulk}	1900	$\mathrm{kg/m^3}$	Experimental
	Open porosity	ϕ_o	0.280	–	Experimental
	Capillary moisture content	w_{cap}	240	$\mathrm{kg/m^3}$	Experimental
	Fitting parameter for sorption isotherm	ψ	1.0070	–	Experimental
	Water absorption coefficient (∥ bed face)	$A_{w,\parallel}$	0.104	$\mathrm{kg/(m^2 \cdot s^{0.5})}$	Experimental
	Water absorption coefficient (⊥ bed face)	$A_{w,\perp}$	0.075	$\mathrm{kg/(m^2 \cdot s^{0.5})}$	Experimental
	Water vapour resistance factor	μ	34.14	–	Experimental
	Specific heat capacity	C_p	825	$\mathrm{J/(kg \cdot K)}$	Kočí et al. (2018)
	Thermal conductivity	λ_0	0.59	$\mathrm{W/(m \cdot K)}$	Kočí et al. (2018)
	Thermal conductivity supplement	b	12.74	–	Kočí et al. (2018)

Table 6.1 (Continued). Summary of material properties used for the hygrothermal simulations.

Material	Property	Symbol	Value	Units	Source
LMJ	Bulk density	ρ_{bulk}	2060	$\mathrm{kg/m^3}$	Experimental
	Open porosity	ϕ_o	0.230	–	Experimental
	Capillary moisture content	w_{cap}	190	$\mathrm{kg/m^3}$	Experimental
	Fitting parameter for adsorption isotherm	a_{ads}	3.80E–6	$1/\mathrm{Pa}$	Experimental
		m_{ads}	0.352	–	Experimental
	Fitting parameter for desorption isotherm	a_{des}	1.19E–5	$1/\mathrm{Pa}$	Experimental
		m_{des}	0.235	–	Experimental
	Water absorption coefficient (isotropic)	$A_{w,ISO}$	0.080	$\mathrm{kg/(m^2 \cdot s^{0.5})}$	Experimental
	Water vapour resistance factor	μ	15.00	–	Prangnell (1971)
	Specific heat capacity	C_p	840	$\mathrm{J/(kg \cdot K)}$	Kumaran (1996)
	Thermal conductivity	λ_0	0.85	$\mathrm{W/(m \cdot K)}$	Kumaran (1996)
	Thermal conductivity supplement	b	9.53	–	Kumaran (1996)
CM	Bulk density	ρ_{bulk}	2000	$\mathrm{kg/m^3}$	Experimental
	Open porosity	ϕ_o	0.210	–	Experimental
	Capillary moisture content	w_{cap}	180	$\mathrm{kg/m^3}$	Experimental
	Fitting parameter for adsorption isotherm	a_{ads}	1.43E–6	$1/\mathrm{Pa}$	Experimental
		m_{ads}	0.285	–	Experimental
	Fitting parameter for desorption isotherm	a_{des}	2.51E–5	$1/\mathrm{Pa}$	Experimental
		m_{des}	0.213	–	Experimental
	Water absorption coefficient (isotropic)	$A_{w,ISO}$	0.060	$\mathrm{kg/(m^2 \cdot s^{0.5})}$	Experimental
	Water vapour resistance factor	μ	25.00	–	Prangnell (1971)
	Specific heat capacity	C_p	932	$\mathrm{J/(kg \cdot K)}$	Kumaran (1996)
	Thermal conductivity	λ_0	1.72	$\mathrm{W/(m \cdot K)}$	Kumaran (1996)
	Thermal conductivity supplement	b	9.29	–	Kumaran (1996)

The hygrothermal simulations were performed through both steady–state (SS) and time–dependent (TD) analyses. The SS analysis was used to evaluate the final hygrothermal equilibrium attained by the wall considering constant environmental conditions as explained in the previous paragraph. Moreover, two sets of time–dependent analyses were defined. In particular, TD1 was performed to evaluate the evolution of temperature and relative humidity profiles across the wall from the initial state to hygrothermal equilibrium with the environment. Therefore, the final stage of TD1 is analogous to the results obtained with the stationary analysis SS. Additionally, the transient study TD2 considered the wall already in

equilibrium with the environment (the initial conditions were taken from the results of SS or the final stage of TD1) and then imposed variable external conditions. In particular, the external conditions for TD2 were assumed to vary with time following a sinusoidal law such as:

$$\vartheta(t) = 13.5 + 10 \cdot \cos(2\pi t - \pi/2) \tag{6.17}$$

$$\varphi(t) = 0.74 + 0.12 \cdot \cos(2\pi t + \pi/2) \tag{6.18}$$

for the external temperature and relative humidity, respectively, with t expressed in days. The proposed thermal variation corresponds to the average maximum temperature excursion that can be experienced in a single day during mid–season periods, i.e. $\Delta\vartheta \approx 20$ °C. Additionally, average values of the seasonal relative humidity were selected to determine the range of daily moisture variation and the corresponding sinusoidal function was set to follow an opposite trend to the one defined for temperature.

The initial and boundary conditions used for the hygrothermal simulations of the masonry wall are summarised in Table 6.2. Neumann boundary conditions were imposed on the external and internal faces of the wall. Therefore, heat and moisture fluxes were defined with commonly accepted values for the convective transfer coefficients. In particular, heat transfer coefficients $h_{T,ext} = 25\ \mathrm{W/(m^2 \cdot K)}$ and $h_{T,int} = 8\ \mathrm{W/(m^2 \cdot K)}$ were imposed at the external and internal faces, respectively (Hagentoft et al., 2004). It is noted that the heat transfer coefficient selected for the external surface already takes into account the radiative contribution. On the other hand, convective mass transfer coefficients $h_{m,ext} = 2.0\mathrm{E{-}7\ s/m}$ and $h_{m,int} = 3.0\mathrm{E{-}8\ s/m}$ were considered for the external and the internal faces of the wall, respectively (Hagentoft et al., 2004).

Table 6.2. Summary of the initial and boundary conditions used for the hygrothermal simulations.

Analysis	Initial conditions		Exterior boundary conditions				Interior boundary conditions			
	ϑ_0 [°C]	φ_o [–]	ϑ_{ext} [°C]	$h_{T,ext}$ [W/(m² K)]	φ_{ext} [–]	$h_{m,ext}$ [s/m]	ϑ_{int} [°C]	$h_{T,int}$ [W/(m² K)]	φ_{int} [–]	$h_{m,int}$ [s/m]
SS	13.5	0.74	13.5	25	0.74	2.0E–7	20.0	8	0.50	3.0E–8
TD1	13.5	0.74	13.5	25	0.74	2.0E–7	20.0	8	0.50	3.0E–8
TD2	SS results (1)	SS results (1)	Eq. (6.17)	25	Eq. (6.18)	2.0E–7	20.0	8	0.50	3.0E–8

(1) Analogous to the final stage of TD1

Two–dimensional quadrilateral elements with quadratic shape functions were used for the discretization of the models. After preliminary sensitivity analyses to determine the optimal mesh size, the average element size was set to 5 mm. The primary variables, namely temperature and relative humidity, were

interpolated based on standard Lagrangian shape functions. Moreover, the backward finite difference method was used for automatic time discretization during the transient analyses. Finally, an iterative procedure based on the Newton–Raphson method was applied to solve the non–linear differential equations.

6.2.2 Hygrothermal behaviour of a brick masonry wall

The results of the hygrothermal analyses presented in the previous section are examined in this sub–section. First, the steady–state case is discussed, with special emphasis on the temperature and moisture content distributions obtained for the average environmental conditions. Subsequently, the time–dependent studies are analysed, and the obtained results are assessed in terms of temperature and moisture content evolution across the wall and for different points of the external and internal surfaces. For each group of analyses, a distinction is made between the brick masonry wall with lime mortar (LMJ) and the one with cement mortar (CM).

Steady–state analysis (SS)

The temperature and relative humidity profiles obtained for the steady–state analyses are shown in Figure 5.3 and Figure 6.3, respectively. The results show only minor differences between the two studied cases, namely the wall with lime mortar (LMJ) and the wall with cement mortar (CM). This is expected considering that the stationary analysis focuses on the final equilibrium state, which is mostly dependent on the external boundary conditions. Moreover, any difference observed in the response of the wall stems from the different behaviour of the selected type of mortar, which ultimately accounts for less than 26 % of the total cross–sectional area.

It is noted that the temperature and relative humidity values obtained at the external and internal surfaces do not reach the values defined for the boundary conditions, namely 13.5 °C and 74 % RH for the exterior, and 20 °C and 50 % RH for the interior. This is due to the kind of boundary conditions imposed on the model, i.e. convective flux or Neumann boundary conditions. Therefore, the convective heat transfer and the convective mass transfer coefficients induce, respectively, a temperature and a relative humidity exchange between the environment and the surface of the wall.

Regarding the thermal field (see Figure 5.3), the temperature profiles for both cases show an overall linear distribution across the thickness of the wall. In a multi–layered material, the transition between adjacent layers with dissimilar thermal conductivity translates into a change of slope in the temperature profile before and after the interface. For the LMJ case, the presence of mortar joints is barely noticeable since the thermal conductivity properties of bricks and lime mortar are quite similar. On the contrary, the

presence of joints is clearer for the CM case due to the more dissimilar thermal conductivity of bricks and cement mortar. Therefore, for the CM case, it is possible to perceive slight changes in the slope of the temperature profiles at the location of the vertical head joints.

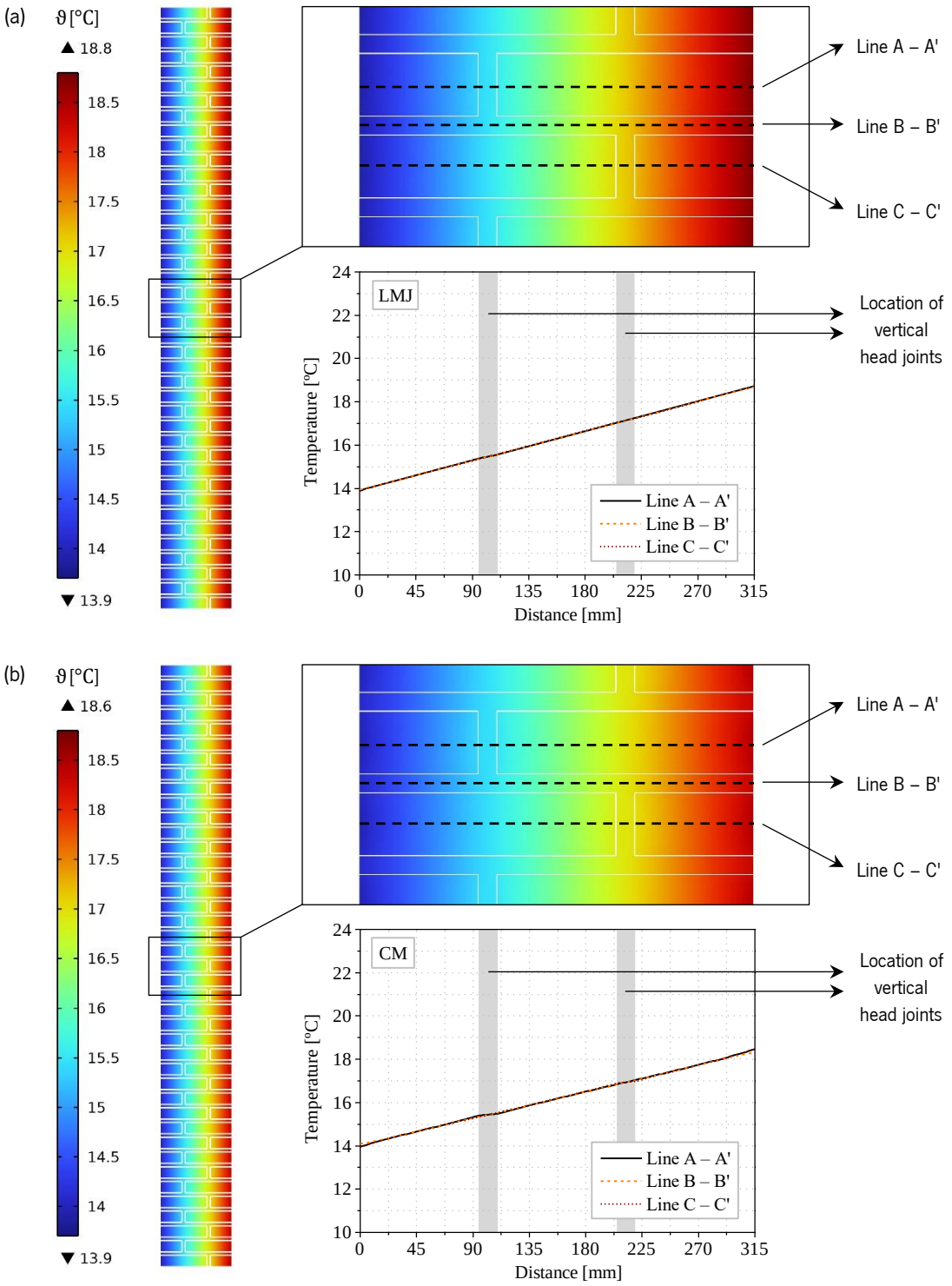

Figure 6.2. Steady–state analysis (SS). Temperature distribution across the studied three–wythe brick masonry wall: (a) joints with natural hydraulic lime mortar (LMJ); (b) joints with cement mortar (CM).

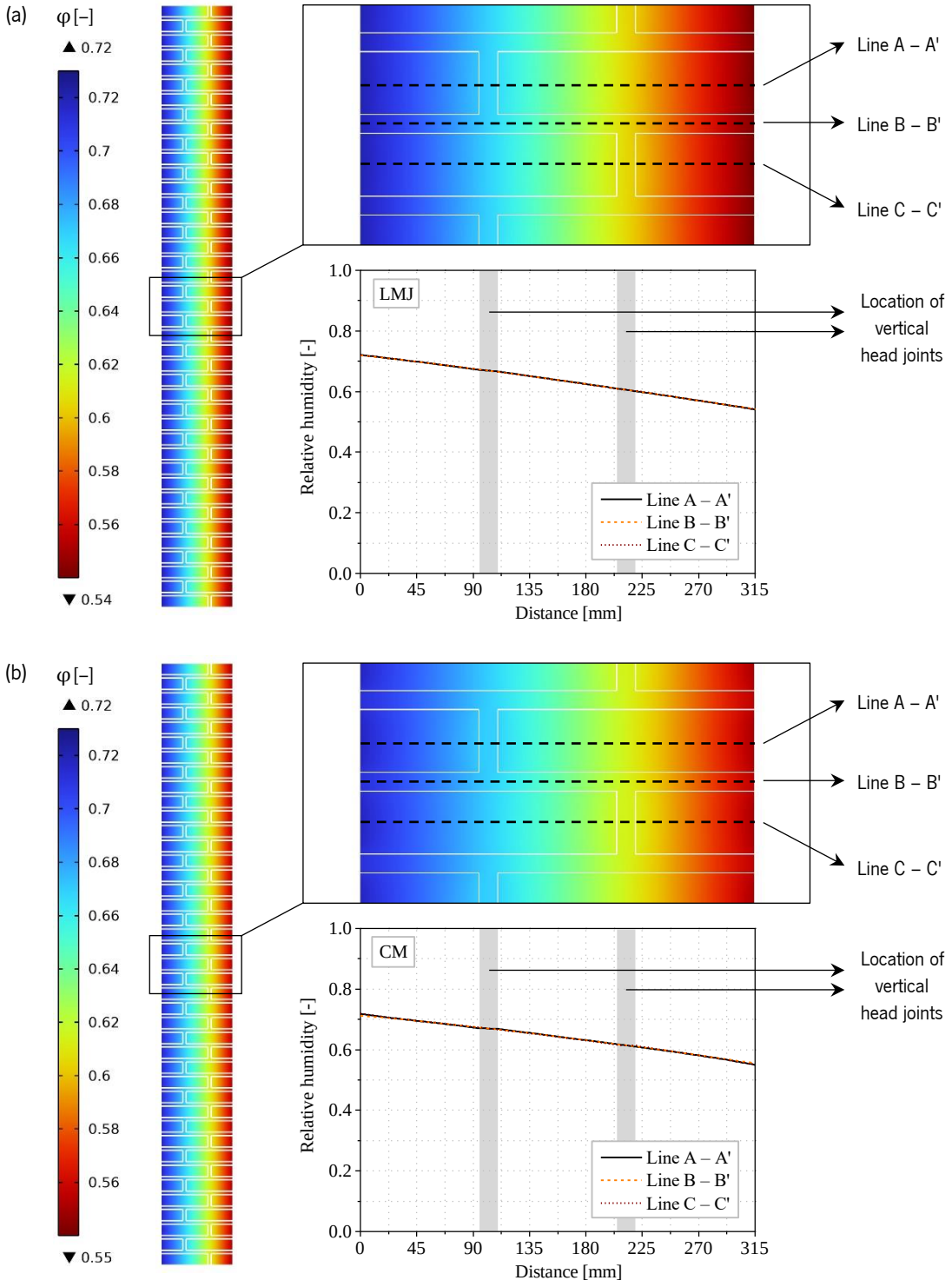

Figure 6.3. Steady–state analysis (SS). Relative humidity distribution across the studied three–wythe brick masonry wall: (a) joints with natural hydraulic lime mortar (LMJ); (b) joints with cement mortar (CM).

Regarding the hygric response (see Figure 6.3), the relative humidity profiles for both models show a nearly linear distribution between the two faces of the wall. Similarly, slight disturbances in the moisture profiles reveal the presence of mortar joints. It is noted that the CM case shows a somewhat less linear trend and slightly higher values of relative humidity across the wall thickness. Moreover, the presence of

vertical head joints is clearer for the CM case as well. These aspects can be explained by the marked hygroscopic nature of cement mortar, which contrasts with the less hygroscopic behaviour of lime mortar and the barely hygroscopic behaviour of bricks.

Considering the results of the hygrothermal steady–state analysis, rather homogenous temperature and moisture distributions are obtained for the studied wall configuration. Moreover, the differences between the two types of mortar are not significant. Thus, it is concluded that a macro–modelling approach with equivalent masonry properties (see Section 5.4) would be expedient. It is recalled that this simulation methodology implies lesser material and geometrical complexity, with an associated reduction of the computational cost. Furthermore, the simplification to a 1–D type of analysis would be appropriate as well.

Time–dependent analysis with constant boundary conditions (TD1)

The previous section dealt with the steady–state equilibrium attained by the studied three–wythe brick masonry wall considering an environment with constant boundary conditions. In this section, the first group of time–dependent analyses, labelled TD1, focuses on the process required for the wall to reach the same state of hygrothermal equilibrium.

Considering the TD1 results, the evolution of temperature and relative humidity profiles is shown in Figure 6.4 and Figure 6.5, respectively. It is worth noting the time difference needed for both processes to reach equilibrium. On one hand, the thermal field attains the steady–state equilibrium in about 60 hours. Conversely, moisture transport is a much slower process and hygric equilibrium is only attained after 450 days (more than 10000 hours). Taking this into account, heat transfer can be treated as an immediate process in comparison with mass transport. Furthermore, it is possible to conclude that a real structure will not likely attain a full hygric equilibrium considering the usual variability of environmental conditions and the long time required for the materials to accommodate the moisture processes.

There are some differences between the wall with lime mortar (LMJ) and the one with cement mortar (CM). On one hand, the temperature evolution is faster for the CM case. In other words, the wall with cement mortar requires less time to reach thermal equilibrium. This is consistent with the higher thermal conductivity of cement mortar in comparison with lime. Conversely, the relative humidity evolution is slower for the CM case. This can be explained by the transport properties as well: cement mortar has lower liquid diffusivity and higher water vapour resistance than its lime counterpart.

As it was pointed out in the SS analysis, the presence of mortar joints can be distinguished by slope changes in the temperature and relative humidity profiles at the location of the brick–mortar interfaces.

It is noted that the TD1 results for the CM case show the location of the vertical head joints more evidently. Once again, this can be explained by the more dissimilar properties between bricks and cement mortar in comparison with lime mortar.

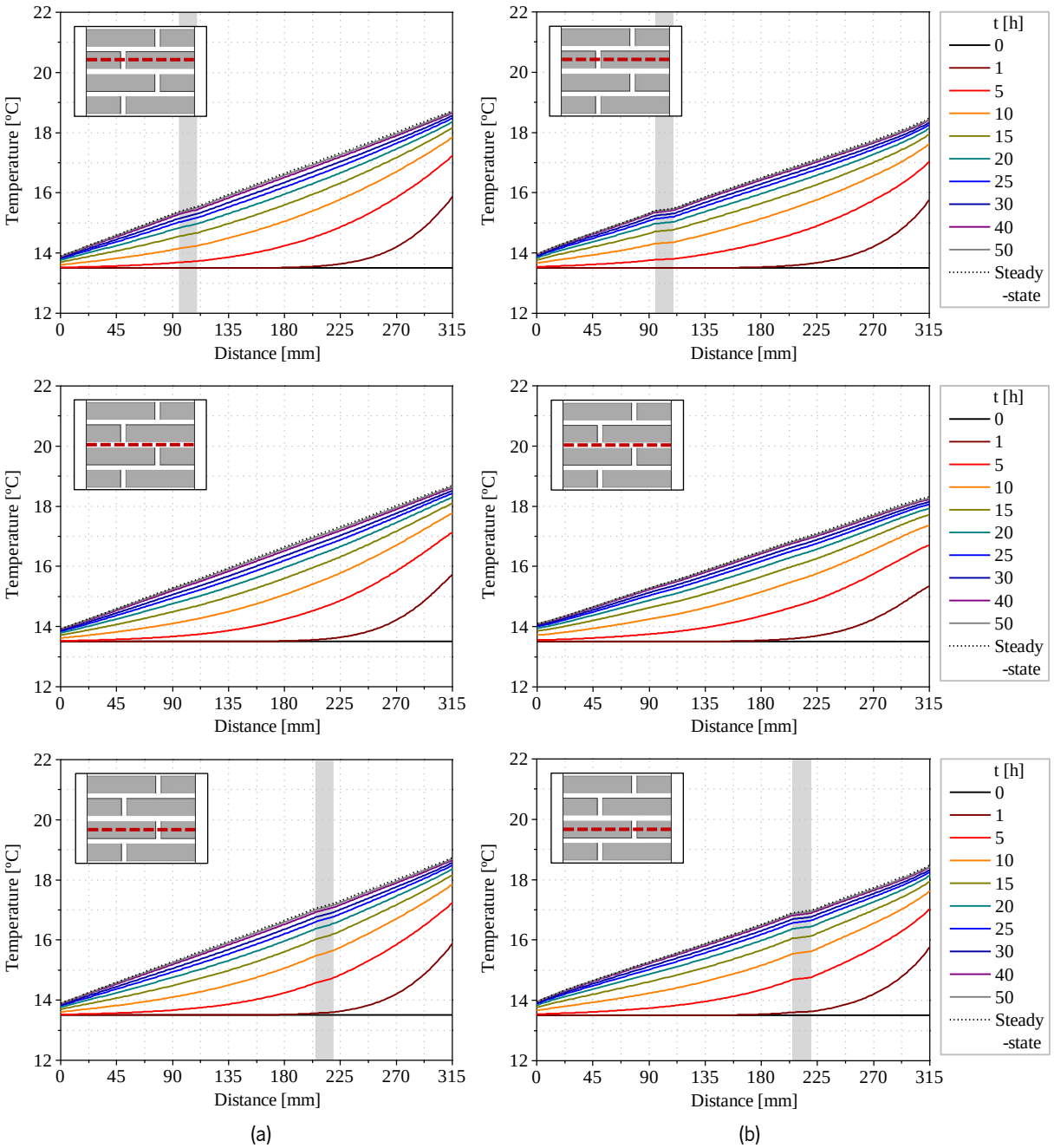

Figure 6.4. Time–dependent analysis (TD1). Temperature evolution across the studied three–wythe brick masonry wall: (a) joints with natural hydraulic lime mortar (LMJ); (b) joints with cement mortar (CM).

Besides the previous analyses, a parametric study was performed in order to evaluate the influence of the hydraulic resistance on the evolution of relative humidity. In particular, different values of the interface resistance, R_{IF}, were implemented but the results did not show significant differences. Therefore, it was

concluded that the impact of the interface resistance is not significant for the moisture conditions considered in this problem. It must be pointed out, however, that the hydraulic resistance may become non–negligible for higher moisture levels.

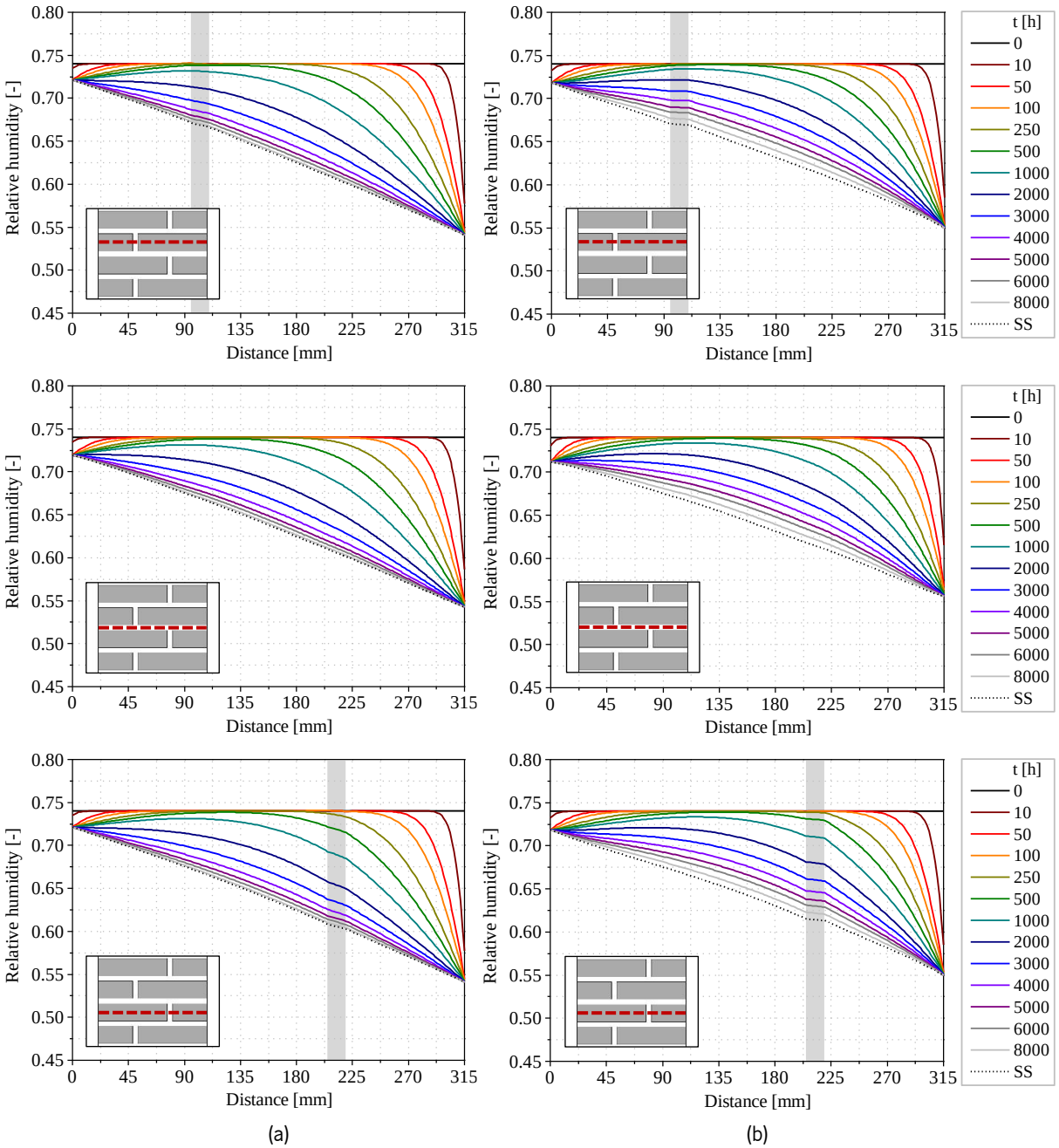

Figure 6.5. Time–dependent analysis (TD1). Evolution of the relative humidity across the studied three–wythe brick masonry wall: (a) joints with natural hydraulic lime mortar (LMJ); (b) joints with cement mortar (CM).

Considering the results of the time–dependent analysis TD1, for each case (LMJ and CM) only slight differences are noticed between the three studied sections of the wall. Therefore, a macro–modelling simulation with equivalent masonry properties (see Section 5.4) could be used to reproduce the observed

temperature and moisture content evolution. Notwithstanding the loss of detail, a simplified 1–D model could be considered as well with minor impact on the overall accuracy.

Time–dependent analysis with variable external boundary conditions (TD2)

For the second group of time–dependent analyses, labelled TD2, the steady–state equilibrium (resulting from the SS analysis or the final stage of TD1) is taken as the initial condition of the wall. Moreover, the sinusoidal expressions for variable temperature and relative humidity described in Eq. (6.18) and Eq. (6.19) are implemented so that the effect of time–dependent boundary conditions can be studied.

The results of the time–dependent analysis with variable boundary conditions, TD2, are shown in Figure 6.6 and Figure 6.7, in terms of temperature and relative humidity variations, respectively. Note that the corresponding graphs show the imposed boundary conditions together with the response obtained for different points on the external and internal faces of the wall.

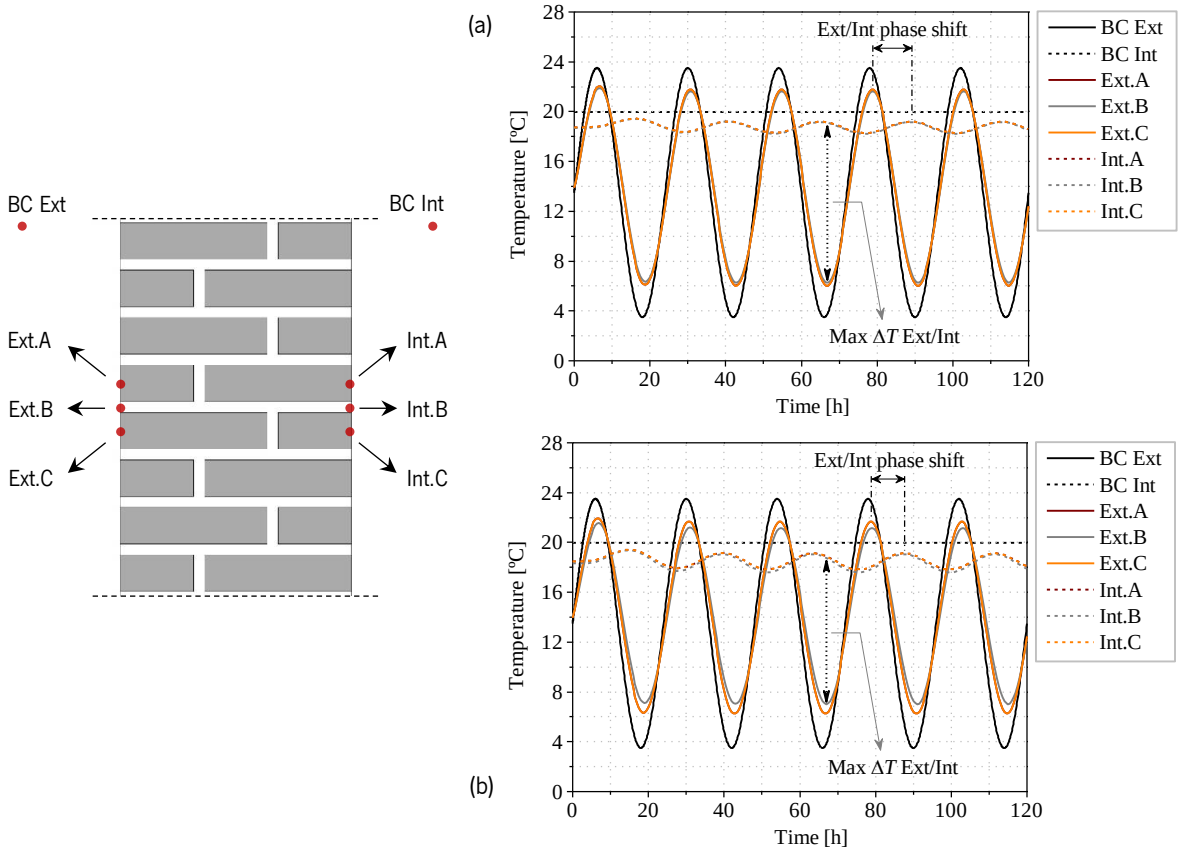

Figure 6.6. Time–dependent analysis with variable external boundary conditions (TD2). Temperature evolution for different points of the studied three–wythe brick masonry wall: (a) joints with natural hydraulic lime mortar (LMJ); (b) joints with cement mortar (CM).

Considering the thermal response (see Figure 6.6), there are some discrepancies between the wall with lime mortar (LMJ) and the one with cement mortar (CM). In particular, the thermal properties of bricks

and lime mortar are rather similar, thus the obtained trends show comparable temperature values for the selected points on each side of the wall. Conversely, for the CM case, the results show different temperatures for the points located on mortar joints and brick surfaces. Moreover, the thermal excursion on the external side of the wall is similar in both cases. However, the temperature variation range for the CM case is slightly greater on the internal face. This can be explained by the higher conductivity of cement mortar. It is noted that the temperature on the outer surface shows a phase shift with respect to the external input. There is an additional shift between the external and the internal faces of the wall. In particular, the maximum and minimum temperature values are detected on the internal surface around 9–10 hours later with respect to the peak values on the outer surface. The external/internal delay is shorter for the CM case, which can be related to the higher thermal conductivity of cement mortar mentioned above.

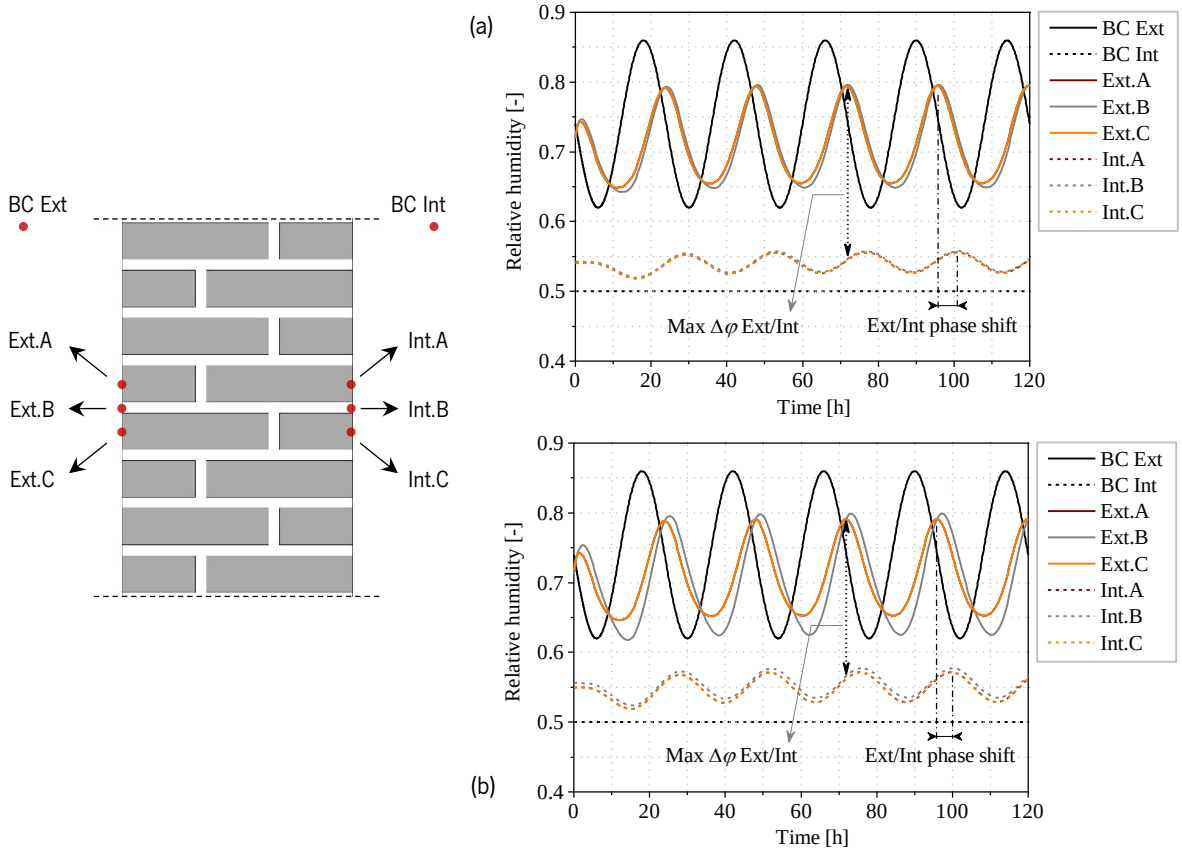

Figure 6.7. Time–dependent analysis with variable external boundary conditions (TD2). Evolution of the relative humidity for different points of the studied three–wythe brick masonry wall: (a) joints with natural hydraulic lime mortar (LMJ); (b) joints with cement mortar (CM).

Concerning the moisture response (see Figure 6.7), there are considerable differences between the two studied cases. In particular, the relative humidity values obtained for the LMJ case show only small

disparities between the external points on mortar joints and brick surfaces. On the contrary, for the CM case, the results show significant differences between the relative humidity values obtained for the points depending on their location. Furthermore, the relative humidity variation on the external side of the wall is greater for the cement mortar joints. In this context, the slower moisture response of the cement mortar (lower liquid diffusivity and water vapour permeability) can explain the greater and more shifted relative humidity excursion obtained for the mortar joints on the exterior surface. On the internal face, the CM case also shows a wider relative humidity range. At this point, it must be noted that for any of the cases, the moisture response obtained for the internal face is directly related to the temperature variation, which affects the relative humidity through the saturation vapour pressure, such as $\varphi = p_v/p_{v,sat}(T)$. There is a significant delay between the external boundary condition and the moisture evolution on the external surface. It can be observed that the shift between the imposed conditions and the response of the external face of the wall is greater for moisture than for temperature. This is expected since mass transport is a slower process. Finally, there is an additional shift between the external and the internal faces of the wall. The external/internal shift is shorter for the CM case due to the shorter temperature delay mentioned before.

Additionally, a parametric study was performed for the time–dependent analysis TD2 in order to evaluate the role of the brick–mortar interface on the moisture response. Consequently, the same analysis was performed using higher and lower values of the hydraulic resistance. However, the results obtained with the new R_{IF} values did not show significant differences. Therefore, it was concluded that the impact of the hydraulic resistance is not significant for the boundary conditions considered in this problem. Nonetheless, it must be recalled that the influence of the interface may become non–negligible for higher moisture levels.

Independently of the studied case, the response of the wall stabilizes (dynamic equilibrium) after a couple of cycles. It is noted that external/internal phase delay entails temperature and relative humidity gradients higher than the ones expected if the shift was not considered and maximum and minimum values were occurring simultaneously at one and the other sides of the wall. In particular, the maximum thermal gradient obtained for the average temperatures between the two faces are $\Delta T = 13.0$ °C for the LMJ case and $\Delta T = 12.4$ °C for the CM case. In turn, the maximum moisture gradient obtained for the average relative humidity values between the two faces are $\Delta\varphi = 0.18$ for the LMJ case and $\Delta\varphi = 0.17$ for the CM case. Considering these aspects, a time–dependent analysis with variable boundary conditions may produce more severe scenarios and is therefore recommended for a better approximation of real environmental conditions.

Considering the results described in the previous paragraphs, it is evident that the hygrothermal behaviour of brick masonry walls depends to a great extent on the type of mortar. Considering the wall with natural hydraulic lime mortar (LMJ case), the temperature and relative humidity trends showed comparable values for the groups of studied points, independently of their location on brick or mortar joints. Therefore, this type of hygrothermal problem could be simulated for the LMJ case by means of a macro–modelling approach with an equivalent masonry material (see Section 5.4) or a simplified 1–D model with hardly any loss of information. Conversely, the wall with cement mortar (CM case) showed some differences in temperature and relative humidity depending on the material where the studied point was located. Thus, for the CM case, the macro–modelling approach or the reduction to a 1–D problem would entail a certain loss of detail and accuracy.

6.3 HYGRO–THERMO–MECHANICAL MODEL

This section presents the numerical model employed for hygro–thermo–mechanical analysis. The main hypotheses and simplifications previously explained for the hygrothermal models (see Section 6.1) are valid here as well. With respect to the structural mechanics field, a series of new assumptions must be introduced. First, the environmental loads induced by normal exposure conditions are not expected to cause damage (at least not in the short term). Thus, the materials are likely to behave within the linear elastic range and material non–linearity is disregarded. Moreover, materials and structural elements are considered to be in an undamaged initial state. Finally, infinitesimal strains and small deformations and rotations are assumed.

6.3.1 Coupling between heat, moisture and mechanical fields

The mechanical problem is linked to the thermal and moisture fields through the extended Duhamel–Neumann equation or total strain additive decomposition (Szekeres, 2014): the total strain can be divided into different components, namely mechanical strains, thermal strains and moisture–induced strains. This is based on the assumption of infinitesimal strains and small deformations and rotations, which is generally applicable to masonry structures (Ramézani & Jeong, 2011):

$$\varepsilon = \varepsilon_{elastic} + \varepsilon_{plastic} + \varepsilon_{thermal} + \varepsilon_{swelling} \tag{6.19}$$

The mechanical strains, $\varepsilon_{elastic}$ and $\varepsilon_{plastic}$, account for the effects caused by forces and moments, either in the elastic or inelastic ranges. On the other hand, the thermal and hygric strains are related to deformations caused by temperature and moisture variations, respectively.

The temperature–induced strain for an isotropic material is defined as:

$$\varepsilon_{thermal} = \alpha_T \, \Delta T = \alpha_T \left(T - T_{ref} \right) \tag{6.20}$$

where α_T is the coefficient of thermal expansion of the material and T_{ref} is the reference temperature at which the thermally induced strain is zero.

An analogous relation may be written for the moisture–induced strain:

$$\varepsilon_{swelling} = \alpha_h \, \Delta w_g = \alpha_h \left(w_g - w_{g,ref} \right) \tag{6.21}$$

where α_h is the coefficient of hygric expansion of the material, w_g [kg/kg] is the gravimetric moisture content, and $w_{g,ref}$ is the reference moisture content for which the moisture–induced strain is zero. Note that the moisture content may also appear as mass of absorbed water per volume of dry material, w [$\mathrm{kg/m^3}$]. In that case, if α_h is initially given in terms of gravimetric moisture content (dimensionless), it must be divided by the density of the material, ρ_{bulk} [$\mathrm{kg/m^3}$], to maintain the consistency of the units. Since the moisture content is dependent on the relative humidity by means of the moisture storage function, the moisture–induced strain is also a non–linear function of the relative humidity.

It is noted that the hygro–mechanical and thermo–mechanical coupling processes defined in this way involve a two–step procedure. First, the temperature and moisture profiles are obtained by means of the hygrothermal analysis. Subsequently, the temperature and moisture results are used as input for the mechanical problem. Consequently, the proposed model consists of a one–way or unidirectional type of coupling, that is, heat and moisture fields have an impact on each other, and the hygrothermal results are linked to the mechanical response, but the effects of the structural response on the temperature and moisture fields are not considered. Indeed, the development of stresses and strains within a porous material may affect the hygric and thermal responses. For instance, Carmeliet et al. (2013) studied the so–called mechano–sorptive behaviour of porous materials and concluded that the amount of moisture adsorbed by the material reduces as the specimens are subjected to higher compressive stresses. Additionally, the authors observed that the stress effect on the sorption behaviour is more pronounced for higher relative humidity values. However, these mechanically–induced effects are expected to be of minor importance for the stress limits considered in this work (Khoshbakht & Lin, 2010). Thus, a schematic diagram of the proposed HTM model is provided in Figure 6.8.

A direct influence of thermal variations on the mechanical properties of masonry materials can be considered negligible for the temperature range of interest in this study. On the contrary, the mechanical performance of porous materials is generally affected by moisture, which may lead to a reduction of the mechanical properties (Castellazzi, de Miranda, Formica, et al., 2015). Nonetheless, considering the lack

of specific research dedicated to the moisture–dependent mechanical behaviour of masonry materials, these aspects are neglected in the present study and further works on this topic are suggested.

Under the assumption of linear elasticity and the described one–way coupled problem, the temperature– and moisture–induced strains are directly proportional to the results of the hygrothermal problem by means of the thermal and hygric expansion coefficients.

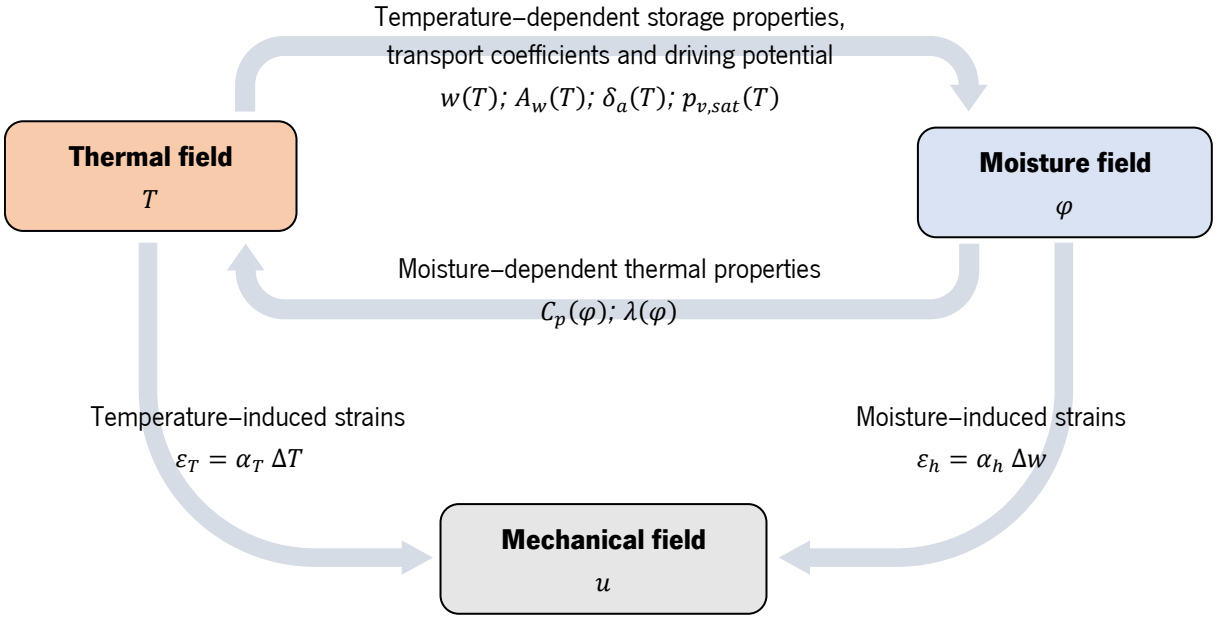

Figure 6.8. Schematic diagram of the one–way coupled hygro–thermo–mechanical model used in this study.

6.3.2 Initial and boundary conditions

As it has been discussed, the equilibrium state of a porous building material is intimately related to the surrounding environmental conditions. Specifically, temperature and moisture content increments cause material dilation, whereas shrinkage takes place when temperature and relative humidity decrease. Moreover, these material responses give rise to the appearance and evolution of internal stresses. It is worth noting that the stresses induced by thermal or hygric volumetric variations are necessarily associated with a deformation constraint. In other words, if deformations are not restrained, the material will experience a free dimensional change and internal stresses will not appear. Nonetheless, constraints always exist in real applications, usually linked to the external boundary conditions or the presence of interfaces. Therefore, internal stresses caused by temperature and moisture content variations are expected. In this context, the initial conditions of the system are usually assumed as the initial equilibrium state. Since they are associated with no internal deformations, the initial conditions are commonly known as free–strain or zero–strain conditions.

6.4 HYGRO–THERMO–MECHANICAL SIMULATIONS OF A BRICK MASONRY WALL

This section demonstrates the application of the hygro–thermo–mechanical (HTM) model using the previously introduced brick masonry wall as a case study. First, the description of the model is recalled, and the new parameters and boundary conditions needed for the mechanical component are defined. Then, the results of the HTM analyses are presented and discussed.

6.4.1 Description of the numerical model and boundary conditions

The same three–wythe brick masonry wall presented for the hygrothermal simulations was used for the HTM analyses (see description of the model in Section 6.2.1). Similarly, the physical, thermal, and hygric material properties presented in Table 2.2 were employed for the model definition. The newly added properties needed for the mechanical field are introduced in Table 6.3. It is noted that the numerical simulations presented in the following paragraphs were performed with a 2–D plane strain finite element model using the software COMSOL Multiphysics (COMSOL, 2021).

Two different scenarios were studied, namely a gravitational load case alone and a combined hygro–thermo–mechanical case. For the gravitational case, body forces were considered, including a uniformly distributed load, $L = 12.5\ \mathrm{kN/m}$, applied on top of the wall to simulate the weight of a simply supported roof. The HTM scenario was built upon the gravitational case so that the body forces were also included. Moreover, for the HTM case, the same temperature and moisture conditions defined for the time–dependent hygrothermal analysis TD2 (see Section 6.2.1) were imposed on the wall. It is recalled that the TD2 analysis considers an initial step for the wall to reach the steady–state equilibrium with the environment. In other words, the wall is already in a deformed configuration (initial conditions to steady–state equilibrium) before the application of the variable boundary conditions.

With regard to the mechanical boundary conditions, the bottom of the wall is assumed fixed, that is, all degrees of freedom are constrained. Conversely, the uppermost edge is not restrained, and all degrees of freedom remain free. The wall is assumed in a non–deformed configuration before the application of the gravitational and environmental loads. The initial temperature and relative humidity of the wall are $\vartheta_0 = 13.5\ ^\circ\mathrm{C}$ and $\varphi_0 = 0.74$, respectively. For these conditions, the temperature– and moisture–induced strains are zero.

Assuming the applicability of Saint Venant's principle, the following discussion focuses on a section of the mid–portion of the wall (height around $1.20\ \mathrm{m}$). In other words, the area selected for the study is reasonably distant from any applied load or boundary condition that could directly influence the local stress/strain distribution.

Table 6.3. Summary of mechanical, thermo–mechanical and hygro–mechanical properties used for the simulations.

Material	Property	Symbol	Value or expression	Units	Source
B	Young's modulus	E	5580	MPa	Ghiassi et al. (2013)
	Poisson's ratio	ν	0.20	–	Ghiassi et al. (2013)
	Compressive strength	f_c	19.80	MPa	Ghiassi et al. (2013)
	Tensile strength	f_t	2.00	MPa	Ghiassi et al. (2013)
	Coefficient of thermal expansion	α_T	2.56E–6	1/°C	Experimental
	Coefficient of hygric expansion	α_h	$1.40E{-}4/w_g{}^{0.72}$	–	Experimental
LMJ	Young's modulus	E	3330	MPa	Penas et al. (2008)
	Poisson's ratio	ν	0.20	–	Penas et al. (2008)
	Compressive strength	f_c	1.10	MPa	Penas et al. (2008)
	Flexural strength	f_b	0.40	MPa	Penas et al. (2008)
	Coefficient of thermal expansion	α_T	3.04E–6	1/°C	Experimental (1)
	Coefficient of hygric expansion	α_h	$3.00E{-}4/w_g{}^{0.62}$	–	Experimental (1)
CM	Young's modulus	E	2370	MPa	D'Altri et al. (2018)
	Poisson's ratio	ν	0.20	–	D'Altri et al. (2018)
	Compressive strength	f_c	8.20	MPa	D'Altri et al. (2018)
	Tensile strength	f_t	1.50	MPa	D'Altri et al. (2018)
	Coefficient of thermal expansion	α_T	7.38E–6	1/°C	Experimental
	Coefficient of hygric expansion	α_h	$1.32E{-}4/w_g{}^{0.78}$	–	Experimental

(1) Taken from moulded lime mortar (LM)

6.4.2 Hygro–thermo–mechanical behaviour of a brick masonry wall

The results of the HTM model presented in the previous section are examined in the following paragraphs. In particular, the behaviour of the wall is studied in terms of minimum and maximum principal stresses, σ_3 and σ_1, according to the type of material and case scenario. The general sign convention is followed, thus negative stresses indicate compression, and positive stresses denote tension. For the HTM analyses, the moment with maximum induced deformation (maximum horizontal displacement of the top of the wall) is chosen for the study. The selected deformed state is shown in Figure 6.9 and Figure 6.10 for the LMJ and the CM cases, respectively, together with the history of displacements for the top of the wall and the imposed boundary conditions. It is recalled that the discussion is focused solely on a selected mid–height section of the wall.

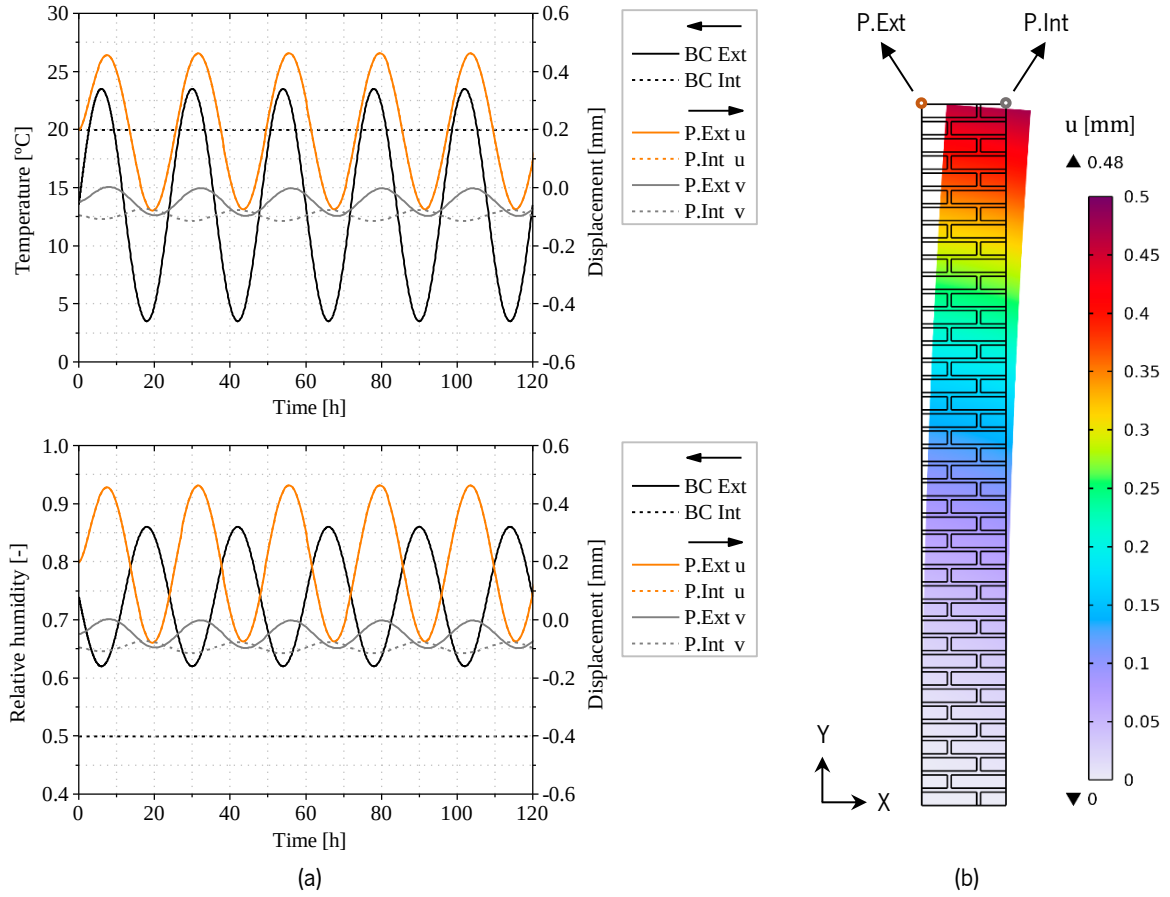

Figure 6.9. Hygro–thermo–mechanical analysis of the three–wythe brick masonry wall with natural hydraulic lime mortar: (a) imposed boundary conditions and displacement history measured at the top of the wall; (b) deformed shape selected for the study (maximum horizontal displacement).

Considering the displacement history for the LMJ case (Figure 6.9), it is possible to observe the initial deformed configuration of the wall before the application of the variable external boundary conditions. In particular, the wall presents a horizontal displacement towards the interior caused by moisture shrinkage of the internal face ($\varphi_{int} = 0.50 < \varphi_0 = 0.74$), which prevails over thermal dilation ($\vartheta_{int} = 20$ °C > $\vartheta_0 = 13.5$ °C). On the other hand, the vertical displacement is rather small and remains always below 0.1 mm during the duration of the analysis. When the variable boundary conditions are implemented, the wall oscillates following the sinusoidal trend of the external temperature and relative humidity. In fact, the maximum horizontal displacement occurs with some delay after the external temperature peak (overall thermal expansion with greater dilation of the exterior face, i.e. $\vartheta_{ext} > \vartheta_{int} > \vartheta_0$) and after the minimum value of the external relative humidity (general shrinkage of the wall still more prominent on the internal face, i.e. $\varphi_{int} < \varphi_{ext} < \varphi_0$).

The displacements obtained for the wall with cement mortar (Figure 6.10) follow the same trends described above for the LMJ case. However, the CM case shows larger deformations. This is expected

considering the higher thermal expansion and hygric expansion coefficients of cement with respect to the lime mortar.

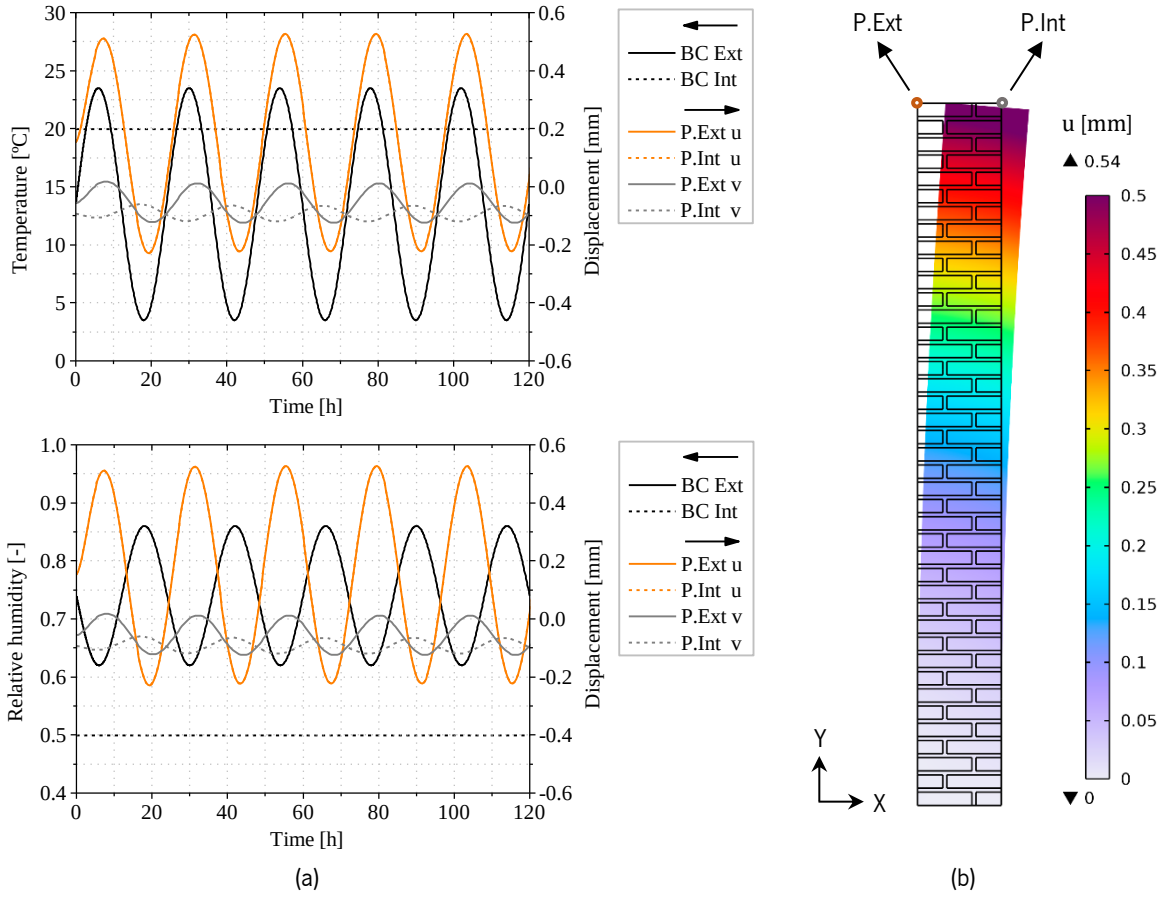

Figure 6.10. Hygro–thermo–mechanical analysis of the three–wythe brick masonry wall with cement mortar: (a) imposed boundary conditions and displacement history measured at the top of the wall; (b) deformed shape selected for the study (maximum horizontal displacement).

The stress state obtained for the LMJ case under the self–weight condition (body force + roof weight) is shown in Figure 6.11. As expected, the distribution of minimum principal stresses (Figure 6.11a and Figure 6.11b) reveals a uniform level of compression in bricks and bed mortar joints, around –0.09 MPa for the selected area (note that compression increases with wall depth). Conversely, a 2–D effect can be seen in the vertical head joints, which experience a lower compression level, around –0.06 MPa. A more detailed analysis of the stress distribution in bricks brings to light two aspects: (a) the compression stress is slightly lower, around –0.08 MPa, in the mid–section of the header course bricks, that is, the portion of the brick aligned with the vertical head joints; (b) higher compression values, ca. –0.10 MPa, are found on the vertical edges of the bricks adjacent to mortar head joints. Therefore, the brick–mortar interaction is associated with 2–D phenomena that affect the distribution of stresses within the masonry wall.

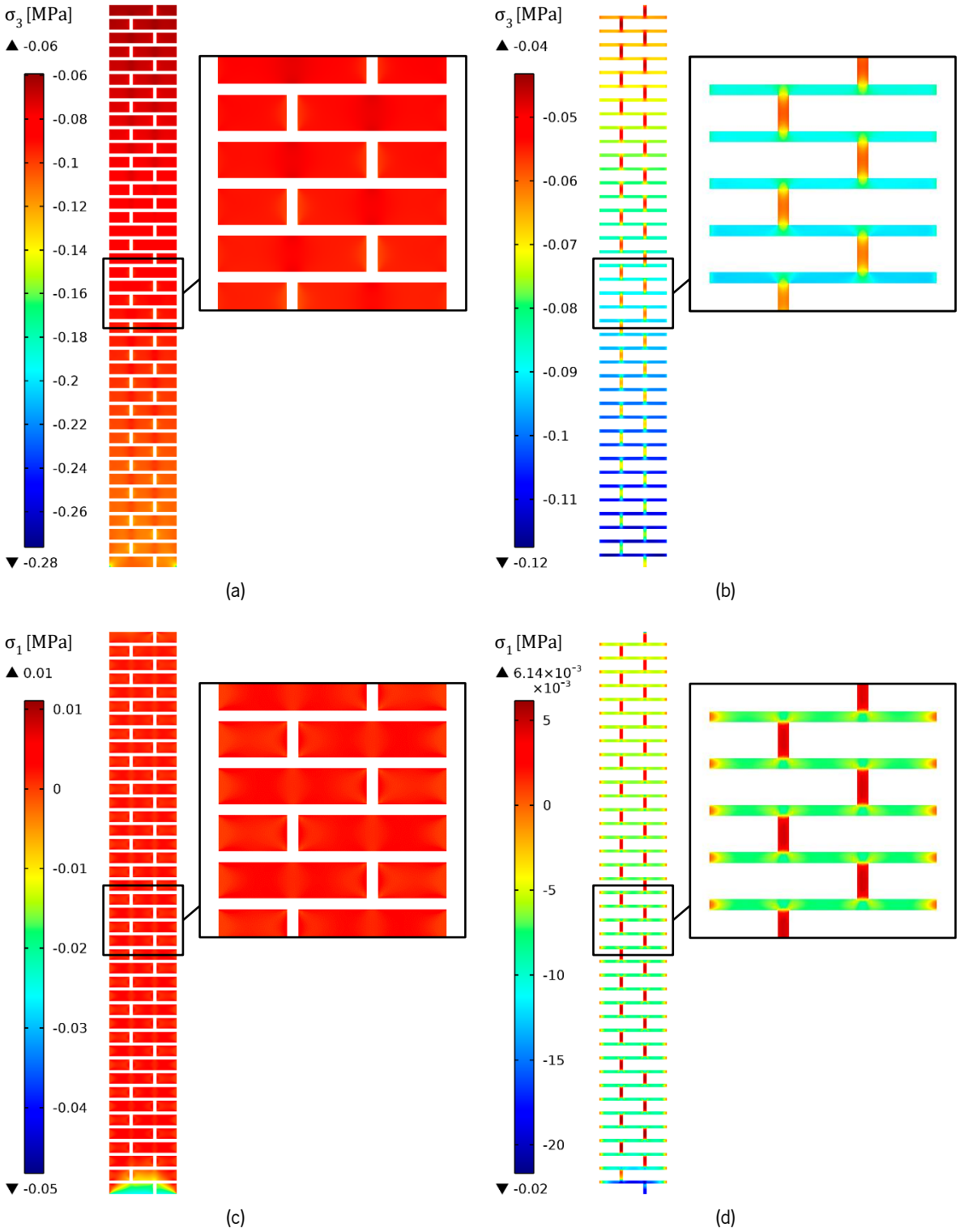

Figure 6.11. Hygro–thermo–mechanical analysis of the three–wythe brick masonry wall with natural hydraulic lime mortar. Principal stress distribution obtained for the gravitational loads alone: minimum principal stress, σ_3 [MPa], in (a) bricks, and (b) mortar joints; maximum principal stress, σ_1 [MPa], in (c) bricks, and (d) mortar joints.

The maximum principal stresses obtained for the gravitational case reveal expected trends as well (see Figure 6.11c and Figure 6.11d). On one hand, the positive component of the principal stress for bricks is practically zero, whereas it presents low positive values for the vertical head joints, around 5.0E-3 MPa.

Even though the obtained value is not significant, this observation is consistent with the fact that head joints typically act as tension planes within the wall geometry. On the other hand, the results for the horizontal joints show small negative values for σ_1, around –8.0E-3 MPa, which indicates that the bed mortar joints experience biaxial compression. It is noted that the maximum principal stress in the bed joints drops to zero in the regions near the external and internal faces of the wall.

The distribution of stresses for the CM wall under gravitational loads is shown in Figure 6.12. It is noted that the obtained results are analogous to the ones previously discussed for the LMJ case. The distribution of minimum principal stresses for bricks and mortar bed joints (Figure 6.12a and Figure 6.12b) presents the same average compression, i.e. –0.09 MPa for the selected area. Likewise, the areas of the bricks aligned with vertical joints show lower stresses, ca. –0.08 MPa. On the other hand, small differences between the two cases can be pointed out as well. For instance, the compression values on the vertical edges of the bricks adjacent to mortar head joints are slightly higher, around –0.11 MPa. Moreover, the head mortar joints present less compressive stresses, ca. –0.05 MPa.

The distribution of maximum principal stresses for the wall with cement mortar (Figure 6.12c and Figure 6.12d) shows some differences with respect to the LMJ case as well. The positive component of the principal stress for bricks is still negligible for most of the wall but higher values appear close to the brick corners, between 5.0–6.0E-3 MPa. Furthermore, higher σ_1 values can be found in the vertical head joints as well, ca. 7.0E-3 MPa. Although the observed tensile stresses are low, they may contribute to crack propagation when cracks are already present. On the other hand, the horizontal joints show lower negative values, around –0.01 MPa, thus they undergo a biaxial compression state. Finally, the maximum principal stress in bed joints falls to zero in the regions near the faces of the wall.

In conclusion, for the two studied models, the outcomes of the gravitational case reveal a complex 2–D stress distribution derived from the multi–layered nature of the material. Moreover, the stress distribution results for the LMJ and CM walls are analogous, although slightly higher stress states are obtained for the wall with cement mortar.

Regarding the HTM analysis, the stress distribution results obtained for the LMJ case are shown in Figure 6.13. It is recalled that the instant with maximum horizontal displacement is selected for the analysis (see Figure 6.9). At that moment, the imposed boundary conditions lead to shrinkage of the internal face of the wall. It is noted that the corresponding deformed configuration is intimately linked to the stress distribution. As expected, the distribution of stresses is not uniform across the wall thickness. Considering the minimum principal stresses (Figure 6.13a and Figure 6.13b), lower compression values are found in the middle portion of the wall, around –0.07 MPa. Conversely, higher stresses appear near

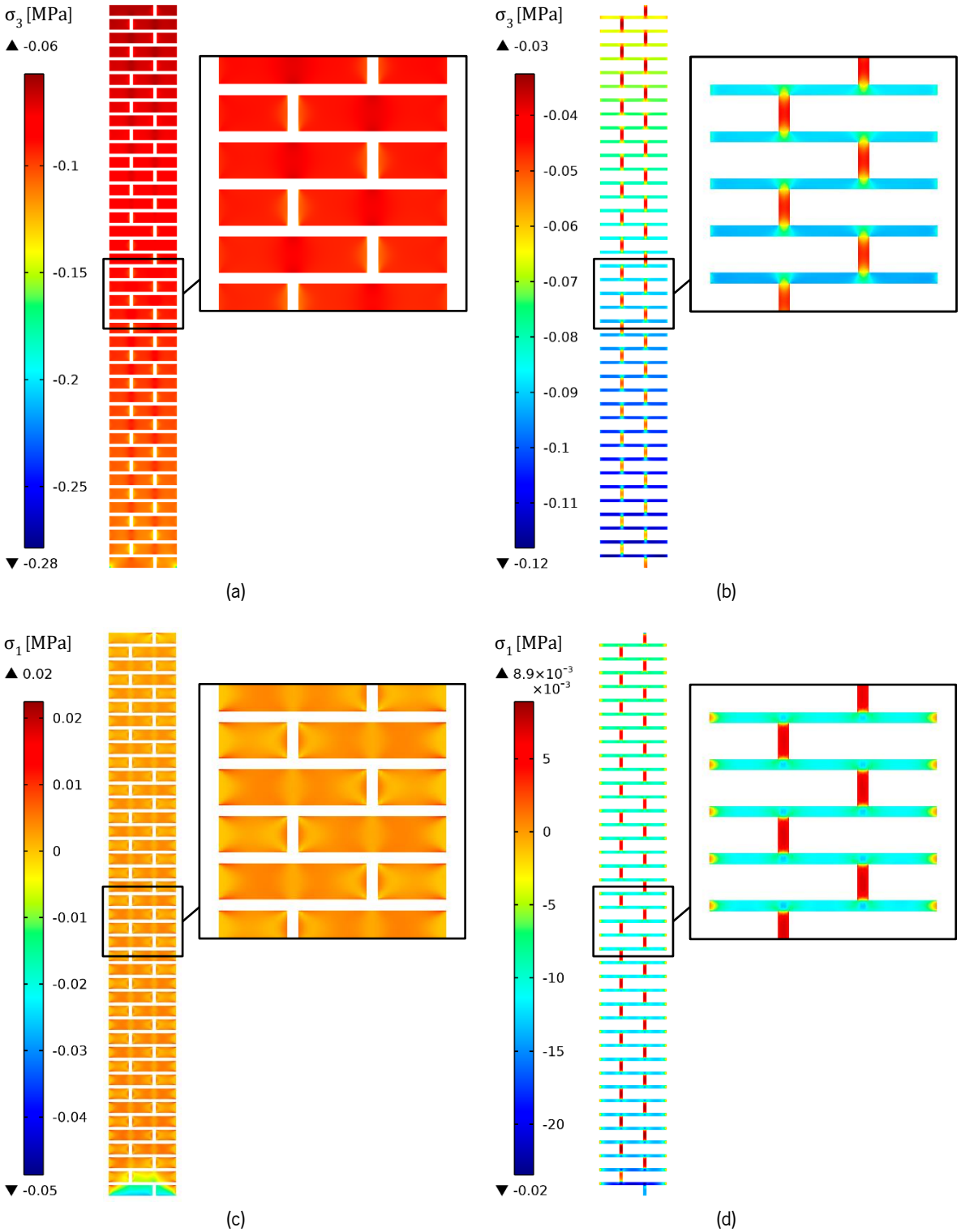

Figure 6.12. Hygro–thermo–mechanical analysis of the three–wythe brick masonry wall with cement mortar. Principal stress distribution obtained for the gravitational loads alone: minimum principal stress, σ_3 [MPa], in (a) bricks, and (b) mortar joints; maximum principal stress, σ_1 [MPa], in (c) bricks, and (d) mortar joints.

the external and internal faces, ca. –0.12 MPa. The compressive stresses in bed mortar joints follow a similar trend with values up to –0.13 MPa near the wall boundaries. On the other hand, the results of σ_3 in head mortar joints show lower compression levels, with values around –0.05 MPa and –0.04 MPa for

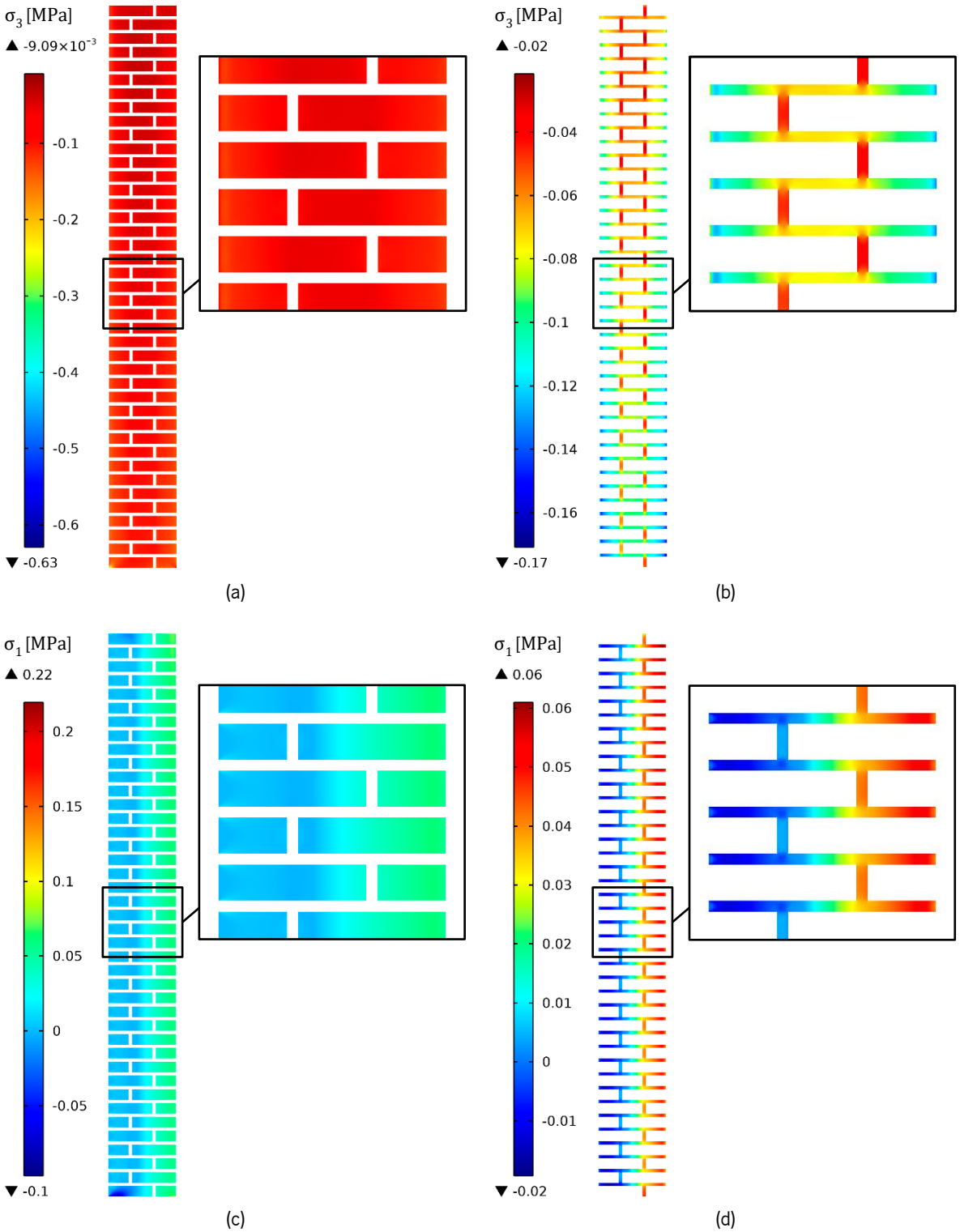

Figure 6.13. Hygro–thermo–mechanical analysis of the three–wythe brick masonry wall with natural hydraulic lime mortar. Principal stress distribution obtained for the hygro–thermo–mechanical case: minimum principal stress, σ_3 [MPa], in (a) bricks, and (b) mortar joints; maximum principal stress, σ_1 [MPa], in (c) bricks, and (d) mortar joints.

the vertical joints located closer to the external and the internal surfaces, respectively. Finally, it is noted that the bricks repeat the same trends obtained for the gravitational case, namely lower compressive

stresses in the areas aligned with the vertical joints and higher concentration of stresses near the vertical edges adjacent to the head joints.

The distribution of maximum principal stresses for the LMJ case (Figure 6.13c and Figure 6.13d) presents a relatively uniform gradient across the wall thickness with negligible negative values near the external surface and higher tensile stresses close to the internal side of the wall. In fact, the highest positive values are detected in the outermost layer of the elements facing the interior, namely 0.06 MPa for bricks and 0.05 MPa for bed mortar joints. The maximum principal stresses for vertical head joints depend on the location, namely 0.01 MPa and 0.04 MPa in the joints closer to the exterior and the interior, respectively.

The HTM results for the CM wall are depicted in Figure 6.14. As it happened with the gravitational loads, the overall stress distribution is analogous to the one obtained for the LMJ case. This is expected since the deformed shape is similar for both cases. Nonetheless, several differences can be pointed out as well. The minimum principal stresses for bricks (Figure 6.14a) present a non–uniform distribution with lower values in the middle section, ca. –0.07 MPa, and higher stress concentration near the external and internal faces, namely –0.14 MPa and –0.12 MPa, respectively. A similar distribution is found in the horizontal joints (Figure 6.14b), with greater compressive stresses near the outer surface, ca. –0.15 MPa. On the other hand, the head joints show values around –0.07 MPa and –0.04 MPa for the vertical joints located closer to the external and internal surfaces, respectively. As for the previous cases, the bricks present lower compressive stresses in the areas aligned with the vertical joints and a higher concentration of stresses near the vertical edges adjacent to the head joints.

The maximum principal stresses obtained for the CM case (Figure 6.14c and Figure 6.14d) present a more or less uniform gradient across the thickness of the wall. The σ_1 results for bricks (Figure 6.14c) show generalized tensile stresses, with increasing values for areas closer to the internal face, around 0.06 MPa. Moreover, significant concentrations of tensile stresses (values up to 0.12 MPa) appear on the brick corners adjacent to horizontal joints near the external face. Additionally, the σ_1 results for bed joints (Figure 6.14d) show a rather uniform stress gradient through the wall thickness, with negative values near the external face, ca. –0.07 MPa, and a transition towards tensile values on the internal side, up to 0.02 MPa. It is noted that the maximum principal stress in the bed joints drops to negligible values in the regions near the external and internal faces of the wall. Finally, the maximum principal stresses for vertical joints are around 0.01 MPa, slightly higher on the head joints closer to the interior boundary.

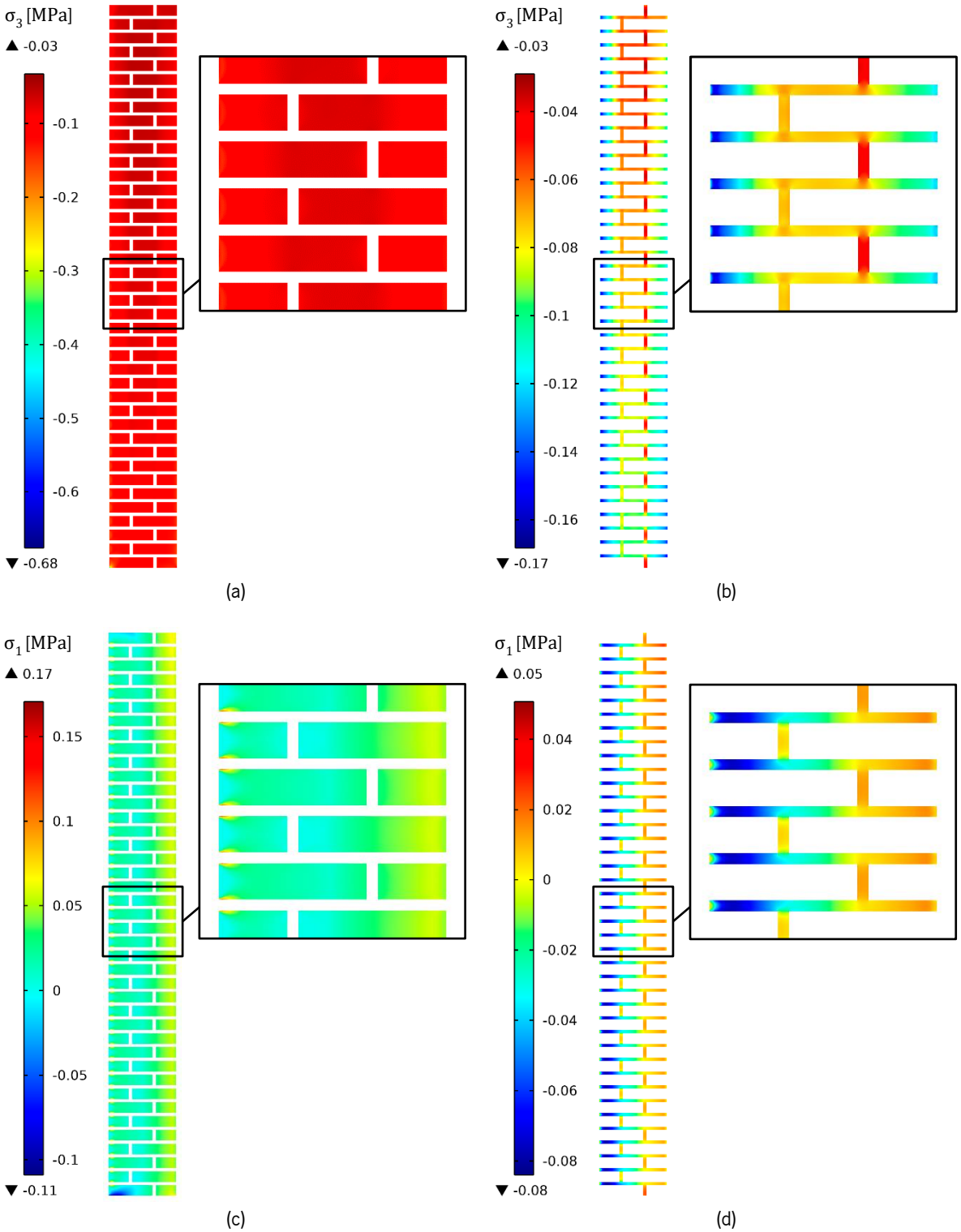

Figure 6.14. Hygro–thermo–mechanical analysis of the three–wythe brick masonry wall with cement mortar. Principal stress distribution obtained for the hygro–thermo–mechanical case: minimum principal stress, σ_3 [MPa], in (a) bricks, and (b) mortar joints; maximum principal stress, σ_1 [MPa], in (c) bricks, and (d) mortar joints.

In conclusion, for both models, the imposed hygrothermal conditions induce deformations and lead to relevant changes in the stress state of the wall with respect to the gravitational case. For the specific

boundary conditions considered in this study, the shrinkage of the internal face of the wall results in an uneven distribution of stresses across the wall thickness. In general, lower compression values appear in the middle portion, whereas higher compressive stresses are found in the elements near the wall surfaces. The vertical joints show a non–symmetrical stress distribution as well, with higher compression and higher tensile levels in the joints closer to the external and the internal faces, respectively. For the same hygrothermal boundary conditions, the wall with cement mortar presents greater deformations (see Figure 6.10). Consequently, the HTM results for the CM case reveal higher stress levels in comparison with the LMJ wall. In particular, larger compression values are found on the external face, which can be explained by the higher coefficient of thermal expansion of cement mortar.

6.4.3 Influence of the initial conditions on the hygro–thermo–mechanical response

As it was previously mentioned, the thermal– and moisture–induced strains are dependent on specific initial temperature and relative humidity values for which the free–strain or zero–strain condition is assumed. As a result, the initial conditions play a major role in the HTM analysis. For instance, the results presented in the previous section were calculated assuming that the wall had initial conditions equal to the average temperature and relative humidity of the exterior environment, i.e. 13.5 °C and 74 % RH. However, if the initial conditions of the wall were assumed equal to the interior environment, i.e. 20 °C and 50 % RH, the obtained results would change drastically. Note that the steady–state hygrothermal equilibrium reached by any of the two cases would be the same since it only depends on the external conditions. However, the deformed configuration attained with the steady–state equilibrium does depend on the chosen hygrothermal conditions used as a reference (see Eq. (6.20) and Eq. (6.21)). For the sake of clarity, Figure 6.15 shows the maximum horizontal displacement obtained for the HTM analysis discussed in the previous section performed on the same LMJ and CM cases but assuming different initial conditions.

It is worth recalling that the coefficient of thermal expansion, α_T, has been assumed constant. Therefore, the thermally induced strains are directly proportional to the imposed temperature gradient, ΔT. Consequently, assuming $\Delta T = T_{high} - T_{low}$, where $T_{high} > T_{low}$, the resulting positive gradient leads to a positive strain and thus dilation or swelling. Conversely, the same gradient with a negative sign, i.e. $\Delta T = T_{low} - T_{high}$, will produce the same absolute value for the strain but, in this case, it will be associated with shrinkage. As a result, the initial conditions defined for a thermo–mechanical analysis determine whether the material undergoes dilation or contraction, but the absolute value of the resulting strain would be the same.

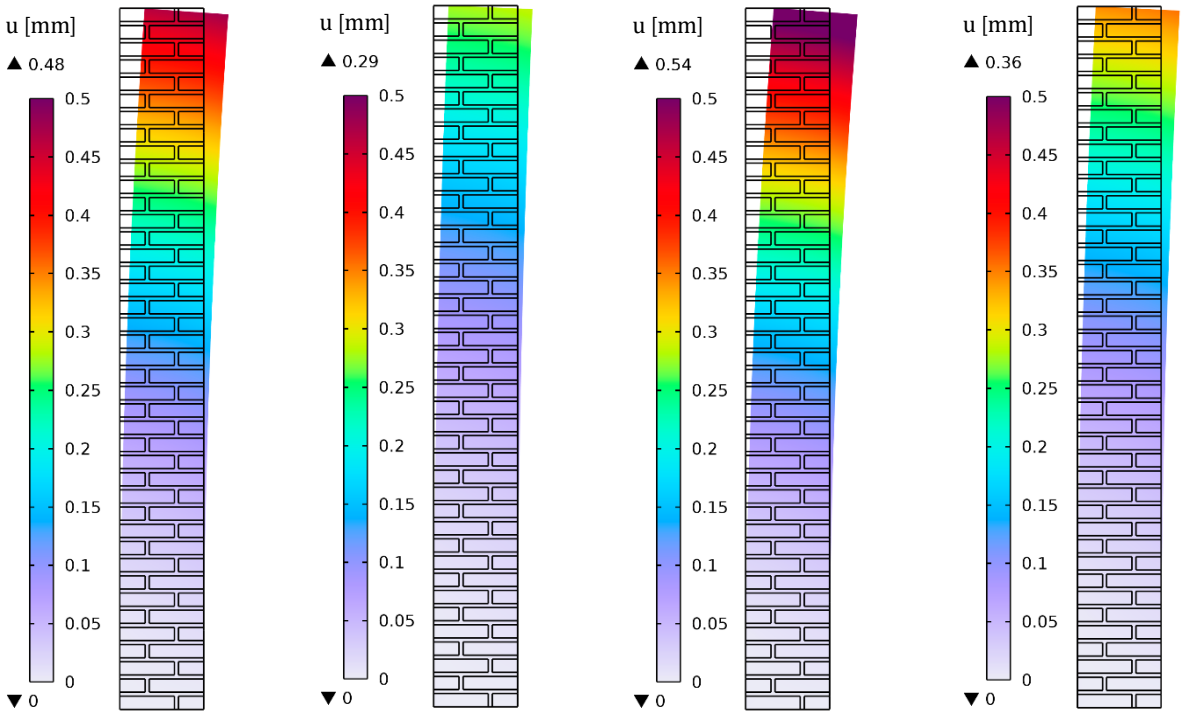

Figure 6.15. Hygro–thermo–mechanical analysis of the studied three–wythe brick masonry wall: maximum displacement obtained for the wall with natural hydraulic lime mortar assuming initial conditions equal to (a) external conditions, and (b) internal conditions; maximum displacement for the wall with cement mortar assuming initial conditions equal to (c) external conditions, and (d) internal conditions.

On the contrary, it must be noted that the moisture–induced strains greatly depend on the initial conditions for which the zero–strain configuration is assumed. This behaviour is due to the non–linear nature of the coefficient of hygric expansion, α_h. In order to illustrate this, the previously analysed wall with natural hydraulic lime mortar can be used as an example. Assuming $\varphi_{50} = 0.50$, the coefficient of hygric expansion for brick is $\alpha_h(\varphi_{50}) = 11.8\text{E–}6\ \mathrm{m^3/kg}$. Nonetheless, for $\varphi_{74} = 0.74$, the corresponding coefficient for brick is $\alpha_h(\varphi_{74}) = 5.6\text{E–}6\ \mathrm{m^3/kg}$. Lime mortar presents a similar trend, namely $\alpha_h(\varphi_{50}) = 7.9\text{E–}6\ \mathrm{m^3/kg}$ and $\alpha_h(\varphi_{74}) = 4.2\text{E–}6\ \mathrm{m^3/kg}$. Therefore, the coefficients of hygric expansion of both materials double for φ_{50} in comparison with φ_{74}. This implies that if the initial conditions are considered as the free–strain equilibrium, a wall drying ($\Delta\varphi = \varphi_{74} - \varphi_{50}$) will experience greater deformations than the same material wetting ($\Delta\varphi = \varphi_{50} - \varphi_{74}$). In conclusion, the initial conditions defined for a hygro–mechanical problem not only determine whether the material experiences swelling or shrinkage, but also affect the extent of such deformation. Hence, a careful examination of the initial conditions must be considered for the analysis and interpretation of hygro–mechanical results.

6.5 CHAPTER CONCLUSIONS

This chapter presents a hygro–thermo–mechanical (HTM) model and its application to simulate how different hygrothermal phenomena affect the structural behaviour of masonry elements. First, the hygrothermal model is presented together with the coupling assumptions needed to link the temperature and moisture fields. Subsequently, a finite element masonry wall is prepared and different hygrothermal simulations are performed using COMSOL Multiphysics. In the second stage, the hygrothermal model is extended to incorporate mechanical effects and a unidirectionally coupled HTM model is presented. The capabilities of the HTM analysis are tested on the same masonry wall studied in the hygrothermal analyses.

The proposed hygrothermal model combines a muti–phase diffusivity moisture transport model with a thermal model based on conductive heat transfer and with an explicit account for the heat of vaporization. Moreover, the model conforms to the so–called two–way or fully–coupled layout, that is, the thermal parameters are dependent on moisture content and the hygric parameters are dependent on temperature as well. Consequently, a series of analytical expressions are introduced to establish the necessary links between the two fields. It is noted that while the reliability of the thermal parameters is well established in general, the most accurate approach to modelling the influence of temperature on hygric properties is still under debate. For the definition of convective flux boundary conditions, the incorporation of simplified convective transfer coefficients is generally adopted. The convective heat transfer coefficient, h_T, and the convective mass transfer coefficient, h_m, are usually taken from tabulated values in the literature or calibrated based on experimental results, e.g. drying tests. The convective coefficients h_T and h_m can be calibrated separately; otherwise, h_T can be calibrated first, and then h_m is calculated based on h_T by means of the Lewis analogy. Finally, for cases that include thermal radiation, a lumped convective coefficient accounting for the radiation component is generally used.

A 2–D finite element model is prepared to simulate a three–wythe brick masonry wall under different hygrothermal scenarios. Two types of mortars are considered, namely natural hydraulic lime mortar (LMJ) and cement mortar (CM). The corresponding boundary conditions are defined based on the climate records of Guimarães (Portugal). Subsequently, steady–state (SS), time–dependent analysis with constant boundary conditions (TD1), and time–dependent analysis with variable boundary conditions (TD2) are performed. The results of these hygrothermal studies are evaluated in terms of temperature and relative humidity distributions across the thickness of the wall as well as for different points on the external and internal surfaces. It is found that for the SS and TD1 analyses, there are only minor differences between the LMJ and the CM cases. Moreover, for these scenarios the wall can be simulated

following a macro–modelling approach with equivalent masonry properties. Similarly, the system can be simplified into a 1–D analysis without compromising the accuracy of results. The evolution of temperature and relative humidity profiles obtained by transient analyses show that heat transfer is significantly faster than moisture transport. In fact, thermal processes can be considered instantaneous in comparison with mass transfer. Considering the transient analysis TD2, the results show differences in the hygrothermal performance of the wall depending on the type of mortar. As expected, the LMJ case shows a more uniform response due to the similar behaviour of bricks and lime mortar. On the contrary, the CM case presents localized behaviour depending on the material. Thus, the LMJ case can be simplified to a 1–D macro–modelling approach but the same process applied on the CM wall may result in a loss of detail and accuracy. Finally, the interface hydraulic resistance does not play a role for the moisture conditions considered in this study.

The mechanical problem is coupled with the thermal and moisture fields through the total strain additive decomposition principle, that is, the total strain can be divided into different components, namely mechanical strains, temperature–induced strains and moisture–induced strains. The thermal and hygric strains stem from the presence of a temperature gradient or a moisture gradient, respectively. Moreover, the induced strains are proportional to thermo–mechanical and hygro–mechanical parameters, namely the coefficient of thermal expansion and the coefficient of hygric expansion. In the proposed HTM model, the link between the mechanical component and the hygrothermal fields consists of a one–way coupled relationship. In other words, the hygrothermal results affect the mechanical response, but mechanical stresses/strains do not influence heat and moisture transport. Additionally, temperature and moisture dependencies of the mechanical properties are not considered. The HTM model is completed with the implementation of mechanical boundary conditions as well as the initial or free–strain conditions. A careful definition of initial and boundary conditions is of special importance for mechanical analyses since the appearance and distribution of stresses largely depend on these parameters. In particular, considering the non–linear behaviour of the coefficient of hygric expansion, the definition of the initial moisture conditions (and therefore the associated free–strain state) greatly affects the stress evolution.

The three–wythe brick masonry model defined for the hygrothermal analysis is further used to study the internal distribution of stresses when the wall is subjected to temperature and moisture gradients. In particular, the temperature and moisture results from the time–dependent analysis TD2 are used as input for the mechanical study. The instant of maximum displacement is chosen, and the corresponding stress distribution induced by the hygrothermal loads is compared with the self–weight scenario. The analysis is focused on a section of the mid–portion of the wall in order to avoid disturbances caused by the

proximity of loads or boundary conditions. It is proven that temperature and moisture variations change the natural stress distribution of the wall subjected to gravitational loads alone. Moreover, the brick wall with cement mortar undergoes higher stress levels in comparison with the wall with natural hydraulic lime mortar. This is caused by the higher thermal expansion and hygric expansion coefficients of cement in comparison with lime mortar. Although the induced tensile stresses are low, they may contribute to crack propagation when cracks are already present. Similarly, the hygrothermally–induced deformations may add up to previous damage and magnify existing problems such as tilting in structures with moisture deterioration at the base or soil permanent deformation. Finally, the hygro–thermo–mechanical behaviour of the masonry wall is a 2–D phenomenon derived from the multi–layered nature of the material.

This page has been intentionally left blank

CHAPTER 7

Case study: The Civic Tower of Pavia

This chapter builds upon the hygro–thermo–mechanical model presented in the previous chapter and demonstrates its application to simulate the structural behaviour of full–scale buildings. For this purpose, the Civic Tower of Pavia (Italy) is selected as a case study. This historical masonry structure is chosen due to a series of advantages with respect to the modelling possibilities, namely its simple morphology, the peculiarities of its history, loading conditions and eventual failure, and the existence of previous studies with a comprehensive compilation of structural information and material data.

7.1 BRIEF HISTORY AND DESCRIPTION OF THE STRUCTURE

The Civic Tower of Pavia (Italy) is most known because of its tragic collapse in 1989 (Figure 7.1). The structure was located on the northwest corner of the Cathedral of Pavia. Originally, it worked as the bell tower for two pre–existing Romanesque churches, which were later replaced by the current Cathedral. The construction of the tower started in the 11th century and continued in different phases during the two following centuries. At the end of the 16th century, the original belfry was replaced by a new one in granite stone. Since then, the tower underwent minor repair works and rebuilding of the roof (Binda et al., 1992). On 17 March 1989, eight centuries after the beginning of its construction, the masonry structure failed suddenly without any apparent warning.

(a) (b)

Figure 7.1. Civic Tower of Pavia, Italy: (a) tower and cathedral before the collapse; (b) ruins after the collapse. Images from Binda et al. (2007), Anzani et al. (2009).

After the collapse of the tower, a considerable amount of research work was developed in order to identify and understand the causes of the failure, e.g. Binda et al. (1992), Anzani et al. (2000), Ferretti & Bazant (2006a, 2006b), Lourenço & Pina–Henriques (2007), Taliercio & Papa (2007), among others. Especially relevant was the investigation conducted by Binda et al. (1992), who carried out a comprehensive experimental campaign involving the analysis of remains on site and in the laboratory. Moreover, these authors prepared and calibrated a finite element model that set up the basis for further simulation works.

By the time the collapse occurred, there was not sufficient documentation to reconstruct the morphology of the tower. Thus, a geometric survey of the building was done after the collapse, based on the material remains, historical documents and photographs. The resulting geometry is shown in Figure 7.2a and Figure 7.2b. The tower had a square plan with dimensions 12.30 m × 12.30 m and was about 60 m high. Externally, the façades were divided into six levels or architectural orders. Inside, the tower had two timber floors at a height of 11 m and 24 m, approximately. Two vaults further divided the interior space at heights around 35 m and 46 m. Finally, the belfry had big arched openings and was covered by a dome and a hip roof.

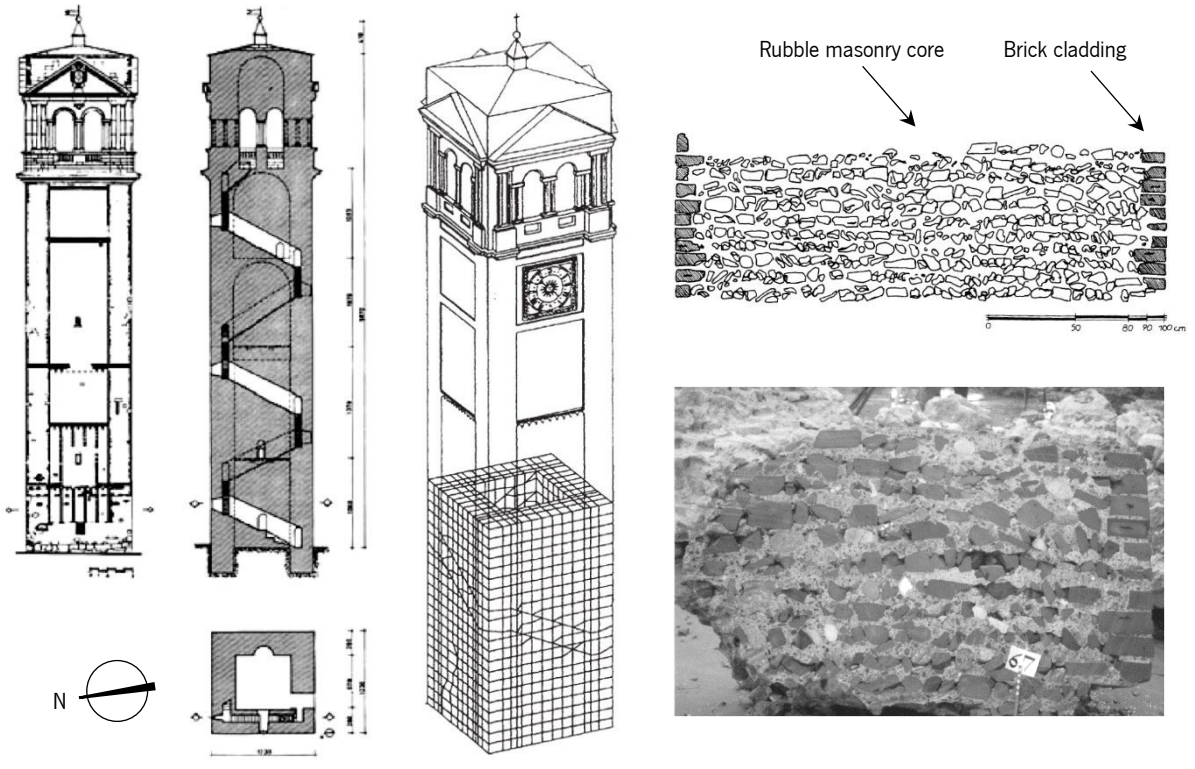

(a) (b) (c)

Figure 7.2. Civic Tower of Pavia, Italy: (a) geometric survey; (b) outlook of the tower and finite element mesh of the original model by Binda et al. (1992); (c) cross–section of the wall and detail of a retrieved wall fragment showing the external brick cladding. Images adapted from Ferretti & Bazant (2006a), and Binda et al. (2007).

The load–bearing structure consisted of masonry walls, 2.80 m wide at the base. These massive walls were composed of a rubble masonry core and an external brick cladding (Figure 7.2c). The thickness of the external cladding was variable, with an average of 0.15 m. The external brick layers additionally served as formwork during construction for casting the core. The core was made up of a sort of conglomerate or 'ancient concrete', that is, successive courses of irregular stones and brick pieces embedded in mortar alternating with thick layers of lime–based mortar.

A staircase 0.80 m wide was built into the masonry walls, running clockwise along the four façades from the southwest corner on the ground floor up to the belfry level. The staircase divided the cross–section of the wall into two parts, namely an external wall 1.40 m thick and an internal one 0.60 m thick. The external part had the same morphology of rubble core and brick cladding, whereas the internal wall was made up of rubble masonry alone. Finally, the stairwell was covered by a barrel vault and had small openings towards the external façades and the interior space of the tower.

Blocks of masonry of different sizes and fragments of the main constituent materials (stone, brick and mortar) were recovered from the ruins for laboratory testing. The experimental campaign comprised monotonic compressive tests, uniaxial cyclic tests and creep tests. For the description of the experimental methodology and a more detailed discussion of the results, the reader is referred to Binda et al. (1992), Anzani et al. (2000). It is noted that the experiments were performed in controlled laboratory conditions, i.e. 20 °C and 50 % RH.

The material properties reported by Binda et al. (1992) are presented in Table 7.1. The compression tests performed on brick specimens gave an average strength equal to 13.4 MPa (CoV = 1.9 %). In turn, the average compressive strength of the mortar specimens (small cubes taken from mortar joints) was 6.4 MPa (CoV = 7.6 %). The elastic modulus of the materials was calculated as the slope of the stress–strain relation between 20 % and 60 % of the peak stress. Thus, the elastic moduli obtained for brick and mortar were 1970 MPa and 900 MPa, respectively. On the other hand, the compressive strength of masonry specimens ranged between 2.0–4.1 MPa, with ultimate strains from 3.0E–3 to 5.5E–3. The Young's modulus of masonry was calculated between 20 % and 40 % of the peak stress and resulted in values between 720–1800 MPa.

Table 7.1. Mechanical properties determined experimentally from the material remains (Binda et al., 1992).

Material property	Symbol	Units	Brick	Mortar	Masonry
Compressive strength	f_c	MPa	13.4	6.4	2.0–4.1
Young's modulus	E	MPa	1970	900	720–1800

Regarding the failure mechanism, the collapse was almost vertical with a slight inclination toward south–west. The failure would have started from the bottom where the highest level of stress was likely to occur and major concentrations were expected due to the presence of the entrance and the staircase (Anzani et al., 2009). No evidence of sudden or differential soil settlement was found. Moreover, there were no records of any atmospheric or accidental event in the preceding months that could be directly related to the collapse. Upon inspection of the debris, it was concluded that the cause of the collapse was not associated with the degradation state of the building materials. Once these causes had been discarded, researchers turned their attention toward the time–dependent material behaviour and how the evolution and combination of dead and live loads might have affected the mechanical response. In this context, numerical models were developed to aid the investigation process and evaluate the different hypotheses.

With the retrieved information regarding geometrical and material aspects, Binda et al. (1992) produced a finite element model and tested it against different loading scenarios. It was found that under self–weight conditions, the average normal compressive stress at the base of the tower was about 1.1 MPa (Binda et al., 1992). However, higher compression values between 1.7–2.0 MPa were found on the southwest corner and at the base of the staircase, near the entrance to the tower (Anzani et al., 2000; Taliercio & Papa, 2007). It is noted that these stress concentrations are compatible with the compressive strength of the masonry determined experimentally, i.e. 2.0–4.1 MPa, although rather close to the lower limit. However, it is important to consider that such stress levels acting for a prolonged time could eventually bring the material to failure, as indicated by Taliercio & Papa (2007). These authors performed numerical simulations as well and confirmed that the failure mechanism (deformed shape at incipient failure) was defined by crushing of the corner near the entrance, in agreement with the survey of the tower ruins.

Based on the collected information, researchers concluded that the accumulation of creep–induced damage prompted by high stress concentrations was the main cause of the collapse (Anzani et al., 2000). This was supported by the results of creep tests on specimens extracted from the remains, some of which failed at stress levels equivalent to the maximum values obtained from the numerical analyses (Lourenço & Pina–Henriques, 2007; Taliercio & Papa, 2007). Moreover, the combination of time–dependent behaviour with cyclic loads (thermal variations, wind, soil vibrations or vibrations produced by bells) probably contributed to the failure in a synergetic way (Binda et al., 2007). Aside from these phenomena, Ferretti & Bazant (2006a, 2006b) included other factors as a potential cause for the failure, namely the redistribution of stresses related to the non–uniform evolution of carbonation, drying shrinkage and drying creep, all of which derive from the slow diffusion of pore humidity in time.

7.2 DESCRIPTION OF THE NUMERICAL MODEL

A finite element model was prepared in order to study the mechanical response of the tower under different loading conditions and environmental actions. Considering the morphological and material characteristics described previously, a macro–modelling approach was chosen to simulate the hygro–thermo–mechanical behaviour of the masonry structure. It must be noted that the main purpose of the model was to study the stress distribution at the base of the tower, which was the most vulnerable part of the structure as pointed out by earlier studies. Taking this into account, only the lowest portion of the building was modelled. In particular, the model comprised the bottom of the tower from the ground level up to a height of 6 m. Windows and other openings above the ground level were not modelled since their presence was assumed to have a minor impact on the distribution of the stresses at the base. The non–modelled geometry corresponding to the upper portion of the building was considered as an additional load applied on top of the modelled volume. Thus, the total weight applied on top of the model was 71100 kN. This value was estimated through a calibration process so that the maximum normal compressive stresses obtained at the base fitted the values reported in the literature (see Section 7.4).

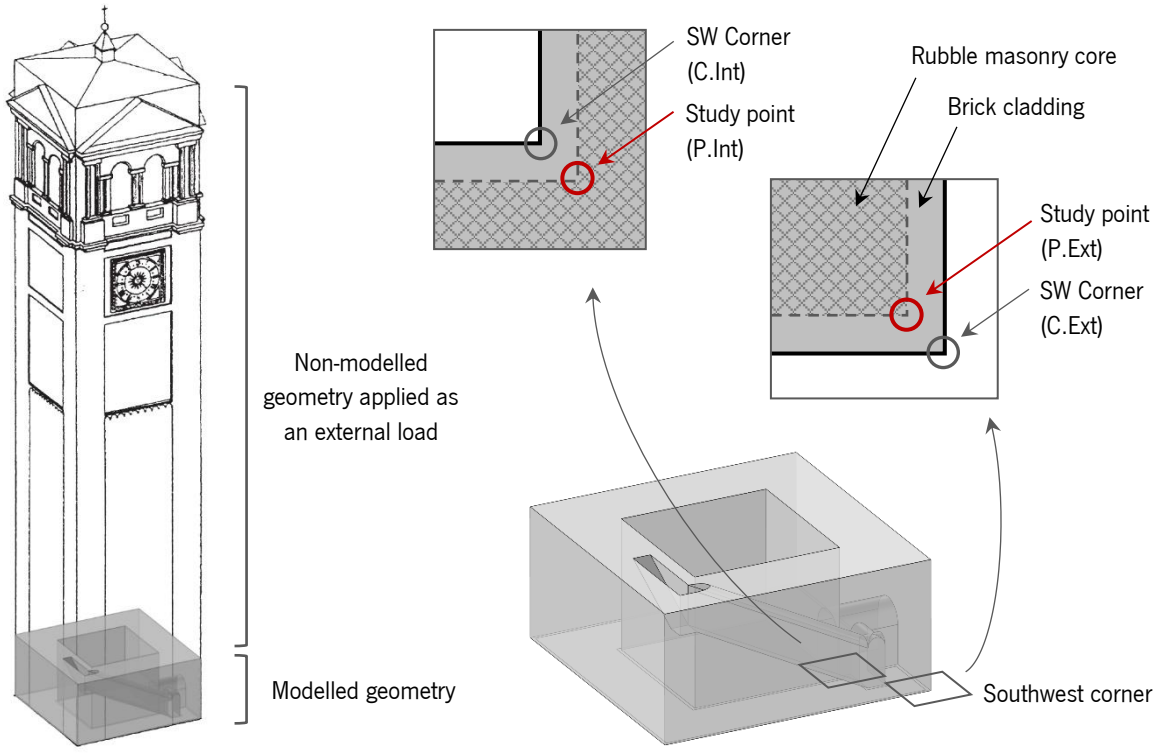

Figure 7.3. Outlook of the tower (adapted from Ferretti & Bazant (2006a)) and geometry modelled in the present work.

The material properties of stone rubble masonry were chosen for the model. Thus, an explicit distinction of the external brick layer was not accounted for. Moreover, it was assumed that the material was

homogeneous and isotropic, with linear elastic behaviour. In their studies for moisture diffusion and carbonation, Ferretti & Bazant (2006a, 2006b) treated the core material as a low–strength Portland cement concrete. An analogous approach was adopted for the current model and the necessary material parameters were drawn from specialized literature or directly extrapolated from the mortar properties previously analysed in this work (see Chapter 4). The resulting material properties defined for the numerical simulations are summarised in Table 7.2.

Table 7.2. Material properties of masonry used in the simulations.

Material parameter	Symbol	Units	Value or expression	Source
Specific weight	γ	$\mathrm{kN/m^3}$	18.00	Binda et al. (1992)
Young's modulus	E	MPa	1500	Binda et al. (1992)
Poisson's ratio	ν	–	0.10	Binda et al. (1992)
Compressive strength	f_c	MPa	3.10	Ferretti & Bazant (2006b)
Tensile strength	f_t	MPa	0.16	Ferretti & Bazant (2006b)
Specific heat capacity	C_p	$\mathrm{J/(kg \cdot K)}$	1000	EN ISO 10456 (2007)
Thermal conductivity	λ_0	$\mathrm{W/(m \cdot K)}$	1.00	EN ISO 10456 (2007)
Coefficient of thermal expansion	α_T	$1/℃$	3.04E–6	Experimental (1)
Capillary moisture content	w_{cap}	$\mathrm{kg/m^3}$	190	Experimental (1)
Fitting parameter for sorption isotherm	a	$1/\mathrm{Pa}$	3.80E–6	Experimental (1)
Fitting parameter for sorption isotherm	m	–	0.352	Experimental (1)
Capillary absorption coefficient	A_w	$\mathrm{kg/(m^2 \cdot s^{0.5})}$	0.080	Experimental (1)
Water vapour resistance factor	μ	–	15.00	Prangnell (1971)
Coefficient of hygric expansion	α_h	–	$3.00\mathrm{E{-}4}/{w_g}^{0.62}$	Experimental (1)

(1) Taken from mortar analysed in this study

The numerical model was discretized using solid elements, namely four–node isoparametric tetrahedra. In order to avoid mesh–dependent results, a sensitivity analysis was carried out and different mesh sizes were tested, as shown in Figure 7.4. The self–weight condition was used as a reference for the sensitivity study and the response was analysed in terms of vertical stresses, σ_Z [MPa], in different points of the base near the entrance. On the external side, the southwest corner was selected together with the point at the hypothetical interface between the inner core and the cladding, that is $0.15\ \mathrm{m} \times 0.15\ \mathrm{m}$ away from the corner. Moreover, the opposite corner on the internal side was chosen as well as the corresponding point at the core/cladding interface, i.e. the point distant $0.15\ \mathrm{m} \times 0.15\ \mathrm{m}$ from the corner. Expectedly, the corners lead to a geometric singularity: the solution is mesh–dependent and inconsistent stress values

are obtained for increasingly refined meshes. On the contrary, the results obtained for the points representing the core/cladding transition show little variation throughout the mesh refinement process. This means that the selected nodes are at an adequate distance from the corner and not affected by the singularity. Therefore, the core/cladding interface points were chosen as a reference for the analysis of stresses at the base of the tower. The final discretization was done with a maximum mesh size equal to 0.40 m. As a result, the final model contains 282633 elements and 53723 nodes.

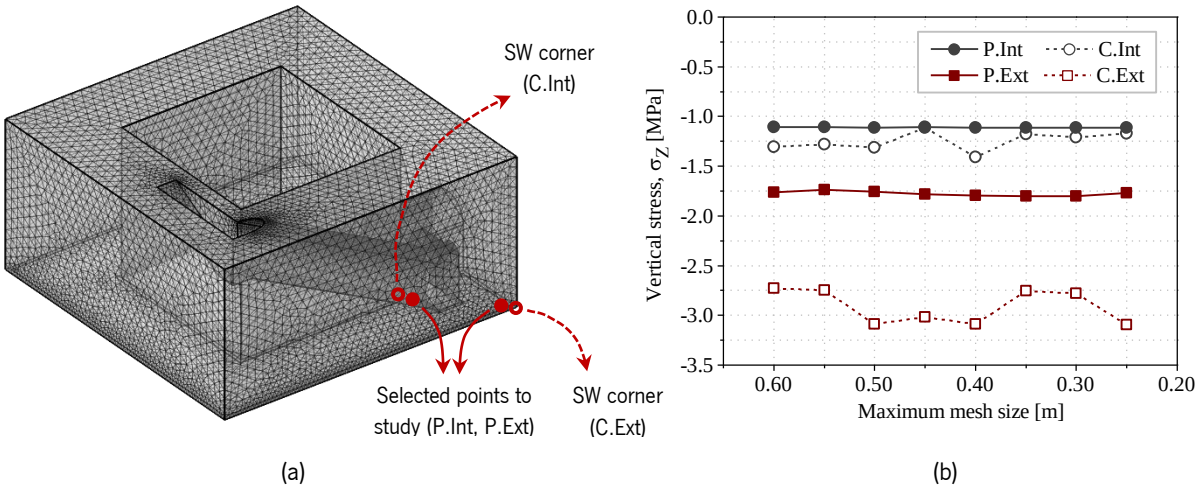

Figure 7.4. Mesh sensitivity study: (a) finite element mesh with maximum mesh size 0.40 m; (b) vertical stress, σ_Z [MPa], for self–weight condition in different points of the southwest corner at ground level.

7.3 LOADING AND ENVIRONMENTAL CONDITIONS

Different scenarios were considered for the numerical analysis, namely a gravitational load case (self–weight) and several hygrothermal combinations. For this group of analyses, the hygrothermal cases were studied independently of the gravitational loads. In other words, the analysis involving temperature and/or moisture did not consider the weight of the structure. Thus, the stresses obtained from the hygrothermal cases were compared directly against the gravitational results. It is noted that the different temperature and moisture scenarios were studied by means of steady–state analyses. Therefore, fixed boundary conditions were imposed on the vertical surfaces of the model representing the external and internal sides of the tower. The steady–state approach ignores the slow evolution of hygrothermal processes (especially in thick massive walls) but is considered a valid approximation to understand the magnitude of temperature– and moisture–induced stresses.

The gravitational case included the dead weight of the modelled geometry and the weight of the non–modelled upper part of the tower, which was implemented as an evenly distributed load on the upper surface of the model.

Regarding the environmental scenarios, real data from the location was used to determine the temperature and moisture loads. According to the climate records, Pavia has an annual average temperature $\vartheta = 13$ °C, and an annual average relative humidity $\mathrm{RH} = 70$ % (*Climate and Average Weather Year–Round in Pavia, Italy*, 2022). These yearly average values were taken as the initial conditions for the walls, thus $\vartheta_0 = 13$ °C and $\varphi_0 = 0.70$. The climatic data were used as well to locate the coldest and warmest day of the year and define the lowest and highest expected temperatures, respectively. As shown in Figure 5.6a, the lowest temperature would occur on 12 January at dawn, $\vartheta_{low} = -4$ °C. On the other hand, Figure 5.6b shows the highest expected temperature, $\vartheta_{high} = 34$ °C, documented on 26 July during the afternoon.

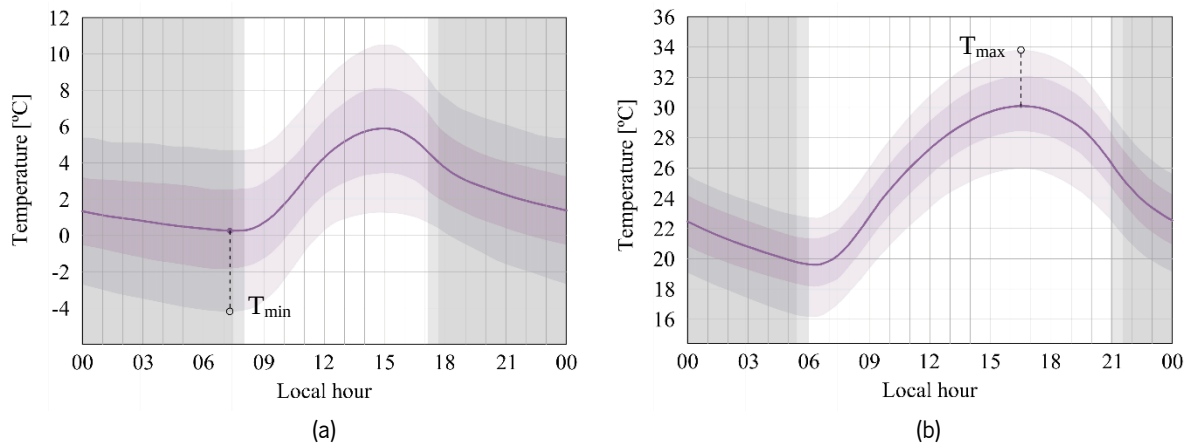

Figure 7.5. Temperature records for the city of Pavia: (a) coldest day of the year; (b) warmest day of the year. Adapted from *Climate and Average Weather Year–Round in Pavia, Italy* (2022).

The final load cases proposed for the simulations with their corresponding environmental conditions are presented in Table 7.3. More specifically, the values in the table were used as fixed boundary conditions imposed on the external and internal surfaces of the model. The highest and lowest temperatures previously introduced were selected for the extreme thermal cases. Additionally, a more severe summer scenario was considered by adding the contribution of direct solar exposure. Thus, a thermal supplement from solar radiation was added as indicated by Holm et al. (2004), which recorded +20 °C for a sunny summer day in a west–facing wall with dark finishing. A soaked façade after wind–driven rain was considered the most severe moisture condition, i.e. 100 % RH. It is worth mentioning that some of the presented scenarios are unlikely to occur or to sustain for prolonged times, for instance the simultaneous incidence of high temperature and high relative humidity (HT-HH), or the combination of high temperature, solar radiation and high relative humidity (HTS-HH). Nonetheless, the corresponding

analyses are proposed as an academic exercise to understand the impact that such severe conditions could have on the structure.

Table 7.3. Load cases and environmental scenarios studied for the Civic Tower of Pavia.

Type of exposure	Label	Exterior			Interior (1)	
		Temperature	Solar radiation	Relative humidity	Temperature	Relative humidity
		[°C]	[°C]	[%]	[°C]	[%]
No exposure (only gravitational loads)	SW	NA	NA	NA	NA	NA
High temperature	HT	34	NA	NA	13 / 30	NA
High temperature + Solar radiation	HTS	34	+20	NA	13 / 30	NA
Low temperature	LT	–4	NA	NA	13 / 0	NA
High humidity	HH	NA	NA	100	NA	70 / 90
High temperature + High humidity	HT-HH	34	NA	100	13 / 30	70 / 90
High temperature + Solar radiation + High humidity	HTS-HH	34	+20	100	13 / 30	70 / 90

Note: NA stands for 'not applicable'

(1) First number refers to a poorly–ventilated inner space; second number refers to a well–ventilated inner space.

Considering its function, the interior space of the tower was assumed to lack any kind of hygrothermal conditioning system to control temperature and relative humidity. Taking this into account, two scenarios were proposed for the interior conditions, namely an indoor space with little effective contact with the exterior, and a well–ventilated space with a reasonable air renovation rate. In the first case, the massive thickness of the walls would guarantee high thermal and hygric inertia, so the internal temperature and relative humidity were assumed constant and equal to the annual average, i.e. 13 °C and 70 % RH, respectively. For the second scenario, the constant air renovation would bring about variable internal conditions, so the indoor temperature and relative humidity would stay closer to the external conditions. Based on monitoring data collected in other historical towers, e.g. Froli & Formichi (2002), Saisi & Gentile (2015), di Tommaso et al. (2021), a thermal difference ±4 °C with respect to the exterior temperature was assumed on the inner space. For the moisture conditions in the well–ventilated scenario, a common value of air relative humidity during a rainy day was assumed, i.e. 90 % RH.

7.4 HYGRO–THERMO–MECHANICAL ANALYSIS OF THE CIVIC TOWER OF PAVIA

The results of the analyses presented in the previous section are examined in the following paragraphs. In particular, the proposed model is used to analyse the distribution of stresses at the base of the tower. Thus, the hygro–thermo–mechanical response is studied in terms of minimum principal stresses, σ_3, according to the load case scenario. In the following discussion, the general sign convention is adopted: compression is indicated by negative stress values, whereas tension is represented by positive stresses.

The gravitational case or self–weight scenario is used first to validate the model with respect to the normal stress values reported in the literature. As illustrated in Figure 7.6, all the points at the base of the tower present compressive stresses. Moreover, high stress concentrations are found on the southwest corner and at the base of the stairs near the entrance. The average normal compression obtained at the base of the tower is $-0.81\ \mathrm{MPa}$. It must be noted that this value refers to the area of the base corresponding to the core, i.e. neglecting the $0.15\ \mathrm{m}$ external layer in order to avoid unreliable stress concentrations caused by singularities. Additionally, the compressive stresses for the points at the interface core/cladding are $-1.70\ \mathrm{MPa}$ and $-1.11\ \mathrm{MPa}$ for the external and the internal studied point, respectively. These values are consistent with the numerical results reported by Binda et al. (1992), Anzani et al. (2000), and Taliercio & Papa (2007). Therefore, it is concluded that the model is able to reproduce the self–weight response with reasonable accuracy.

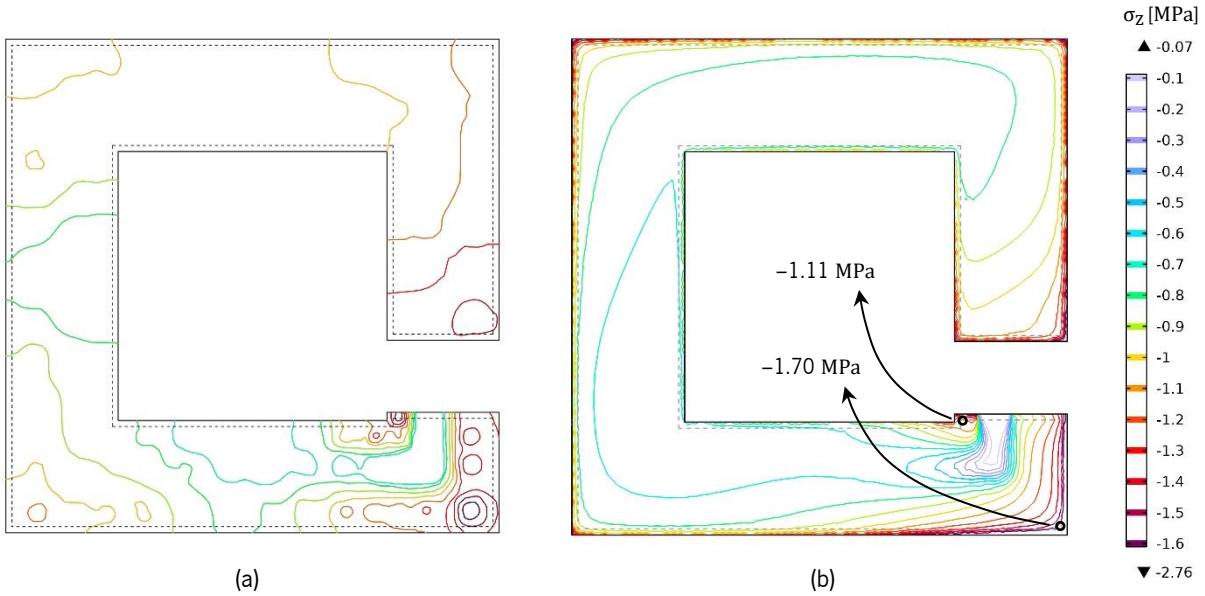

Figure 7.6. Vertical stress, σ_Z [MPa], at the base of the tower for self–weight condition: (a) results reported by Binda et al. (1992); (b) results obtained with the model developed in the present work.

In the following discussion, the effects of the proposed environmental scenarios are evaluated in terms of minimum principal stresses, σ_3 [MPa], which is the value assumed to control failure in a simplified

approach. The results obtained for the different load cases are presented in Figure 7.7. Note that the graphs are organised according to the studied element (shown in different rows) and the approach adopted for the internal boundary conditions of the tower due to the ventilation scenarios (left or right columns).

To begin with, the stresses obtained for the point close to the external face, labelled P.Ext, are shown in Figure 7.7a. The results demonstrate that the environmental actions considered have a significant impact on the structural response. In particular, the compressive stresses induced by high temperature (HT) and the combination of high temperature and solar radiation (HTS) account for 38 % and 73 % of the stress calculated for the self–weight condition. The low temperature condition (LT) is the only action that causes tension on the outer surface, but its influence is negligible. The rain or high humidity case (HH) causes swelling, and the resulting compressive stresses are equivalent to about 62 % of the self–weight. Finally, the most severe scenarios induce stresses that equal or even surpass the compressive values of the dead loads. In particular, the high temperature and high humidity combination (HT-HH) produces the same compressive stresses as the self–weight condition alone, whereas the simultaneous action of high temperature, solar radiation and high humidity (HTS-HH) results in compression levels $\times 1.35$ times higher than the self–weight. Nonetheless, as it was previously mentioned, these scenarios are unlikely to occur or to sustain in time long enough for such stresses to develop.

The stresses for the point near the internal face, labelled P.Int, are presented in Figure 7.7c. The results show expected trends considering the poorly–ventilated scenario where the internal conditions are stable and equal to the assumed initial conditions of the walls. The low temperature (LT) case is the most relevant scenario and causes around 9 % of the stress value estimated from dead loads. Additionally, the cases HTS and HTS-HH induce minor compressive stresses, namely 6 % and 7 %, respectively, with respect to the stress caused by dead loads. The rest of the cases produce negligible compression below 5 % of the value calculated for self–weight.

The average stresses at the base are shown in Figure 7.7e. It is recalled that the presented values refer to the core area of the cross–section, that is without the outermost $0.15\ \mathrm{m}$. The results reveal similar trends to the ones discussed previously for the point P.Ext near the southwest corner. This is expected since the environmental loads are being applied from the outside to the inside (the wall has initial conditions equal to the interior temperature and relative humidity), thus a point close to the outer surface such as P.Ext might be understood as a paradigmatic case. However, the average stress levels at the base induced by the environmental loads reveal smaller proportions with respect to the self–weight condition, which is an indication of how the perturbations caused by external variations dissipate across

the thickness of the walls. In other words, the environmental actions defined in this manner, i.e. fixed, constant internal conditions, do not have a generalized effect over the whole structure but instead affect local areas close to the exposed surfaces. Therefore, the cases HT, HTS and HH result in average stresses equal to 18 %, 35 % and 18 %, respectively, of the average stresses caused by dead loads. The external lowest temperature (LT) has only a minor impact on the structural response. Finally, the most severe combinations, i.e. HT-HH and HTS-HH, cause average compressive stresses at the base equivalent to 36 % and 54 % of the self–weight.

The second group of analyses with a well–ventilated inner space is discussed hereafter. First, it is noted that the shift of internal boundary conditions does not imply major changes in the trends observed at the point close to the exterior P.Ext (Figure 7.7b) nor in the average response obtained at the base of the tower (Figure 7.7f). It is observed, however, that the stress levels for the new scenario are higher than the ones calculated with the poorly–ventilated assumption. This is expected since the updated environmental conditions defined for the interior imply an additional perturbance (note that the initial conditions were kept as in the previous group of analyses equal to the annual averages $\vartheta_0 = 13$ °C and $\varphi_0 = 0.70$). Therefore, for the well–ventilated scenario, the compressive values calculated at P.Ext for the different hygrothermal cases are equivalent to the self–weight condition in the following percentages: HT, 42 %; HTS, 78 %; LT, –2 % (tension); HH, 70 %; HT-HH, 112 %; and HTS-HH, 147 %. On the other hand, the average stress at the base of the tower induced by the environmental actions is related to the average compressive stress of the self–weight case as follows: HT, 28 %; HTS, 45 %; LT, 8 %; HH, 32 %; HT-HH, 60 %; and HTS-HH, 77 %.

As expected, the response obtained at the point P.Int with the well–ventilated indoor scenario (see Figure 7.7d) presents the greatest changes with respect to the poorly–ventilated assumption. For all cases and combinations of environmental actions, compressive stresses are found on the internal side of the wall. In particular, the cases HT and HTS induce 19 % and 22 %, respectively, of the compressive stress produced by dead loads at the same point. Moreover, the scenarios LT and HH result in lower stress levels, namely 10 % and 14 %, respectively, of the self–weight response. Finally, the combinations HT-HH and HTS-HH produce similar stresses, around 35 % of the compression obtained for the self–weight.

Considering the previous results, it is demonstrated that the mechanical response of the tower can be greatly influenced by the hygrothermal conditions. Apart from the least expected cases, some common environmental scenarios may already induce considerable stress levels. Between the most expected, most aggressive cases, we may point out direct solar exposure during a hot summer day (HTS), or wind–driven rain soaking the façade (HH).

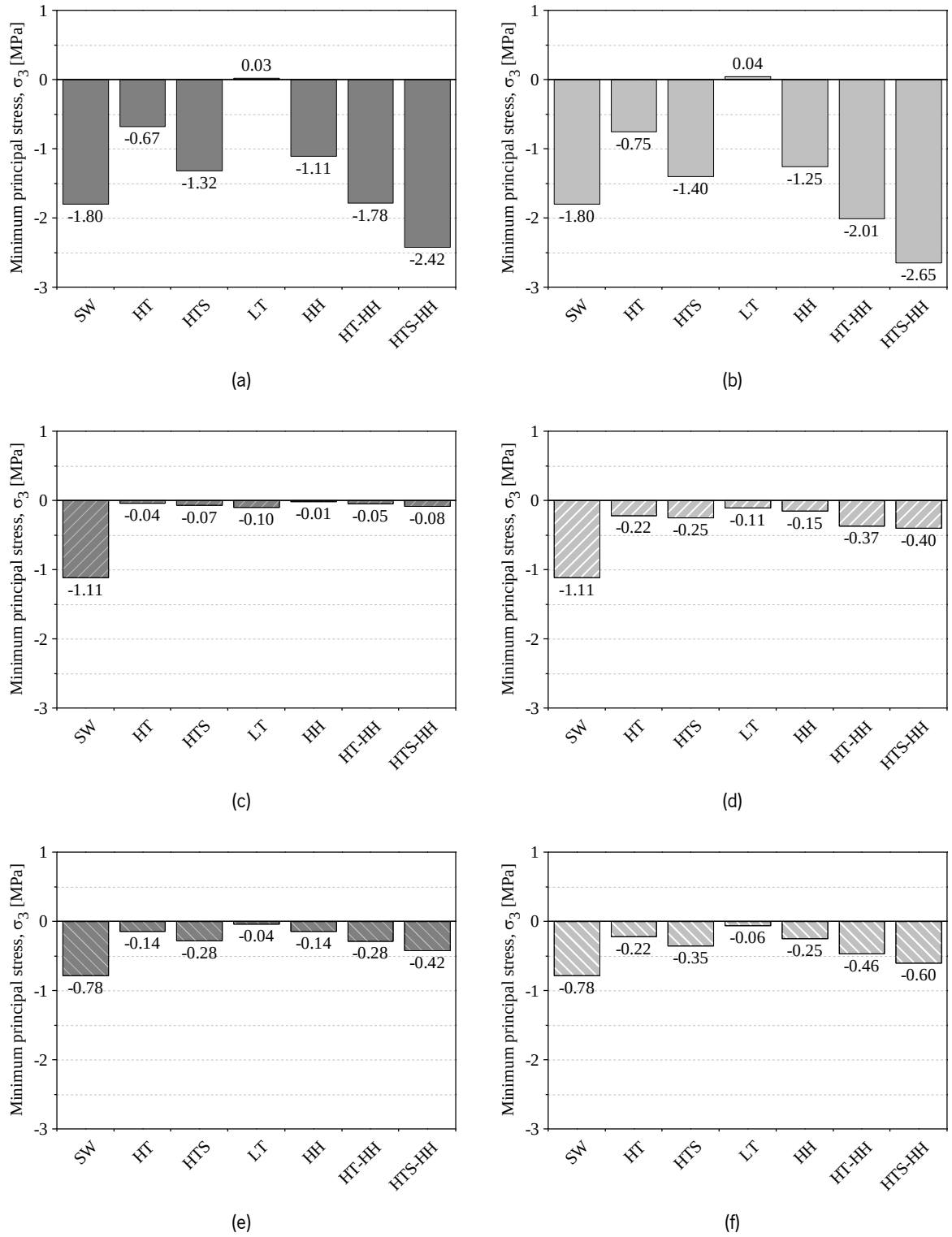

Figure 7.7. Minimum principal stress, σ_3 [MPa], obtained at the base of the tower for different load cases: (a) P.Ext, poorly–ventilated inner space; (b) P.Ext, well–ventilated inner space; (c) P.Int, poorly–ventilated inner space; (d) P.Int, well–ventilated inner space; (e) Core, poorly–ventilated inner space; (f) Core, well–ventilated inner space.

Uncertainties and shortcomings of the model have been discussed already, namely the adequacy of extreme environmental scenarios, or the lack of information regarding the hygrothermal properties of the

material. Other limitations are, for instance, the assumption of elastic behaviour or the steady–state approach. For more accurate simulations, a non–linear (possibly anisotropic) constitutive model should be used, with different behaviour for tension and compression, and the capacity to reproduce the time–dependent (creep) damage observed in the experimental tests (Binda et al., 1992). On the other hand, hygrothermal steady–state analyses deal with equilibrium states rarely achievable in real cases. As demonstrated by Ferretti & Bazant (2006a), the humidity field inside massive structures is not uniform and its evolution lasts for centuries. With respect to this topic, it might be presumed that most environmental loads, e.g. thermal cycles, rain or moisture variation, probably affect no more than a thin layer of the exposed wall surfaces. Considering the scarce amount of experimental data retrieved from real cases, more research on this topic is still needed. As it was previously mentioned, the results of thermo– and hygro–mechanical analyses are greatly dependent on the initial conditions for which free–strain equilibrium is defined. Appropriate monitoring of the building envelope would contribute as well to defining more consistent initial conditions. Finally, it is recalled that the calculated temperature– and moisture–induced stresses are directly proportional to the coefficients of thermal and hygric expansion, respectively. Consequently, the results are sensitive to these parameters and appropriate material characterization is needed to guarantee accurate, reasonable results.

7.5 CHAPTER CONCLUSIONS

This chapter presents the application of a hygro–thermo–mechanical (HTM) model to simulate how different hygrothermal phenomena affect the structural behaviour of a massive masonry structure. In particular, the former Civic Tower of Pavia (Italy) is chosen as a case study. Based on the available documentation, a model of the tower is prepared following a finite element macro–modelling approach. Furthermore, material properties are taken from specialized literature or extrapolated from experimental data. The main purpose of the study is to evaluate the distribution of stresses at the base of the tower and analyse the impact of different temperature and moisture loads on the structural response.

Initially, a mesh sensitivity study is performed, and the self–weight response is analysed. The results of the gravitational case are validated against stress values reported in the literature. Then, a series of environmental scenarios are proposed according to the climate records of the city of Pavia. For the interior conditions, two cases are considered, namely a closed or poorly–ventilated space and a more open or well–ventilated scenario. Finally, a comparative strategy is adopted to contrast the environmentally–induced stresses with the stress levels calculated for the self–weight condition. Thus, steady–state analyses are performed for the different temperature and moisture cases while neglecting the contribution

of dead loads. It is shown that the highest concentration of thermal and hygric stresses occurs in areas close to the external side of the walls where the hygrothermal loads are applied.

As evidenced by the presented case study, the hygro–thermo–mechanical response of a structure can be significantly affected by environmental conditions. Disregarding the most unlikely events, it is proven that common hygrothermal scenarios such as direct sun exposure during a hot summer day or particularly rainy periods can induce stresses up to 70–80 % of the stress level caused by the self–weight alone. This can be particularly problematic for structures already subjected to high stress levels as well as buildings with existing damage or material deterioration.

The presented model constitutes a simplified approach and introduces a series of assumptions, e.g. linear elastic material behaviour, steady–state conditions or macro–modelling technique. A non–linear (possibly anisotropic) material model is recommended, with different constitutive laws for tension and compression and the capacity to reproduce creep behaviour. Moreover, transient analyses based on detailed monitored data could be used to replicate scenarios closer to real environmental conditions. Finally, it is recalled that hygrothermal phenomena are mostly cyclic loads. Therefore, the consideration of material fatigue is strongly recommended for the vulnerability assessment of similar historical masonry structures. Nonetheless, it is acknowledged that the consideration of all these phenomena simultaneously still poses great challenges due to the availability of data as well as computational limitations of available software.

This page has been intentionally left blank

CHAPTER 8

Conclusions and future work

This final chapter summarises the main results and conclusions of the presented works. First, a brief review of the research process and methodology is provided. Then, the main findings of the experimental and numerical works are recalled. Moreover, the reported outcomes open the door to new questions and possibilities in the field of hygro–thermo–mechanical analysis of masonry elements and structures. Consequently, some suggestions for future works are given at the end of the chapter.

8.1 RESEARCH OUTLINE

The investigation presented in this thesis addresses the hygro–thermo–mechanical analysis of masonry elements and structures subjected to real environmental conditions. The research was organized into different tasks including the experimental characterization of material properties, as well as numerical simulations of heat and moisture transport and their influence on the mechanical behaviour of masonry.

An extensive experimental campaign was conducted to determine the physical and hygric properties of brick masonry together with some relevant thermo–mechanical and hygro–mechanical parameters. First, the constituent materials were assessed individually. Subsequently, masonry was studied as a multi–layered composite material. The experimental program included vacuum saturation, immersion at atmospheric pressure, gravimetric tests to determine the moisture storage curves, water vapour permeability, initial rate of absorption, capillary absorption, drying tests, tests to determine the coefficients of thermal and hygric expansion, and mercury intrusion porosimetry.

Regarding the numerical simulations, a muti–phase diffusivity moisture transport model was used to reproduce water absorption and drying in single materials and multi–layered masonry specimens. To this aim, a series of finite element models were prepared using COMSOL Multiphysics. The simulation results were compared against the experimental evidence, and the corresponding material parameters were calibrated to improve curve fitting. A parametric study was conducted in parallel to analyse the sensitivity of the models to the different parameters involved in their definition. Similarly, a hysteresis model was defined in order to capture the differences observed between water absorption and drying. Finally, different modelling approaches commonly used for the structural analysis of masonry were tested in their application to moisture transport problems.

A fully–coupled hygrothermal model was employed to simulate heat and mass transfer in a brick masonry wall. The proposed model combines the previous muti–phase diffusivity moisture transport model with a thermal model based on conductive heat transfer with an explicit account for the heat of vaporization. Steady–state and time–dependent analyses were performed and the hygrothermal response of the wall was examined for different scenarios. Likewise, the influence of using different types of mortar was investigated. Subsequently, the hygrothermal model was extended to incorporate mechanical effects and a unidirectionally coupled hygro–thermo–mechanical model was employed to analyse the stress distribution of masonry elements as affected by temperature and moisture loads. The capabilities of the hygro–thermo–mechanical analysis were tested on the same masonry wall studied for the hygrothermal analyses and on a real massive masonry structure selected as a case study.

8.2 CONCLUSIONS

The main objective of this thesis was to advance our understanding of the hygro–thermo–mechanical behaviour of masonry and thus contribute to the characterization of masonry materials and structures. The concluding remarks on the developed research are summarised in the following subsections. The outcome of the experimental tasks is presented first, followed by the conclusions derived from the numerical investigation.

8.2.1 Conclusions from the experimental work

The experimental results have contributed to extend the available database on physical, moisture–related, thermo– and hygro–mechanical properties of masonry constituent materials, namely extruded fired–clay brick, natural hydraulic lime mortar and cement mortar. The obtained properties make up a consistent dataset which might be used as input for numerical models as well as for validation of simulation results. Regarding the testing methods for the moisture–related properties, it is shown that the results from the different experimental procedures are consistent and present acceptable variation. Nevertheless, cup tests showed poorer reliability and a revision of the methodology should be considered.

With respect to the hygric performance of single materials, extruded fired–clay bricks (B) showed a characteristic anisotropic behaviour, more noticeable for faster processes such as water absorption. This behaviour can be explained by the existence of imperfections resulting from the extrusion process. On the other hand, there were notable differences between the hygric response of the two moulded mortars. Lime mortar (LM) showed low hygroscopicity and strong capillary–active behaviour with negligible hysteresis. Conversely, cement mortar (CM) showed both hygroscopic and capillary–active behaviour with a marked hysteresis. Thus, the behaviour of LM was more similar to the one of the fired–clay brick.

The properties of the lime mortar prepared in moulds (LM) differed from the same mixture cured in masonry bed joints (LMJ). The observed discrepancies can be related to the different water–binder ratio resulting from water extraction by the bricks upon placement. In particular, LMJ showed a more hygroscopic behaviour than its moulded counterpart, with non–negligible hysteresis. From the results of water absorption tests on masonry cylinders, it was concluded that LMJ has a lower water absorption coefficient in comparison with LM. Furthermore, drying tests on masonry specimens revealed mass loss curves with a short initial drying stage, which is indicative of an enhanced water retention capacity and the presence of finer pores.

Considering the results for multi–layered masonry specimens, the existence of an imperfect hydraulic contact at the brick–mortar interface was demonstrated for water absorption. The imperfect contact manifested as a hydraulic resistance and its effect ranged from a slight reduction to considerable retardation of the water flow. The interfacial effect was more evident when the water moved from LMJ to B. Thus, discontinuity in the pore structure of the materials (finer pores in LMJ) was assumed as the main reason for the interfacial effect. On the contrary, the drying results from multi–layered specimens could not confirm the existence of interfacial effects on the drying kinetics of masonry.

Due to the existence of an imperfect interfacial contact, the hygric properties obtained individually from testing the constituent materials in isolation cannot be directly extrapolated to multi–layered cases. Two main phenomena must be taken into consideration in order to avoid erroneous estimations, namely: (a) for water absorption, the dissimilar pore structure between the materials in contact generates a hydraulic interfacial resistance; (b) for water absorption and drying, the impact of curing conditions on the properties of mortars cast in masonry joints must be considered.

The results from mercury intrusion porosimetry (MIP) allowed for a comparison of the microstructure of the materials and confirmed the assumptions made from water absorption and drying tests. The percentage of porous volume occupied by macro–pores was the highest in LM, followed by B, LMJ and finally CM, which showed a significant volume of finer pores. The larger presence of finer pores can be related to the hygroscopic character of the materials, especially CM and LMJ to a lesser degree. Moreover, the different curing conditions of LM and LMJ entailed significant changes in the pore structures of the two mortars. In particular, LMJ presented a shift towards smaller pore diameters and a less accentuated distribution in comparison with its moulded counterpart.

8.2.2 Conclusions from the numerical simulations

The proposed moisture transport model was able to capture water absorption and drying processes in multi–layered masonry materials with great accuracy. The set of input parameters needed for the definition of the model comprises bulk density, open porosity, capillary moisture content, capillary absorption coefficient, moisture storage curves (for both adsorption and desorption if the material presents hysteresis), and water vapour permeability/resistance. Moreover, two additional parameters were chosen as calibration variables to fit the experimental results. In particular, the interface hydraulic resistance was selected as the calibration parameter for capillary absorption in multi–layered cases, whereas the diffusivity factor γ defined for the liquid water diffusivity function was used to calibrate drying.

It was demonstrated that the diffusivity function needs to be adjusted depending on the process, namely wetting or drying. Hence, a diffusivity factor γ was proposed as an adjustable parameter within the liquid water diffusivity function in order to accommodate both processes. The diffusivity factor for desorption, γ_{des}, can be calibrated from drying test results. Since the materials exhibit different behaviour according to the type of process, validation of moisture transport models should always consider both absorption and drying.

No analytical method was found in the literature to evaluate the interface hydraulic resistance consistently. The results presented here for multi–layered cases were not sufficient to provide a definitive answer either. Nonetheless, based on the evidence collected from experimental tests and numerical simulations, it was possible to conclude that the interface behaviour depends on (a) the materials in contact, (b) the geometric arrangement of the layers, and (c) the existence (or absence) of previous interfaces. For the simulations of water absorption in masonry specimens, the interface impact was calibrated by an iterative process of curve–fitting. Moreover, it was proven that for the imposed conditions the interface resistance had no impact on drying.

A hysteresis model was defined to capture the observed differences between water absorption and drying processes. In particular, a hysteresis index was implemented to control the transition between the adsorption and desorption liquid diffusivity functions. The hysteresis model was able to reproduce the transition from wetting to drying but showed less accuracy for the case where drying was followed by wetting since that situation requires a much more abrupt change between the diffusivity functions.

Different modelling approaches commonly used for the structural analysis of masonry were applied to the study of moisture transport problems. Depending on the adopted model, different parameters can be used to calibrate the hygric behaviour. The models with an explicit account of the interfaces, namely detailed micro– and discrete micro–modelling, showed higher accuracy and flexibility. Conversely, the

macro–modelling approach required less input parameters but was less accurate as well. In turn, the continuous micro–modelling approach was a good compromise between accuracy and simplicity. All these modelling strategies are suitable for coupling with mechanical studies to define hygro–mechanical models.

The hygrothermal analyses performed on the three–wythe brick masonry wall led to several key points according to the type of study. It was found that for the steady–state analysis, there were no significant differences between the wall with lime mortar (LMJ) and the wall with cement mortar (CM). Similarly, for the transient study with constant boundary conditions (from initial conditions until steady–state equilibrium), only minor differences were observed between the two mortar cases. Therefore, both scenarios could be simulated following a macro–modelling approach with equivalent masonry properties or be simplified into a 1–D analysis without compromising the accuracy of the results. Furthermore, considering the results of the time–dependent hygrothermal study, it was observed that heat transfer is significantly faster than moisture transport. In fact, thermal processes can be considered instantaneous in comparison with mass transfer, which requires a significant amount of time to reach equilibrium. On the other hand, the time–dependent study with variable boundary conditions showed differences in the hygrothermal performance of the wall depending on the type of mortar. As expected, the LMJ case showed a more uniform response due to the similar behaviour of bricks and lime mortar. On the contrary, the CM case presented localized behaviour depending on the material. Independently of the type of mortar, the interface hydraulic resistance had a negligible impact for the moisture conditions considered. Thus, assuming variable boundary conditions, the LMJ case could be simplified to a 1–D macro–modelling approach but the same strategy applied to the CM wall would result in a loss of detail and accuracy.

Considering the hygro–thermo–mechanical simulations of the three–wythe brick masonry wall, it was demonstrated that the imposed temperature and moisture variations significantly changed the internal stress distributions when compared to the gravitational loads acting alone. Moreover, the brick wall with cement mortar presented higher stress levels in comparison with the wall with natural hydraulic lime mortar. This was caused by the higher thermal expansion and hygric expansion coefficients of cement in comparison with lime mortar. In this sense, the studied fired–clay brick and lime mortar would be more compatible from a hygrothermal point of view. Furthermore, it was proven that the hygro–thermo–mechanical behaviour of masonry is a 2–D phenomenon derived from the multi–layered nature of the material. Although the induced tensile stresses are generally low, they might contribute to crack propagation where cracks were already present. Similarly, the hygrothermally–induced deformations may add up to previous damage and magnify existing problems such as tilting in structures with moisture

deterioration at the base or soil permanent deformation. Lastly, the definition of initial and boundary conditions is essential for the hygro–thermo–mechanical analyses since the appearance and distribution of stresses largely depend on these parameters. In particular, considering the non–linear behaviour of the coefficient of hygric expansion, the definition of the initial moisture conditions (and therefore the associated free–strain state) greatly affects the stress evolution.

The numerical model of a historical masonry tower was used as a case study to analyse the hygro–thermo–mechanical behaviour of a real scale structure subjected to normal environmental conditions as well as more severe scenarios. It was shown that the highest concentration of thermal and hygric stresses occurred in areas close to the external side of the walls where the hygrothermal loads were applied. The conditions chosen for the interior also had an impact on the distribution and magnitude of the induced stresses. Therefore, monitoring of the hygrothermal conditions inside the buildings must be done in parallel with the recording of local climate data. As evidenced by the presented case study, the hygro–thermo–mechanical response of a structure can be significantly affected by the environmental conditions. In particular, common hygrothermal scenarios such as direct sun exposure during a hot summer day or particularly rainy periods can induce stresses up to 70–80 % of the stress level caused by the self–weight alone.

8.3 FUTURE WORK

The scientific contribution of this thesis represents a step in a greater framework of related research. Therefore, there are still critical gaps that need to be further studied. In this context, some suggestions concerning future works and parallel lines of investigation connected to this thesis are reported below:

- Development and validation of hygro–thermo–mechanical models accounting for non–linear mechanical behaviour and damage. For this purpose, damage and smeared crack models are normally used for the definition of continuum media, e.g. Mazars' damage model originally developed for concrete (Mazars et al., 2015), whereas cohesive zone modelling offers promising capabilities for the definition of interfaces in composite or multi–layered materials.
- Further hygro–mechanical characterization of porous building materials to attain a fully coupled definition between the moisture and mechanical fields. This task comprises two steps, namely the characterization of moisture–dependent mechanical properties, and the study of moisture transport accounting for mechanical effects. Furthermore, the latter step can be subdivided into two different levels depending on whether the porous material exhibits diffuse micro–cracks or macroscopic cracks. In the former case, damage can be introduced into the moisture transport

governing equations by modifying the transport coefficients or by assuming updated physical properties such as the open porosity, e.g. Castellazzi, de Miranda, Formica, et al. (2015). In the case of materials with macroscopic cracks, few studies on moisture transport in fracture media may provide useful insight, e.g. Carmeliet (2001), Roels, Vandersteen, et al. (2003).

- Future works should further go in depth over the characterization of interface hydraulic resistances in multi–layered systems, with a special emphasis on the additive effect of consecutive discontinuities. In this context, moisture profile measurements are recommended to obtain a more complete set of data and detailed information about local interface phenomena. Similarly, further studies on the drying behaviour of multi–layered masonry specimens are necessary. In particular, more severe environmental conditions are suggested since laboratory conditions may cause reduced moisture flow not sufficient to trigger interfacial phenomena.
- Investigation of the hygro–thermo–mechanical performance of different masonry wall configurations, e.g. influence of the type of bond system or presence of additional layers such as rendering mortar, thermal isolation, water vapour barrier, etc. Likewise, future research should extend to other kinds of masonry units, e.g. concrete blocks, perforated/hollow fired–clay bricks, calcium silicate bricks, etc. Subsequent studies should also account for the presence of vertical head joints and possible differences with respect to horizontal bed joints.
- Numerical studies on the hygrothermal compatibility between masonry and different types of strengthening materials and solutions. A numerical framework like the one proposed in this thesis can be extended to assess the development of internal stresses due to hygrothermal loads on strengthened masonry structures.
- Experimental research on the evolution of the hygrothermal properties of porous building materials according to the type of environment and exposure time. For this purpose, accelerated ageing tests are recommended so that the long–term hygrothermal behaviour of the materials can be studied in a shorter period. Additionally, a real–time exposure dataset must be produced in order to provide a reference baseline to the accelerated ageing tests results.
- Further investigation on the limitations and capabilities of the different modelling approaches proposed for the hygro–thermo–mechanical analysis of masonry structures. In this context, the focus should be put on a systematic study of the different homogenization techniques usually used for mechanical models and their application to heat and mass transport.

Additionally, a number of HTM–related topics should become the subject of future research:

- Moisture transport of liquid solutions and salt crystallization in porous building materials. It is known that the presence of dissolved ions changes the hygrothermal performance of porous materials, whereas salt precipitation can lead to damage due to the internal pressure caused by the formation of crystals. Several authors have already contributed with significant results in this area, e.g. Koniorczyk & Gawi (2012), Castellazzi et al. (2016).
- Assessment of building envelopes exposed to hygrothermal conditions and associated processes such as condensation, loss of thermal performance, mould growth and material decay, among others. The study of moisture–related damage risk has received more attention in recent years, e.g. Vereecken & Roels (2019), X. Zhou et al. (2021, 2022), but further research is still needed.
- Fatigue and long–term durability of masonry elements and structures exposed to hygrothermal conditions. In this context, a few works have been developed for concrete and composite materials and can be used as a reference, e.g. Ullah et al. (2017) developed a HTM model to predict long–term durability and degradation of composite structures due to environmental ageing.

Appendices

This page has been intentionally left blank

APPENDIX 1

Thermophysical properties of water

This appendix collects relevant properties of liquid water with a special emphasis on their dependence upon temperature. A detailed list of values is provided in Table A1.1 for temperatures 0–100 °C.

Table A1.1 Thermophysical properties of saturated water. Adapted from Bergman & Lavine (2017).

Temperature	Density	Dynamic viscosity	Specific heat capacity	Thermal conductivity	Heat of vaporization	Surface tension
T [K]	ρ_w [kg/m^3]	$\eta_w \cdot 10^{-6}$ [Pa · s]	C_w [J/kg]	$\lambda \cdot 10^{-3}$ [W/(m · K)]	L_v [kJ/kg]	$\sigma \cdot 10^{-3}$ [N/m]
273.15	1000.00	1750	4217	569	2502	75.6
275	1000.00	1652	4211	574	2497	75.4
280	1000.00	1422	4198	582	2485	74.7
285	1000.00	1225	4189	590	2473	73.9
290	999.00	1080	4184	598	2461	73.2
293.15	998.23	1002	4182	600	2458	72.8
295	998.00	959	4181	606	2449	72.4
300	997.01	855	4179	613	2438	71.7
305	995.02	769	4178	620	2426	70.9
310	993.05	695	4178	628	2414	70.0
315	991.08	631	4179	634	2402	69.2
320	989.12	577	4180	640	2390	68.3
325	987.17	528	4182	645	2378	67.5
330	984.25	489	4184	650	2366	66.6
335	982.32	453	4186	656	2354	65.8
340	979.43	420	4188	660	2342	64.9
345	976.56	389	4191	664	2329	64.1
350	973.71	365	4195	668	2317	63.2
355	970.87	343	4199	671	2304	62.3
360	967.12	324	4203	674	2291	61.4
365	963.39	306	4209	677	2278	60.5
370	960.61	289	4214	679	2265	59.5
373.15	957.85	279	4217	680	2257	58.9

The reader is referred to Wagner & Kretzschmar (2008) for more detailed tables with thermophysical properties of liquid water and water vapour. In addition to the tabulated values, some empirical expressions and general assumptions are presented in the following sections.

A1.1 WATER DENSITY

Liquid water density has a weak temperature dependence for the temperature range of interest in building applications. For simplicity, water density is generally assumed equal to 1000 $\mathrm{kg/m^3}$. In case more detailed calculations are necessary, the following empirical expression can be used (Kell, 1975):

$$\rho_w = (999.86760 + 17.801161\,\vartheta - 7.9425010 \cdot 10^{-3}\,\vartheta^2 - 52.56328 \cdot 10^{-6}\,\vartheta^3 + 137.68910 \cdot 10^{-9}\,\vartheta^4 - 364.46470 \cdot 10^{-12}\,\vartheta^5)/(1 + 17.735441 \cdot 10^{-3}\,\vartheta) \tag{A1.1}$$

where ϑ [°C] is the temperature.

A1.2 WATER VISCOSITY

The dynamic viscosity of a fluid (often simply referred to as viscosity), η [$\mathrm{Pa \cdot s}$], is a measure of its resistance to deformation by shear or tensile stress at a given rate. For the viscosity of water, the following empirical expression can be used for the temperature range $273.15\ \mathrm{K} < T < 413.15\ \mathrm{K}$ (COMSOL, 2021):

$$\eta_w = 1.3799566804 - 0.021224019151\,T + 1.3604562827 \cdot 10^{-4}\,T^2 - 4.6454090319 \cdot 10^{-7}\,T^3 + 8.9042735735 \cdot 10^{-10}\,T^4 - 9.0790692686 \cdot 10^{-13}\,T^5 + 3.8457331488 \cdot 10^{-16}\,T^6 \tag{A1.2}$$

where T [K] is the temperature.

A1.3 HEAT CAPACITY OF WATER

Specific heat is the energy required to raise the temperature of a unit mass of a substance by one degree. In particular, the specific heat at constant pressure or specific isobaric heat capacity, C_p [$\mathrm{J/(kg \cdot K)}$], is the energy required to raise the temperature of a unit mass of a substance by one degree as the pressure is held constant.

The specific heat capacity of liquid water has a weak thermal dependence for the range of temperatures of interest in building applications. Therefore, it is usually taken as a constant. In the present work, $C_w = 4182\ \mathrm{J/(kg \cdot K)}$, which corresponds to the specific heat capacity of water at 20 °C.

A1.4 THERMAL CONDUCTIVITY OF WATER

Thermal conductivity, λ [$\mathrm{W/(m \cdot K)}$], is the ability of a material to conduct heat and can be defined as the quantity of heat transmitted through a unit thickness of a material (in the direction normal to the surface) due to a unit temperature gradient under steady–state conditions.

Thermal conductivity is a temperature–dependent property and presents mild variations for the usual temperature range in building applications. For general purposes, the thermal conductivity of water can be taken as a constant and assumed $\lambda = 0.60\ \mathrm{W/(m \cdot K)}$, which corresponds to the thermal conductivity of water at 20 °C. For more detailed calculations, the expression proposed by Ramires et al. (1995) can be used:

$$\lambda = -0.90032 + 2.50055 \cdot \left(\frac{T}{298.15}\right) - 0.99385 \cdot \left(\frac{T}{298.15}\right)^2 \quad \text{(A1.3)}$$

where T [K] is the temperature.

A1.5 LATENT HEAT OF VAPORIZATION

Latent heat of vaporization (also known as latent heat of evaporation or enthalpy of vaporization), L_v [J/kg], is the energy required to transform a unit mass of liquid into gas under standard atmospheric pressure (101325 Pa). Moreover, the latent heat of vaporization is commonly quoted at the boiling point of the liquid. In the case of water, $L_v = 2257\ \mathrm{kJ/kg}$ measured at 100 °C and standard atmospheric pressure. Although the heat of vaporization is temperature–dependent, it is also common to assume a constant value for small temperature ranges.

A1.6 SURFACE TENSION OF WATER

Surface tension, σ [N/m], is the tendency of a liquid surface at rest to adopt the shape with the least possible surface area. At liquid–air interfaces, surface tension results from the cohesion between liquid molecules, which exerts a greater attraction between them than the adhesion forces to the molecules in the air. In order to represent the temperature dependence, Vargaftik et al. (1983) proposed the following expression for the surface tension of water in equilibrium with air at atmospheric pressure:

$$\sigma = 253.8 \cdot 10^{-3} \left(\frac{647.15-T}{647.15}\right)^{1.256} \left(1 - 0.625 \left(\frac{647.15-T}{647.15}\right)\right) \quad \text{(A1.4)}$$

where T [K] is the temperature.

This page has been intentionally left blank

APPENDIX 2

Material properties

This appendix contains a summary of relevant properties of masonry materials found in the literature. In particular, the focus is placed on physical and hygro–thermo–mechanical properties of fired–clay bricks and different types of mortar, namely cement mortar (OPC), hydrated lime mortar (HL), blended cement–lime mortar (OPC–HL), and natural hydraulic lime mortar (NHL). The compilation of hygrothermal, thermo–mechanical and hygro–mechanical properties of the selected materials is represented graphically in Figure A2.1. In turn, the corresponding values for all the studied properties are presented in Table A2.1 through Table A2.4, organized as follows:

- Table A2.1. Summary of physical and hygrothermal properties of fired–clay brick.
- Table A2.2. Summary of mechanical, thermo–mechanical and hygro–mechanical properties of fired–clay brick.
- Table A2.3. Summary of physical and hygrothermal properties of cement and lime mortars.
- Table A2.4. Summary of mechanical, thermo–mechanical and hygro–mechanical properties of cement and lime mortars.

It must be noted that the information presented in this appendix does not constitute a systematic review. Nevertheless, the number of works is sufficient to provide a general overview of the current state of the research on hygro–thermo–mechanical properties of masonry materials. In particular, some interesting conclusions can be drawn:

- Besides the study of physical properties, most research works focus on a single field, i.e. thermal, hygric or mechanical. Few works provide a comprehensive report of physical and hygrothermal properties. Expectedly, the available research including physical, thermal, hygric and mechanical properties is even more scarce.
- The results show a significant scatter. The observed deviations could be caused by intrinsic variability of the materials, different proportion of components and curing conditions for mortars, or variations derived from the testing procedure itself, e.g. lack of a unified experimental setup, operator expertise, neglected factors such as ambient temperature, etc.
- From the selected materials, brick is the most studied masonry constituent. Regarding the different types of mixes, most research works have focused on cement mortar, while hydrated

lime mortar has been studied to some extent. Conversely, the works on blended cement–lime and natural hydraulic lime mixes are scarce and do not cover all the chosen properties.

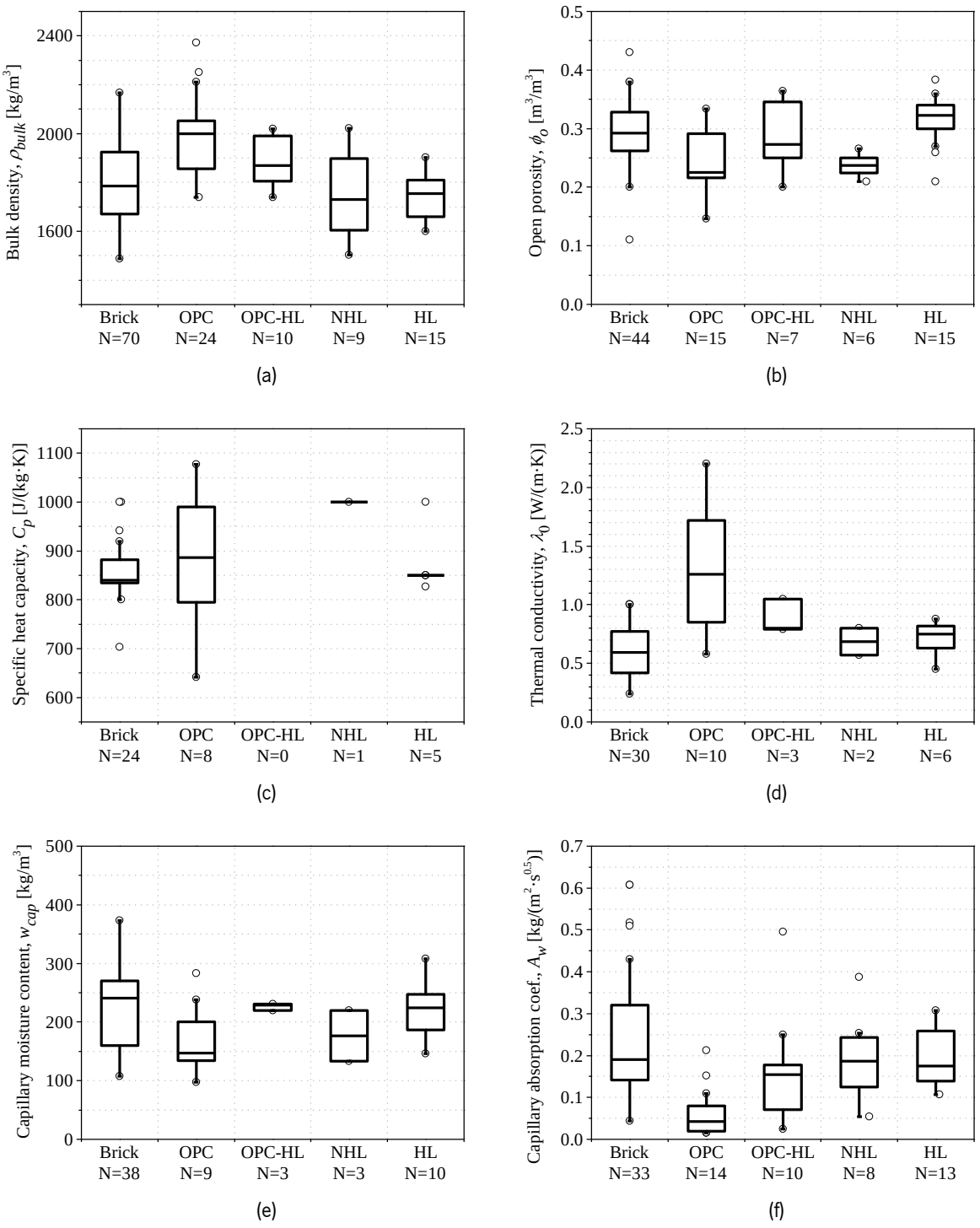

Figure A2.1. Summary of material properties collected from the literature: (a) bulk density; (b) open porosity; (c) specific heat capacity; (d) thermal conductivity; (e) capillary moisture content; (f) capillary absorption coefficient; (g) water vapour resistance (dry cup); (h) water vapour resistance (wet cup); (i) coefficient of thermal expansion; (j) coefficient of hygric expansion. 'N' stands for number of data points in each population. Edges of the boxes mark 25th and 75th percentile.

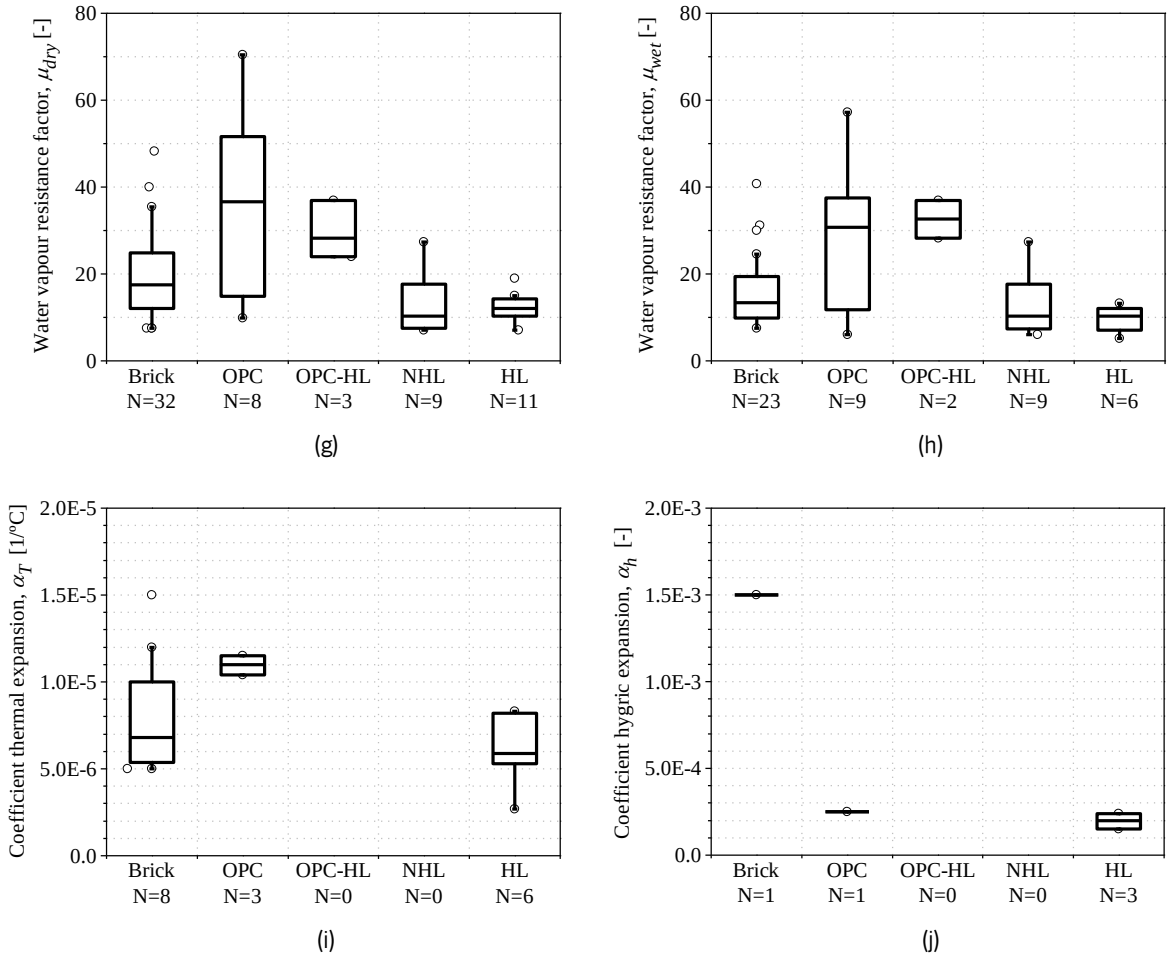

Figure A2.1 (Continued). Summary of material properties collected from the literature: (a) bulk density; (b) open porosity; (c) specific heat capacity; (d) thermal conductivity; (e) capillary moisture content; (f) capillary absorption coefficient; (g) water vapour resistance (dry cup); (h) water vapour resistance (wet cup); (i) coefficient of thermal expansion; (j) coefficient of hygric expansion. 'N' stands for number of data points in each population. Edges of the boxes mark 25th and 75th percentile.

Table A2.1. Summary of physical and hygrothermal properties of fired–clay brick.

Source	Bulk density ρ_{bulk} [kg/m³]	Open porosity ϕ_o [–]	Specific heat capacity C_p [J/(kg K)]	Thermal conductivity λ_0 [W/(m K)]	Capillary moisture content w_{cap} [kg/m³]	Capillary absorption coefficient A_w [kg/(m²s$^{0.5}$)]	Water vapour resistance μ [–]	Moisture storage function w [kg/m³]	Liquid transport model D_w or K_l [m²/s] or [s]
Alawadhi (2008)	1600.0	ND	840	0.70	ND	ND	ND	ND	ND
Bianchi Janetti & Janssen (2020)	1912.5	0.326	ND	ND	210.0	ND	ND	Retention curve	ND
Brocken (1998)	1630.0	0.360	ND	ND	270.0	0.430	ND	Sorption isotherm + Retention curve	Diffusivity
Brocken (1998)	1650.0	0.360	ND	ND	260.0	0.420	ND	Sorption isotherm + Retention curve	Diffusivity
Carmeliet & Roels (2001)	2005.0	0.240	ND	ND	160.0	0.165	48.30 (1) 31.20 (2)	Sorption isotherm + Retention curve	Permeability + Diffusivity
Castellazzi et al. (2013)	1759.0	0.260	ND	ND	264.0	0.185	23.66	Sorption isotherm	Permeability + Diffusivity
Castellazzi, de Miranda, Grementieri, et al. (2015)	1700.0	0.200	840	0.77	ND	0.185	24.53	Sorption isotherm	Permeability + Diffusivity
COMSOL (2021)	2000.0	ND	900	0.50	ND	ND	ND	ND	ND
de Freitas et al. (1996)	1925.0	0.280	ND	ND	250.0	ND	ND	ND	Diffusivity
Defraeye et al. (2013)	2005.0	ND	840	0.50	157.0	ND	30.00 (1)	Retention curve	Permeability
Delgado et al. (2019b)	1800.0	0.320	ND	0.40	261.4	0.100	33.10 (1)	Sorption isotherm	Diffusivity

ND stands for 'not defined'; (1) Dry cup test; (2) Wet cup test'; (3) The authors provide water vapour permeability as a function of capillary pressure.

Table A2.1 (Continued). Summary of physical and hygrothermal properties of fired–clay brick.

Source	Bulk density ρ_{bulk} [kg/m³]	Open porosity ϕ_o [–]	Specific heat capacity C_p [J/(kg K)]	Thermal conductivity λ_0 [W/(m K)]	Capillary moisture content w_{cap} [kg/m³]	Capillary absorption coefficient A_w [kg/(m²s$^{0.5}$)]	Water vapour resistance μ [–]	Moisture storage function w [kg/m³]	Liquid transport model D_w or K_l [m²/s] or [s]
Delgado et al. (2019b)	1600.0	0.380	ND	0.38	233.1	0.190	24.90 (1)	Sorption isotherm	Diffusivity
EN ISO 10456 (2007)	2000.0	ND	800	1.00	ND	ND	40.00 (1) 30.00 (2)	ND	ND
Feng et al. (2020)	1857.8	0.291	ND	ND	191.4	0.517	12.93 (1) 9.83 (2)	ND	ND
Feng & Janssen (2016)	2081.7	0.209	ND	ND	107.6	0.052	23.02 (1)	Sorption isotherm	ND
Feng & Janssen (2021)	1818.3	0.326	ND	ND	209.6	0.607	12.10 (1) 11.07 (2)	Sorption isotherm + Retention curve	Permeability + Diffusivity
Fernandes & Lourenço (2007)	1656.0	0.275	ND	ND	248.4	ND	ND	ND	ND
Fernandes & Lourenço (2007)	1739.0	0.304	ND	ND	326.9	ND	ND	ND	ND
Fernandes & Lourenço (2007)	1742.0	0.330	ND	ND	371.0	ND	ND	ND	ND
Fernandes & Lourenço (2007)	1747.0	0.292	ND	ND	311.0	ND	ND	ND	ND
Fernandes & Lourenço (2007)	1754.0	0.263	ND	ND	277.1	ND	ND	ND	ND
(Fernandes & Lourenço, 2007)	1800.0	0.282	ND	ND	316.8	ND	ND	ND	ND

ND stands for 'not defined'; (1) Dry cup test; (2) Wet cup test'; (3) The authors provide water vapour permeability as a function of capillary pressure.

Table A2.1 (Continued). Summary of physical and hygrothermal properties of fired–clay brick.

Source	Bulk density ρ_{bulk} [kg/m³]	Open porosity ϕ_o [–]	Specific heat capacity C_p [J/(kg K)]	Thermal conductivity λ_0 [W/(m K)]	Capillary moisture content w_{cap} [kg/m³]	Capillary absorption coefficient A_w [kg/(m²s$^{0.5}$)]	Water vapour resistance μ [–]	Moisture storage function w [kg/m³]	Liquid transport model D_w or K_l [m²/s] or [s]
Fernandes et al. (2010)	1200.0–1900.0	0.250–0.350	ND	ND	240.0–300.0	0.207–0.258	ND	ND	ND
Franzoni et al. (2019)	1679.0	0.430	ND	ND	ND	0.327	ND	ND	ND
Groot (1991)	1990.0	0.250	ND	ND	ND	0.190	ND	ND	ND
Guizzardi et al. (2016)	1550.0	0.350	840	0.68	300.0	0.187	16.00	Retention curve	Permeability
Güney & Caner (2015)	1820.0	0.270	ND	ND	ND	ND	ND	ND	ND
Güney & Caner (2015)	1800.0	0.310	ND	ND	ND	ND	ND	ND	ND
Güney & Caner (2015)	1800.0	0.270	ND	ND	ND	ND	ND	ND	ND
Hagentoft et al. (2003)	1600.0	0.374	1000	0.68	ND	ND	7.50 (1)	Retention curve	Permeability
K. K. Hansen (1986)	1860.0	0.310	ND	ND	ND	ND	ND	Sorption isotherm	ND
T. K. Hansen et al. (2016)	1790.0	0.360	ND	0.87	ND	0.230	14.00	ND	ND
T. K. Hansen et al. (2016)	2060.0	0.250	ND	1.00	ND	0.100	19.00	ND	ND

ND stands for 'not defined'; (1) Dry cup test; (2) Wet cup test'; (3) The authors provide water vapour permeability as a function of capillary pressure.

Table A2.1 (Continued). Summary of physical and hygrothermal properties of fired–clay brick.

Source	Bulk density ρ_{bulk} [kg/m³]	Open porosity ϕ_o [–]	Specific heat capacity C_p [J/(kg K)]	Thermal conductivity λ_0 [W/(m K)]	Capillary moisture content w_{cap} [kg/m³]	Capillary absorption coefficient A_w [kg/(m²s$^{0.5}$)]	Water vapour resistance μ [–]	Moisture storage function w [kg/m³]	Liquid transport model D_w or K_l [m²/s] or [s]
T. K. Hansen et al. (2016)	1713.0	0.380	ND	0.52	ND	0.310	12.00	ND	ND
Janssen et al. (2007)	2005.0	ND	840	0.50	157.0	0.141	ND [3]	Retention curve	Permeability
Jensen et al. (2020)	1643.0	ND	ND	0.60	ND	0.278	16.90 [1]	ND	ND
Karaman et al. (2006)	1710.0	ND	ND	ND	296.7	ND	ND	ND	ND
Knarud et al. (2021)	2166.0	ND	ND	ND	116.7	0.044	40.78 [2]	ND	ND
Knarud et al. (2021)	1723.0	ND	ND	ND	255.7	0.188	13.36 [2]	ND	ND
Kočí et al. (2018)	1831.0	0.279	825	0.59	ND	0.262	22.10 [1] 8.80 [2]	Sorption isotherm	Diffusivity
Koniorczyk & Gawin (2012)	1834.0	0.293	ND	0.77	ND	ND	ND	Retention curve	Permeability
Kumaran (1996)	1780.0	0.315	840	ND	220.0	0.119	ND [3]	Sorption isotherm	Diffusivity
Kumaran (1996)	1800.0	0.110	920	1.00	ND	ND	7.50 [1] 7.50 [2]	Sorption isotherm + Retention curve	Diffusivity
Kumaran (1996)	1980.0	0.250	ND	ND	ND	ND	17.75 [1] 8.50 [2]	Sorption isotherm	Diffusivity

ND stands for 'not defined'; [1] Dry cup test; [2] Wet cup test'; [3] The authors provide water vapour permeability as a function of capillary pressure.

Table A2.1 (Continued). Summary of physical and hygrothermal properties of fired–clay brick.

Source	Bulk density ρ_{bulk} [kg/m³]	Open porosity ϕ_o [–]	Specific heat capacity C_p [J/(kg K)]	Thermal conductivity λ_0 [W/(m K)]	Capillary moisture content w_{cap} [kg/m³]	Capillary absorption coefficient A_w [kg/(m²s$^{0.5}$)]	Water vapour resistance μ [–]	Moisture storage function w [kg/m³]	Liquid transport model D_w or K_l [m²/s] or [s]
Kumaran (1996)	1676.0	ND	ND	0.42	270.0	0.112	ND	ND	Diffusivity
Kumaran (1996)	1890.0	ND	ND	ND	ND	ND	ND	Sorption isotherm	ND
Kumaran (1996)	1800.0	ND	ND	ND	ND	0.330	35.50 (1)	Sorption isotherm	ND
Kumaran (1996)	1676.0	ND	ND	ND	ND	ND	17.30 (1) 13.50 (2)	ND	ND
Kumaran (2001)	1670.0	ND	840	0.40	195.4	0.110	ND (3)	Sorption isotherm	Permeability + Diffusivity
Künzel (1995)	1600.0	ND	ND	ND	ND	ND	9.50 (1) 8.00 (2)	ND	ND
Laaroussi et al. (2014)	1777.0	ND	820	0.35	ND	ND	ND	ND	ND
Laaroussi et al. (2014)	1652.0	ND	820	0.35	ND	ND	ND	ND	ND
Lucchi (2017)	1487.0	ND	830	0.48	ND	ND	ND	ND	ND
Moonen et al. (2010)	2086.5	ND	900	1.00	130.0	ND	ND (3)	Retention curve	Permeability
Nunes et al. (2017)	2000.0	0.330	ND	ND	ND	ND	ND	ND	ND

ND stands for 'not defined'; (1) Dry cup test; (2) Wet cup test'; (3) The authors provide water vapour permeability as a function of capillary pressure.

Table A2.1 (Continued). Summary of physical and hygrothermal properties of fired–clay brick.

Source	Bulk density ρ_{bulk} [kg/m³]	Open porosity ϕ_o [–]	Specific heat capacity C_p [J/(kg K)]	Thermal conductivity λ_0 [W/(m K)]	Capillary moisture content w_{cap} [kg/m³]	Capillary absorption coefficient A_w [kg/(m²s$^{0.5}$)]	Water vapour resistance μ [–]	Moisture storage function w [kg/m³]	Liquid transport model D_w or K_l [m²/s] or [s]
Pavlík et al. (2012)	1675.0	0.360	ND	ND	250.0	ND	ND	Sorption isotherm	ND
Prangnell (1971)	1560.0	ND	ND	ND	ND	ND	8.00	ND	ND
Raimondo et al. (2007)	1840.9	0.253	ND	ND	ND	ND	ND	ND	ND
Raimondo et al. (2007)	1773.2	0.320	ND	ND	ND	ND	ND	ND	ND
Roels, Vandersteen, et al. (2003)	2004.8	0.240	ND	ND	157.0	0.184	ND	Retention curve	Permeability
Roels et al. (2004)	2002.9	0.238	ND	ND	147.5	0.160	12.30 (1) 10.60 (2)	ND	ND
Sassine et al. (2017)	1640.0	ND	703	0.69	ND	ND	ND	ND	ND
Soulios et al. (2020)	1886.1	0.312	ND	ND	208.0	0.607	11.60 (1) 10.20 (2)	ND	ND
Soulios et al. (2021)	1643.0	0.290	942	0.63	275.0	0.320	11.90	ND	ND
Sýkora et al. (2012)	1690.0	ND	840	0.25	229.3	0.510	16.80	Sorption isotherm	Diffusivity
Vivancos et al. (2009)	1634.0	ND	843	0.24	ND	ND	ND	ND	ND

ND stands for 'not defined'; (1) Dry cup test; (2) Wet cup test'; (3) The authors provide water vapour permeability as a function of capillary pressure.

Table A2.1 (Continued). Summary of physical and hygrothermal properties of fired–clay brick.

Source	Bulk density ρ_{bulk} [kg/m³]	Open porosity ϕ_o [–]	Specific heat capacity C_p [J/(kg K)]	Thermal conductivity λ_0 [W/(m K)]	Capillary moisture content w_{cap} [kg/m³]	Capillary absorption coefficient A_w [kg/(m²s$^{0.5}$)]	Water vapour resistance μ [–]	Moisture storage function w [kg/m³]	Liquid transport model D_w or K_l [m²/s] or [s]
Wasik et al. (2019)	2087.0	ND	840	ND	130.0	ND	24.79 (1)	Retention curve	Permeability
Zhao et al., (2022)	1952.2	0.263	863	0.96	161.0	0.142	19.40	Retention curve	Permeability
X. Zhou et al. (2018)	2005.0	ND	840	0.50	157.0	ND	30.00 (1)	Retention curve	Permeability
X. Zhou et al. (2021)	1600.0	ND	1000	0.68	373.5	0.262	7.50 (1)	Retention curve	Permeability

ND stands for 'not defined'; (1) Dry cup test; (2) Wet cup test'; (3) The authors provide water vapour permeability as a function of capillary pressure.

Table A2.2. Summary of mechanical, thermo–mechanical and hygro–mechanical properties of fired–clay brick.

Source	Young's modulus E [MPa]	Poisson's ratio ν [–]	Compressive strength f_c [MPa]	Fracture energy in compression G_c [N/mm]	Tensile strength f_t [MPa]	Fracture energy in tension G_f^I [N/mm]	Flexural strength f_b [MPa]	Coefficient of thermal expansion α_T [1/K]	Coefficient of hygric expansion α_h [–]
Bellini et al. (2019)	ND	ND	18.59	ND	2.59	ND	4.66	ND	ND
Bellini et al. (2019)	ND	ND	23.05	ND	3.14	ND	4.86	ND	ND
Brooks (2015)									
Carvill (1993)	ND	ND	ND	ND	ND	ND	ND	5.0E–6	ND
COMSOL (2021) (1)	17000	0.20	ND	ND	ND	ND	ND	6.0E–6	ND
D'Altri et al. (2018)	16700	0.15	11.50	ND	3.50	ND	ND	ND	ND
D'Altri & de Miranda (2020)	4000	0.20	4.00	9.00	1.20	0.80	ND	ND	ND
D'Altri & de Miranda (2020)	1785	0.20	7.50	10.00	2.00	1.00	ND	ND	ND
Fernandes et al. (2010) (1)	200–350 × f_c	ND	6.7–21.8	ND	0.03–0.10 × f_c	ND	ND	ND	0.1–0.2 %
Franzoni et al. (2018)	ND	ND	20.30	ND	3.16	ND	ND	ND	ND
Gentilini et al. (2019)	6200	ND	18.70	ND	1.60	ND	ND	ND	ND
Ghiassi et al. (2012)	1120	ND	19.80	ND	1.95	ND	ND	ND	ND

ND stands for 'not defined'; (1) Hygrothermal properties in Table A2.1.

Table A2.2 (Continued). Summary of mechanical, thermo–mechanical and hygro–mechanical properties of fired–clay brick.

Source	Young's modulus E [MPa]	Poisson's ratio ν [–]	Compressive strength f_c [MPa]	Fracture energy in compression G_c [N/mm]	Tensile strength f_t [MPa]	Fracture energy in tension G_f^I [N/mm]	Flexural strength f_b [MPa]	Coefficient of thermal expansion α_T [1/K]	Coefficient of hygric expansion α_h [–]
Ghiassi et al. (2013)	5580	0.20	19.80	12.50	2.00	0.19	ND	ND	ND
Güney & Caner (2015) (1)	ND	ND	ND	ND	ND	ND	ND	5.0E–6	ND
Güney & Caner (2015) (1)	ND	ND	ND	ND	ND	ND	ND	8.0E–6	ND
Güney & Caner (2015) (1)	ND	ND	ND	ND	ND	ND	ND	7.6E–6	ND
Koniorczyk & Gawin (2012)	4000	0.18	ND	ND	1.00	ND	ND	ND	ND
Krakowiak et al. (2011)	2000	ND	42.60	ND	ND	ND	ND	ND	ND
Maljaee et al. (2016a)	ND	ND	15.38	ND	ND	ND	ND	1.5E–5	ND
Maljaee et al. (2016b)	ND	ND	16.76	ND	ND	ND	ND	ND	ND
Moonen et al. (2010)	16605	0.15	ND	ND	2.00	ND	ND	1.2E–5	ND
Muñoz & Lourenço (2019)	9700	ND	19.90	ND	2.10	ND	ND	ND	ND
D. V. Oliveira et al. (2006)	12700	ND	56.80	ND	ND	ND	ND	ND	ND
Vermeltfoort et al. (1999)	ND	ND	ND	ND	ND	ND	ND	5.7E–6	ND

ND stands for 'not defined'; (1) Hygrothermal properties in Table A2.1.

Table A2.3. Summary of physical and hygrothermal properties of cement and lime mortars.

Source	Type of binder	Proportion (C:L:S;WC)	Bulk density ρ_{bulk} [kg/m³]	Open porosity ϕ_o [–]	Specific heat capacity C_p [J/(kg K)]	Thermal conductivity λ_0 [W/(m K)]	Capillary moisture content w_{cap} [kg/m³]	Capillary absorption coefficient A_w [kg/(m²s$^{0.5}$)]	Water vapour resistance μ [–]	Moisture storage function w [kg/m³]	Liquid transport model D_w or K_l [m²/s] or [s]
Brocken (1998)	OPC–HL	1:0.7:4.5; 1.2	2000.0	0.250	ND	ND	220.0	0.160	ND	S. isotherm + Retention c.	Diffusivity
Bromblet (1999)	HL	0:1:3; 0.25	ND	0.383	ND	ND	307.5	0.203	ND	ND	ND
Bromblet (1999)	HL	0:1:3; 0.20	ND	0.323	ND	ND	222.0	0.107	ND	ND	ND
Bromblet (1999)	HL	0:1:3; 0.24	ND	0.359	ND	ND	289.5	0.158	ND	ND	ND
Cardani et al. (2015)	HL	0:1:3; ND	1902.0	ND	ND	ND	228.2	0.279	ND	ND	ND
Castellazzi et al. (2013)	NHL	ND	1603.6	0.210	ND	ND	ND	0.179	23.66	Sorption isotherm	Permeability + Diffusivity
Castellazzi, de Miranda, Formica, et al. (2015)	OPC	ND	2053.0	0.230	ND	ND	ND	0.015	9.86	Sorption isotherm	Permeability + Diffusivity
Coelho et al. (2018)	HL	ND	1600.0	0.300	850	0.70	ND	ND	7.00	ND	ND
Corinaldesi et al. (2011)	OPC	1:0:3 (1); 0.60	2031.0	ND	ND	0.74	ND	ND	ND	ND	ND
Cerný et al. (2000)	OPC	1:0:3; 0.50	2250.0	0.146	750	2.20	ND	ND	57.25	ND	Diffusivity
Delgado et al. (2019b)	OPC–HL	1:1:6; 1.08	1878.0	0.200	ND	0.79	228.6	0.150	23.90 (2)	Sorption isotherm	Diffusivity

ND stands for 'not defined'; (1) Proportion by weight; (2) Dry cup test; (3) Wet cup test'; (4) The authors provide water vapour permeability as a function of capillary pressure.

Table A2.3 (Continued). Summary of physical and hygrothermal properties of cement and lime mortars.

Source	Type of binder	Proportion (C:L:S;WC)	Bulk density ρ_{bulk} [kg/m³]	Open porosity ϕ_o [–]	Specific heat capacity C_p [J/(kg K)]	Thermal conductivity λ_0 [W/(m K)]	Capillary moisture content w_{cap} [kg/m³]	Capillary absorption coefficient A_w [kg/(m²s$^{0.5}$)]	Water vapour resistance μ [–]	Moisture storage function w [kg/m³]	Liquid transport model D_w or K_l [m²/s] or [s]
Delgado et al. (2019b)	HL	0:1:3; 1.05	1810.0	0.210	ND	0.80	186.6	0.120	14.25 (2)	Sorption isotherm	Diffusivity
Depraetere et al. (1999)	OPC	1:0:3; 0.58	2000.0	0.220	ND	ND	200.0	0.073	ND	Retention curve	Diffusivity
Depraetere et al. (1999)	OPC	1:0:5; 1.15	1850.0	0.280	ND	ND	238.0	0.109	ND	Retention curve	Diffusivity
Derluyn et al. (2011)	OPC	ND	2166.0	0.160	ND	ND	120.0	0.015	35.86	Retention curve	Permeability + Diffusivity
EN ISO 10456 (2007)	NHL	ND	1600.0	ND	1000	0.80	ND	ND	10.00 (2) 6.00 (3)	ND	ND
EN ISO 10456 (2007)	OPC	ND	1800.0	ND	1000	1.00	ND	ND	10.00 (2) 6.00 (3)	ND	ND
Faria & Silva (2019)	NHL	0:1:3; 1.23	1502.0	0.250	ND	0.57	133.0	0.387	ND	ND	ND
Fort et al. (2018)	HL	0:1:3 (1); 0.50	1755.5	0.330	ND	ND	ND	0.175	10.28 (2)	ND	ND
Franzoni et al. (2019)	OPC	ND	2005.0	0.225	ND	ND	ND	0.020	ND	ND	ND
Franzoni et al. (2019)	NHL	ND	1898.0	0.266	ND	ND	ND	0.054	ND	ND	ND
Güney & Caner (2015)	HL	ND	1660.0	0.350	ND	ND	ND	ND	ND	ND	ND

ND stands for 'not defined'; (1) Proportion by weight; (2) Dry cup test; (3) Wet cup test'; (4) The authors provide water vapour permeability as a function of capillary pressure.

Table A2.3 (Continued). Summary of physical and hygrothermal properties of cement and lime mortars.

Source	Type of binder	Proportion (C:L:S;WC)	Bulk density ρ_{bulk} [kg/m³]	Open porosity ϕ_o [–]	Specific heat capacity C_p [J/(kg K)]	Thermal conductivity λ_0 [W/(m K)]	Capillary moisture content w_{cap} [kg/m³]	Capillary absorption coefficient A_w [kg/(m²s$^{0.5}$)]	Water vapour resistance μ [–]	Moisture storage function w [kg/m³]	Liquid transport model D_w or K_l [m²/s] or [s]
Güney & Caner (2015)	HL	ND	1610.0	0.310	ND	ND	ND	ND	ND	ND	ND
Güney & Caner (2015)	HL	ND	1720.0	0.340	ND	ND	ND	ND	ND	ND	ND
Hall & Tse (1986)	OPC–HL	1:3:10; 3.20	1760.0	0.364	ND	ND	ND	0.250	ND	ND	ND
Hall & Tse (1986)	OPC–HL	1:2:8; 2.20	1860.0	0.346	ND	ND	ND	0.178	ND	ND	ND
Hall & Tse (1986)	OPC–HL	1:1:5; 1.55	1830.0	0.328	ND	ND	ND	0.169	ND	ND	ND
Hall & Tse (1986)	OPC–HL	1:0.5:4; 0.93	1990.0	0.273	ND	ND	ND	0.072	ND	ND	ND
Hall & Tse (1986)	OPC–HL	1:0.25:3; 0.85	2020.0	0.265	ND	ND	ND	0.071	ND	ND	ND
Hall & Tse (1986)	OPC	1:0:7; 1.15	1740.0	0.334	ND	ND	ND	0.152	ND	ND	ND
Hall & Tse (1986)	OPC	1:0:6; 1.10	1820.0	0.326	ND	ND	ND	0.080	ND	ND	ND
Hall & Tse (1986)	OPC	1:0:5; 0.95	1830.0	0.291	ND	ND	ND	0.066	ND	ND	ND
Hall & Tse (1986)	OPC	1:0:3; 0.63	1930.0	0.262	ND	ND	ND	0.044	ND	ND	ND

ND stands for 'not defined'; (1) Proportion by weight; (2) Dry cup test; (3) Wet cup test'; (4) The authors provide water vapour permeability as a function of capillary pressure.

Table A2.3 (Continued). Summary of physical and hygrothermal properties of cement and lime mortars.

Source	Type of binder	Proportion (C:L:S;WC)	Bulk density ρ_{bulk} [kg/m³]	Open porosity ϕ_o [–]	Specific heat capacity C_p [J/(kg K)]	Thermal conductivity λ_0 [W/(m K)]	Capillary moisture content w_{cap} [kg/m³]	Capillary absorption coefficient A_w [kg/(m²s$^{0.5}$)]	Water vapour resistance μ [–]	Moisture storage function w [kg/m³]	Liquid transport model D_w or K_l [m²/s] or [s]
K. Hansen (1986)	OPC	1:0:4; 0.80	2000.0	0.220	ND	ND	ND	ND	ND	Sorption isotherm	ND
T. K. Hansen et al. (2016)	HL	ND	1800.0	0.300	ND	0.82	ND	0.130	12.0	ND	ND
Janssen et al. (2012)	OPC	ND	ND	ND	ND	ND	147.0	0.019	ND	ND	ND
Jensen et al. (2020)	OPC–HL	ND	1739.0	ND	ND	1.05	ND	0.495	28.3	ND	ND
Jensen et al. (2020)	OPC–HL	ND	1878.0	ND	ND	0.80	ND	0.036	36.9	ND	ND
Knarud et al. (2021)	OPC–HL	1:1:12.2 (1); ND	1805.5	ND	ND	ND	230.5	0.025	ND	ND	ND
Kumaran (1996)	OPC	ND	1870.0	ND	840	0.85	283.0	0.042	ND (4)	Sorption isotherm	Diffusivity
Kumaran (1996)	OPC	ND	2050.0	ND	932	1.72	ND	ND	70.50 (2) 11.70 (3)	Retention curve	Diffusivity
Kumaran (1996)	OPC	ND	2210.0	ND	980	1.71	ND	ND	ND	ND	ND
Kumaran (1996)	OPC	ND	1786.0	0.327	ND	ND	ND	ND	30.75 (3)	S. isotherm + Retention c.	Diffusivity
Kumaran (1996)	OPC	1:0:4; 0.70	2000.0	ND	ND	ND	ND	ND	ND	Sorption isotherm	ND

ND stands for 'not defined'; (1) Proportion by weight; (2) Dry cup test; (3) Wet cup test'; (4) The authors provide water vapour permeability as a function of capillary pressure.

Table A2.3 (Continued). Summary of physical and hygrothermal properties of cement and lime mortars.

Source	Type of binder	Proportion (C:L:S;WC)	Bulk density ρ_{bulk} [kg/m³]	Open porosity ϕ_o [–]	Specific heat capacity C_p [J/(kg K)]	Thermal conductivity λ_0 [W/(m K)]	Capillary moisture content w_{cap} [kg/m³]	Capillary absorption coefficient A_w [kg/(m²s$^{0.5}$)]	Water vapour resistance μ [–]	Moisture storage function w [kg/m³]	Liquid transport model D_w or K_l [m²/s] or [s]
Kumaran (1996)	OPC	1:0:4; 0.80	2000.0	0.220	ND	ND	ND	ND	ND	Sorption isotherm	ND
Moonen et al. (2010)	OPC	ND	2371.0	ND	840	1.95	97.0	ND	ND (3)	Retention curve	Permeability
Mosquera et al. (2006)	HL	0:1:3; ND	1896.0	0.269	ND	ND	ND	ND	10.89	ND	ND
Mosquera et al. (2006)	NHL	0:1:3; 0.50	2022.0	0.224	ND	ND	ND	ND	11.98	ND	ND
Nunes et al. (2017)	HL	0:1:3; 1.01	1900.0	0.330	ND	ND	ND	ND	ND	ND	ND
Pavlíková et al. (2019)	HL	0:1:3; 1.00	1742.0	0.324	827	0.88	ND	0.307	12.20 (2)	ND	ND
Penas et al. (2008)	NHL	0:1:3; 0.11	1740.0	ND	ND	ND	ND	0.232	7.48	ND	ND
Penas et al. (2008)	NHL	0:1:3; 0.12	1710.0	ND	ND	ND	ND	0.194	7.02	ND	ND
Penas et al. (2008)	NHL	0:1:3; 0.12	1730.0	ND	ND	ND	ND	0.155	7.34	ND	ND
Prangnell (1971)	OPC	ND	2015.0	ND	ND	ND	ND	ND	37.43	ND	ND
Prangnell (1971)	NHL	ND	1960.0	ND	ND	ND	ND	ND	10.30	ND	ND

ND stands for 'not defined'; (1) Proportion by weight; (2) Dry cup test; (3) Wet cup test'; (4) The authors provide water vapour permeability as a function of capillary pressure.

Table A2.3 (Continued). Summary of physical and hygrothermal properties of cement and lime mortars.

Source	Type of binder	Proportion (C:L:S;WC)	Bulk density ρ_{bulk} [kg/m^3]	Open porosity ϕ_o [–]	Specific heat capacity C_p [J/(kg K)]	Thermal conductivity λ_0 [W/(m K)]	Capillary moisture content w_{cap} [kg/m^3]	Capillary absorption coefficient A_w [kg/(m^{2}s$^{0.5}$)]	Water vapour resistance μ [–]	Moisture storage function w [kg/m^3]	Liquid transport model D_w or K_l [m^2/s] or [s]
Sassine et al. (2017)	OPC	ND	1863.0	ND	1077	1.41	ND	ND	ND	ND	ND
Silva et al. (2014)	HL	0:1:3; 1.52	ND	0.259	ND	ND	187.8	0.139	13.18	ND	ND
Silva et al. (2014)	NHL	0:1:3; 0.82	ND	0.235	ND	ND	219.3	0.094	27.28	ND	ND
Silva et al. (2015)	NHL	0:1:5; 1.35	ND	0.240	ND	ND	176.2	0.254	17.61	ND	ND
Silva et al. (2015)	OPC	1:0:3; 0.60	ND	0.188	ND	ND	142.9	0.034	46.12	ND	ND
Silva et al. (2015)	OPC	1:0:6; 1.26	ND	0.216	ND	ND	148.6	0.212	19.57	ND	ND
Siwinska & Garbalinska, (2011)	OPC	1:0:3; 1.80	2066.0	ND	ND	1.11	ND	ND	ND	ND	ND
Soulios et al. (2020)	HL	ND	1804.3	0.312	ND	ND	227.0	0.258	11.70 [(2)] 5.10 [(3)]	ND	ND
Sýkora et al. (2012)	HL	ND	1670.0	ND	1000	0.45	160.0	0.820	9.63	Sorption isotherm	Diffusivity
Xu & Chung (2000)	OPC	1:0:1; 0.35	2040.0	ND	642	0.58	ND	ND	ND	ND	ND

ND stands for 'not defined'; [(1)] Proportion by weight; [(2)] Dry cup test; [(3)] Wet cup test'; [(4)] The authors provide water vapour permeability as a function of capillary pressure.

Table A2.3 (Continued). Summary of physical and hygrothermal properties of cement and lime mortars.

Source	Type of binder	Proportion (C:L:S;WC)	Bulk density ρ_{bulk} [kg/m³]	Open porosity ϕ_o [–]	Specific heat capacity C_p [J/(kg K)]	Thermal conductivity λ_0 [W/(m K)]	Capillary moisture content w_{cap} [kg/m³]	Capillary absorption coefficient A_w [kg/(m²s$^{0.5}$)]	Water vapour resistance μ [–]	Moisture storage function w [kg/m³]	Liquid transport model D_w or K_l [m²/s] or [s]
X. Zhou et al. (2018)	HL	ND	1785.0	ND	850	ND	247.6	0.153	15.00 (2)	Retention curve	Permeability
X. Zhou et al. (2021)	HL	ND	1623.0	ND	850	0.63	146.0	0.195	19.00 (2)	Retention curve	Permeability

ND stands for 'not defined'; (1) Proportion by weight; (2) Dry cup test; (3) Wet cup test'; (4) The authors provide water vapour permeability as a function of capillary pressure.

Table A2.4. Summary of mechanical, thermo–mechanical and hygro–mechanical properties of cement and lime mortars.

Source	Type of binder	Proportion (C:L:S;WC)	Young's modulus E [MPa]	Poisson's ratio ν [–]	Compressive strength f_c [MPa]	Fracture energy in compression G_c [N/mm]	Tensile strength f_t [MPa]	Fracture energy in tension G_f^I [N/mm]	Flexural strength f_b [MPa]	Coefficient of thermal expansion α_T [1/K]	Coefficient of hygric expansion α_h [–]
Arandigoyen & Alvarez (2007)	OPC	1:0:3; ND	ND	ND	18.90	ND	ND	ND	3.60	ND	ND
Arandigoyen & Alvarez (2007)	HL	0:1:3; ND	ND	ND	1.80	ND	ND	ND	0.80	ND	ND
Bellini et al. (2019)	NHL	ND	ND	ND	6.01	ND	ND	ND	2.76	ND	ND
Bromblet (1999)	HL	0:1:3; 0.25	ND	ND	1.70	ND	ND	ND	0.50	2.7E–6	2.4E–4
Bromblet (1999)	HL	0:1:3; 0.20	ND	ND	1.35	ND	ND	ND	0.70	6.3E–6	1.5E–4
Bromblet (1999)	HL	0:1:3; 0.24	ND	ND	1.20	ND	ND	ND	0.70	5.3E–6	2.0E–4
Cardani et al. (2015) (1)	HL	0:1:3; ND	ND	ND	1.40	ND	0.40	ND	ND	ND	ND
Carvill (1993)	OPC	ND	ND	ND	ND	ND	ND	ND	ND	11.0E–6	ND
Cerný et al. (2000)	OPC	1:0:3; 0.50	ND	ND	ND	ND	ND	ND	ND	11.5E–6	2.5E–4
Corinaldesi et al. (2011) (1)	OPC	1:0:3; 0.60	ND	ND	32.00	ND	ND	ND	12.00	ND	ND
D'Altri et al. (2018)	OPC	ND	2300	0.15	8.20	ND	1.50	ND	ND	ND	ND
Delgado et al. (2019b) (1)	OPC–HL	1:1:6; 1.08	ND	ND	10.00	ND	ND	ND	2.90	ND	ND

ND stands for 'not defined'; (1) Hygrothermal properties in Table A2.3.

Table A2.4 (Continued). Summary of mechanical, thermo–mechanical and hygro–mechanical properties of cement and lime mortars.

Source	Type of binder	Proportion (C:L:S;WC)	Young's modulus E [MPa]	Poisson's ratio ν [–]	Compressive strength f_c [MPa]	Fracture energy in compression G_c [N/mm]	Tensile strength f_t [MPa]	Fracture energy in tension G_f^I [N/mm]	Flexural strength f_b [MPa]	Coefficient of thermal expansion α_T [1/K]	Coefficient of hygric expansion α_h [–]
Delgado et al. (2019b) (1)	HL	0:1:3; 1.05	ND	ND	1.30	ND	ND	ND	0.60	ND	ND
Faria & Silva (2019) (1)	NHL	0:1:3; 1.23	3540	ND	0.70	ND	ND	ND	0.70	ND	ND
Franzoni et al. (2018)	NHL	ND	ND	ND	12.70	ND	ND	ND	2.80	ND	ND
Güney & Caner (2015) (1)	HL	ND	ND	ND	ND	ND	ND	ND	ND	5.5E–6	ND
Güney & Caner (2015) (1)	HL	ND	ND	ND	ND	ND	ND	ND	ND	8.2E–6	ND
Güney & Caner (2015) (1)	HL	ND	ND	ND	ND	ND	ND	ND	ND	8.3E–6	ND
Lanas et al. (2004)	NHL	0:1:1; ND	ND	ND	6.50	ND	ND	ND	2.20	ND	ND
Maravelaki-Kalaitzaki et al. (2005)	NHL	0:6:14 (2); 0.54	7120	ND	3.80	ND	ND	ND	ND	ND	ND
Moonen et al. (2010) (1)	OPC	ND	2371	0.20	ND	ND	0.40	ND	ND	10.4E–6	ND
Muñoz & Lourenço (2019)	NHL	0:1:2.5; ND	2200	ND	1.40	ND	0.40	ND	ND	ND	ND
Pavlíková et al. (2019) (1)	HL	0:1:3; 1.0	2500	ND	1.08	ND	ND	ND	0.79	ND	ND
Penas et al. (2008) (1)	NHL	0:1:3; 0.11	2143	ND	1.20	ND	ND	ND	0.40	ND	ND

ND stands for 'not defined'; (1) Hygrothermal properties in Table A2.3.

Table A2.4 (Continued). Summary of mechanical, thermo–mechanical and hygro–mechanical properties of cement and lime mortars.

Source	Type of binder	Proportion (C:L:S;WC)	Young's modulus E [MPa]	Poisson's ratio ν [–]	Compressive strength f_c [MPa]	Fracture energy in compression G_c [N/mm]	Tensile strength f_t [MPa]	Fracture energy in tension G_f^I [N/mm]	Flexural strength f_b [MPa]	Coefficient of thermal expansion α_T [1/K]	Coefficient of hygric expansion α_h [–]
Penas et al. (2008) (1)	NHL	0:1:3; 0.12	1415	ND	0.70	ND	ND	ND	0.17	ND	ND
Penas et al. (2008) (1)	NHL	0:1:3; 0.12	3327	ND	1.10	ND	ND	ND	0.40	ND	ND
Pineda et al. (2017)	HL	ND	500	0.20	ND	ND	ND	ND	ND	ND	ND
Silva et al. (2014) (1)	HL	0:1:3; 1.50	ND	ND	0.48	ND	ND	ND	0.24	ND	ND
Silva et al. (2014) (1)	NHL	0:1:3; 0.80	ND	ND	3.70	ND	ND	ND	1.20	ND	ND
Silva et al. (2015) (1)	NHL	0:1:5; 1.35	ND	ND	0.60	ND	ND	ND	0.30	ND	ND
Silva et al. (2015) (1)	OPC	1:0:3; 0.60	ND	ND	24.80	ND	ND	ND	4.75	ND	ND
Silva et al. (2015) (1)	OPC	1:0:6; 1.26	ND	ND	2.15	ND	ND	ND	0.80	ND	ND

ND stands for 'not defined'; (1) Hygrothermal properties in Table A2.3.

APPENDIX 3

Parametric studies

In Chapter 5, a moisture transport model was used to simulate water absorption and drying processes in masonry materials. Based on the experimental results and back–calculated parameters discussed there, this section investigates how possible uncertainties in material properties and model configuration may affect the predictions of moisture–related phenomena. First, the main hygric parameters (material properties and boundary conditions) are studied for absorption and drying cases of mono–layered materials. Then, a series of sensitivity analyses are performed to assess the impact of uncertainties in multi–layered assemblies.

The following sections focus solely on moisture transport simulations and the associated hygric parameters. For sensitivity studies on the parameters affecting heat transport and the thermal response of porous building materials, the reader is referred to Li et al. (2013).

A3.1 PARAMETRIC STUDIES FOR MONO–LAYERED MATERIALS

A sensitivity analysis consists of an exploratory process for assessing the sensitivity of a model with respect to specific variables. The scope is to identify and characterise the influence that each parameter has on the numerical response. Therefore, the response of the system is studied with respect to fixed variations in certain parameters included in the model.

For the current parametric studies, the properties of fired–clay brick were chosen as reference. The one–at–a–time sensitivity analysis procedure was applied, which means that tor each set of simulations, only one material parameter was changed while the other properties were kept with their default value. The results obtained from each parameter variation were then contrasted with the reference case. In particular, the response of the system was analysed in terms of moisture mass variation, namely mass gain and mass loss for absorption and drying cases, respectively.

The material properties used for the single–material sensitivity analyses are summarised in Table A3.1. In general, each material parameter was shifted to values 50 % below (lower bound, LB) and above (upper bound, UB) the reference value (REF). Note that a 50 % variation is an extreme case, much higher than the usual uncertainties expected for parameter estimation. Nonetheless, such a high value was chosen on purpose to obtain clearer outcomes. For drying cases, the influence of the boundary conditions was also analysed.

The following analyses consist of 1–D moisture transport simulations on brick cubes with dimensions $40\ \mathrm{mm} \times 40\ \mathrm{mm} \times 40\ \mathrm{mm}$. The imposed initial and boundary conditions are summarized as follows:

a) Water absorption simulations. Initial condition, $\varphi(t = 0) = 0$, i.e. dry conditions. Boundary conditions, $\varphi(t > 0) = 1$ to represent liquid water at the base and $g = 0\ \mathrm{kg/(m^2 \cdot s)}$ or null flux condition at the top face. The boundary condition at the base is introduced progressively using a smoothed step function.

b) Drying simulations. Initial condition, $\varphi(t = 0) = 1$, i.e. capillary moisture content. For the boundary conditions, the bottom node is insulated whereas a convective flux is imposed at the top face, such as $g = h_m\ (p_v - p_{v,ext})$, with $h_m = 6.50\mathrm{E}{-08}\ \mathrm{s/m}$. Laboratory conditions are assumed for the surrounding environment, that is 23 °C and 55 % RH.

Table A3.1. Model parameters used for the mono–layered material sensitivity analyses.

Process	Parameter	Lower bound (LB)	Reference value (REF)	Upper bound (UB)
Water absorption and drying	Capillary moisture content, w_{cap} [$\mathrm{kg/m^3}$]	220	240	260
	Sorption isotherm fitting coefficient, ψ [–]	1.0040	1.0080	1.0120
	Water vapour resistance factor, μ [–]	10	20	30
	Water absorption coefficient, A_w [$\mathrm{kg/(m^2 \cdot s^{0.5})}$]	0.050	0.100	0.150
	Height, H [mm]	20	40	60
	Exposed surface, A_c [$\mathrm{mm^2}$]	28.3 × 28.3	40.0 × 40.0	49.0 × 49.0
Drying	Temperature, ϑ [°C]	10	23	36
	Relative humidity, RH [%]	30	55	80
	Convective mass transfer coefficient, h_m [s/m]	4.0E–8	6.5E–8	9.0E–8

A3.1.1 Sensitivity analysis for the capillary moisture content

The capillary moisture content, w_{cap} [$\mathrm{kg/m^3}$], indicates the saturation capacity of a porous material in contact with water under atmospheric conditions. In the proposed moisture transport model, w_{cap} is mainly associated with the liquid transport term since it appears within the analytical expressions for the sorption isotherm, $w(\varphi)$ (see Eqs. (4.1)–(4.3)), and the water diffusivity function, $D_w(\varphi)$ (see Eq. (5.3)).

Figure A3.1a and Figure A3.1b compare the results obtained by modifying the capillary moisture content for absorption and drying cases, respectively. As expected, w_{cap} is related to the saturation plateau at the end of the water absorption process and the total mass loss at the end of drying. It is noted

that variations in w_{cap} do not influence the water absorption rate. Likewise, the mass loss rate during the first stage of drying is always the same for different limits of w_{cap}.

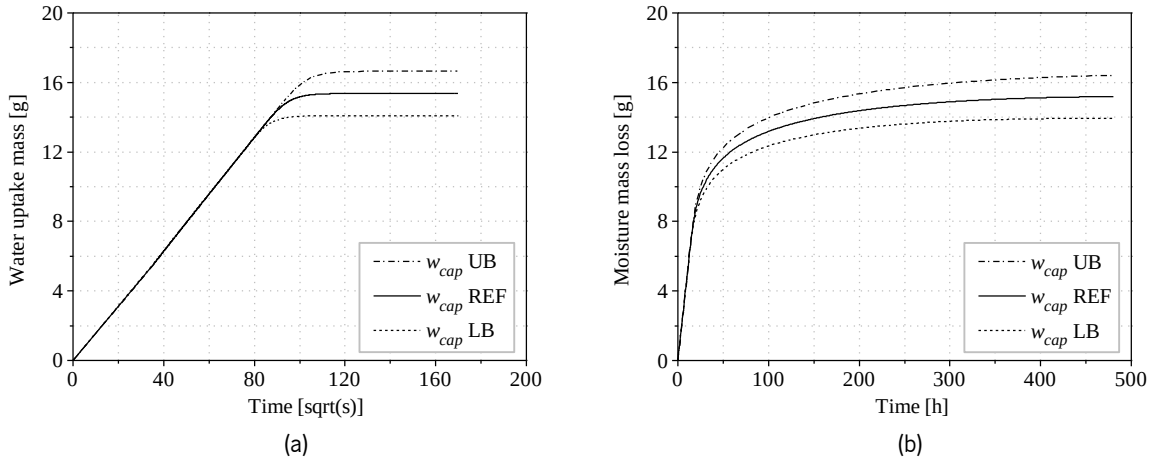

Figure A3.1. Sensitivity analysis for the capillary moisture content: (a) water absorption; (b) drying.

A3.1.2 Sensitivity analysis for the moisture content curve

Assuming Künzel's model to describe the moisture storage curve (see Eq. (4.1)), the fitting parameter ψ controls the shape of the exponential function. Since ψ must be greater than unity, only upper and lower bounds for the decimal component are considered for the sensitivity analysis. The reference sorption isotherm as well as the curves obtained with the upper and lower values of ψ are shown in Figure A3.2.

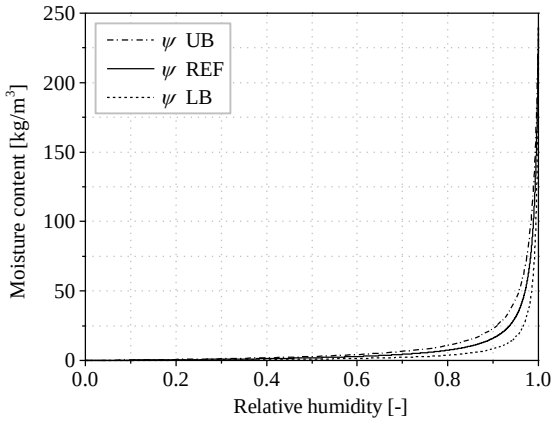

Figure A3.2. Sorption isotherms employed in the sensitivity analysis for the moisture content curve.

The results obtained by modifying the moisture content curves are shown in Figure A3.3a and Figure A3.3b for absorption and drying cases, respectively. The variations associated to the fitting parameter ψ have no impact on absorption. Similarly, the drying curves obtained with different values of ψ are nearly identical. This negligible impact on the drying process can be explained by the fact that the final equilibrium state, i.e. 55 % RH, translates into a similar moisture content value for the three studied

cases (see Figure A3.2). More significant deviations would be expected for the upper range of moisture content, for instance drying in an environment with 80 % RH.

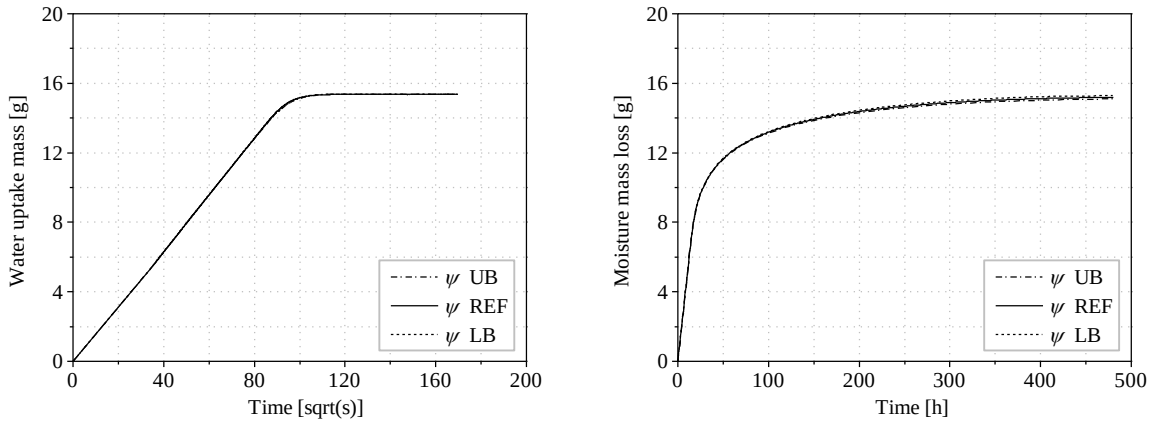

Figure A3.3. Sensitivity analysis for the moisture content curve: (a) water absorption; (b) drying.

A3.1.3 Sensitivity analysis for the water absorption coefficient

In the proposed moisture transport model, the water absorption coefficient, A_w, is the main factor controlling the liquid diffusivity (see Eq. (5.3)). The results obtained by modifying this parameter for absorption and drying cases are shown in Figure A3.4a and Figure A3.4b, respectively. It is evident that A_w has a significant impact on both processes. For water uptake, A_w is directly related to the rate of absorption: higher A_w causes faster mass gain and vice versa. For drying cases, A_w is related to the duration of the first drying phase and the mass loss rate of the second phase: higher A_w values extend the initial drying stage and produce faster mass loss rates, whereas the opposite happens for lower A_w.

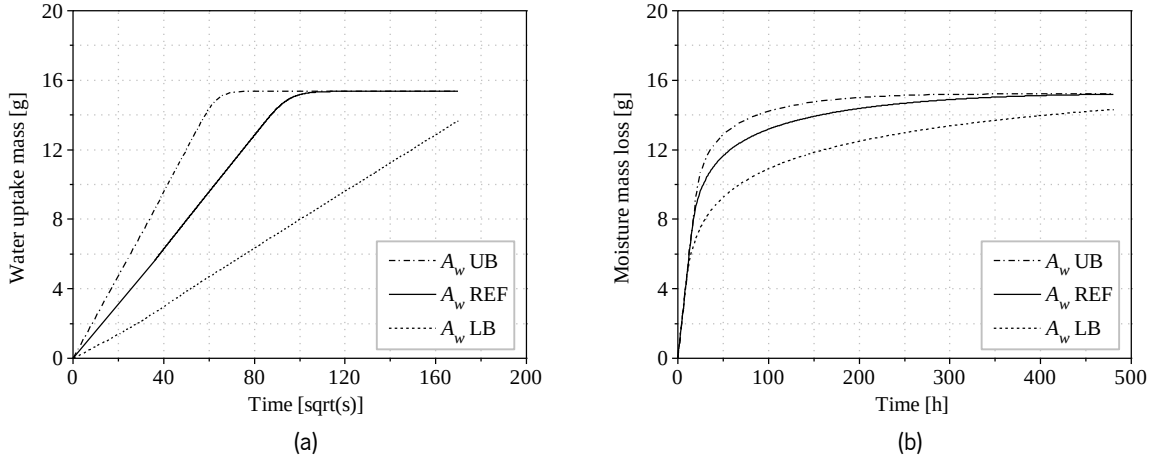

Figure A3.4. Sensitivity analysis for the water absorption coefficient: (a) water absorption; (b) drying.

A3.1.4 Sensitivity analysis for the water vapour resistance

In the proposed model, the water vapour resistance factor (or alternatively the water vapour permeability, see Eq. (3.6)) is the main parameter controlling vapour diffusion. The results for the imposed variations on μ are shown in Figure A3.5a and Figure A3.5b for water uptake and drying cases, respectively. The impact on the absorption process is negligible. For drying, changes in the water vapour resistance affect the second phase of the process: expectedly, higher resistances reduce the mass loss rate.

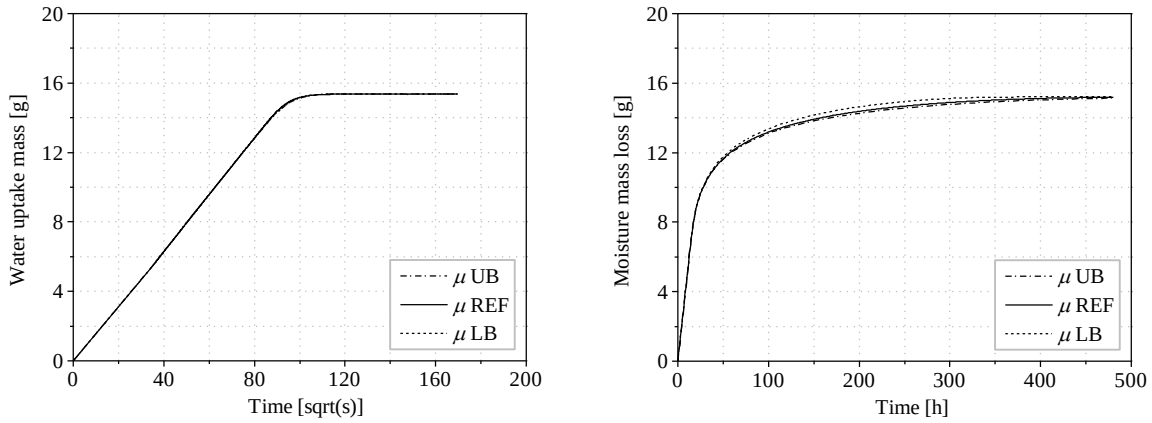

Figure A3.5. Sensitivity analysis for the water vapour resistance: (a) water absorption; (b) drying.

It must be noted that μ–values found in the literature present a great variability, even for the same material. Since the imposed variations caused minor deviations on the drying results, a much higher resistance ($\mu = 80$) was analysed as well but the overall response did not fall too far from the original. In conclusion, the vapour resistance factor may be used to tune the second drying phase, but it cannot change the overall behaviour significantly.

A3.1.5 Sensitivity analysis for the geometry of the specimens: Height and exposed surface

The dimensions of a specimen define the overall moisture volume that the porous material can absorb. In order to analyse this and other possible geometry–related effects, the present section presents a series of parametric analyses with focus on the height and the exposed surface of the specimens.

The first group of analyses related to the height are shown in Figure A3.6. The simulations for free water uptake are shown in Figure A3.6a. The height of the specimen is mainly associated with the final amount of absorbed water but it does not change the slope of the water uptake curve with respect to the square root of time. This fact would discard any uncertainty stemming from the specimen height in the calculation of the water absorption coefficient. It is noted that the transition from the first absorption stage to the saturation plateau is relatively slower for higher specimens.

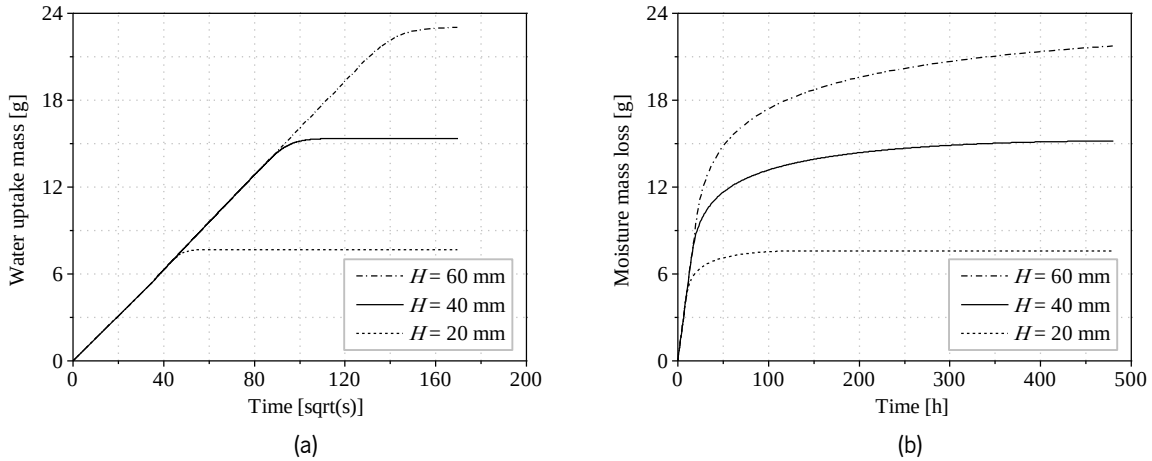

Figure A3.6. Sensitivity analysis for the height of the specimen: (a) water absorption; (b) drying.

Subsequently, Figure A3.6b shows the drying results for different specimen heights. As in the previous case, height is related to the total amount of moisture that the specimen may contain and consequently lose by drying. It may be pointed out that the initial mass loss rate (drying stage I) is constant and equal for all cases, thus height is not a factor involved in this drying phase. Conversely, the duration of the first drying stage (end of the linear mass loss) may be associated with height. In general, the first linear portion of the mass loss curve is shorter for shorter specimens. Nonetheless, the first drying stage is longer for shorter specimens when compared to the total duration.. In other words, for shorter samples, the first drying phase occupies a bigger portion of the total drying duration. Finally, the higher the specimen, the larger the development of the second drying stage. This trend implies that higher specimens take proportionally much longer to reach equilibrium with the environment than thinner samples, as expected.

The second group of parametric studies involving the geometric features of the specimens focused on the exposed surface of the materials, see Figure A3.7. As it was mentioned for the height parameter, the surface of the specimen is directly related to the total volume of moisture that the material may contain. Figure A3.7a shows the results for water absorption for specimens with different exposed surface areas (remember that height is kept constant in all these cases). Expectedly, specimens with greater exposed surfaces absorb more water, and their mass gain is faster. However, since area and time are taken into account in the definition of the water absorption coefficient, A_w $[\mathrm{kg}/(\mathrm{m}^2 \cdot \mathrm{s}^{0.5})]$, all the cases result in the same A_w value.

The results for 1–D isothermal drying of specimens with different areas are shown in Figure A3.7b. Note that the initial mass loss rate (first drying stage) does change according to the amount of surface exposed to the environment. On the contrary, the duration of this first phase (constant mass loss rate) is

the same for all. Likewise, the development of the second drying stage and the total amount of time necessary to reach equilibrium is analogous for all the specimens.

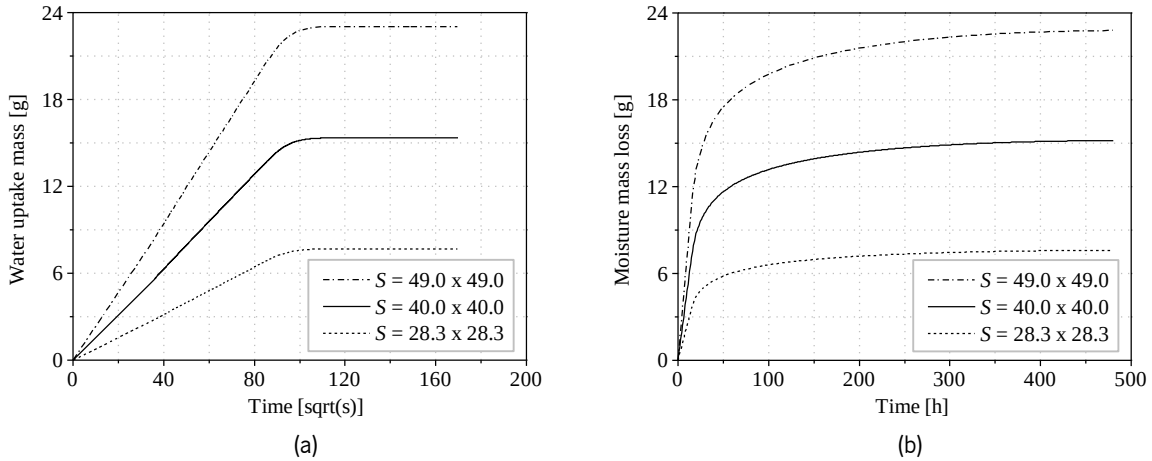

Figure A3.7. Sensitivity analysis for the exposed surface of the specimen: (a) water absorption; (b) drying.

In conclusion, the derivation of A_w is independent of the geometry. The dimensions of the specimens do not play a significant role in the water uptake process, having only a minor influence in the transition between the first and the second absorption stages: slightly slower for higher specimens and smaller areas. On the contrary, the dimensions of the specimens have a significant impact on the overall drying behaviour. The exposed area is one of the parameters controlling the initial mass loss rate. Moreover, the height of the specimen is associated with the duration of the first drying stage and the development of the second phase: higher specimens have a longer non–linear stage and take more time to reach equilibrium with the environment.

A3.1.6 Sensitivity analysis for the boundary conditions in drying cases: Temperature and relative humidity

Boundary conditions (BCs) are key parameters to determine the response of any system. In absorption processes, the temperature determines the viscosity of water, which in turn influences the water absorption coefficient (Feng & Janssen, 2016). The sensitivity analysis for A_w has already been presented so no more attention will be devoted to this matter. On the other hand, the external temperature and relative humidity conditions have direct implications on drying cases. Both parameters are related through:

$$\varphi = p_v / p_{v,sat}(T) \tag{A3.1}$$

where p_v [Pa] is the partial vapour pressure, and $p_{v,sat}(T)$ [Pa] is the saturated vapour pressure, which is defined through the following empirical formulation:

$$p_{v,sat} = 610.7[\text{Pa}] \cdot 10^{7.5\left(\frac{T-273.15}{T-35.85}\right)} \tag{A3.2}$$

For the current one–at–a–time sensitivity analysis, both variables will be treated independently. However, their actual inversely proportional non–linear relation should be considered when dealing with real cases with varying temperature and relative humidity.

The results for 1–D isothermal drying of specimens subjected to different temperature and relative humidity BCs are shown in Figure A3.8a and Figure A3.8b, respectively. Note that the reference values correspond to standard laboratory conditions. Lower and higher bounds are established to represent more severe environments.

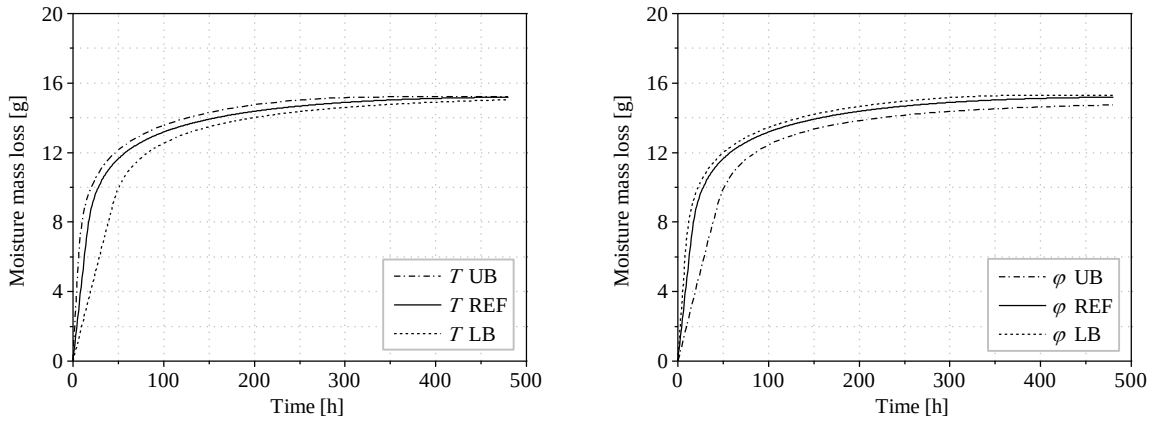

Figure A3.8. Sensitivity analysis for the boundary conditions in drying cases: (a) temperature; (b) relative humidity.

According to the results, the external temperature controls the mass loss rate of the first drying phase, that is the slope of the initial portion of the mass loss curve. The influence of the temperature is slightly noticeable in the development of the second drying phase as well. On the other hand, the external relative humidity is also related to the mass loss rate of the first drying phase. Moreover, the environmental relative humidity controls the level of the final plateau (moisture content in equilibrium with the environment). Finally, the curves show the inversely proportional relation between the two factors: higher temperature and lower relative humidity result into faster drying, and the opposite occurs for lower temperature or higher relative humidity.

A3.1.7 Sensitivity analysis for the boundary conditions in drying cases: Convective mass transfer coefficient

The convective mass transfer coefficient, h_m [s/m], is the proportionality constant in the moisture convective flux boundary condition:

$$g = h_m \left(p_v - p_{v,ext}\right) \tag{A3.3}$$

In reality, h_m is a phenomenological parameter that takes into account a series of environmental conditions, namely temperature, relative humidity and air velocity, as well as certain properties of the material, such as surface roughness. However, in practice it is seldom possible to separate the contribution of each of those factors and most analytical expressions in the literature only link it with the air velocity.

The drying curves obtained by changing the convective mass transfer coefficient are shown in Figure A3.9. According to the results, h_m controls the mass loss rate during the first drying phase, that is the slope of the initial portion of the mass loss curve. The same trend was observed for the external temperature and relative humidity. However, opposite to the temperature and moisture boundary conditions, the impact of h_m is only noticeable during the first drying phase.

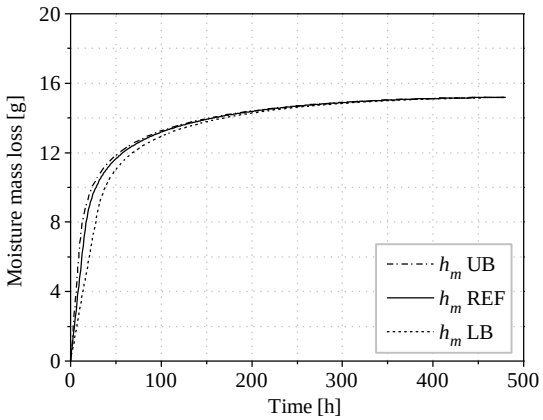

Figure A3.9. Sensitivity analysis for the convective mass transfer coefficient in drying cases.

A3.1.8 Sensitivity analysis for the initial moisture content in absorption and drying cases

Like the boundary conditions, initial conditions can also have a strong influence on the response of the system. The results from absorption and drying simulations with different initial conditions are shown in Figure A3.10a and Figure A3.10b, respectively.

For absorption cases, the initial moisture content has some influence on the overall water uptake process. There is a minor impact on the water absorption rate, which is only noticeable for high initial moisture contents: the water uptake rate diminishes as the material is closer to saturation. Moreover, the final plateau at the end of the absorption process is also related to the initial moisture content as it marks the quantity of water absorbed to reach saturation: the higher the initial moisture content, the least water the material will need to attain capillary saturation. Note that all the cases take approximately the same amount of time to reach the plateau, so that the initial moisture content does not play a major role on the

total duration of the process. In practice, we may conclude that the uncertainties derived from the initial conditions of a specimen during a water absorption test are negligible (at least for barely hygroscopic materials).

For drying cases, minimum variations in the initial moisture content of the material have a great impact on the response. For instance, a reduction in the order of 1E–4, i.e. $\varphi(t=0)=0.9999$, is already visible in the plot for moisture mass loss. Opposite to the water absorption test, drying experiments are especially sensitive to the initial conditions. This is explained by the exponential trend of the sorption isotherm for the upper moisture range (see Figure A3.2). Considering the mass loss, the initial drying rate is the same for all the studied scenarios. Moreover, the second drying phase is analogous for all the cases, but it is moved up/down the line defined by the initial drying rate.

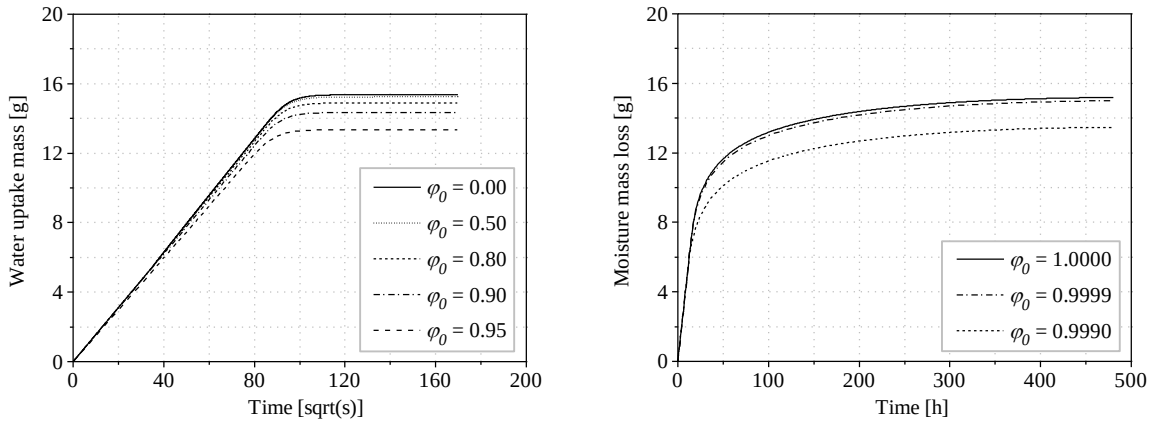

(a) (b)

Figure A3.10.Sensitivity analysis for the initial moisture content: (a) water absorption; (b) drying.

A3.2 PARAMETRIC STUDIES FOR MULTI–LAYERED MONO–MATERIAL ASSEMBLIES

Beyond the monolithic level, several uncertainties may appear at the multi–layered scale, namely the existence of a hydraulic interface resistance, the arrangement of the assembly (relative proportion and stacking order), and the difference between the material properties of each constituent layer. To better distinguish each case, the corresponding parametric studies are firstly focused on multi–layered configurations of the same material. In the following section, the sensitivity analyses will be extended to assemblies made up of different material layers.

For mono–material assemblies, 1–D moisture transport simulations were performed on cylinders with diameter $51.3\ \mathrm{mm}$ and different heights depending on the focus of the study. The imposed initial and boundary conditions are summarized as follows:

a) Water absorption simulations. Initial condition, $\varphi(t=0)=0.01$. This small value is chosen because the expression for the hydraulic resistance (see Eq. (5.6)) is incompatible with $\varphi=0$.

Nonetheless, the proposed initial condition can still be considered equivalent to the dry state. Boundary conditions, $\varphi(t > 0) = 1$ to represent liquid water in contact with the base and $g = 0\ \mathrm{kg/(m^2 \cdot s)}$ or null flux condition at the top face. The boundary condition at the base is introduced progressively using a smoothed step function.

b) Drying simulations. Initial condition, $\varphi(t = 0) = 1$, i.e. capillary moisture content. For the boundary conditions, the bottom node is insulated whereas a convective flux is imposed at the top face, such as $g = h_m\ (p_v - p_{v,ext})$, with $h_m = 6.50\text{E}{-}08\ \mathrm{s/m}$. Controlled laboratory conditions, 23 °C and 55 % RH, are assumed for the surrounding environment.

A3.2.1 Sensitivity analysis for the interface hydraulic resistance in two–layer mono–material assemblies

In multi–layered assemblies, the contact area between neighbouring layers may introduce additional uncertainties. In particular, the type of interface between adjacent media will determine the overall behaviour of the system. If perfect hydraulic contact is assumed, the moisture driving potential, namely capillary pressure or relative humidity, will be continuous across the interface. Consequently, an assembly made up of layers of the same material with perfect hydraulic contact will be analogous to the monolithic case. However, the perfect contact case is mostly theoretical, and an imperfect contact is more likely to occur. An imperfect hydraulic contact will cause a driving potential drop across the interface. The moisture flux across an interface with imperfect hydraulic contact is determined by Eq. (5.6). In order to study the transport effects associated with this type of contact, absorption and drying models were prepared with different hydraulic resistance values, R_{IF} [m/s]. The results obtained from these models were then compared with the monolithic scenario or multi–layered case with perfect hydraulic contact. It is noted that two–layered brick cylinders $40\ \mathrm{mm} + 40\ \mathrm{mm}$ height were used for these simulations.

Figure A3.11a and Figure A3.11b compare the results obtained for different interface hydraulic resistances in absorption and drying cases, respectively. For water absorption, resistance values in the order of $1.0\text{E}{+}09\ \mathrm{m/s}$ already entail a noticeable mass uptake retardation. As expected, higher resistance values produce larger deviations with respect to the monolithic case. For drying cases, the presence of an imperfect contact does not play a relevant role and only significantly high resistance values produce slight deviations with respect to the monolithic case.

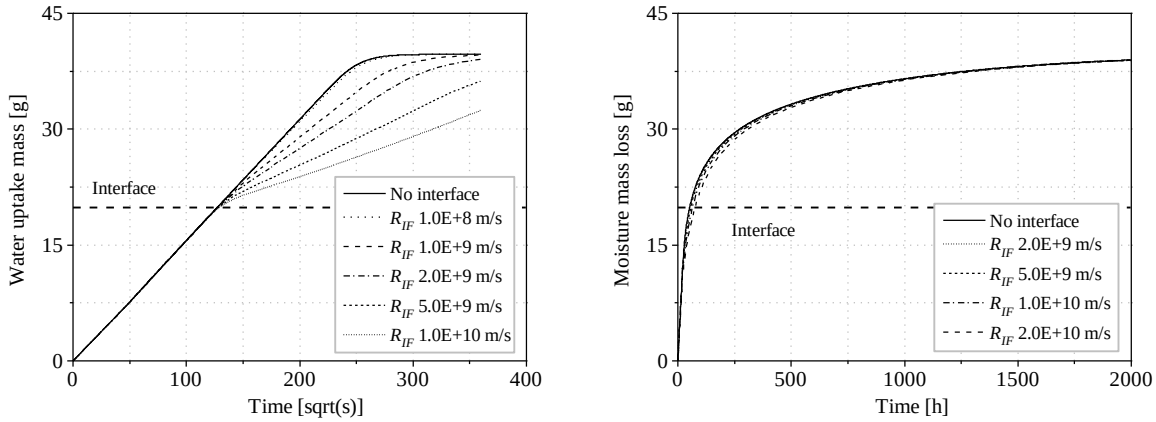

Figure A3.11. Sensitivity analysis for the interface hydraulic resistance in two–layer mono–material assemblies: (a) water absorption; (b) drying.

A3.2.2 Sensitivity analysis for the stacking arrangement of multi–layered mono–material assemblies

The present section aims at understanding how the arrangement of different layers influences the overall behaviour of a multi–layered assembly with imperfect hydraulic contact. In other words, the focus is set now on the geometry of the layers and therefore the location of the interface within the assembly. To this purpose, parametric analyses are performed on a two–layer brick assembly with imperfect hydraulic contact and different stacking layouts. Two different scenarios are proposed, namely fixing the dimensions of the first layer and the second layer, respectively. For each set of analyses, the same interface hydraulic resistance is assumed, and the results are compared with the perfect hydraulic contact (no–interface or monolithic) case. The studied configurations are summarised in Table A3.2.

Table A3.2. Model parameters used for the multi–layered mono–material sensitivity analyses.

Interface scenario	Layer	Height [mm]							
No Interface (perfect contact or monolithic)	I	40	40	40	40	20	30	40	50
	II	20	30	40	50	40	40	40	40
$R_{IF1} =$ 1.0E+09 [m/s]	I	40	40	40	40	20	30	40	50
	II	20	30	40	50	40	40	40	40
$R_{IF2} =$ 2.0E+09 [m/s]	I	40	40	40	40	20	30	40	50
	II	20	30	40	50	40	40	40	40

In the previous section, the impact of moderate R_{IF} values on drying was proven to be negligible. It follows that the drying response of a multi–layered assembly with imperfect hydraulic contact is equivalent to its

analogous monolithic (or perfect contact) counterpart. The effect of geometric features on drying of single–material specimens has already been discussed (see Section A1.1.5), thus drying cases will not be further addressed here.

The obtained results are collected in Figure A3.12 and Figure A3.13 for the models with a fixed first layer and a fixed second layer, respectively.

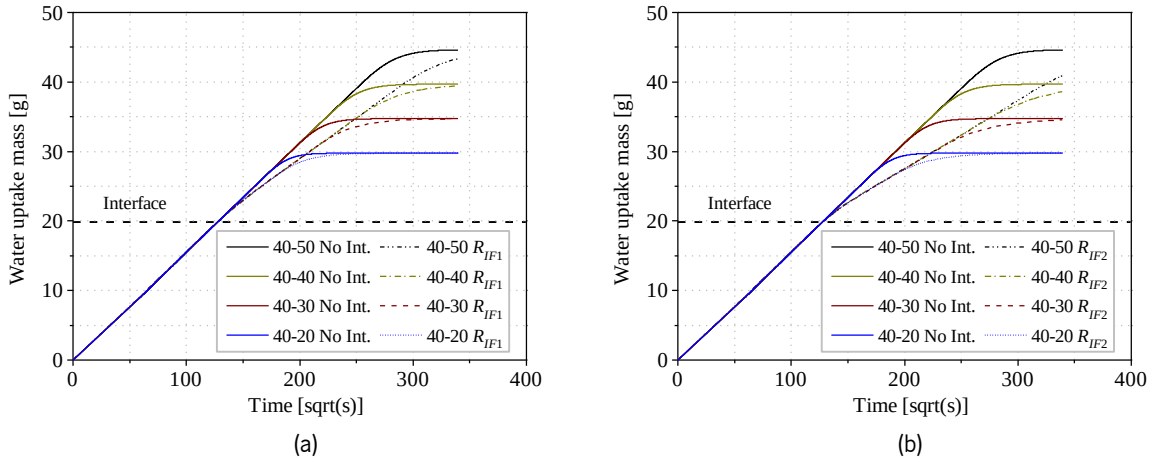

Figure A3.12. Sensitivity analysis for the stacking arrangement of multi–layered mono–material assemblies with imperfect hydraulic contact: (a) fixed first layer, $R_{IF} = 1.0\text{E+}09\ \mathrm{m/s}$; (b) fixed first layer, $R_{IF} = 2.0\text{E+}09\ \mathrm{m/s}$.

The cases with a fixed first layer reveal a consistent response for all the configurations. As expected, the absorption curve deviates from the monolithic behaviour when the interface is reached. Moreover, after the interface, the slope of the water uptake mass with respect to the square root of time is parallel for all the cases, independently of the height of the second layer.

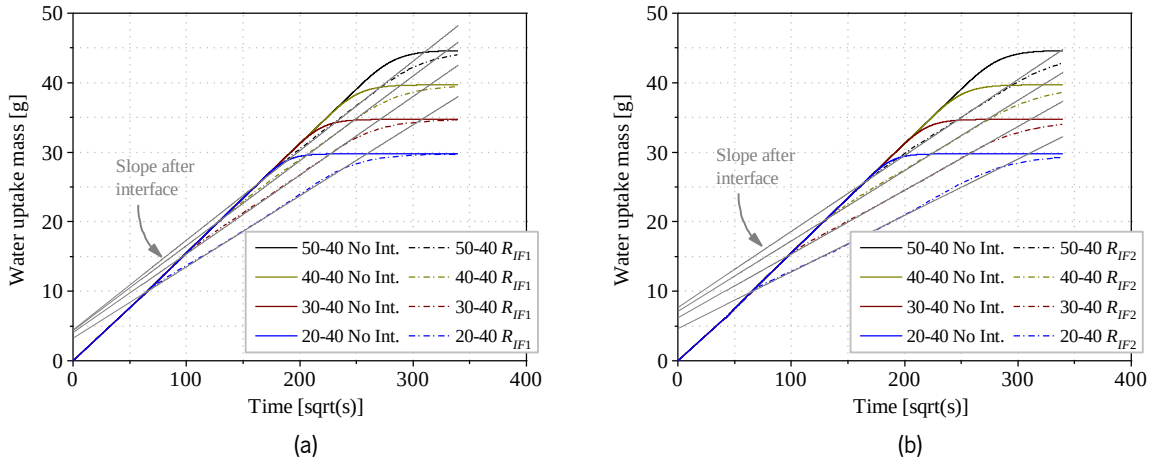

Figure A3.13. Sensitivity analysis for the stacking arrangement of multi–layered mono–material assemblies with imperfect hydraulic contact: (a) variable first layer, $R_{IF} = 1.0\text{E+}09\ \mathrm{m/s}$; (b) variable first layer, $R_{IF} = 2.0\text{E+}09\ \mathrm{m/s}$.

On the contrary, the cases with a variable first layer reveal a more complex behaviour. The curves produced by interfaces with the same R_{IF} but located at different heights are not perfectly parallel to each

other with respect to the square root of time: the closer to the water plane, the lower the slope. In other words, the sooner the water front encounters the interface, the more the curve deviates from the monolithic behaviour. In conclusion, the location of the interface (or alternatively the geometry of the layers) plays a role in the overall behaviour.

A3.3 PARAMETRIC STUDIES FOR MULTI–LAYERED MULTI–MATERIAL ASSEMBLIES

In multi–layered assemblies, besides the existence of an interface and the effects derived from the geometry of each constituent layer, the transition from one porous medium to an adjacent one with different properties may induce the appearance of specific transport phenomena. In order to assess the impact of each material parameter within the assembly, a two–layer composite is modelled, and generic brick properties are assigned to both layers. Then, a series of sensitivity analyses are performed by changing only one parameter of each layer at a time. In this way, the relative change of properties between adjacent layers may be distinguished and weighed. The material properties used for the sensitivity analysis on these heterogeneous two–layer material assemblies are summarised in Table A3.3.

Table A3.3. Model parameters used for the multi–layered multi–material sensitivity analyses.

Parameter	Layer	I.LB	I.REF	I.UB	II.LB	II.REF	II.UB
Sorption isotherm fitting parameter ψ [–]	I	1.0040	1.0080	1.0120	1.0080	1.0080	1.0080
	II	1.0080	1.0080	1.0080	1.0040	1.0080	1.0120
Water vapour resistance factor, μ [–]	I	10	20	30	20	20	20
	II	20	20	20	10	20	30
Water absorption coefficient, A_w $[\mathrm{kg}/(\mathrm{m}^2 \cdot \mathrm{s}^{0.5})]$	I	0.050	0.100	0.150	0.100	0.100	0.100
	II	0.100	0.100	0.100	0.050	0.100	0.150

For the sensitivity analyses on heterogeneous multi–layered assemblies, the basic geometric features of the mono–material assemblies were used as well as the same initial and boundary conditions (see previous section). Note that perfect hydraulic contact between the layers is assumed for all the cases. In the following, we assume that the first layer or Layer I is the one in contact with the water for absorption simulations and in contact with the environment for drying simulations.

A3.3.1 Sensitivity analysis for the moisture content curve of adjacent materials in a two–layer assembly

The first set of parametric studies for heterogeneous assemblies is focused on the moisture content curve of the constituent materials, in particular the fitting parameter ψ for the sorption isotherm (see Eq. (4.1)).

The reference sorption isotherm as well as the curves obtained with the upper and lower values of ψ are shown in Figure A3.2. The results obtained by modifying the moisture content curves of the upper and lower material layers are shown in Figure A3.14a and Figure A3.14b for absorption and drying cases, respectively.

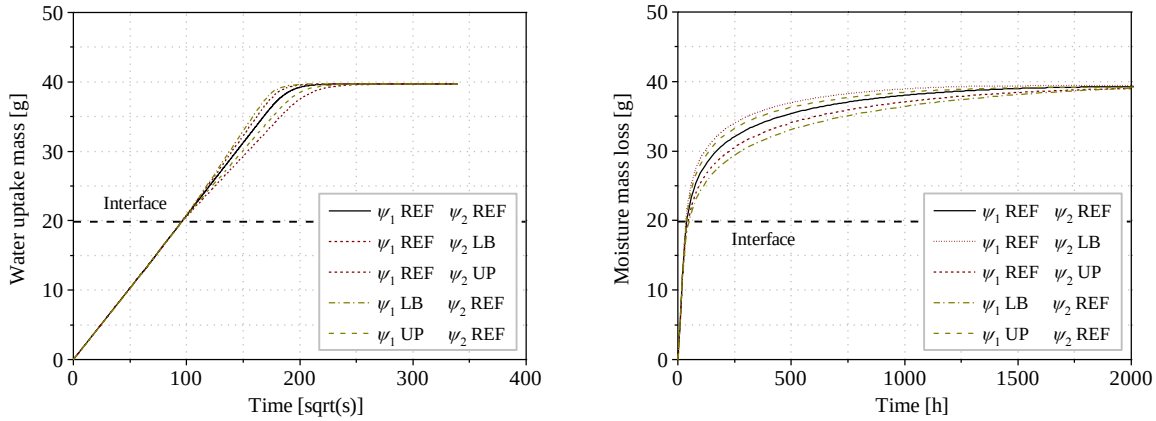

Figure A3.14. Sensitivity analysis for the moisture content curve of adjacent materials in a two–layer assembly: (a) water absorption; (b) drying.

For the studied absorption cases, the sorption isotherm of each constituent layer has a different impact on the absorption behaviour depending on the layout configuration. Note that the deviations with respect to the reference cases are only perceivable for longer times but not during the first hours. Considering the reference value for the first layer, the absorption process is faster when the second layer is more hygroscopic (higher ψ) and slower in the opposite case (lower ψ). If the second layer adopts the reference value, a more hygroscopic first layer (higher ψ) results in a slower process, whereas first layer with a less hygroscopic material (lower ψ) enhances the water uptake rate.

On the other hand, the drying behaviour of the studied assembly changes significantly depending on the moisture content curve of each constituent material. Assuming reference values for the first layer, the mass loss rate is slower when the second layer has a more marked hygroscopic behaviour (upper bound of the sorption isotherm), whereas the fastest drying occurs when the second layer presents a less hygroscopic behaviour (lower bound of the sorption isotherm). If the properties of the second layer are considered fixed instead, drying is faster for a more hygroscopic first layer (upper bound of the sorption isotherm) whereas the slowest drying results from a less hygroscopic first layer (lower bound of the sorption isotherm).

A3.3.2 Sensitivity analysis for the water absorption coefficient of adjacent materials in a two–layer assembly

The effect of combining materials with different water absorption coefficients is analysed in this section. The results of the parametric analyses for absorption and drying cases are presented in Figure A3.15a and Figure A3.15b, respectively.

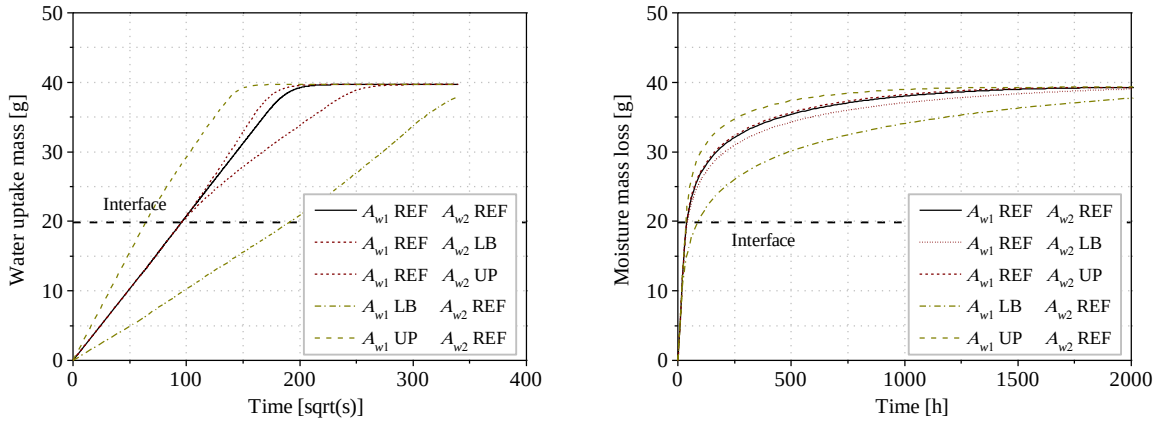

Figure A3.15. Sensitivity analysis for the water absorption coefficient of adjacent materials in a two–layer assembly: (a) water absorption; (b) drying.

The water absorption coefficient is intimately linked to the water uptake process and therefore it greatly influences the absorption behaviour. In heterogeneous assemblies, the properties of each layer contribute to the overall response. The sorptivity of the second layer becomes noticeable after the water front reaches the interface: lower A_w causes slower absorption and vice versa. Additionally, the water absorption coefficient of the layer in contact with the water shapes the overall trend of the system: a high initial A_w allows for a fast absorption process, whereas lower A_w values result in equally lower absorption rates.

The water absorption properties of the different layers play a significant role in the drying process. In particular, the water absorption coefficient of the first layer greatly influences the overall behaviour: lower A_w produce a considerably slower process (shorter first drying stage and longer development of stage II) whereas higher values result in faster drying (longer first drying phase and shorter stage II). On the contrary, the sorptivity of the second layer has a much lower impact. Nonetheless, lower A_w values for the second layer produce a noticeable decrease in mass loss rate (slower drying).

A3.3.3 Sensitivity analysis for the water vapour resistance of adjacent materials in a two–layer assembly

The impact produced by dissimilar vapour resistance factors for adjacent layers in an assembly is analysed now. Using the parameters defined in Table A3.3, a series of parametric analyses are performed and the results are shown in Figure A3.16a and Figure A3.16b for absorption and drying cases, respectively.

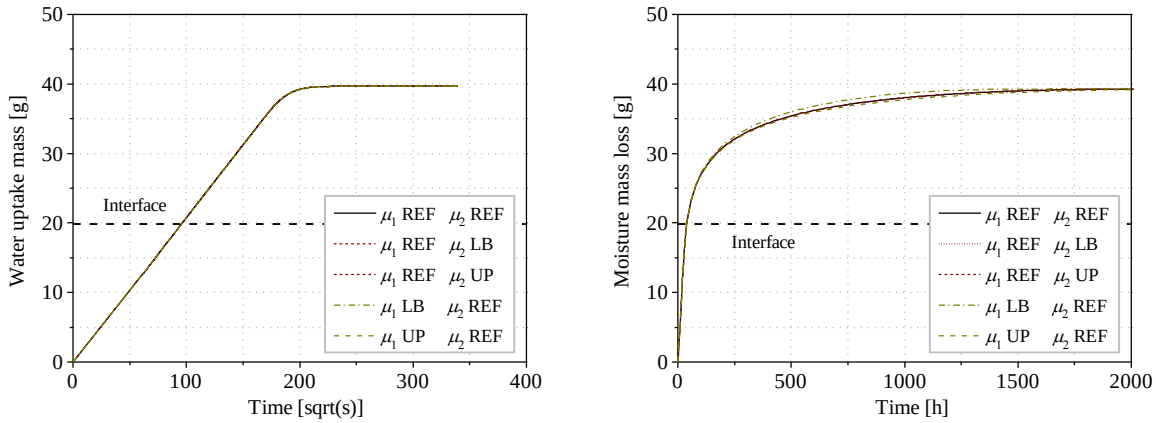

Figure A3.16. Sensitivity analysis for the water vapour resistance of adjacent materials in a two–layer assembly: (a) water absorption; (b) drying.

As it happened with the single–material cases (see Section A1.1.4), the water vapour resistance does not play a role in the absorption process for multi–layered heterogeneous assemblies.

For drying cases, the vapour resistance factor of the second layer is not relevant. Moreover, the vapour resistance of the first layer has a slight impact on the development of the second drying phase: lower resistance causes faster drying and vice versa.

This page has been intentionally left blank

APPENDIX 4

Hygrothermal simulation of drying

In Chapter 5, the drying process of several building materials was simulated using a moisture transport model. As it was mentioned in the corresponding section, drying is expected to cause a thermal variation due to the latent heat of vaporization. This is particularly important during the first drying stage (linear mass loss or constant drying rate), when a temperature drop is likely to occur at the exposed surface due to the evaporation of water. Although the first drying stage can be approximated with a mass transfer model alone, a fully coupled hygrothermal simulation is expedient. Hence, this section deals with the simulation of drying by means of a hygrothermal model. Additionally, a series of sensitivity analyses are performed in order to evaluate the influence of the convective heat and mass transfer coefficients on the drying process. First, the hygrothermal model is introduced together with the prescribed boundary conditions. Subsequently, the results of the parametric studies are presented and discussed. It is noted that the experimental results presented in Chapter 4 are used as a reference for the simulations.

A4.1 HYGROTHERMAL MODEL

The hygrothermal model presented in Chapter 6 is recalled here for clarity. The heat transfer and moisture transport governing equations are given as:

$$\rho C \frac{\partial T}{\partial t} = \nabla \cdot (\lambda \nabla T) + L_v \nabla \cdot \left(\frac{\delta_a}{\mu} \nabla (\varphi \, p_{v,sat}) \right) \tag{A4.1}$$

$$\frac{\partial w}{\partial \varphi} \frac{\partial \varphi}{\partial t} = \nabla \cdot \left(\frac{\partial w}{\partial \varphi} D_w \nabla \varphi \right) + \nabla \cdot \left(\frac{\delta_a}{\mu} \nabla (\varphi \, p_{v,sat}) \right) \tag{A4.2}$$

where ρC $[\mathrm{J/(m^3 \cdot K)}]$ is the volumetric heat capacity at constant pressure, T $[\mathrm{K}]$ is the temperature, t $[\mathrm{s}]$ is time, λ $[\mathrm{W/(m \cdot K)}]$ is the thermal conductivity, L_v $[\mathrm{J/kg}]$ is the latent heat of evaporation, w $[\mathrm{kg/m^3}]$ is the moisture content, φ [–] is the relative humidity, D_w $[\mathrm{m^2/s}]$ is the liquid water diffusivity, δ_a $[\mathrm{kg/(m \cdot s \cdot Pa)}]$ is the water vapour permeability of still air, μ [–] is the water vapour resistance of the material, and $p_{v,sat}$ $[\mathrm{Pa}]$ is the vapour saturation pressure.

Moreover, the boundary conditions are defined by means of convective heat and convective mass fluxes, such as:

$$q = h_T\,(T - T_{ext}) \tag{A4.3}$$

$$g = h_m\,(p_v - p_{v,ext}) \tag{A4.4}$$

where h_T $[\mathrm{W/(m^2 \cdot K)}]$ is the convective heat transfer coefficient, and h_m $[\mathrm{s/m}]$ is the convective mass transfer coefficient.

A4.2 PARAMETRIC STUDIES

Considering the previous model, a series of parametric studies were performed in order to evaluate the influence of the convective heat and mass transfer coefficients on the drying process. In particular, two sets of sensitivity analyses were designed: (a) fixing h_m and recalculating the drying process with different values of h_T; (b) varying both coefficients in parallel by use of the Lewis analogy, i.e. $h_{m,Le} = 7.7\mathrm{E}{-9}\ h_T$. It is worth noting that the heat and mass transfer analogy is extensively employed in the literature, e.g. Bianchi Janetti et al. (2018), X. Zhou et al. (2022), among others. The case of brick drying in the extrusion direction (Figure 4.6 in Chapter 4) was selected as a reference for the hygrothermal simulations. Consequently, the physical, thermal and hygric properties of fired–clay brick were used for the definition of the model (see Table 6.1 in Chapter 6). The obtained results are presented herein in terms of moisture mass loss and surface temperature evolution as a function of time.

A4.2.1 Parametric study I

The results of the first group of sensitivity analyses are presented in Figure A4.1. It is shown that for a fixed value of h_m, the variation of h_T produces changes in the mass loss rate during the first drying stage. As expected, the heat transfer coefficient affects the surface temperature and its evolution during the drying process. It is noted that the duration of the first drying stage varies according to the imposed boundary conditions. In particular, the end of the first drying phase is marked by increasing surface temperature, which eventually balances with the environment as the material reaches moisture equilibrium. Thus, higher h_T represents faster thermal transfer and entails a shorter first drying stage, whereas lower h_T implies slower thermal exchange and consequently a longer first stage.

The previous analysis exemplifies the assumption of instantaneous thermal equilibrium with the environment considered in the moisture transport model. In other words, thermal variations are assumed to dissipate instantly so that the system is in constant thermal equilibrium with the environment. As it is shown in Figure A4.1, if the convective mass transfer coefficient is kept fixed as the value calibrated for the moisture transport model alone, higher heat transfer coefficients approach the solution of the moisture

transport model. Moreover, the temperature variation also diminishes for higher h_T. Note that the solutions reach a plateau for high values of the heat transfer coefficient. Therefore, the moisture transport model is analogous to a hygrothermal model with an infinite convective heat transfer coefficient (any temperature difference dissipates instantly).

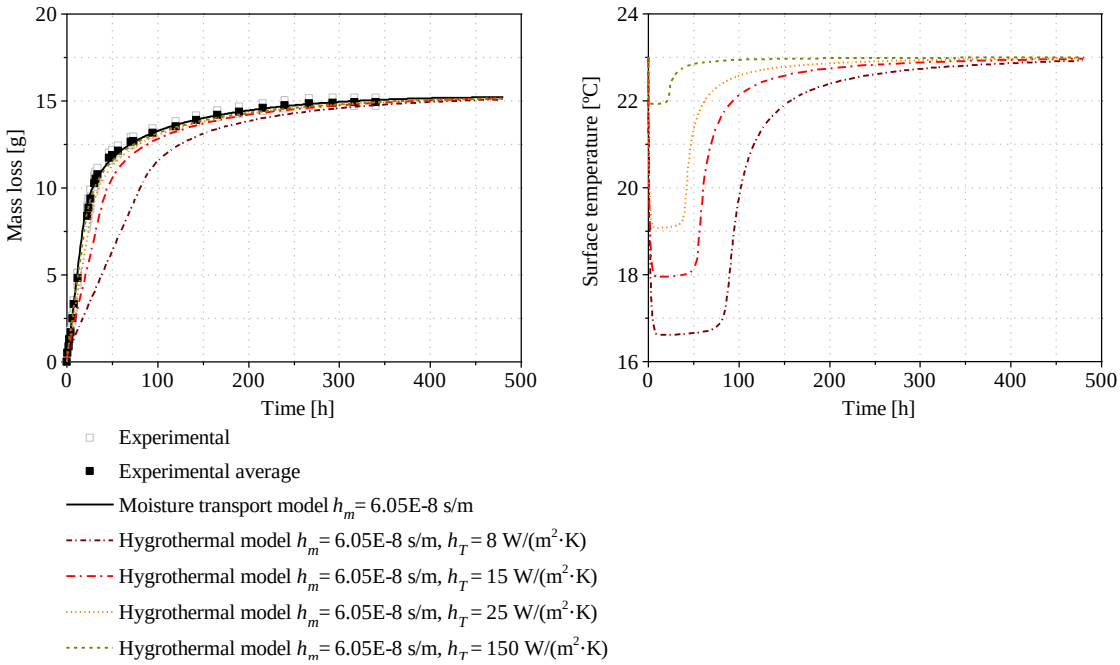

Figure A4.1. Hygrothermal simulation of drying using a fixed convective mass transfer coefficient: (a) moisture mass loss as a function of time; (b) temperature at the exposed surface as a function of time. Note: The experimental results of brick cubes drying in the extrusion direction are used as a reference.

A4.2.2 Parametric study II

The results of the second group of sensitivity analyses are presented in Figure A4.2. It is shown that the parallel variation of h_T and h_m following the Lewis analogy also affects the mass loss rate during the first drying stage. Interestingly, the parallel variation does not affect the temperature drop at the exposed surface of the material, merely the duration of such temperature decrease. As in the previous case, the end of the first drying stage is marked by increasing surface temperature.

Assuming the validity of the Lewis analogy, the best-fitting value of h_T lies around 25 $\mathrm{W/(m^2 \cdot K)}$, therefore $h_{m,Le} = 1.93\mathrm{E{-}7\ s/m}$. With these convective transfer coefficients, the simulated mass loss evolution matches the experimental results quite accurately and the surface temperature falls around 17 °C, which is the expected wet bulb temperature according to the environmental conditions.

In conclusion, the hygrothermal model can be used to simulate drying processes with great accuracy. Nonetheless, the first drying stage must be ultimately calibrated by means of both the convective heat and convective mass transfer coefficients. If the Lewis analogy is assumed, the calibration can be done

with the heat transfer coefficient alone. In practice and considering the agreement of mass loss results between both models, the hygrothermal methodology is equivalent to the use of a moisture transport model with the convective mass transfer coefficient employed as the main variable for calibration. Provided that the analysis of temperature is not a major objective of the work, the moisture transport model is still preferred for the simulation of drying processes.

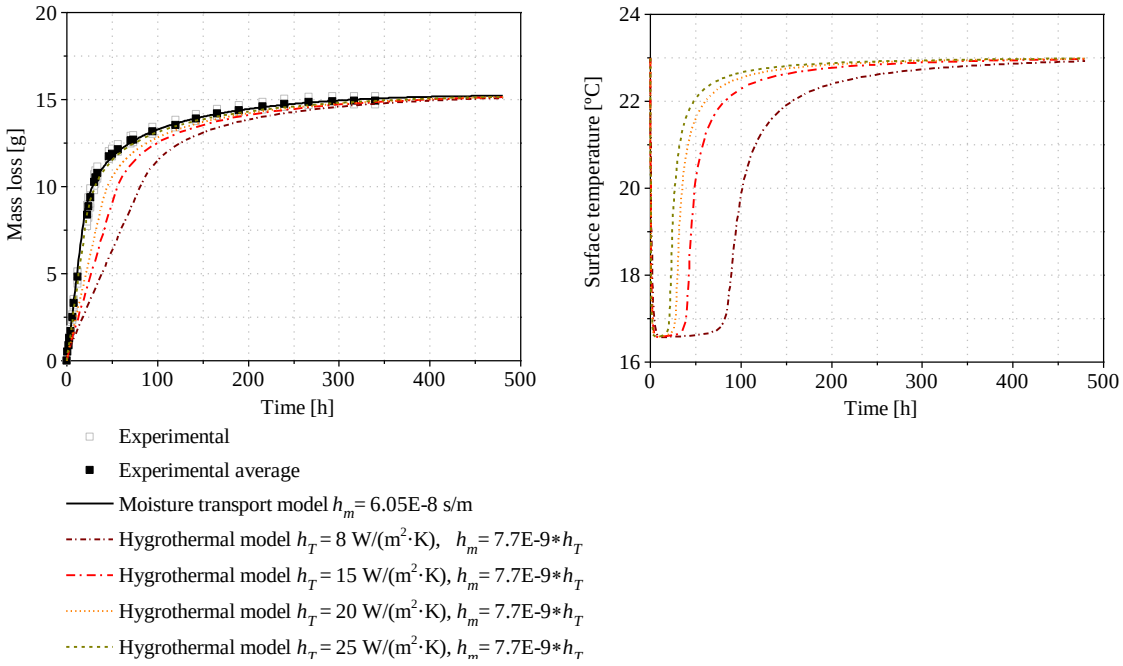

Figure A4.2. Hygrothermal simulation of drying considering the Lewis analogy: (a) moisture mass loss as a function of time; (b) temperature at the exposed surface as a function of time. Note: The experimental results of brick cubes drying in the extrusion direction are used as a reference.

References

Aït Oumériane, Y., Pierre, A., el Mankibi, F., Lepiller, V., Gasnier, M., & Désévaux, P. (2021). Hygrothermal properties of an early 20th century clay brick from eastern France: Experimental characterization and numerical modelling. *Construction and Building Materials*, *273*, 121763. https://doi.org/10.1016/j.conbuildmat.2020.121763

Alawadhi, E. M. (2008). Thermal analysis of a building brick containing phase change material. *Energy and Buildings*, *40*(3), 351–357. https://doi.org/10.1016/j.enbuild.2007.03.001

Allam, R., Issaadi, N., Belarbi, R., El-Meligy, M., & Altahrany, A. (2018). Hygrothermal behavior for a clay brick wall. *Heat and Mass Transfer*, *54*(6), 1579–1591. https://doi.org/10.1007/s00231-017-2271-5

Amde, A. M., Martin, J. v., & Colville, J. (2004). The effects of moisture on compressive strength and modulus of brick masonry. *13th International Brick and Block Masonry Conference (IB2MaC)*.

Anzani, A., Binda, L., & Roberti, G. M. (2000). The effect of heavy persistent actions into the behaviour of ancient masonry. *Materials and Structures*, *33*(4), 251–261. https://doi.org/10.1007/BF02479335

Anzani, A., Garavaglia, E., & Binda, L. (2009). Long-term damage of historic masonry: A probabilistic model. *Construction and Building Materials*, *23*(2), 713–724. https://doi.org/10.1016/j.conbuildmat.2008.02.010

Arandigoyen, M., & Alvarez, J. I. (2007). Pore structure and mechanical properties of cement–lime mortars. *Cement and Concrete Research*, *37*(5), 767–775. https://doi.org/10.1016/j.cemconres.2007.02.023

ASTM D4404-18. (2018). *Standard Test Method for Determination of Pore Volume and Pore Volume Distribution of Soil and Rock by Mercury Intrusion Porosimetry*.

ASTM E96/E96M-22. (2022). *Standard Test Methods for Water Vapor Transmission of Materials*.

Azenha, M. (2009). *Numerical simulation of the structural behavior of concrete since its early ages*. Ph.D. dissertation, Dept. Civil Engineering, University of Porto.

Azevedo, A. (2019). *Interface Influence on Moisture Transport in Building Components*. Ph.D. dissertation, Dept. Civil Engineering, University of Porto.

Bažant, Z. P., & Thonguthai, W. (1987). Pore pressure and drying of concrete at high temperature. *Journal of the Engineering Mechanics Division*, *104*(5), 1059–1079.

Bear, J., & Bachmat, Y. (1990). *Introduction to Modeling of Transport Phenomena in Porous Media*. Springer Netherlands. https://doi.org/10.1007/978-94-009-1926-6

Belarbi, R., Qin, M., Aït-Mokhtar, A., & Nilsson, L.-O. (2008). Experimental and theoretical investigation of non-isothermal transfer in hygroscopic building materials. *Building and Environment*, *43*(12), 2154–2162. https://doi.org/10.1016/j.buildenv.2007.12.014

Belleudy, C., Woloszyn, M., Chhay, M., & Cosnier, M. (2016). A 2D model for coupled heat, air, and moisture transfer through porous media in contact with air channels. *International Journal of Heat and Mass Transfer*, *95*, 453–465. https://doi.org/10.1016/j.ijheatmasstransfer.2015.12.030

Bellini, A., Bovo, M., & Mazzotti, C. (2019). Experimental and numerical evaluation of fiber–matrix interface behaviour of different FRCM systems. *Composites Part B: Engineering*, *161*, 411–426. https://doi.org/10.1016/j.compositesb.2018.12.115

Bergman, T. L., & Lavine, A. S. (2017). *Fundamentals of Heat and Mass Transfer* (8th ed.). John Wiley & Sons.

Bianchi Janetti, M., Colombo, L. P. M., Ochs, F., & Feist, W. (2018). Effect of evaporation cooling on drying capillary active building materials. *Energy and Buildings*, *166*, 550–560. https://doi.org/10.1016/j.enbuild.2017.12.048

Bianchi Janetti, M., & Janssen, H. (2020). Impact of the drying rate on the moisture retention curve of porous building materials. *Construction and Building Materials*, *258*, 119451. https://doi.org/10.1016/j.conbuildmat.2020.119451

Binda, L., Anzani, A., & Saisi, A. (2007). Failures due to long-term behaviour of heavy structures. In *Learning from Failure* (pp. 1–28). WIT Press. https://doi.org/10.2495/978-1-84564-057-6/01

Binda, L., Gatti, G., Mangano, G., Poggi, C., & Landriani, G. (1992). The Collapse of the Civic Tower of Pavia: A Survey of the Materials and Structure. *Masonry International*, *6*(1), 11–20.

Bompa, D. v., & Elghazouli, A. Y. (2020a). Experimental and numerical assessment of the shear behaviour of lime mortar clay brick masonry triplets. *Construction and Building Materials*, *262*, 120571. https://doi.org/10.1016/j.conbuildmat.2020.120571

Bompa, D. v., & Elghazouli, A. Y. (2020b). Compressive behaviour of fired–clay brick and lime mortar masonry components in dry and wet conditions. *Materials and Structures*, *53*(3), 60. https://doi.org/10.1617/s11527-020-01493-w

Bompa, D. v., & Elghazouli, A. Y. (2021). Mechanical properties of hydraulic lime mortars and fired clay bricks subjected to dry–wet cycles. *Construction and Building Materials*, *303*, 124458. https://doi.org/10.1016/j.conbuildmat.2021.124458

Börjesson, F. (2013). *An investigation of the water vapour resistance*. Master's Thesis, Dept. Physics and Engineering Physics, Chalmers University.

Brocken, H. J. P. (1998). *Moisture transport in brick masonry: the grey area between bricks*. Ph.D. dissertation, Dept. Built Environment, Technische Universiteit Eindhoven.

Bromblet, P. (1999). Properties and durability of air lime-based mortars for limestone repairs on monuments. In P. Bartos, C. J. W. P. Groot, & J. J. Hughes (Eds.), *International RILEM Workshop on Historic Mortars: Characteristics and Tests* (pp. 327–337). RILEM Publications SARL.

Brooks, J. J. (2015). Moisture Movement of Clay Brick Masonry. In *Concrete and Masonry Movements* (pp. 223–253). Elsevier. https://doi.org/10.1016/B978-0-12-801525-4.00008-X

Brunauer, S., Emmett, P. H., & Teller, E. (1938). Adsorption of Gases in Multimolecular Layers. *Journal of the American Chemical Society*, *60*(2), 309–319.

BS EN 772-21. (2011). *Methods of test for masonry units – Part 21: Determination of water absorption of clay and calcium silicate masonry units by cold water absorption*.

Calle, K., de Kock, T., Cnudde, V., & van den Bossche, N. (2019). Liquid moisture transport in combined ceramic brick and natural hydraulic lime mortar samples: Does the hygric interface resistance dominate the moisture transport? *Journal of Building Physics*, *43*(3), 208–228. https://doi.org/10.1177/1744259119857762

Cammerer, W. F. (1995). *Wärme- und Kälteschutz im Bauwesen und in der Industrie* (5th ed.). Springer Berlin Heidelberg. https://doi.org/10.1007/978-3-642-78635-8

Cardani, G., Valluzzi, M. R., Panizza, M., Girardello, P., & Binda, L. (2015). Influence of salt crystallization on composites–to–masonry bond evaluated on site by pull–off tests. *Key Engineering Materials*, *624*, 338–345. https://doi.org/10.4028/www.scientific.net/KEM.624.338

Carmeliet, J. (2001). Coupling of Damage and Fluid-solid Interactions in Quasi-brittle Unsaturated Porous Materials. In W. Ehlers (Ed.), *IUTAM Symposium on Theoretical and Numerical Methods in Continuum Mechanics of Porous Materials* (pp. 307–312). Kluwer Academic Publishers. https://doi.org/10.1007/0-306-46953-7_43

Carmeliet, J. (2015). Influence of Damage and Moisture on the Nonlinear Hysteretic Behavior of Quasi-Brittle Materials. In A. H. Kim & R. A. Guyer (Eds.), *Nonlinear Elasticity and Hysteresis: Fluid-Solid Coupling in Porous Media* (1st ed., pp. 81–104). Wiley-VCH Verlag GmbH & Co. KGaA. https://doi.org/10.1002/9783527665068.ch4

Carmeliet, J., Delerue, J.-F., Vandersteen, K., & Roels, S. (2004). Three-dimensional liquid transport in concrete cracks. *International Journal for Numerical and Analytical Methods in Geomechanics*, *28*(78), 671–687. https://doi.org/10.1002/nag.373

Carmeliet, J., Derome, D., Dressler, M., & Guyer, R. A. (2013). Nonlinear Poro-Elastic Model for Unsaturated Porous Solids. *Journal of Applied Mechanics*, *80*(2). https://doi.org/10.1115/1.4007921

Carmeliet, J., Hens, H., Roels, S., Adan, O., Brocken, H., Cerny, R., Pavlik, Z., Hall, C., Kumaran, K., & Pel, L. (2004). Determination of the Liquid Water Diffusivity from Transient Moisture Transfer Experiments. *Journal of Thermal Envelope and Building Science*, *27*(4), 277–305. https://doi.org/10.1177/1097196304042324

Carmeliet, J., Janssen, H., & Derluyn, H. (2007). An improved moisture diffusivity model for porous building materials. *Proceedings of the 12th Symposium for Building Physics*, 228–235.

Carmeliet, J., & Roels, S. (2001). Determination of the Isothermal Moisture Transport Properties of Porous Building Materials. *Journal of Thermal Envelope and Building Science*, *24*, 183–210. https://doi.org/10.1106/Y6T2-9LLP-04Y5-AN6T

Carmeliet, J., & Roels, S. (2002). Determination of the Moisture Capacity of Porous Building Materials. *Journal of Thermal Envelope and Building Science*, *25*(3), 209–237. https://doi.org/10.1106/109719602022835

Carvill, J. (1993). Engineering materials. In *Mechanical Engineer's Data Handbook* (pp. 218–266). Elsevier. https://doi.org/10.1016/B978-0-7506-1014-8.50011-8

Castellazzi, G., Colla, C., de Miranda, S., Formica, G., Gabrielli, E., Molari, L., & Ubertini, F. (2013). A coupled multiphase model for hygrothermal analysis of masonry structures and prediction of stress induced by salt crystallization. *Construction and Building Materials*, *41*, 717–731. https://doi.org/10.1016/j.conbuildmat.2012.12.045

Castellazzi, G., de Miranda, S., Formica, G., Molari, L., & Ubertini, F. (2015). Coupled hygro-mechanical multiscale analysis of masonry walls. *Engineering Structures*, *84*, 266–278. https://doi.org/10.1016/j.engstruct.2014.11.034

Castellazzi, G., de Miranda, S., Grementieri, L., Molari, L., & Ubertini, F. (2014). Modelling of Non-Isothermal Salt Transport and Crystallization in Historic Masonry. *Key Engineering Materials*, *624*, 222–229. https://doi.org/10.4028/www.scientific.net/KEM.624.222

Castellazzi, G., de Miranda, S., Grementieri, L., Molari, L., & Ubertini, F. (2015). Multiphase model for hygrothermal analysis of porous media with salt crystallization and hydration. *Materials and Structures*, *49*(3), 1039–1063. https://doi.org/10.1617/s11527-015-0557-y

Castellazzi, G., de Miranda, S., Grementieri, L., Molari, L., & Ubertini, F. (2016). Multiphase model for hygrothermal analysis of porous media with salt crystallization and hydration. *Materials and Structures*, *49*(3), 1039–1063. https://doi.org/10.1617/s11527-015-0557-y

Celia, M. A., Bouloutas, E. T., & Zarba, R. L. (1990). A general mass-conservative numerical solution for the unsaturated flow equation. *Water Resources Research*, *26*(7), 1483–1496. https://doi.org/10.1029/WR026i007p01483

Cerný, R., Maděra, J., Poděbradská, J., Toman, J., Drchalová, J., Klecka, T., Jurek, K., & Rovnaníková, P. (2000). The effect of compressive stress on thermal and hygric properties of Portland cement mortar in wide temperature and moisture ranges. *Cement and Concrete Research*, *30*(8), 1267–1276. https://doi.org/10.1016/S0008-8846(00)00310-0

Choo, J., & Sun, W. (2018). Cracking and damage from crystallization in pores: Coupled chemo-hydro-mechanics and phase-field modeling. *Computer Methods in Applied Mechanics and Engineering*, *335*, 347–379. https://doi.org/10.1016/j.cma.2018.01.044

Climate and Average Weather Year–Round in Guimarães, Portugal. (2022). Weather Spark. https://weatherspark.com/y/32437/Average-Weather-in-Guimar%C3%A3es-Portugal-Year-Round

Climate and Average Weather Year–Round in Pavia, Italy. (2022). Weather Spark. https://weatherspark.com/y/62495/Average-Weather-in-Pavia-Italy-Year-Round

Coelho, G. B. A., Silva, H. E., & Henriques, F. M. A. (2018). Calibrated hygrothermal simulation models for historical buildings. *Building and Environment*, *142*, 439–450. https://doi.org/10.1016/j.buildenv.2018.06.034

COMSOL. (2021). *COMSOL Multiphysics ® Version 6.0* (6.0). COMSOL AB.

Conceição, J., Faria, R., & Azenha, M. (2017). Thermo–Mechanical Analysis of an Arch Dam Monolith During Construction. *Proceedings of the Congress on Numerical Methods in Engineering CMN 2017, Valencia, Spain, 3–5 July 2017*.

Corinaldesi, V., Mazzoli, A., & Moriconi, G. (2011). Mechanical behaviour and thermal conductivity of mortars containing waste rubber particles. *Materials and Design*, *32*(3), 1646–1650. https://doi.org/10.1016/j.matdes.2010.10.013

Cultrone, G., Sebastián, E., Elert, K., de la Torre, M. J., Cazalla, O., & Rodriguez–Navarro, C. (2004). Influence of mineralogy and firing temperature on the porosity of bricks. *Journal of the European Ceramic Society*, *24*, 547–564. https://doi.org/10.1016/S0955-2219(03)00249-8

D'Altri, A. M., & de Miranda, S. (2020). Environmentally-induced loss of performance in FRP strengthening systems bonded to full-scale masonry structures. *Construction and Building Materials*, *249*, 118757. https://doi.org/10.1016/j.conbuildmat.2020.118757

D'Altri, A. M., de Miranda, S., Castellazzi, G., & Sarhosis, V. (2018). A 3D detailed micro–model for the in–plane and out–of–plane numerical analysis of masonry panels. *Computers & Structures*, *206*, 18–30. https://doi.org/10.1016/j.compstruc.2018.06.007

de Freitas, V. P., Abrantes, V., & Crausse, P. (1996). Moisture migration in building walls: Analysis of the interface phenomena. *Building and Environment*, *31*(2), 99–108. https://doi.org/10.1016/0360-1323(95)00027-5

de Miranda, S., D'Altri, A. M., & Castellazzi, G. (2019). Modeling environmental ageing in masonry strengthened with composites. *Engineering Structures*, *201*, 109773. https://doi.org/10.1016/j.engstruct.2019.109773

Defraeye, T., Blocken, B., & Carmeliet, J. (2013). Influence of uncertainty in heat–moisture transport properties on convective drying of porous materials by numerical modelling. *Chemical Engineering Research and Design*, *91*(1), 36–42. https://doi.org/10.1016/j.cherd.2012.06.011

Delgado, J. M. P. Q., Azevedo, A. C., & Guimarães, A. S. (2019a). *Drying Kinetics in Building Materials and Components: The Interface Influence*. Springer. https://doi.org/10.1007/978-3-030-31860-4

Delgado, J. M. P. Q., Azevedo, A. C., & Guimarães, A. S. (2019b). Hygrothermal Properties of the Tested Materials. In *Drying Kinetics in Building Materials and Components* (pp. 3–32). Springer. https://doi.org/10.1007/978-3-030-31860-4_2

Depraetere, W., Carmeliet, J., & Hens, H. (1999). Moisture transfer at interfaces of porous materials: Measurements and simulations. In P. Bartos, C. J. W. P. Groot, & J. J. Hughes (Eds.), *International RILEM Workshop on Historic Mortars: Characteristics and Tests* (pp. 249–259).

Derluyn, H., Janssen, H., & Carmeliet, J. (2011). Influence of the nature of interfaces on the capillary transport in layered materials. *Construction and Building Materials*, *25*(9), 3685–3693. https://doi.org/10.1016/j.conbuildmat.2011.03.063

Derluyn, H., Moonen, P., & Carmeliet, J. (2014). Deformation and damage due to drying-induced salt crystallization in porous limestone. *Journal of the Mechanics and Physics of Solids*, *63*, 242–255. https://doi.org/10.1016/j.jmps.2013.09.005

Descamps, F. (1997). *Continuum and discrete modelling of isothermal water and air flow in porous media*. Ph.D. dissertation, Building physics laboratory, KU Leuven.

di Tommaso, A., Olivetti, G. C., Lacidogna, G., Invernizzi, S., & Carpinteri, A. (2021). Garisenda tower in Bologna (Italy): Structural assessment and numerical simulation. *7th International Conference on Mechanics of Masonry Structures Strengthened with Composite Materials (MuRiCo7)*, 325–332.

EN 197-1:2011. (2011). *Cement. Composition, specifications and conformity criteria for common cements*.

EN 772-1:2011. (2011). *Methods of test for masonry units – Part 1: Determination of compressive strength*. European Committee for Standardization.

EN 772-11:2011. (2011). *Methods of test for masonry units – Part 11: Determination of water absorption of aggregate concrete, autoclaved aerated concrete, manufactured stone and natural stone masonry units due to capillary action and the initial rate of water absorption of clay*.

EN 13009:2000. (2000). *Hygrothermal performance of building materials and products — Determination of hygric expansion coefficient*.

EN 15803:2009. (2009). *Conservation of cultural property - Test methods - Determination of water vapour permeability (δp)*.

EN 16322:2013. (2013). *Conservation of cultural property - Test methods - Determination of drying properties*.

EN ISO 10456:2007. (2007). *Building materials and products – Hygrohtermal properties: Tabulated design values and procedures for determining declared and design thermal values (ISO 10456:2007)*. International Organization for Standardization. https://doi.org/10.15713/ins.mmj.3

EN ISO 12570:2000 + A1:2013. (2000). *Hygrothermal performance of building materials and products - Determination of moisture content by drying at elevated temperature*.

EN ISO 12571:2013. (2013). *Hygrothermal performance of building materials and products – Determination of hygroscopic sorption properties*.

EN ISO 12572:2016. (2016). *Hygrothermal performance of building materials and products – Determination of water vapour transmission properties – Cup method*.

EN ISO 15148:2002+A1:2016. (2016). *Hygrothermal performance of building materials and products – Determination of water absorption coefficient by partial immersion*.

Faria, P., & Silva, V. (2019). Natural Hydraulic Lime Mortars: Influence of the Aggregates. In J. Hughes, J. Válek, & C. J. W. P. Groot (Eds.), *Historic Mortars: Advances in Research and Practical Conservation* (pp. 185–199). Springer International Publishing. https://doi.org/10.1007/978-3-319-91606-4_14

Feng, C., Guimarães, A. S., Ramos, N., Sun, L., Gawin, D., Konca, P., Hall, C., Zhao, J., Hirsch, H., Grunewald, J., Fredriksson, M., Hansen, K. K., Pavlík, Z., Hamilton, A., & Janssen, H. (2020). Hygric properties of porous building materials (VI): A round robin campaign. *Building and Environment*, *185*, 107242. https://doi.org/10.1016/j.buildenv.2020.107242

Feng, C., & Janssen, H. (2016). Hygric properties of porous building materials (II): Analysis of temperature influence. *Building and Environment*, *99*, 107–118. https://doi.org/10.1016/j.buildenv.2016.01.016

Feng, C., & Janssen, H. (2017). The influence of temperature on the capillary absorption coefficient - A confrontation of two recent papers in building and environment. *Building and Environment*, *116*, 257–258. https://doi.org/10.1016/j.buildenv.2016.11.049

Feng, C., & Janssen, H. (2018). Hygric properties of porous building materials (III): Impact factors and data processing methods of the capillary absorption test. *Building and Environment*, *134*, 21–34. https://doi.org/10.1016/j.buildenv.2018.02.038

Feng, C., & Janssen, H. (2021). Hygric properties of porous building materials (VII): Full-range benchmark characterizations of three materials. *Building and Environment*, *195*, 107727. https://doi.org/10.1016/j.buildenv.2021.107727

Feng, C., Janssen, H., Feng, Y., & Meng, Q. (2015). Hygric properties of porous building materials: Analysis of measurement repeatability and reproducibility. *Building and Environment*, *85*, 160–172. https://doi.org/10.1016/j.buildenv.2014.11.036

Feng, C., Janssen, H., Wu, C., Feng, Y., & Meng, Q. (2013). Validating various measures to accelerate the static gravimetric sorption isotherm determination. *Building and Environment*, *69*, 64–71. https://doi.org/10.1016/j.buildenv.2013.08.005

Fernandes, F. M., & Lourenço, P. B. (2007). Estado da arte sobre tijolos antigos. *3º Congresso Nacional Da Construção, Coimbra, Portugal*.

Fernandes, F. M., Lourenço, P. B., & Castro, F. (2010). Ancient clay bricks: manufacture and properties. In D. M. Bostenaru, R. Přikryl, & A. Török (Eds.), *Materials, Technologies and Practice in Historic Heritage Structures*. Springer. https://doi.org/10.1007/978-90-481-2684-2

Ferretti, D., & Bazant, Z. P. (2006a). Stability of ancient masonry towers: Moisture diffusion, carbonation and size effect. *Cement and Concrete Research*, *36*(7), 1379–1388. https://doi.org/10.1016/j.cemconres.2006.03.013

Ferretti, D., & Bazant, Z. P. (2006b). Stability of ancient masonry towers: Stress redistribution due to drying, carbonation, and creep. *Cement and Concrete Research*, *36*(7), 1389–1398. https://doi.org/10.1016/j.cemconres.2006.03.014

Ferroukhi, M. Y., Abahri, K., Belarbi, R., Limam, K., & Nouviaire, A. (2016). Experimental validation of coupled heat, air and moisture transfer modeling in multilayer building components. *Heat and Mass Transfer*, *52*(10), 2257–2269. https://doi.org/10.1007/s00231-015-1740-y

Foraboschi, P., & Vanin, A. (2014). Experimental investigation on bricks from historical Venetian buildings subjected to moisture and salt crystallization. *Engineering Failure Analysis*, *45*, 185–203. https://doi.org/10.1016/j.engfailanal.2014.06.019

Fořt, J., Čáchová, M., Vejmelková, E., & Černý, R. (2018). Mechanical and hygric properties of lime plasters modified by biomass fly ash. *IOP Conference Series: Materials Science and Engineering*, *365*(3). https://doi.org/10.1088/1757-899X/365/3/032059

Franzoni, E., Gentilini, C., Graziani, G., & Bandini, S. (2014). Towards the assessment of the shear behaviour of masonry in on–site conditions: A study on dry and salt/water conditioned brick masonry triplets. *Construction and Building Materials*, *65*, 405–416. https://doi.org/10.1016/j.conbuildmat.2014.05.002

Franzoni, E., Gentilini, C., Graziani, G., & Bandini, S. (2015). Compressive behaviour of brick masonry triplets in wet and dry conditions. *Construction and Building Materials*, *82*, 45–52. https://doi.org/10.1016/j.conbuildmat.2015.02.052

Franzoni, E., Gentilini, C., Santandrea, M., & Carloni, C. (2018). Effects of rising damp and salt crystallization cycles in FRCM–masonry interfacial debonding: Towards an accelerated laboratory test method. *Construction and Building Materials*, *175*, 225–238. https://doi.org/10.1016/j.conbuildmat.2018.04.164

Franzoni, E., Santandrea, M., Gentilini, C., Fregni, A., & Carloni, C. (2019). The role of mortar matrix in the bond behavior and salt crystallization resistance of FRCM applied to masonry. *Construction and Building Materials*, *209*, 592–605. https://doi.org/10.1016/j.conbuildmat.2019.03.059

Froli, M., & Formichi, P. (2002). Statistical analysis of temperature measurements in the Leaning Tower of Pisa in comparison with theoretical predictions Statistische Auswertung der Temperaturmessungem am Schiefen Turm von Pisa im Vergleich mit den theoretischen Vorhersagen. *Bautechnik*, *79*(10), 691–696. https://doi.org/10.1002/bate.200204680

Galbraith, G. H. (1992). *Heat and mass transfer within porous building materials*. Ph.D. dissertation, Dept. Mechanical Engineering, University of Strathclyde.

Gasch, T., Malm, R., & Ansell, A. (2016). A coupled hygro-thermo-mechanical model for concrete subjected to variable environmental conditions. *International Journal of Solids and Structures*, *91*, 143–156. https://doi.org/10.1016/j.ijsolstr.2016.03.004

Gentilini, C., Franzoni, E., Santandrea, M., & Carloni, C. (2019). Salt–Induced Deterioration on FRP–Brick Masonry Bond. In R. Aguilar, D. Torrealva, S. Moreira, M. A. Pando, & L. F. Ramos (Eds.), *Structural Analysis of Historical Constructions* (pp. 1914–1921). Springer. https://doi.org/10.1007/978-3-319-99441-3_205

Ghiassi, B., & Lourenço, P. B. (Eds.). (2019). *Long-term Performance and Durability of Masonry Structures: Degradation Mechanisms, Health Monitoring and Service Life Design.* (1st ed.). Woodhead Publishing. https://doi.org/10.1016/C2016-0-03710-5

Ghiassi, B., Oliveira, D. v., Lourenço, P. B., & Marcari, G. (2013). Numerical study of the role of mortar joints in the bond behavior of FRP-strengthened masonry. *Composites Part B: Engineering*, *46*, 21–30. https://doi.org/10.1016/j.compositesb.2012.10.017

Ghiassi, B., Silva, M., Marcari, G., Oliveira, D. v., & Lourenço, P. B. (2012). Moisture effects on the bond strength of FRP–masonry elements. *Proceedings of Cice 2012*.

Glucklich, J., & Korin, U. (1975). Effect of moisture content on strength and strain energy release rate of cement mortar. *Journal of the American Ceramic Society*, *58*(11–12), 517–521. https://doi.org/10.1111/j.1151-2916.1975.tb18772.x

Granja, J. L., Azenha, M., de Sousa, C., Faria, R., & Barros, J. (2014). Hygrometric assessment of internal relative humidity in concrete: Practical application issues. *Journal of Advanced Concrete Technology*, *12*(8), 250–265. https://doi.org/10.3151/jact.12.250

Grementieri, L., Daghia, F., Molari, L., Castellazzi, G., Derluyn, H., Cnudde, V., & de Miranda, S. (2017). A multi-scale approach for the analysis of the mechanical effects of salt crystallisation in porous media. *International Journal of Solids and Structures*, *126–127*, 225–239. https://doi.org/10.1016/j.ijsolstr.2017.08.009

Groot, C. J. W. P. (1991). First minutes water transport from mortar to brick. *9th International Brick/Block Masonry Conference (IBMaC), Berlin, Germany*, 71–78.

Groot, C. J. W. P. (1997). The characterisation of brick and mortar considering mortar/brick bond. In M. Wu & Y. Qian (Eds.), *Proceedings of the 11th International Brick/Block Masonry Conference* (pp. 50–58). ECS (Engineering Construction Standardization).

Groot, C. J. W. P., & Gunneweg, J. (2010a). The influence of materials characteristics and workmanship on rain penetration in historic fired clay brick masonry. *Heron*, *55*(2), 141–154.

Groot, C. J. W. P., & Gunneweg, J. (2010b). Two views to deal with rain penetration problems in historic fired clay brick masonry. In J. Válek, J. J. Hughes, & C. J. W. P. Groot (Eds.), *Proceedings of the 2nd Conference on Historic Mortars - HMC 2010 and Final Workshop of RILEM TC 203-RHM* (pp. 1005–1014). RILEM Publications SARL.

Groot, C. J. W. P., & Larbi, J. (1999). Influence of water flow (reversal) on bond strength development in young masonry. *Heron*, *44*(2), 63–78.

Guizzardi, M., Derome, D., & Carmeliet, J. (2016). Water uptake in clay brick at different temperatures: Experiments and numerical simulations. *Journal of Building Physics*, *39*(4), 373–389. https://doi.org/10.1177/1744259115578227

Guizzardi, M., Derome, D., Vonbank, R., & Carmeliet, J. (2015). Hygrothermal behavior of a massive wall with interior insulation during wetting. *Building and Environment*, *89*, 59–71. https://doi.org/10.1016/j.buildenv.2015.01.034

Gummerson, R. J., Hall, C., & Hoff, W. D. (1980). Water movement in porous building materials II. Hydraulic suction and sorptivity of brick and other masonry materials. *Building and Environment*, *15*, 101–108. https://doi.org/10.1016/0360-1323(80)90015-3

Güney, B. A., & Caner, E. (2015). Thermal and hygric expansion characteristics of mortars and bricks used in the dome structures of Turkish Baths from 14th and 15th centuries. *Construction and Building Materials*, *95*, 757–761. https://doi.org/10.1016/j.conbuildmat.2015.07.176

Hagentoft, C. E., Adan, O., Adl-Zarrabi, B., Becker, R., Brocken, H., Carmeliet, J., Djebbar, R., Funk, M., Grunewald, J., Hens, H., Kumaran, K., Roels, G., Kalagasidis, A., & Shamir, D. (2003). *HAMSTAD Work Package 2: Final Report - Benchmark Package*.

Hagentoft, C. E., Kalagasidis, A. S., Adl-Zarrabi, B., Roels, S., Carmeliet, J., Hens, H., Grunewald, J., Funk, M., Becker, R., Shamir, D., Adan, O., Brocken, H., Kumaran, K., & Djebbar, R. (2004). Assessment Method of Numerical Prediction Models for Combined Heat, Air and Moisture Transfer in Building Components: Benchmarks for One-dimensional Cases. *Journal of Thermal Envelope and Building Science*, *27*(4), 327–352. https://doi.org/10.1177/1097196304042436

Hall, C., & Hoff, W. D. (2007). Rising damp: capillary rise dynamics in walls. *Proceedings of the Royal Society A: Mathematical, Physical and Engineering Sciences*, *463*, 1871–1884. https://doi.org/10.1098/rspa.2007.1855

Hall, C., & Hoff, W. D. (2009). *Water Transport in Brick, Stone and Concrete* (2nd ed.). CRC Press.

Hall, C., & Tse, T. K.-M. (1986). Water movement in porous building materials VII. The sorptivity of mortars. *Building and Environment*, *21*(2), 113–118. https://doi.org/10.1016/0360-1323(86)90017-X

Hansen, K. K. (1986). *Sorption isotherms. A catalogue* (BYG Rapport TR-192). Technical University of Denmark (DTU).

Hansen, T. K., Bjarlov, S. P., & Puhkuri, R. (2016). Moisture transport properties of brick – Comparison of exposed, impregnated and rendered brick. In *International RILEM Conference on Materials, Systems and Structures in Civil Engineering 2016: segment on Moisture in Materials and Structures* (pp. 351–360). RILEM Publications.

Hanumanthu, K., & Sarkar, K. (2021). Statistical quantification of the effect of temperature on capillary water absorption in some porous building materials. *Building and Environment*, *198*, 107889. https://doi.org/10.1016/j.buildenv.2021.107889

Hendrickx, R., & de Clercq, H. (2019). Heat and Moisture Simulations of Repair Mortars: Benchmark Experiments and Practical Casesin Conservation. In J. J. Hughes, J. Válek, & C. J. W. P. Groot (Eds.), *Historic Mortars: Advances in Research and Practical Conservation* (pp. 319–336). Springer.

Hens, H. (2007). Modeling the Heat, Air, and Moisture Response of Building Envelopes: What Material Properties are Needed, How Trustful Are the Predictions? *Journal of ASTM International*, *4*(2), 1–11. https://doi.org/10.1520/JAI100460

Hens, H. (2016). *Applied Building Physics: Ambient Conditions, Building Performance and Material Properties* (2nd ed.). Ernst & Sohn. https://doi.org/10.1002/9783433607114

Holm, A., Zillig, W., & Künzel, H. (2004). Exterior Surface Temperature and Humidity of Walls — Comparison of Experiment and Numerical Simulation. *Proceedings of the Performance of Exterior Envelopes of Whole Buildings IX International Conference*.

IUPAC. (1972). Manual of Symbols and Terminology for Physicochemical Quantities and Units, Appendix II, Part I, Definitions, Terminology and Symbols in Colloid and Surface Chemistry. *Pure and Applied Chemistry*, *31*.

Jakieła, S., Bratasz, Ł., & Kozłowski, R. (2008). Numerical modelling of moisture movement and related stress field in lime wood subjected to changing climate conditions. *Wood Science and Technology*, *42*, 21–37. https://doi.org/10.1007/s00226-007-0138-5

Janssen, H. (2011). Thermal diffusion of water vapour in porous materials: Fact or fiction? *International Journal of Heat and Mass Transfer*, *54*(7–8), 1548–1562. https://doi.org/10.1016/j.ijheatmasstransfer.2010.11.034

Janssen, H., Blocken, B., & Carmeliet, J. (2007). Conservative modelling of the moisture and heat transfer in building components under atmospheric excitation. *International Journal of Heat and Mass Transfer*, *50*(5–6), 1128–1140. https://doi.org/10.1016/j.ijheatmasstransfer.2006.06.048

Janssen, H., Derluyn, H., & Carmeliet, J. (2012). Moisture transfer through mortar joints: A sharp–front analysis. *Cement and Concrete Research*, *42*(8), 1105–1112. https://doi.org/10.1016/j.cemconres.2012.05.004

Jendele, L., Šmilauer, V., & Červenka, J. (2014). Multiscale hydro-thermo-mechanical model for early-age and mature concrete structures. *Advances in Engineering Software*, *72*, 134–146. https://doi.org/10.1016/j.advengsoft.2013.05.002

Jensen, N. F., Bjarløv, S. P., Rode, C., & Møller, E. B. (2020). Hygrothermal assessment of four insulation systems for interior retrofitting of solid masonry walls through calibrated numerical simulations. *Building and Environment*, *180*, 107031. https://doi.org/10.1016/j.buildenv.2020.107031

Johansson, P., Geving, S., Hagentoft, C. E., Jelle, B. P., Rognvik, E., Kalagasidis, A. S., & Time, B. (2014). Interior insulation retrofit of a historical brick wall using vacuum insulation panels: Hygrothermal numerical simulations and laboratory investigations. *Building and Environment*, *79*, 31–45. https://doi.org/10.1016/j.buildenv.2014.04.014

Kaluarachchi, J. J., & Parker, J. C. (1987). Effects of hysteresis with air entrapment on water flow in the unsaturated zone. *Water Resources Research*, *23*(10), 1967–1976. https://doi.org/10.1029/WR023i010p01967

Karagiannis, N., Karoglou, M., Bakolas, A., & Moropoulou, A. (2016). Building Materials Capillary Rise Coefficient: Concepts, Determination and Parameters Involved. In J. M. P. Q. Delgado (Ed.), *New Approaches to Building Pathology and Durability. Building Pathology and Rehabilitation* (Vol. 6, pp. 27–44). Springer, Singapore. https://doi.org/10.1007/978-981-10-0648-7_2

Karagiozis, A. N. (2001). Advanced Numerical Models for Hygrothermal Research. In H. R. Trechsel (Ed.), *Moisture Analysis and Condensation Control in Building Envelopes – ASTM Manual Series MNL 40* (pp. 90–106). American Society for Testing and Materials.

Karaman, S., Ersahin, S., & Günal, H. (2006). Firing temperature and firing time influence on mechanical and physical properties of clay bricks. *Journal of Scientific & Industrial Research*, *65*, 153–159.

Kell, G. S. (1975). Density, thermal expansivity, and compressibility of liquid water from 0° to 150°: Correlations and tables for atmospheric pressure and saturation reviewed and expressed on 1968 temperature scale. *Journal of Chemical & Engineering Data*, *20*(1), 97–105. https://doi.org/10.1021/je60064a005

Khoshbakht, M., & Lin, M. W. (2010). A finite element model for hygro-thermo-mechanical analysis of masonry walls with FRP reinforcement. *Finite Elements in Analysis and Design*, *46*(10), 783–791. https://doi.org/10.1016/j.finel.2010.04.002

Khoshbakht, M., Lin, M. W., & Berman, J. B. (2006). Analysis of moisture-induced stresses in an FRP composite reinforced masonry structure. *Finite Elements in Analysis and Design*, *42*(5), 414–429. https://doi.org/10.1016/j.finel.2004.12.013

Knarud, J. I., Geving, S., & Kvande, T. (2021). Moisture performance of interior insulated brick wall segments subjected to wetting and drying – A laboratory investigation. *Building and Environment*, *188*, 107488. https://doi.org/10.1016/j.buildenv.2020.107488

Kočí, V., Čáchová, M., Koňáková, D., Vejmelková, E., Jerman, M., Keppert, M., Maděra, J., & Černý, R. (2018). Heat and Moisture Transport and Storage Parameters of Bricks Affected by the Environment. *International Journal of Thermophysics*, *39*, 63. https://doi.org/10.1007/s10765-018-2383-2

Koniorczyk, M., & Gawin, D. (2012). Modelling of salt crystallization in building materials with microstructure – Poromechanical approach. *Construction and Building Materials*, *36*, 860–873. https://doi.org/10.1016/j.conbuildmat.2012.06.035

Krakowiak, K. J., Lourenço, P. B., & Ulm, F. J. (2011). Multitechnique Investigation of Extruded Clay Brick Microstructure. *Journal of the American Ceramic Society*, *94*(9), 3012–3022. https://doi.org/10.1111/j.1551-2916.2011.04484.x

Krus, M. (1996). *Moisture Transport and Storage Coefficients of Porous Mineral Building Materials: Theoretical Principles and New Test Methods*. Fraunhofer IRB Verlag.

Krus, Martin., & Holm, A. (1999). Simple methods to approximate the liquid transport coefficients describing the absorption and drying process. *5th Sympossium Building Physics in the Nordic Countries*, 241–248.

Kumaran, K. (1996). *IEA Annex 24: Heat, Air and Moisture Transfer in Insulated Envelope Parts. Final Report, Volume 3, Taks 3: Material Properties*.

Kumaran, K. (2001). Hygrothermal Properties of Building Materials. In *Moisture Analysis and Condensation Control in Building Envelopes – ASTM Manual Series MNL 40* (pp. 29–65).

Kumaran, K. (2006). A thermal and moisture property database for common building and insulation materials. *ASHRAE Transactions*, *112*(2), 485–497.

Künzel, H. M. (1995). *Simultaneous heat and moisture transport in building components: One- and two-dimensional calculation using simple parameters*. Ph.D. dissertation, Dept. Building Physics, Fraunhofer Institute of Building Physics.

Künzel, H. M., Karagiozis, A. N., & Holm, A. H. (2001). A Hygrothermal Design Tool for Architects and Engineers (WUFI ORNL/IBD). In H. R. Trechsel (Ed.), *Moisture Analysis and Condensation Control in Building Envelopes – ASTM Manual Series MNL 40* (pp. 136–151). American Society for Testing and Materials.

Laaroussi, N., Lauriat, G., Garoum, M., Cherki, A., & Jannot, Y. (2014). Measurement of thermal properties of brick materials based on clay mixtures. *Construction and Building Materials*, *70*, 351–361. https://doi.org/10.1016/j.conbuildmat.2014.07.104

Lanas, J., Pérez Bernal, J. L., Bello, M. A., & Alvarez Galindo, J. I. (2004). Mechanical properties of natural hydraulic lime-based mortars. *Cement and Concrete Research*, *34*(12), 2191–2201. https://doi.org/10.1016/j.cemconres.2004.02.005

Li, H., Harvey, J., & Jones, D. (2013). Multi-dimensional transient temperature simulation and back-calculation for thermal properties of building materials. *Building and Environment*, *59*, 501–516. https://doi.org/10.1016/j.buildenv.2012.09.019

Lin, M. W., Berman, J. B., Khoshbakht, M., Feickert, C. A., & Abatan, A. O. (2006). Modeling of moisture migration in an FRP reinforced masonry structure. *Building and Environment*, *41*(5), 646–656. https://doi.org/10.1016/j.buildenv.2005.02.026

Lourenço, P. B. (1996). *Computational strategies for masonry structures*.

Lourenço, P. B., & Pina–Henriques, J. (2007). Collapse prediction and creep effects. In L. Binda (Ed.), *Learning from Failure: Long–term Behaviour of Heavy Masonry Structures* (pp. 57–81). WIT Press. https://doi.org/10.2495/978-1-84564-057-6/03

Lucchi, E. (2017). Thermal transmittance of historical brick masonries: A comparison among standard data, analytical calculation procedures, and in situ heat flow meter measurements. *Energy and Buildings*, *134*, 171–184. https://doi.org/10.1016/j.enbuild.2016.10.045

Luikov, A. v. (1964). Heat and Mass Transport in Capillary-Porous Bodies. In T. Irvine & J. Hartnett (Eds.), *Advances in Heat Transfer* (Vol. 1, pp. 123–184). Academic Press.

Ma, H. (2014). Mercury intrusion porosimetry in concrete technology: Tips in measurement, pore structure parameter acquisition and application. *Journal of Porous Materials*, *21*(2), 207–215. https://doi.org/10.1007/s10934-013-9765-4

Maekawa, K., Ishida, T., & Kishi, T. (2009). *Multi-scale Modeling of Structural Concrete*. Taylor & Francis.

Maljaee, H., Ghiassi, B., Lourenço, P. B., & Oliveira, D. v. (2016a). FRP–brick masonry bond degradation under hygrothermal conditions. *Composite Structures*, *147*, 143–154. https://doi.org/10.1016/j.compstruct.2016.03.037

Maljaee, H., Ghiassi, B., Lourenço, P. B., & Oliveira, D. v. (2016b). Moisture-induced degradation of interfacial bond in FRP-strengthened masonry. *Composites Part B: Engineering*, *87*, 47–58. https://doi.org/10.1016/j.compositesb.2015.10.022

Maravelaki-Kalaitzaki, P., Bakolas, A., Karatasios, I., & Kilikoglou, V. (2005). Hydraulic lime mortars for the restoration of historic masonry in Crete. *Cement and Concrete Research*, *35*(8), 1577–1586. https://doi.org/10.1016/j.cemconres.2004.09.001

Matysek, P., Stryszewska, T., Kańka, S., & Witkowski, M. (2016). The influence of water saturation on mechanical properties of ceramic bricks – tests on 19th- century and contemporary bricks. *Materiales de Construcción*, *66*(323), e095. https://doi.org/10.3989/mc.2016.07315

Mazars, J., Hamon, F., & Grange, S. (2015). A new 3D damage model for concrete under monotonic, cyclic and dynamic loadings. *Materials and Structures*, *48*(11), 3779–3793. https://doi.org/10.1617/s11527-014-0439-8

McLean, R. C., Galbraith, G. H., & Sanders, C. H. (1990). Testing building materials. *Batiment International, Building Research and Practice*, *18*(2), 82–91. https://doi.org/10.1080/01823329008727018

Medjelekh, D., Ulmet, L., Gouny, F., Fouchal, F., Nait-Ali, B., Maillard, P., & Dubois, F. (2016). Characterization of the coupled hygrothermal behavior of unfired clay masonries: Numerical and experimental aspects. *Building and Environment*, *110*, 89–103. https://doi.org/10.1016/j.buildenv.2016.09.037

Mertens, S. (2009). *Hysteresis, damage and moisture effects in quasi-brittle porous materials*. Ph.D. dissertation, Katholieke Universiteit Leuven.

Monteith, J. L., & Shatleworth, M. H. (2013). *Principles of Environmental Physics* (4th ed.). Elsevier Ltd.

Moonen, P., Sluys, L. J., & Carmeliet, J. (2010). A continuous–discontinuous approach to simulate physical degradation processes in porous media. *International Journal for Numerical Methods in Engineering*, *84*(9), 1009–1037. https://doi.org/10.1002/nme.2924

Mosquera, M. J., Silva, B., Prieto, B., & Ruiz-Herrera, E. (2006). Addition of cement to lime-based mortars: Effect on pore structure and vapor transport. *Cement and Concrete Research*, *36*(9), 1635–1642. https://doi.org/10.1016/j.cemconres.2004.10.041

Mualem, Y. (1976). A new model for predicting the hydraulic conductivity of unsaturated porous media. *Water Resources Research*, *12*, 593–622.

Muñoz, R., & Lourenço, P. B. (2019). Mechanical Behaviour of Metal Anchors in Historic Brick Masonry: An Experimental Approach. In R. Aguilar, D. Torrealva, S. Moreira, M. A. Pando, & L. F. Ramos (Eds.), *Structural Analysis of Historical Constructions - An Interdisciplinary Approach* (pp. 788–798). Springer. https://doi.org/10.1007/978-3-319-99441-3_85

Murray, F. W. (1967). On the computation of saturation vapor pressure. *Journal of Applied Meteorology*, *6*, 203–204. https://doi.org/10.1175/1520-0450(1967)006<0203:OTCOSV>2.0.CO;2

Nunes, C., Pel, L., Kunecký, J., & Slížková, Z. (2017). The influence of the pore structure on the moisture transport in lime plaster–brick systems as studied by NMR. *Construction and Building Materials*, *142*, 395–409. https://doi.org/10.1016/j.conbuildmat.2017.03.086

Ochs, F., Heidemann, W., & Müller-Steinhagen, H. (2008). Effective thermal conductivity of moistened insulation materials as a function of temperature. *International Journal of Heat and Mass Transfer*, *51*(3–4), 539–552. https://doi.org/10.1016/j.ijheatmasstransfer.2007.05.005

Oliveira, R. G., Rodrigues, J. P. C., Miguel Pereira, J., Lourenço, P. B., & Lopes, R. F. R. (2021). Experimental and numerical analysis on the structural fire behaviour of three–cell hollowed concrete masonry walls. *Engineering Structures*, *228*, 111439. https://doi.org/10.1016/j.engstruct.2020.111439

Oliveira, D. v., Lourenço, P. B., & Roca, P. (2006). Cyclic behaviour of stone and brick masonry under uniaxial compressive loading. *Materials and Structures*, *39*(2), 247–257. https://doi.org/10.1617/s11527-005-9050-3

Pavlík, Z., Žumár, J., Medved, I., & Černý, R. (2012). Water Vapor Adsorption in Porous Building Materials: Experimental Measurement and Theoretical Analysis. *Transport in Porous Media*, *91*(3), 939–954. https://doi.org/10.1007/s11242-011-9884-9

Pavlíková, M., Zemanová, L., Pokorný, J., Záleská, M., Jankovský, O., Lojka, M., & Pavlík, Z. (2019). Influence of Wood–Based Biomass Ash Admixing on the Structural, Mechanical, Hygric, and Thermal Properties of Air Lime Mortars. *Materials*, *12*(14), 2227. https://doi.org/10.3390/ma12142227

Pel, L. (1995). *Moisture transport in porous building materials*. Ph.D. dissertation, Technical University of Eindhoven.

Pel, L., Brocken, H., & Kopinga, K. (1996). Determination of moisture diffusivity in porous media using moisture concentration profiles. *International Journal of Heat and Mass Transfer*, *39*, 1273–1280.

Penas, F., Veiga, R., & Gomes, A. (2008). Hydraulic lime mortars to use in old buildings: advantages and drawbacks. *HMC08—1st Historical Mortars Conference 2008: Characterization, Diagnosis, Conservation, Repair and Compatibility*.

Petracca, M., Pelà, L., Rossi, R., Zaghi, S., Camata, G., & Spacone, E. (2017). Micro–scale continuous and discrete numerical models for nonlinear analysis of masonry shear walls. *Construction and Building Materials*, *149*, 296–314. https://doi.org/10.1016/j.conbuildmat.2017.05.130

Philip, J. R., & de Vries, D. A. (1957). Moisture movement in porous materials under temperature gradients. *Eos, Transactions, American Geophysical Union*, *38*(2), 222–232. https://doi.org/10.1029/TR038i002p00222

Pineda, P., García–Martínez, A., & Castizo–Morales, D. (2017). Environmental and structural analysis of cement–based vs. natural material–based grouting mortars. Results from the assessment of strengthening works. *Construction and Building Materials*, *138*, 528–547. https://doi.org/10.1016/j.conbuildmat.2017.02.013

Ponce–Farfán, C., Santillán, D., & Toledo, M. Á. (2020). Thermal Simulation of Rolled Concrete Dams: Influence of the Hydration Model and the Environmental Actions on the Thermal Field. *Water*, *12*(3), 858. https://doi.org/10.3390/w12030858

Prangnell, R. D. (1971). The water vapour resistivity of building materials: A literature survey. *Matériaux et Constructions*, *4*(24), 399–405.

Qin, M., Aït-Mokhtar, A., & Belarbi, R. (2010). Two-dimensional hygrothermal transfer in porous building materials. *Applied Thermal Engineering*, *30*(16), 2555–2562. https://doi.org/10.1016/j.applthermaleng.2010.07.006

Qin, M., Belarbi, R., Aït-Mokhtar, A., & Nilsson, L.-O. (2008). Simultaneous heat and moisture transport in porous building materials: evaluation of nonisothermal moisture transport properties. *Journal of Materials Science*, *43*(10), 3655–3663. https://doi.org/10.1007/s10853-008-2584-3

Qin, M., Belarbi, R., Aït-Mokhtar, A., & Nilsson, L.-O. (2009). Coupled heat and moisture transfer in multi-layer building materials. *Construction and Building Materials*, *23*(2), 967–975. https://doi.org/10.1016/j.conbuildmat.2008.05.015

Qiu, X. (2003). *Moisture transport across interfaces between building materials*. Ph.D. dissertation, Dept. Building, Civil and Environmental Engineering, Concordia University.

Rachwał, B., Bratasz, Ł., Łukomski, M., & Kozłowski, R. (2012). Response of wood supports in panel paintings subjected to changing climate conditions. *Strain*, *48*(5), 366–374. https://doi.org/10.1111/j.1475-1305.2011.00832.x

Raimondo, M., Dondi, M., Mazzanti, F., Stefanizzi, P., & Bondi, P. (2007). Equilibrium moisture content of clay bricks: The influence of the porous structure. *Building and Environment*, *42*, 926–932. https://doi.org/10.1016/j.buildenv.2005.10.017

Ramézani, H., & Jeong, J. (2011). Environmentally motivated modeling of hygro-thermally induced stresses in the layered limestone masonry structures: Physical motivation and numerical modeling. *Acta Mechanica*, *220*, 107–137. https://doi.org/10.1007/s00707-011-0463-5

Ramires, M. L. v., Nieto de Castro, C. A., Nagasaka, Y., Nagashima, A., Assael, M. J., & Wakeham, W. A. (1995). Standard reference data for the thermal conductivity of water. *Journal of Physical and Chemical Reference Data*, *24*(3), 1377–1381. https://doi.org/10.1063/1.555963

Ramirez, R., Ghiassi, B., Pineda, P., & Lourenço, P. B. (2021). Experimental characterization of moisture transport in brick masonry with natural hydraulic lime mortar. *Building and Environment*, *205*, 108256. https://doi.org/10.1016/j.buildenv.2021.108256

Ramirez, R., Ghiassi, B., Pineda, P., & Lourenço, P. B. (2023). Simulation of moisture transport in fired-clay brick masonry structures accounting for interfacial phenomena. *Building and Environment*, *228*, 109838. https://doi.org/10.1016/j.buildenv.2022.109838

RILEM TC 25-PEM. (1980). Recommended tests to measure the deterioration of stone and to assess the effectiveness of treatment methods (Test No. I.1 Porosity accessible to water). In *Matériaux et Constructions* (Vol. 13, Issue 75, pp. 176–179).

Roels, S. (2000). *Modelling unsaturated moisture transport in heterogeneous limestone*. Ph.D. dissertation, Dept. Civil Engineering, Katholieke Universiteit Leuven.

Roels, S., Carmeliet, J., Hens, H., Adan, O., Brocken, H., Cerny, R., Pavlik, Z., Hall, C., Kumaran, K., Pel, L., & Plagge, R. (2004). Interlaboratory Comparison of Hygric Properties of Porous Building Materials. *Journal of Thermal Envelope and Building Science*, *27*(4), 307–325. https://doi.org/10.1177/1097196304042119

Roels, S., Carmeliet, J., Hens, H., Adan, O., Brocken, H., Czerny, R., Hall, C., Hamilton, A., Kumaran, K., Pavlik, Z., Pel, L., Plagge, R., & Tariku, F. (2003). *HAMSTAD Work Package 1: Final Report - Moisture Transfer Properties and Materials Characterisation* (EU Contract G6RD-2000-00260).

Roels, S., Vandersteen, K., & Carmeliet, J. (2003). Measuring and simulating moisture uptake in a fractured porous medium. *Advances in Water Resources*, *26*(3), 237–246. https://doi.org/10.1016/S0309-1708(02)00185-9

Saisi, A., & Gentile, C. (2015). Post-earthquake diagnostic investigation of a historic masonry tower. *Journal of Cultural Heritage*, *16*(4), 602–609. https://doi.org/10.1016/j.culher.2014.09.002

Salager, S., Youssoufi, M. S. el, & Saix, C. (2007). Influence of Temperature on the Water Retention Curve of Soils. Modelling and Experiments. In T. Schanz (Ed.), *Experimental Unsaturated Soil Mechanics* (pp. 251–258). Springer Berlin Heidelberg. https://doi.org/10.1007/3-540-69873-6_24

Sassine, E., Younsi, Z., Cherif, Y., Chauchois, A., & Antczak, E. (2017). Experimental determination of thermal properties of brick wall for existing construction in the north of France. *Journal of Building Engineering*, *14*, 15–23. https://doi.org/10.1016/j.jobe.2017.09.007

Scheffler, G. (2008). *Validation of hygrothermal material modelling under consideration of the hysteresis of moisture storage*. Ph.D. dissertation, Dept. Civil Engineering, Dresden University of Technology.

Schirmer, R. (1938). Die Diffusionswiderstandszahl von Wasserdampf-Luftgemischen und die Verdampfungsgeschwindigkeit. *VDI Beiheft Verfahrenstechnik*, *6*(170).

Sciolti, M. S., Aiello, M. A., & Frigione, M. (2015). Effect of thermo-hygrometric exposure on FRP, natural stone and their adhesive interface. *Composites Part B: Engineering*, *80*, 162–176. https://doi.org/10.1016/j.compositesb.2015.05.041

Seetharam, S. C., Laloy, E., Jivkov, A., Yu, L., Phung, Q. T., Pham, N. P., Kursten, B., & Druyts, F. (2019). A mesoscale framework for analysis of corrosion induced damage of concrete. *Construction and Building Materials*, *216*, 347–361. https://doi.org/10.1016/j.conbuildmat.2019.04.252

Selih, J., Sousa, A., & Bremner, T. (1996). Moisture transport in initially fully saturated concrete during drying. *Transport in Porous Media*, *24*, 81–106.

Sillers, W. S., Fredlund, D. G., & Zakerzaheh, N. (2001). Mathematical attributes of some soil-water characteristic curve models. *Geotechnical and Geological Engineering*, *19*, 243–283. https://doi.org/10.1023/A:1013109728218

Silva, B. A., Ferreira Pinto, A. P., & Gomes, A. (2014). Influence of natural hydraulic lime content on the properties of aerial lime–based mortars. *Construction and Building Materials*, *72*, 208–218. https://doi.org/10.1016/j.conbuildmat.2014.09.010

Silva, B. A., Ferreira Pinto, A. P., & Gomes, A. (2015). Natural hydraulic lime versus cement for blended lime mortars for restoration works. *Construction and Building Materials*, *94*, 346–360. https://doi.org/10.1016/j.conbuildmat.2015.06.058

Siwinska, A., & Garbalinska, H. (2011). Thermal conductivity coefficient of cement-based mortars as air relative humidity function. *Heat and Mass Transfer*, *47*(9), 1077–1087. https://doi.org/10.1007/s00231-011-0772-1

Soulios, V., Jan de Place Hansen, E., Feng, C., & Janssen, H. (2020). Hygric behavior of hydrophobized brick and mortar samples. *Building and Environment*, *176*, 106843. https://doi.org/10.1016/j.buildenv.2020.106843

Soulios, V., Jan de Place Hansen, E., & Peuhkuri, R. (2021). Hygrothermal performance of hydrophobized and internally insulated masonry walls – Simulating the impact of hydrophobization based on experimental results. *Building and Environment*, *187*, 107410. https://doi.org/10.1016/j.buildenv.2020.107410

Straube, J. F., & Burnett, E. F. P. (2001). Overview of Hygrothermal (HAM) Analysis Methods. In H. R. Trechsel (Ed.), *Moisture Analysis and Condensation Control in Building Envelopes – ASTM Manual Series MNL 40* (pp. 81–89). American Society for Testing and Materials.

Sýkora, J., Krejčí, T., Kruis, J., & Šejnoha, M. (2012). Computational homogenization of non-stationary transport processes in masonry structures. *Journal of Computational and Applied Mathematics*, *236*(18), 4745–4755. https://doi.org/10.1016/j.cam.2012.02.031

Szekeres, A. (2014). Thermo-Hygro-Elasticity (THE). In R. B. Hetnarski (Ed.), *Encyclopedia of Thermal Stresses* (pp. 5918–5924). Springer. https://doi.org/10.1007/978-94-007-2739-7

Taliercio, A., & Papa, E. (2007). Modelling of the long-term behaviour of historical masonry towers. In *Learning from Failure* (pp. 153–173). WIT Press. https://doi.org/10.2495/978-1-84564-057-6/07

Tariku, F., Kumaran, K., & Fazio, P. (2010). Transient model for coupled heat, air and moisture transfer through multilayered porous media. *International Journal of Heat and Mass Transfer*, *53*(15–16), 3035–3044. https://doi.org/10.1016/j.ijheatmasstransfer.2010.03.024

Tveit, A. (1966). *Measurements of moisture sorption and moisture permeability of porous materials* (Rapport 45). Norwegian Building Research Institute.

Ullah, Z., Kaczmarczyk, Ł., Grammatikos, S. A., Evernden, M. C., & Pearce, C. J. (2017). Multi–scale computational homogenisation to predict the long–term durability of composite structures. *Computers & Structures*, *181*, 21–31. https://doi.org/10.1016/j.compstruc.2016.11.002

van Genuchten, M. Th. (1980). A closed form equation predicting the hydraulic conductivity of unsaturated soils. *Soil Science Society of America Journal*, *44*, 892–898.

Vargaftik, N. B., Volkov, B. N., & Voljak, L. D. (1983). International tables of the surface tension of water. *Journal of Physical and Chemical Reference Data*, *12*(3), 817–820. https://doi.org/10.1063/1.555688

Vereecken, E., & Roels, S. (2013). Hygric performance of a massive masonry wall: How do the mortar joints influence the moisture flux? *Construction and Building Materials*, *41*, 697–707. https://doi.org/10.1016/j.conbuildmat.2012.12.024

Vereecken, E., & Roels, S. (2019). Wooden beam ends in combination with interior insulation: An experimental study on the impact of convective moisture transport. *Building and Environment*, *148*, 524–534. https://doi.org/10.1016/j.buildenv.2018.10.060

Vereecken, E., Schůtová, P., & Roels, S. (2020). How effective is kaolin clay for the creation of a perfect hydraulic interface contact between materials? *E3S Web of Conferences*, *172*, 14002. https://doi.org/10.1051/e3sconf/202017214002

Vermeltfoort, A. T., Groot, C. J. W. P., & Wijen, E. (1999). Thermal strains in repointed masonry: Preliminary investigations using ESPI. In *International RILEM Workshop on Historic Mortars: Characteristics and Tests* (pp. 217–226). RILEM Publications SARL.

Viaene, P., Vereecken, H., Diels, J., & Feyen, J. (1994). A statistical analysis of six hysteresis models for the moisture retention characteristic. *Soil Science*, *157*(6), 345–355. https://doi.org/10.1097/00010694-199406000-00003

Vivancos, J. L., Soto, J., Perez, I., Ros-Lis, J. v., & Martínez-Máñez, R. (2009). A new model based on experimental results for the thermal characterization of bricks. *Building and Environment*, *44*(5), 1047–1052. https://doi.org/10.1016/j.buildenv.2008.07.016

Wagner, W., & Kretzschmar, H.-J. (2008). *International Steam Tables* (2nd ed.). Springer Berlin Heidelberg. https://doi.org/10.1007/978-3-540-74234-0

Washburn, E. W. (1921). The Dynamics of Capillary Flow. *Physical Review*, *17*(3), 273–283. https://doi.org/10.1103/PhysRev.17.273

Wasik, M., Łapka, P., Cieslikiewicz, Ł., Seredynski, M., Furmanski, P., Pietrak, K., Kubis, M., Wisniewski, T., & Jaworski, M. (2019). Numerical investigation of influence of the temperature and relative humidity of air on the drying process of porous building. *IOP Conference Series: Materials Science and Engineering*, *660*(1), 012020. https://doi.org/10.1088/1757-899X/660/1/012020

Williams–Portal, N., van Schijndel, A. W. M., & Kalagasidis, A. S. (2014). The multiphysics modeling of heat and moisture induced stress and strain of historic building materials and artefacts. *Building Simulation*, *7*(3), 217–227. https://doi.org/10.1007/s12273-013-0153-4

Wilson, M. A., Hoff, W. D., & Hall, C. (1995a). Water movement in porous building materials—XIII. Absorption into a two–layer composite. *Building and Environment*, *30*(2), 209–219.

Wilson, M. A., Hoff, W. D., & Hall, C. (1995b). Water movement in porous building materials—XIV. Absorption into a two-layer composite (SA < SB). *Building and Environment*, *30*(2), 221–227.

Witzany, J., Cejka, T., & Zigler, R. (2010). The effect of moisture on significant mechanical characteristics of masonry. *Engineering Structures and Technologies*, *2*(3), 79–85. https://doi.org/10.3846/skt.2010.11

Xu, Y., & Chung, D. D. L. (2000). Effect of sand addition on the specific heat and thermal conductivity of cement. *Cement and Concrete Research*, *30*(1), 59–61. https://doi.org/10.1016/S0008-8846(99)00206-9

Zhang, Z., & Scherer, G. (2018). Determination of water permeability for a moisture transport model with minimized batch effect. *Construction and Building Materials*, *191*, 193–205. https://doi.org/10.1016/j.conbuildmat.2018.09.194

Zhang, Z., Thiery, M., & Baroghel-Bouny, V. (2015). Numerical modelling of moisture transfers with hysteresis within cementitious materials: Verification and investigation of the effects of repeated wetting-drying boundary conditions. *Cement and Concrete Research*, *68*, 10–23. https://doi.org/10.1016/j.cemconres.2014.10.012

Zhao, J., Feng, S., Grunewald, J., Meissner, F., & Wang, J. (2022). Drying characteristics of two capillary porous building materials: Calcium silicate and ceramic brick. *Building and Environment*, *216*, 109006. https://doi.org/10.1016/j.buildenv.2022.109006

Zhou, M., Li, X., Feng, C., & Janssen, H. (2022). Hygric properties of porous building materials (VIII): Influence of reduced air pressure. *Building and Environment*, *225*, 109680. https://doi.org/10.1016/j.buildenv.2022.109680

Zhou, X., Carmeliet, J., & Derome, D. (2018). Influence of envelope properties on interior insulation solutions for masonry walls. *Building and Environment*, *135*, 246–256. https://doi.org/10.1016/j.buildenv.2018.02.047

Zhou, X., Carmeliet, J., & Derome, D. (2021). Assessment of moisture risk of wooden beam embedded in internally insulated masonry walls with 2D and 3D models. *Building and Environment*, *193*, 107460. https://doi.org/10.1016/j.buildenv.2020.107460

Zhou, X., Derome, D., & Carmeliet, J. (2022). Analysis of moisture risk in internally insulated masonry walls. *Building and Environment*, *212*, 108734. https://doi.org/10.1016/j.buildenv.2021.108734

Zhou, X., Desmarais, G., Vontobel, P., Carmeliet, J., & Derome, D. (2020). Masonry brick–cement mortar interface resistance to water transport determined with neutron radiography and numerical modeling. *Journal of Building Physics*, *44*(3), 251–271. https://doi.org/10.1177/1744259120908967